HELLENIC REPUBLIC
UNIVERSITY OF IOANNINA
SCHOOL OF ENGINEERING
DEPARTMENT OF MATERIALS SCIENCE AND ENGINEERING

Study and simulation of graphene based optoelectronic devices from near infrared to THz

Spyridon-Chrysovalantis Doukas

PhD Dissertation

Ioannina 2022

ΕΛΛΗΝΙΚΗ ΔΗΜΟΚΡΑΤΙΑ
ΠΑΝΕΠΙΣΤΗΜΙΟ ΙΩΑΝΝΙΝΩΝ
ΠΟΛΥΤΕΧΝΙΚΗ ΣΧΟΛΗ
ΤΜΗΜΑ ΜΗΧΑΝΙΚΩΝ ΕΠΙΣΤΗΜΗΣ ΥΛΙΚΩΝ

Μελέτη και προσομοίωση οπτοηλεκτρονικών διατάξεων γραφενίου από το κοντινό υπέρυθρο έως το THz

Σπυρίδων-Χρυσοβαλάντης Δούκας

Διδακτορική διατριβή

Ιωάννινα 2022

«Η έγκριση της διδακτορικής διατριβής από το Τμήμα Μηχανικών Επιστήμης Υλικών της Πολυτεχνικής Σχολής του Πανεπιστημίου Ιωαννίνων δεν υποδηλώνει αποδοχή των γνωμών του συγγραφέα Ν. 5343/32, άρθρο 202, παράγραφος 2».

Ημερομηνία αίτησης του κ. Σπύρίδωνα-Χρυσοβαλάντη Δούκα: 18-01-2017
Ημερομηνία ορισμού Τριμελούς Συμβουλευτικής επιτροπής: 20-02-2017

Μέλη Τριμελούς Συμβουλευτικής επιτροπής:
Επιβλέπων
Ελευθέριος Λοιδωρίκης, Καθηγητής του Τμήματος Μηχανικών Επιστήμης Υλικών της Πολυτεχνικής Σχολής του Πανεπιστημίου Ιωαννίνων
Μέλη
Δημήτριος Παπαγεωργίου, Αναπληρωτής Καθηγητής του Τμήματος Μηχανικών Επιστήμης Υλικών της Πολυτεχνικής Σχολής του Πανεπιστημίου Ιωαννίνων
Γεώργιος Κοπιδάκης, Αναπληρωτής Καθηγητής του Τμήματος Επιστήμης και Τεχνολογίας Υλικών της Σχολής Θετικών και Τεχνολογικών Επιστημών του Πανεπιστημίου Κρήτης

Ημερομηνία ορισμού θέματος: 20-02-2017
«Μελέτη και προσομοίωση φωτονικών διατάξεων γραφενίου από το κοντινό ως το μακρινό υπέρυθρο»
Ημερομηνία τροποποίησης θέματος: 24-05-2022
«Μελέτη και προσομοίωση οπτοηλεκτρονικών διατάξεων γραφενίου από το κοντινό μακρινό υπέρυθρο έως το THz»

ΔΙΟΡΙΣΜΟΣ ΕΠΤΑΜΕΛΟΥΣ ΕΞΕΤΑΣΤΙΚΗΣ ΕΠΙΤΡΟΠΗΣ: 19-9-2022
1. **Ελευθέριος Λοιδωρίκης**, Καθηγητής του Τμήματος Μηχανικών Επιστήμης Υλικών της Πολυτεχνικής Σχολής του Πανεπιστημίου Ιωαννίνων
2. **Δημήτριος Παπαγεωργίου,** Αναπληρωτής Καθηγητής του Τμήματος Μηχανικών Επιστήμης Υλικών της Πολυτεχνικής Σχολής του Πανεπιστημίου Ιωαννίνων
3. **Γεώργιος Κοπιδάκης,** Αναπληρωτής Καθηγητής του Τμήματος Επιστήμης και Τεχνολογίας Υλικών της Σχολής Θετικών και Τεχνολογικών Επιστημών του Πανεπιστημίου Κρήτης
4. **Λεωνίδας Γεργίδης,** Αναπληρωτής Καθηγητής του Τμήματος Μηχανικών Επιστήμης Υλικών της Πολυτεχνικής Σχολής του Πανεπιστημίου Ιωαννίνων
5. **Εμμανουήλ Κριεζής,** Καθηγητής του Τμήματος Ηλεκτρολόγων Μηχανικών και Μηχανικών Υπολογιστών της Πολυτεχνικής Σχολής του Α.Π.Θ.
6. **Κοσμάς Τσακμακίδης,** Επίκουρος Καθηγητής του Τμήματος Φυσικής της Σχολής Θετικών Επιστημών του Ε.Κ.Π.Α.
7. **Μαρία Καφεσάκη,** του Τμήματος Επιστήμης και Τεχνολογίας Υλικών της Σχολής Θετικών και Τεχνολογικών Επιστημών του Πανεπιστημίου Κρήτης

Έγκριση Διδακτορικής Διατριβής με βαθμό **«ΑΡΙΣΤΑ»** στις 20-12-2022

Ο Πρόεδρος του Τμήματος

Απόστολος Αυγερόπουλος
Καθηγητής

ΤΜΗΜΑ ΜΗΧΑΝΙΚΩΝ ΕΠΙΣΤΗΜΗΣ ΥΛΙΚΩΝ
ΠΑΝΕΠΙΣΤΗΜΙΟ ΙΩΑΝΝΙΝΩΝ

Η Γραμματέας του τμήματος

Μαρία Κόντου

Date of Application of Mr. Spyridon-Chrysovalantis Doukas: 18-01-2017
Date of Appointment of PhD Advisory Committee: 20-02-2017

Members of the three-member Advisory Committee:
Thesis Supervisor
Elefterios Lidorikis, Professor, Department of Materials Science and Engineering, School of Engineering, University of Ioannina
Members
Dimitrios Papageorgiou, Associate Professor, Department of Materials Science and Engineering, School of Engineering, University of Ioannina
George Kopidakis, Associate Professor, Department of Materials Science and Technology, School of Sciences and Engineering, University of Crete

Date of dissertation topic assignment: 20-02-2017
«Study and simulation of graphene-based photonic devices from near to far infrared»
Date of dissertation topic modification: 24-05-2022
«Study and simulation of graphene-based optoelectronic devices from near-infrared to THz»

DATE OF APPOINTMENT OF THE SEVEN-MEMBER EXAMINATION COMMITTEE: 19-9-2022

1. **Elefterios Lidorikis**, Professor, Department of Materials Science and Engineering, School of Engineering, University of Ioannina
2. **Dimitrios Papageorgiou,** Associate Professor, Department of Materials Science and Engineering, School of Engineering, University of Ioannina
3. **George Kopidakis,** Associate Professor, Department of Materials Science and Technology, School of Sciences and Engineering, University of Crete
4. **Leonidas Gergidis,** Associate Professor, Department of Materials Science and Engineering, School of Engineering, University of Ioannina
5. **Emmanouil E. Kriezis,** Professor, Department of Electrical and Computer Engineering, School of Engineering, Aristotle University of Thessaloniki
6. **Kosmas Tsakmakidis,** Assistant Professor, Department of Physics, School of Science, National and Kapodistrian University of Athens
7. **Maria Kafesaki,** Associate Professor, Department of Materials Science and Technology, School of Sciences and Engineering, University of Crete

The PhD dissertation was approved with a grade of **«Excellent»** at 20-12-2022

The chairman of the Department

Apostolos Avgeropoulos
Professor

The Secretary of the Department

Maria Kontou

I have a friend who's an artist and has sometimes taken a view which I don't agree with very well. He'll hold up a flower and say "look how beautiful it is", and I'll agree. Then he says "I as an artist can see how beautiful this is but you as a scientist take this all apart and it becomes a dull thing," and I think that he's kind of nutty. First of all, the beauty that he sees is available to other people and to me too, I believe. Although I may not be quite as refined aesthetically as he is ... I can appreciate the beauty of a flower. At the same time, I see much more about the flower than he sees. I could imagine the cells in there, the complicated actions inside, which also have a beauty. I mean it's not just beauty at this dimension, at one centimeter; there's also beauty at smaller dimensions, the inner structure, also the processes. The fact that the colors in the flower evolved in order to attract insects to pollinate it is interesting; it means that insects can see the color. It adds a question: does this aesthetic sense also exist in the lower forms? Why is it aesthetic? All kinds of interesting questions which the science knowledge only adds to the excitement, the mystery and the awe of a flower. It only adds. I don't understand how it subtracts...

Richard P. Feynman

The pleasure of findings things out: The best short works of Richard P. Feynman

Abstract

The transformation of an electrical signal to an optical one, and vice versa, is the main subject of the research field of optoelectronics. These physical processes are key to a variety of applications, including photodetection and ultrafast optical communications. The ever-growing demand for faster, high-performance and cost-effective devices, with a sufficient response at increasingly lower photon energies, pushes conventional materials to their limits. Graphene, a single-atom-thick plane of carbon atoms, has emerged as a prime candidate to fill that gap, since its first isolation in 2004. Its unique electronic and optical properties have sparked a vast amount of research regarding its use in optoelectronic and photonic applications. As a result, huge advancements have been made during the last decade regarding its synthesis and integration with mature semiconductor technology, to realize novel optoelectronic devices.

In this thesis, the use of graphene, alongside mature Si technology, is computationally explored to design and optimize novel graphene-based photodetection and optical modulation schemes. To do so, a self-consistent multi-physics simulation framework is developed, including all graphene's carrier dynamics, accounting for its optical response, carrier heating and cooling, electronic properties and heterojunction formation. The developed framework can be used for full device representation and is utilized to study optoelectronic devices under realistic considerations spanning from near-infrared up to the THz spectra regime.

The devices designed and studied with the aforementioned simulation framework demonstrate graphene's potential and competitiveness for realizing optoelectronic devices in CMOS-compatible configurations. In the near-infrared a free-space optical modulator operating in reflection mode is designed, combining graphene's electro-absorption tunability with dielectric Bragg cavities. Using practical considerations to optimize the device architecture, it shown that deep amplitude modulation ($\sim$ 30 dB) with small insertion loses ($<$3 dB) at GHz modulation frequencies is possible, independently of graphene quality (i.e., carrier mobility). In the mid-infrared, thermionic graphene/Si Schottky photodetectors integrated with dielectric Bragg cavities are presented, utilizing graphene carrier heating to enable photo-thermionic emission across the Schottky barrier in a multi-spectral photodetection scheme. It is shown that under proper device optimization, external responsivity of $\sim$ 1 A/W and detectivity up to 10^7 cm $\mathrm{Hz}^{0.5}$ W^{-1} can be achieved, in an ultrafast photodetection platform. This photodetection scheme is further expanded in the far-infrared regime, where the plasmonic resonances of graphene nanoribbons, forming a series of graphene/Si Schottky contacts, are exploited to generate thermalized carriers, upon plasmon decay, and enable thermionic emission across the junction. In this configuration, it is demonstrated that photocurrent generation can be achieved, enabling the electrical detection of graphene plasmons, with external responsivity up to $\sim$ 110 mA/W and noise equivalent power $\sim$190 pW/$\mathrm{Hz}^{0.5}$. This novel scheme is further utilized to realize label-free chemical sensing, using the surface-enhanced infrared absorption enhancement method,

where the presence of an analyte molecule in the vicinity of graphene can be detected and directly monitored by photocurrent changes, probing its molecular fingerprints. Finally, the developed framework is utilized to provide theoretical support in THz time domain spectroscopy experiments. Simulations, performed within a fitting scheme, yield perfect agreement with experiments and are utilized to interpret the self-induced absorption modulation of $\sim$ 30 dB, realized in a thin-film graphene-based absorber under intense THz illumination, and provide insight into graphene's carrier dynamics upon photoexcitation.

The methods and computational tools developed in this thesis are validated by experiment and can be used for robust and reliable simulations of graphene-based optoelectronics. Furthermore, they are not material-specific, but they can rather be used with alternative material platforms, alongside graphene, for the design and optimization of realistic optoelectronic devices.

Περίληψη

Ο μετασχηματισμός ενός ηλεκτρικού σήματος σε οπτικό, καθώς και η αντίστροφη διαδικασία, αποτελεί το κύριο αντικείμενο του ερευνητικού κλάδου της οπτοηλεκτρονικής. Αυτές οι φυσικές διεργασίες αποτελούν την βάση για ένα μεγάλο εύρος εφαρμογών, συμπεριλαμβανομένης της φωτοανίχνευσης και των εξαιρετικά γρήγορων οπτικών επικοινωνιών. Η συνεχώς αυξανόμενη ζήτηση για ταχύτερες, υψηλών επιδόσεων και οικονομικά αποδοτικότερες συσκευές, με επαρκή απόκριση σε όλο και μεγαλύτερα μήκη κύματος, ωθεί τα συμβατικά υλικά στα όριά τους. Το γραφένιο, ένα μονοατομικού πάχους εξαγωνικό πλέγμα άνθρακα, έχει αναδειχθεί ως ιδανικό υλικό για να καλύψει αυτά τα κενά, από την στιγμή της απομόνωσης του ως μονοατομικό φύλλο το 2004. Οι μοναδικές ηλεκτρονικές και οπτικές ιδιότητές του έχουν πυροδοτήσει πληθώρα ερευνών σχετικά με τη χρήση του σε οπτοηλεκτρονικές και φωτονικές εφαρμογές. Σαν αποτέλεσμα, τεράστια βήματα έχουν επιτευχθεί κατά την τελευταία δεκαετία όσον αφορά τη σύνθεση και την ενσωμάτωσή του με την ώριμη τεχνολογία ημιαγωγών, για την υλοποίηση πρωτοπόρων οπτοηλεκτρονικών διατάξεων.

Σε αυτή τη διατριβή η χρήση του γραφενίου, σε συνεργασία με την ώριμη τεχνολογία πυριτίου, διερευνάται υπολογιστικά για το σχεδιασμό και τη βελτιστοποίηση πρωτοπόρων διατάξεων φωτοανίχνευσης και οπτικής διαμόρφωσης. Για τον σκοπό αυτό, αναπτύχθηκε ένα αυτοσυνεπές υπολογιστικό πακέτο, το οποίο περιλαμβάνει όλο το εύρος της δυναμικής των φορέων του γραφενίου, λαμβάνοντας υπόψιν την θέρμανση και ψύξη των φορέων αυτών, την οπτική απόκριση και τις ηλεκτρονικές ιδιότητες του γραφενίου καθώς και τον σχηματισμό ετεροεπαφών γραφενίου. Το υπολογιστικό πακέτο αυτό μπορεί να χρησιμοποιηθεί για την πλήρη και ρεαλιστική αναπαράσταση διατάξεων και χρησιμοποιείται για τη μελέτη οπτοηλεκτρονικών εφαρμογών που εκτείνονται από το εγγύς υπέρυθρο έως τα THz.

Οι διατάξεις που σχεδιάστηκαν και μελετήθηκαν με το προαναφερθέν υπολογιστικό πακέτο αναδεικνύουν τις δυνατότητες και την ανταγωνιστικότητα του γραφενίου για την υλοποίηση οπτοηλεκτρονικών σχημάτων, πλήρως συμβατών με την τεχνολογία συμπληρωματικών ημιαγωγών μετάλλου-οξειδίου (CMOS). Στο εγγύς υπέρυθρο σχεδιάστηκε ένας οπτικός διαμορφωτής, με σκοπό την διαμόρφωση ανακλαστικότητας, συνδυάζοντας την μεταβαλλόμενη ηλεκτρικά απορρόφηση του γραφενίου με διηλεκτρικές κοιλότητες Bragg. Υιοθετώντας πρακτικές υποθέσεις για την βελτιστοποίηση της αρχιτεκτονικής της διάταξης, δείχνεται ότι η αποδοτική διαμόρφωση του πλάτους της ανακλαστικότητας ($\sim$ 30 dB) με μικρές απώλειες εισαγωγής ($<$ 3 dB) σε υψηλές συχνότητες διαμόρφωσης (GHz) είναι δυνατή, ανεξάρτητα από την ποιότητα του γραφενίου (δηλαδή, την ευκινησία των φορέων του). Στο μέσο υπέρυθρο παρουσιάζονται θερμιονικοί φωτοανιχνευτές ετεροεπαφών Schottky γραφενίου/πυριτίου, εκμεταλλευόμενοι την θέρμανση των φορέων του γραφενίου, με σκοπό την φωτο-θερμιονική εκπομπή τους πάνω από το φράγμα δυναμικού που σχηματίζεται στην διεπιφάνεια της ετεροεπαφής, σε μια πολυφασματική πλατφόρμα φωτοανίχνευσης. Δείχνεται πώς, ύστερα από κατάλληλο σχεδιασμό και βελτιστο-

ποίηση, αποκρισιμότητα ~ 1 A/W και ανιχνευτικότητα $\sim 10^{7}$ cm $\mathrm{Hz}^{0.5}$ W^{-1} είναι επιτεύξιμες, σε μια πλατφόρμα ικανή για εξαιρετικά γρήγορη (GHz) φωτοανίχνευση. Η πλατφόρμα αυτή στην συνέχεια επεκτείνεται στο μακρινό υπέρυθρο, όπου οι πλασμονικοί συντονισμοί σε νανολωρίδες γραφενίου, με τις τελευταίες να σχηματίζουν μια σειρά επαφών Schottky γραφενίου/πυριτίου, εκμεταλλεύονται ώστε να οδηγήσουν σε θέρμανση των φορέων, επιτρέποντας την θερμιονική εκπομπή τους πάνω από το φράγμα δυναμικού. Στην διάταξη αυτή επιδεικνύεται η ικανότητα παραγωγής φωτορεύματος, επιτρέποντας την ηλεκτρική ανίχνευση πλασμονίων γραφενίου, οδηγώντας σε αποκρισιμότητα της τάξης των ~ 110 mA/W και ισοδύναμη ισχύ θορύβου $\sim$ 190 pW/$\mathrm{Hz}^{0.5}$. Η πρωτότυπη αυτή διάταξη χρησιμοποιείται, επιπλέον, για την υλοποίηση ενός χημικού αισθητήρα, μέσω της μεθόδου επιφανειακής ενίσχυσης της υπέρυθρης απορρόφησης (SEIRA), ικανού να ανιχνεύσει την παρουσία ενός αναλύτη ο οποίος βρίσκεται σε εγγύτητα με το γραφένιο, μεταφράζοντας την παρουσία του σε αλλαγές στο φωτορεύμα, αναδεικνύοντας το μοριακό του αποτύπωμα. Τέλος, το υπολογιστικό πακέτο που αναπτύχθηκε σε αυτήν την διατριβή, υλοποιείται για να παρέχει θεωρητική υποστήριξη σε πειράματα φασματοσκοπίας THz στο πεδίο του χρόνου. Οι προσομοιώσεις, σε τέλεια συμφωνία με τα πειράματα, χρησιμοποιούνται για την ερμηνεία της αυτο-επαγόμενης διαμόρφωσης του πλάτος της απορρόφησης, ~ 30 dB, που παρατηρήθηκε σε μια διάταξη λεπτού υμενίου με βάση το γραφένιο ύστερα από ισχυρή ακτινοβόληση με παλμούς ακτινοβολίας THz, παρέχοντας πληροφορίες για την δυναμική των φωτοδιεγερμένων φορέων.

Οι μέθοδοι και τα υπολογιστικά εργαλεία που αναπτύχθηκαν σε αυτή τη διατριβή επικυρώνονται πειραματικά και μπορούν να χρησιμοποιηθούν για την πραγματοποίηση αξιόπιστων προσομοιώσεων οπτοηλεκτρονικών διατάξεων με βάση το γραφένιο. Τέλος, δεν περιορίζονται σε μια συγκεκριμένη οικογένεια υλικών, αλλά μπορούν να χρησιμοποιηθούν με εναλλακτικές πλατφόρμες, παράλληλα με το γραφένιο, για τον ρεαλιστικό σχεδιασμό και την βελτιστοποίηση διατάξεων οπτοηλεκτρονικής.

Acknowledgments

As I try to write this, I find it hard to put together the words that can express my gratitude for the people that supported and assisted me during my Ph.D. studies.

First and foremost, I wish to express my deepest gratitude to my supervisor, Prof. Elefterios Lidorikis, who has always been supportive, kind, and patient towards me since I joined the group several years ago. His attention to detail, academic rigor, and constant drive towards achieving good results made me adopt these values and has resulted in bringing out the best in me. Prof. Lidorikis' comprehensive knowledge of condensed matter physics is a paradigm, being a great motivation for me towards expanding my knowledge in this field. Beyond sharing his knowledge of physics and scientific modeling, Prof. Lidorikis also taught me how to write academic papers, prepare nice and to-the-point presentations, and effectively express scientific ideas to other people. He has always been diligent in finding and pursuing funding opportunities, without which my research would not have been possible, while bringing me interesting collaborations with experts in the field of graphene research. Lefteris is not only an exceptional scientist but a brilliant character as well. He constantly motivated me and encouraged me when I faced difficulties during my Ph.D. studies. It is not a surprise that he has managed to set up a great team, which I have witnessed growing from its birth. Great people to discuss physics and hang out with. I hope that the team will continue to grow stronger and larger. Wherever life takes me now that my Ph.D. is concluded, I will never forget the afternoons spent with Lefteris discussing while staring at the whiteboard. I am greatly indebted to him and could not have asked for better guidance.

Next, I would also like to thank these members that took the time to review my thesis and take part in my Ph.D. defense committee: Prof. Dimitrios Papageorgiou, Prof. George Kopidakis, Prof. Leonidas Gergidis, Prof. Emmanouil Kriezis, Prof. Kosmas Tsakmakidis and Prof. Maria Kafesaki.

During my Ph.D. studies, I received funding from the Graphene Flagship initiative. It goes without saying that, without this financial support, it would not have been able for me to complete this task. Through graphene flagship not only I received funding to realize my research, but I also had the opportunity to take part in exceptional conferences, organized by this research program. The summer school organized by this research initiative, Graphene Study, was a memorable experience during the first year of my Ph.D. studies, motivating me and bringing me in touch with experts in the field of graphene and 2D materials research.

Speaking of experts, I would like to acknowledge Prof. Andrea Ferrari and Prof. Ilya Goykhman for their valuable pieces of advice, remarks, and constant interest as I was developing the simulation framework built during my Ph.D. studies. I am very thankful for the fact that when I began studying graphene, I was lucky enough to be supported by pioneers in the field.

I would also like to acknowledge Dr. Anastasios Koulouklidis and Prof. Stelios

Tzortzakis from IESL-FORTH for providing me with the experimental results discussed in chapter 8. The analysis of these results, with the aid of Dr. Anna Tasolamprou and Prof. Maria Kafesaki, was critical for experimentally validating my calculations. I would like to especially thank Tasos and Anna for the excellent collaboration atmosphere and supportive attitude during this work. I hope that future studies will allow us to work together again soon.

I would also like to thank all my colleagues in Prof. Lidorikis group, with whom we have been all these years together, during both good and hard times. Special thanks to my friends and fellow Ph.D. candidates Ioannis Vangelidis and Alva Dagkli for the countless hours of discussions and cross-checking of our results. Eleftheria Lampadariou, for her kindness and support, going back to our undergraduate studies. Konstantinos Kaklamanis, for always pushing and assisting me to expand my knowledge in programming and computational physics. Also, Dr Dimitris Bellas for sharing his experience and always offer a good laugh at hard times.

Finally, I was lucky enough to have great people to support me during this journey outside the university campus, and I would also like to express my gratitude to them. My friends, Panagiotis and Vardis who, even a couple of hundred kilometers away, were always there to take my mind off physics when I needed to. Vasilis and Agni, always available to offer support, travel through music and offer great beer, especially when I needed these the most. My friend and colleague Spyros, for our fruitful discussions, the laughs, and the countless hours studying physics together during our undergraduate years. My companion in life Alexandra, for her unconditional love and support. I am very lucky to have met someone so special and kind enough, always willing to share my ups and downs during this “fight”. Last but not least, my parents Kostas and Maria and my sister Anastasia, for their never-ending love and support, without which I would not have made it this far.

Publications and conference presentations

Publications covered in this thesis

- **S. Doukas**, A. Chatzilari, A. Dagkli, A. Papagiannopoulos and E. Lidorikis, *Deep and fast free-space electro-absorption modulation in a mobility-independent graphene-loaded Bragg resonator*, Appl. Phys. Lett. 113, 011102 (2018), https://doi.org/10.1063/1.5030699

- **S. Doukas**, P. Mensz, N. Myoung, A. C. Ferrari, I. Goykhman and E. Lidorikis, *Thermionic graphene/silicon Schottky infrared photodetectors*, Phys. Rev. B 105, 115417 (2022), https://doi.org/10.1103/PhysRevB.105.115417

- **S. Doukas**, P. Sharma, I. Goykhman and E. Lidorikis, *Electrical detection of graphene plasmons for mid-infrared photodetection and chemical sensing: A computational study*, Appl. Phys. Lett. 121, 051103 (2022), https://doi.org/10.1063/5.0093981

- A. Koulouklidis, A. Tasolamprou, **S. Doukas**, E. Kyriakou, S. Ergoktas, C. Daskalaki, E. Economou, C. Kocabas, E. Lidorikis, M. Kafesaki and S. Tzortzakis *Ultrafast Terahertz Self-Induced Absorption and Phase Modulation on a Graphene-Based Thin Film Absorber*, ACS Photonics 2022, 9, 9, 3075–3082 (2022), https://doi.org/10.1021/acsphotonics.2c00828

Conference presentations

- **S. Doukas** and E. Lidorikis. *Spectrometer free sensors based on graphene nanoribbons*, Graphene Week 2017, 25–29 September 2017, Athens, Greece

- **S. Doukas**, A. Chatzilari, A. Dagkli, A. Papagiannopoulos and E. Lidorikis, *Deep and fast free-space electro-absorption modulation in a mobility-independent graphene-loaded Bragg resonator*, Nanotexnology 2018, 3–6 July 2018, Thessaloniki, Greece

- **S. Doukas**, P. Mensz, N. Myoung, I. Vangelidis, A. C. Ferrari, I. Goykhman and E. Lidorikis, *Modeling thermionic Graphene/Silicon Schottky IR photodetectors*, Nanotexnology 2019, 2–5 July 2019, Thessaloniki, Greece

- **S. Doukas**, P. Mensz, N. Myoung, I. Vangelidis, A. C. Ferrari, I. Goykhman and E. Lidorikis, *Simulation of thermionic Graphene/Silicon Schottky IR photodetectors*, Graphene Week 2019, 23–27 September 2019, Helsinki, Finland

- **S. Doukas**, A. Koulouklidis, A. Tasolamprou, S. Tzortzakis, I. Goykhman, A. C. Ferrari and E. Lidorikis, *A self-consistent modelling framework for graphene-based photodetectors, sensors, and modulators from mid-infrared to THz*, Graphene Conference 2022, 5–8 July 2022, Aachen, Germany

- **S. Doukas**, A. Koulouklidis, A. Tasolamprou, S. Tzortzakis, I. Goykhman, A. C. Ferrari and E. Lidorikis, *Self-consistent simulation framework for graphene-based optoelectronic devices*, Graphene Week 2022, 5–9 September 2022, Munich, Germany

- **S. Doukas**, A. Koulouklidis, A. Tasolamprou, S. Tzortzakis, I. Goykhman, A. C. Ferrari and E. Lidorikis, *A self-consistent simulation framework for graphene-based optoelectronic devices*,) XXXVI Panhellenic Conference on Solid State Physics and Materials Science, 26 – 28 September 2022, Heraklion, Greece

Contents

List of Figures

List of Tables

Chapter 1

Introduction

1.1 Motivation

Global demand for digital applications has been on the rise for several decades, driving the need for faster, more efficient, more compact, more stable, and cheaper devices. The expanding internet traffic and networked devices [1] put constant pressure on the development of platforms with increased bandwidth and lower power consumption. Optical communications – which involve the exchange and processing of signals using electromagnetic waves – are expected to play a key role in this direction [2, 3], interconnecting both devices as well as data centers. Naturally, a key requirement for the development of optical communication technologies is the transformation of an optical signal to an electric one and vice versa. The former can be achieved with the help of a photodetector - which can convert and quantify incident light into an electrical signal - while the latter is possible using an optical modulator, i.e. a device capable of translating an electrical input waveform into light pulses. Apart from its crucial role in optical communications, photodetectors are one of the most important type of sensors, with a wide variety of applications on environmental [4] and industrial monitoring [5], imaging [6], night vision [7], biomedicine [8], tomography [9] and astronomical observations [10], just to name a few. At the same time, emerging technologies such as the Internet of things [11] and autonomous vehicles [12] are expected to increase the demand for photodetectors even further.

The development of devices for the above applications and technologies lies in the realm of optoelectronics [13], which involve the study of electronic devices that detect and control light and can be considered as a sub-field of photonics. Naturally, the performance of optoelectronic devices is strongly correlated with the associated materials used for their fabrication. Up to date, the golden standard in optoelectronic applications is Silicon (Si) [14, 15] along with the mature complementary metal-oxide semiconductor (CMOS) fabrication process [16, 17]. However, there are several aspects of the ever-expanding industry requirements that Si is striving to cope with. Si technology has managed to keep up with the need of decreased production cost and power consumption through dimensional scaling, reducing the physical dimensions of the manufactured devices every couple of years, an approach which is commonly referred to as Moore's law. While this approach has managed to meet the demands up to date, regarding both electronics and optoelectronics applications, it is reaching its limits due to both technical difficulties in further size reduction [18] as well as the physical boundaries arising from quantum tunneling phenomena [19]. Furthermore, pure Si is unsuitable for photodetection applications regarding wavelengths longer than $\approx 1.13\,\mu m$, given its indirect bandgap of 1.1 eV [20].

While alternative material platforms have been successfully utilized for infrared photodetection beyond Si bandgap, e.g. III-IV materials [21] and HgCdTe [22, 23], covering the spectral range up to $\approx 10\,\mu m$, their heterogeneous integration with Si technology due to lattice mismatch and severe manufacturing costs remains an obstacle. Moreover, common inorganic semiconducting materials are unsuitable for THz applications, since their bandgap far exceeds THz photon energies [24].

From the above it is clear that existing material platforms cannot simultaneously meet all the requirements for the development of next generation optoelectronics. Graphene, with its combination of unique electronic and optical properties, has emerged as an ideal candidate for the realization of novel, cost and power efficient, broadband optoelectronic devices [25].

1.2 Graphene overview

Graphene, being the building block of graphite, was initially studied as early as 1947. Wallace explored the electronic structure of graphene [26] to derive the band structure and electronic properties of graphite. For a long time, the concept of isolated single layer graphene (SLG) was thought to be impossible, according to Mermin-Wegner's theorem which stated that long-range order should not exist in two dimensions [27].

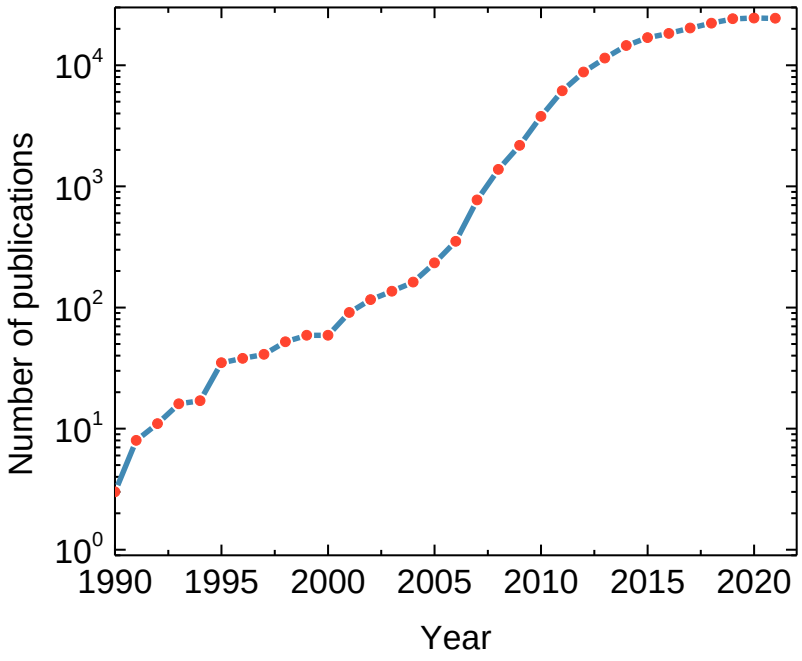

Figure 1.1: Graphene related publications per year. Data retrieved from Scopus (www.scopus.com) searching for the term "Graphene" within the title, abstract or keywords of a publication.

The situation changed in 2004, when Novoselov and Geim isolated graphene flakes (including SLG) with a size of a few micrometers, taking a first glimpse at graphene's exceptional electronic properties [28]. Their groundbreaking work, in which graphene was acquired by exfoliation of highly oriented pyrolytic graphite, set them on a course for winning the 2010 Nobel prize in physics [29, 30]. The isolation of graphene initiated a

vast amount of research regarding this material (fig. 1.1), surpassing 20000 publications per year by the time of the beginning of this thesis. Apart from its potential use in applications, graphene with its unusual electronic properties initiated a new field in condensed matter physics, where quantum relativistic phenomena could be mimicked and studied using table-top experiments [31]. Moreover, the isolation of additional 2D materials, including dielectrics, e.g. hexagonal boron nitride (h-BN) [32], and semiconductors, e.g. MoS_2 [33], along with the semi-metallic graphene, initiated the vivid research field of 2D materials and their heterostructures [34]. The first years after its isolation, graphene related studies were mainly focused on its electronic [28,33,35–39] and mechanical [40,41] properties. However, graphene's optical properties [42] and its potential use in optoelectronics and photonics [25] soon attracted the interest of the research community. The blooming graphene-related research during the mid-2000s resulted in the development of a whole science and technology roadmap with applications related not only to electronics, photonics and optoelectronics but also to sensors, flexible electronics, energy storage and generation, composite materials and biomedical applications [43]. Nevertheless, a significant portion of the large amount of graphene-related research has been dedicated to photonics and optoelectronics [24, 25, 43–48], given its appealing properties for such applications.

The richness of graphene's unique optoelectronic properties include ultra-high mobilities, reaching values up to 200000 $cm^2V^{-1}s^{-1}$ for suspended graphene [49], while mobility in the order of $\sim 5000\,cm^2V^{-1}s^{-1}$ can be achieved these days in technologically relevant substrates [50,51] (e.g. SiO_2 on Si), surpassing Si mobility of $\approx 1000\,cm^2V^{-1}s^{-1}$ [52]. Its Fermi level is tunable, in the range of few meV up to ≈ 1 eV, in a reversible non-destructive manner via electrostatic gating [53–56]. Most importantly, graphene has an ultra-wide absorption spectrum [57], with a flat response in the visible and near-infrared regimes due to interband transitions [42]. Its absorption spectrum is further extended up to THz part of the electromagnetic spectrum, due to intraband transitions (e.g. free carrier absorption) [24, 58]. Given its 2D nature, graphene is additionally an ideal platform for the realization of plasmons (i.e. the collective oscillations of free charge carriers), with unprecedented spatial field confinement and low losses [59–63]. Moreover, graphene with its ultrafast carrier thermalization and slow carrier cooling [64] is ideal for applications relying on hot carriers, e.g., photodetection [65–74], non-linear optics [75–81] and light emitters [80, 82–85]. Furthermore, given its high flexibility [40], graphene can be used as a material for the development of flexible optoelectronic devices [86–88].

A severe constraint towards commercialization of graphene-based optoelectronics is associated with SLG production in a short processing time, industrially-scalable, cost-effective and environmental-friendly manner without compromises to graphene quality (e.g. carrier mobility, defect concentration, wrinkles, vacancies et.c.). Up to date, there are a plethora of graphene synthesis methods, including both top-down [89] and bottom-up [90, 91] approaches to produce both SLG and multi-layer graphene.

Top-down methods usually use graphite or other carbon-based materials as a precursor and include, among else, mechanical exfoliation [28, 92, 93], liquid-phase exfoliation [94, 95], arc-discharge method [96], unzipping of carbon nanotubes [97] and oxidative exfoliation-reduction [98, 99]. Some of these methods, although scalable and capable of producing high quality graphene, have low yield (e.g. mechanical exfoliation) and present difficulties in producing products with consistent properties (e.g. unzipping of carbon nanotubes). Furthermore, some of the above methods rely on the use of expensive and hazardous solvents (e.g. oxidative exfoliation-reduction, liquid-phase exfoliation) and

require high accuracy control while being energy-intensive (e.g. arc-discharge method), making them unsuitable for large-scale industrial implementation.

Bottom-up methods follow a different path using atomic-sized precursors, other than graphite, to yield graphene as a final product. Some of the most famous bottom-up methods are epitaxial growth [100, 101], substrate-free gas-phase synthesis [102], template route [103] and chemical vapor deposition (CVD) [104–106]. Epitaxial growth and substrate free gas-phase synthesis, although promising, are still under review and more comprehensive studies are required to establish their graphene grow mechanisms [91]. Template route is not favorable for commercialization, given the tedious washing steps associated with it and the possibility of destroying the produced graphene during template removal [107]. CVD, on the other hand, is up to date the most promising graphene synthesis method, regarding the scaling up of producing SLG with adequate quality for photonic and optoelectronic applications [50, 106], with even a continuous roll-to-roll CVD graphene fabrication method being demonstrated recently [108].

The CVD synthesis route involves the decomposition of hydrocarbon gaseous (e.g. ethylene, hexane or acetylene), liquid or solid precursors on metallic catalysts (e.g. Cu or Ni) using high temperatures (650 - 1000 ^{0}C). The hydrocarbon precursor, upon touching the hot surface of the metal catalyst, dissociates into free carbon and hydrogen atoms. These carbon atoms subsequently diffuse through the surface of the metal catalyst to form graphene sheets [91, 105, 106]. CVD fabrication methods have the potential to produce high quality, large area graphene in an acceptable cost. Subsequently, the research on CVD fabrication of graphene has expanded, implementing a plethora of different precursors and techniques [91, 105, 106]. Up to date, CVD on Cu is the state-of-the-art (SOTA) fabrication method for obtaining high quality graphene, suitable for photonic and optoelectronic applications, in adequate amounts at a reasonable cost [109–111].

Despite the recent developments in SLG fabrication and graphene's exceptional properties, it is unrealistic to expect from a single material to meet all the modern demands regarding optoelectronic applications. For example, ultra-fast carrier recombination in pristine graphene is a disadvantage for the realization of sensitive photodetectors based solely on SLG [112, 113]. Moreover, graphene's ultra-broadband light absorption, even though impressive given its monoatomic thickness, is relatively weak [42] which is an obstacle for developing high performance optoelectronics such as photodetectors and electroabsorption modulators. In compensation to the above, graphene is highly integrable with other materials [112] allowing for the realization of hybrid graphene-based heterostructures.

One popular approach, during recent years, is the combination of graphene with other 2D materials to fabricate Van der Waals heterostructures for photonics and optoelectronics [24, 114–119]. Another approach utilizes the hybridization of graphene with Si and Si-based substrates (e.g., SiO_2) [44, 120–122], taking advantage of the existing fully fledged semiconductor technology, while exploiting graphene's novel merits to counterbalance Si shortcomings [123–126], discussed in the previous section. The latter approach is extremely promising, allowing for the development of low cost and large scale optoelectronics compatible with the existing CMOS fabrication processes [127, 128], lithography and integration techniques [129]. In this direction, constant advances are reported regarding the wafer-scale integration of graphene [50, 130], while an experimental pilot line was recently launched, with the purpose of standardizing graphene and other 2D materials integration into Si wafers [131]. Furthermore, there are companies that nowadays already offer graphene integrated on Si wafers (fig. 1.2), although with carrier mobilities limited

to $\approx 1500\,\mathrm{cm^2V^{-1}s^{-1}}$ for the moment [132, 133].

Figure 1.2: Graphene integrated in 200 mm, 100 mm and 50 mm wafers. Fabricated from Apllied NanoLayers [132], the photograph depicts samples exhibited during 2022 Graphene Conference.

The up to date relatively low mobilities of SLG in Si based substrates are related to transfer processes. Even though CVD on Cu fabrication process can deliver high quality graphene, SLG heterostructure device fabrication involves additional manufacturing steps, for the transfer of CVD graphene grown on Cu to the desired substrate. During this procedure, graphene is coated with a polymeric resist, e.g. polymethyl methacrylate (PMMA), which acts as support layer during transfer. After the transfer of graphene on the desired substrate, optical or e-beam lithography is used for the removal of the supporting polymeric layer [134]. This procedure, however, can leave graphene contaminated with polymeric residues, greatly affecting its quality and optoelectronic properties [135]. Various methods have been implemented to resolve this issue of polymer contaminants, with wet chemical cleaning being the most widely adopted one [136]. As a result, after all the fabrication and transfer steps described above, typical mobilities in large-area samples does not exceed 5000 $\mathrm{cm^2V^{-1}s^{-1}}$ [50, 137]. However, recent studies have managed to achieve average carrier mobilities up to $\approx$ 7000 $\mathrm{cm^2V^{-1}s^{-1}}$ for non-encapsulated SLG transferred on SiO_2/Si substrates [51], approaching the mark of 10000 $\mathrm{cm^2V^{-1}s^{-1}}$ mobility at $\approx 10^{-12}\,\mathrm{cm^{-2}}$ carrier density, which is considered necessary to realize optoelectronic and photonic devices competitive with the existing technology [47].

The above briefly outline the developments in graphene fabrication towards large scale production, and the endeavor for its integration with existing mature technologies. Advancements regarding these efforts are constantly reported, while the vast amount graphene related research (fig. 1.1) has allowed for a deep understanding in the underlying fundamental physical properties of graphene. With the above tasks near completion, research on graphene-optoelectronics has shifted, during recent years, towards applications and device engineering. This thesis is focused in that direction, with the purpose of developing a reliable simulation framework for full-device representation and the optimization of graphene-based optoelectronic devices.

1.3 Scope of this thesis

This thesis aims to computationally investigate graphene's use in optoelectronic applications operating from the near-infrared up to the THz regime. To achieve this, two objectives need to be met simultaneously. The first one is the development of a robust multiphysics graphene simulation framework while the second one is to utilize this framework to design realistic, novel graphene-based optoelectronic devices.

Regarding the development of the simulation framework, the aim is to include SLG optical, electronic, and thermal properties as well as the interplay between them in a self-consistent manner, to accurately simulate graphene's dynamic optoelectronic response during device operation. However, it is not the purpose of this work to research graphene's fundamental physical properties; this task had already been completed by the time I began my Ph.D. studies. At the present, graphene-related research has reached a level mature enough to start focusing on applications and commercialization of graphene-based optoelectronics. In this regard, the main idea of the simulation framework developed here is to make use of all the conclusions derived from fundamental research, isolate the important parameters regarding graphene's optical, electronic and thermal properties and study their interactions. This study needs to be performed under realistic assumptions for all the relevant parameters, considering the restrictions imposed by present fabrication technology, regarding the quality and properties of both graphene and the materials used along with it. Taking all of the above into consideration, the simulation framework developed in this thesis, can be used for full device representations and aims to be a link between fundamental physics research and device engineering, towards the design and optimization of novel graphene-based optoelectronics competitive with state-of-the-art technologies.

This thesis also aims to address several key issues regarding the operation of graphene based optoelectronic devices. These include, among else, ways to enhance graphene-light interaction, the exploitation of ultra-fast graphene carrier dynamics and their slow cooling and the optimization of carrier transport across graphene-based heterostructures. The devices designed and studied here are focused on free-space photodetection and modulation schemes, covering the spectral region from near-infrared up to the THz regime. Graphene-based heterostructures are studied, mainly utilizing Si and Si-based materials alongside graphene, given the latter's compatibility and integration capabilities with Si, and considering the advantages that can be gained from the exploitation of the mature semiconductor technology and fabrication processes. Nevertheless, the methods we develop and the conclusions we derive from this thesis, are applicable to alternative configurations, with different materials used alongside graphene, including the ever-expanding regime of 2D materials and their heterostructures.

1.4 Thesis layout

This thesis is organized as follows:

- Chapter 2 summarizes the performance metrics regarding the operation of photodetectors and modulators. After a brief summery of graphene-based photodetection and modulation mechanisms, the state-of-the-art performances of similar devices are presented.
- Chapter 3 presents an extensive layout of graphene's electronic, optical and thermal properties, along with a description of graphene/semiconductor heterojunctions.

The concepts outlined in this chapter are the basis upon which the framework that was used to study graphene-based optoelectronic devices in this thesis was developed.

- In chapter 4 the computational methods and tools that are used throughout this thesis are described. The computational methods for acquiring the optical response of the studied devices are presented, followed by a brief outline of the numerical tools utilized for the realization of the simulation framework developed in this thesis.

- Chapter 5 explores the use of graphene for IR optical modulation. A free-space modulator, where graphene is integrated with an asymmetric Fabry-Perot cavity is designed. Calculations show that high performance and fast modulation can be achieved, throughout the IR spectrum, irrespective of graphene quality, upon proper design and optimization. The results of this chapter were published in ref. [138].

- In chapter 6 the optical, electronic and thermal properties of graphene are put together in a self-consistent simulation framework, including all carrier dynamics under realistic assumptions, to design multi-spectral graphene/Si Schottky photodetectors operating in the thermionic regime. A comprehensive study of all the relevant parameters of operation is presented and, utilizing the conclusions derived in chapter 5, SLG/Si Schottky photodetectors are integrated in Bragg cavities. The performance metrics of this photodetection platform are calculated and it is shown that this scheme can lead to fast and efficient photodetection, capable to operate throughout the MWIR in a CMOS compatible configuration based on graphene/Si heterojunctions. The results of this chapter were published in ref. [139].

- In chapter 7 the photo-thermionic emission across SLG/Si Schottky junctions scheme, presented in chapter 6, is expanded in longer wavelengths, in the LWIR regime. Plasmons in graphene nanoribbons, the latter forming a series of Si Schottky contacts with Si, are studied using the FDTD method. Utilizing the methods and conclusions derived in previous chapters, a method for their electrical detection is proposed. Moreover, the unique properties of graphene plasmons are exploited to develop a configuration, based on the surface enhanced infrared absorption technique, able to detect the presence of an analyte molecule in the vicinity of graphene nanoribbons and produce a direct electrical readout. The results of the study presented in this chapter were published in ref. [140].

- In chapter 8 the simulation framework developed in this thesis is utilized to provide theoretical support and explain the response of THz-TDS spectroscopy experiments performed from our colleagues in IESL-FORTH. There, a graphene-based thin film absorber is excited by intense THz pulses, leading to deep self-induced absorption modulation in THz frequencies. The methods and tools developed in this thesis were able to replicate and confirm the experimental findings, while providing strong theoretical support regarding their origins and allowing for an insight into graphene's carrier dynamics at the studied configuration. In this chapter the model developed in this thesis is experimentally validated while, at the same time, an all-optical modulation scheme is presented, which can find application in ultrafast schemes for custom beam and pulse shaping of THz sources. The results of this chapter were published in ref. [141].

- Chapter 9 includes a summary of the major accomplishments of this thesis, regarding both the designed and studied devices as well as the developed simulation framework. Furthermore, an outlook for the future directions, use and capabilities of the multi-physics graphene model developed here is presented.
- In Appendix A, the critical coupling mechanism, which is used to enhance graphene-light interaction in the devices studied in this thesis, is discussed in detail.
- Finally, in Appendix B, computational details about the implementation and efficiency of the developed simulation framework are briefly discussed.

Chapter 2

Optoelectronic devices: Metrics and state-of-the-art

In the context of this thesis we focus on free-space photodetectors and modulators, which can be used in free-space optical communications [142–144], light-radars [145], biomedicine [146] and many more applications. Moreover, in free-space configuration light propagation is taking place through vacuum or ambient air, with an ultra-broadband spectrum ranging from UV to THz available. Furthermore, free-space configuration is able to handle much higher optical power than fiber or chip-integrated configurations, rendering it more suitable for high-power applications, e.g. pulse shaping of intense light pulses [147, 148].

In the following chapter, the metrics regarding the performance of photodetectors and modulators are presented. Afterwards, a brief outline regarding the mechanisms of graphene-based photodetectors and modulators is given, followed by a presentation of the state-of-the-art performances of free-space photodetectors and modulators up to date.

2.1 Photodetectors

Efficient light detection in the IR and THz part of the spectrum is key to a variety of applications ranging from optical communications [2, 3], imaging [6], biomedicine [149, 150], tomography [9] and more. This task can be achieved using photodetectors, which convert input light into an electrical readout. Growing demand pushes for the integration of such detectors with supporting Si based circuitry. It is a challenge for conventional semiconductor devices to meet these specs due to spectral limitations arising from their finite band gap, as well as material incompatibilities. Graphene is compatible with CMOS Si technology, as discussed in the previous chapter, while its broadband absorption makes the SLG-based photodetectors a promising platform. However, despite of SLG compatibility with Si technology and ever-reducing fabrication cost, there are several performance requirements that need to be achieved for graphene PDs to be competitive with SOTA photodetection platforms.

2.1.1 Photodetection performance metrics

Photodetection Noise

Every PD has an inherent noise signal, i.e. spontaneous fluctuations in its electrical readout. Since PDs are mainly used to detect small inputs, spontaneous fluctuations on the current or voltage readout set a lower limit to the signal that can be detected. It is therefore necessary to quantify the noise signal of a PD.

For most PDs the two main noise sources are shot noise and thermal (Johnson) noise [20,151,152]. Shot noise originates from the discreteness of charge carriers that contribute to the electrical readout [20, 151, 152] and depends both on photocurrent, i.e. current readout arising from illumination, as well as dark current, i.e. leakage or reverse saturation current present at dark conditions, usually arising from the application of a bias voltage. The mean-square noise signal due to shot noise, normalized to a fixed reference bandwidth of 1 Hz is [20, 151–153]:

$$\left\langle i_{sh}^2 \right\rangle = 2e\left(I_{ph} + i_d\right) \tag{2.1}$$

where I_{ph} is the photocurrent, i_d the dark current and e the electron charge.

Thermal (Johnson) noise occurs in every conductor or semiconductor at finite temperatures due to thermal motion of carriers. Its mean-square value, normalized to a fixed reference bandwidth of 1 Hz is given by [20, 151–153]:

$$\left\langle i_J^2 \right\rangle = 4k_B\,T/R_{eq} \tag{2.2}$$

with T the ambient temperature and $R_{eq} = dV/dI$ the equivalent resistance of a PD in dark [151, 153].

The total mean-square root noise signal is then given by: [20]:

$$\left\langle i_n^2 \right\rangle = \left\langle i_{sh}^2 \right\rangle + \left\langle i_J^2 \right\rangle \tag{2.3}$$

External responsivity

An important PD figure of merit is its external responsivity R_{ext}, i.e. its efficiency in converting the input signal to an electrical readout. It is defined as [20, 153]:

$$R_{ext} = J_{ph}/P_{in}\ [\mathrm{A/W}] \tag{2.4}$$

where $J_{ph} = J_{el} - J_d$ the photocurrent density, J_{el} the current density readout upon illumination, J_d the dark current density and P_{in} the input power density.

Noise equivalent power

Having determined the external responsivity and the noise level, one can calculate yet another important figure of merit, the noise equivalent power (NEP), which is a metric regarding a PD ability to detect weak signals. NEP is defined as the input power required to generate a signal-to-noise ratio of one in a 1 Hz bandwidth [20, 151], i.e. the minimum required input power to distinguish the photosignal from background noise. NEP is consequently given by the ratio of noise current divided by the external responsivity [20, 152, 153]:

$$\mathrm{NEP} = \frac{i_n}{R_{ext}} \tag{2.5}$$

The unit of NEP is $\mathrm{W/Hz^{0.5}}$ [152].

Specific detectivity

Another important figure of merit regarding PD sensitivity is the specific detectivity (D^*). It was introduced by Jones [154], after he observed that NEP depends on detector area A_d. D^* is used extensively in the literature, since it allows a more direct comparison of PDs with different footprints. It is defined as:

$$D^* = \frac{\sqrt{A_d}}{\text{NEP}} \tag{2.6}$$

where A_d is the PD coverage area. The unit of D^* is cm $\text{Hz}^{0.5}$ W^{-1}, which is also referred to as 1 Jones.

Temporal response

Finally, of great importance is the time response of a photodetector, i.e., the characteristic time that a PD takes to switch from the on state (when illuminated) to the dark state (at dark). The speed performance of a PD can be limited from several factors, e.g. parasitic resistance-capacitance effects (τ_{RC}), transient time of charge carriers across the depletion region of a junction (τ_{tr}) and photon lifetime inside an optical cavity (τ_{ph}) [153]. The longer of the above timescales determines the speed limit of a PD. In most cases, the longer timescale and the consequent speed limitations arise from τ_{RC}, with the PD cutoff frequency:

$$f_{\text{cutoff}} \equiv f_{\text{RC}} = \frac{1}{2\pi\tau_{\text{RC}}} = \frac{1}{2\pi RC} \tag{2.7}$$

with R and C the total resistance and capacitance of the PD respectively.

2.1.2 Graphene-based photodetection mechanisms

Up to date several mechanisms have been utilized to enable photodetection based on graphene [43, 44, 155]. The most commonly used of them are schematically depicted in fig. 2.1. A main distinction between them is whether they utilize photoexcited e-h pairs for photodetection (i.e., photoexcitation-assisted PDs) or thermalized carriers for this manner (i.e. hot-carrier-assisted PDs).

For photoexcitation-assisted PDs [blue frames in fig. 2.1], the first stage of the photodetection process is photocarrier generation. This is achieved by optical absorption of incoming photons. Since e-h pair generation is necessary for this type of PDs, incoming photon energy must be larger than the material bandgap, in the case of conventional semiconductors, or large enough to allow for interband transitions in SLG. This fact sets a limit regarding the spectral response of photon detectors. Afterwards, the photoexcited carriers can either transport across the photoactive material in the presence of an electric field, in the case of photoconductive (PC), photogating (PG) and photovoltaic (PV) PDs or be directly injected across an energy barrier, in the case of internal photoemission (IPE) PDs. If the photoactive material contains mid-gap states, the photoexcited carrier could also relax in these states and get trapped. Finally, in PC, PV, and PG PDs the photocarriers can be collected through contacts applied to the photoactive material or return to their ground state through some relaxation or recombination process.

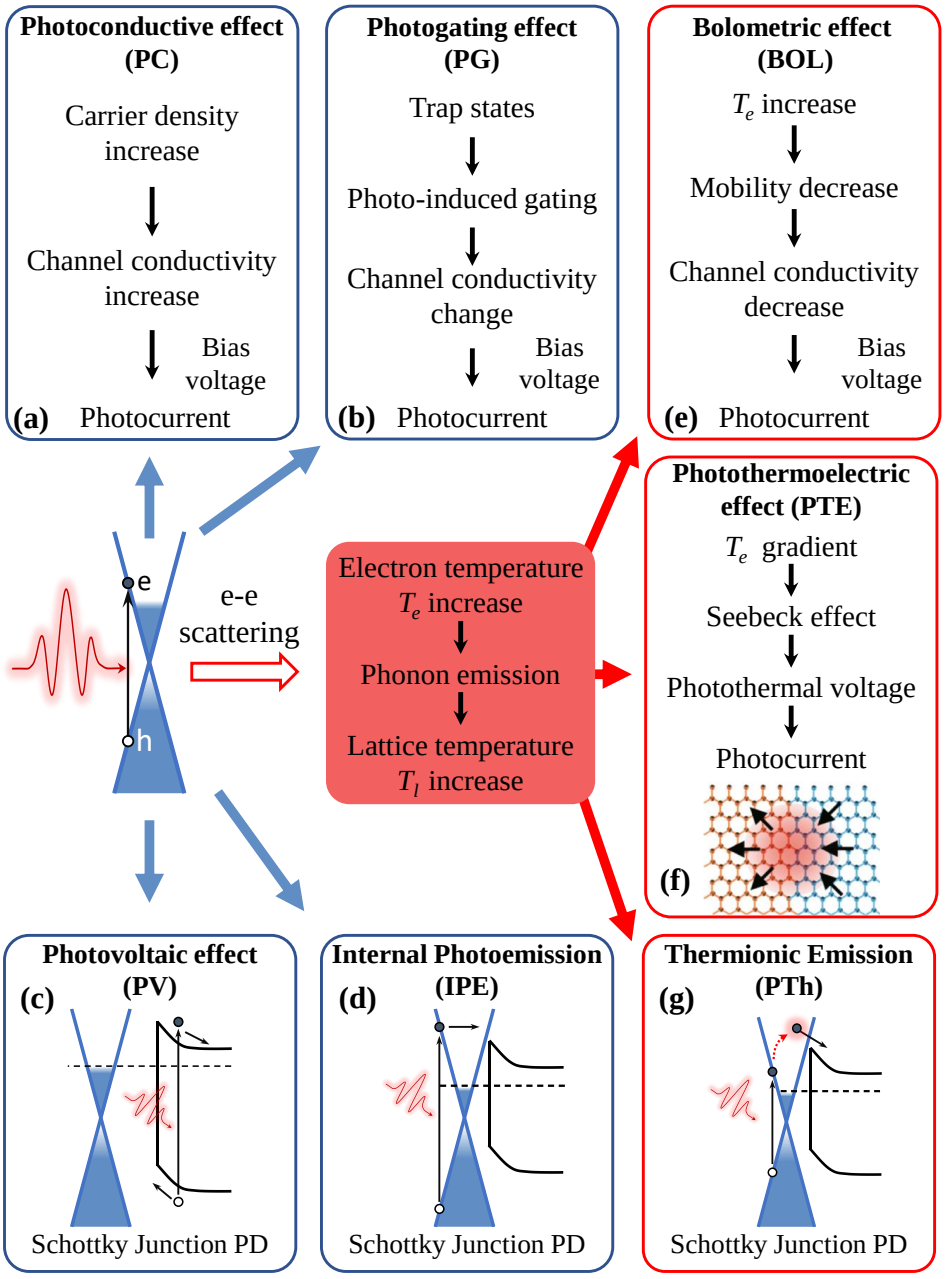

Figure 2.1: Schematic representation of commonly used graphene-based photodetection mechanisms. Blue frames correspond to photoexcitation-assisted PDs and red frames to hot-carrier-assisted PDs. (a) Photoconductive (PC) effect. Photoexcited carriers lead to conductivity increase. Photocurrent can be harvested by applying a bias voltage. (b) Photogating (PG) effect. Trap states lead to photo-induced gating, changing the channel's conductivity. Photocurrent can be harvested by applying a bias voltage. (c) Photovoltaic (PV) effect. Photoexcited e-h pairs, created in the semiconductor, are splitted by the built-in electric field leading to photocurrent. (d) Internal Photoemission (IPE). Photoexcited e-h pairs are created by photons with energy below the semiconductor bandgap in graphene and directly injected over a junction barrier. (e) Bolometric (BOL) effect. Increased T_e leads to reduced mobility. The subsequent reduce in conductivity is translated to an electrical readout by applying a bias voltage. (f) Photothermoelectric effect. T_e gradient results in photovoltage through the Seebeck effect, generating hot-carrier-induced photocurrent. (g) Thermionic emission (PTh). Photoexcited carriers, created by photons with energies below both the bandgap and the barrier height are thermalized via e-e scattering, gaining enough thermal energy to be injected across the junction barrier.

PDs relying on the PC effect [fig. 2.1(a)] utilize the increase of the photoactive material's conductivity, $\Delta\sigma$, due to photogenerated carriers. An electric field, created by applying an external bias voltage between two contact electrodes, is used to harvest the photocurrent originating from this conductivity increase. Following photoexcitation, the generated carriers can either drift-diffuse on the photoactive material or recombine within a characteristic timescale τ_r.

Graphene based PDs utilizing the PC effect have been demonstrated in several studies. However, their photoresponse is low, typically with responsivities $R \lesssim 0.2$ A/W [156–158]. This can be understood since the responsivity in PC effect is proportional to e-h pair lifetime τ_L [151], which in the case of graphene is determined by the ultrafast (< 1 ps) carrier recombination time τ_r [155, 159]. Additionally, the need for a bias application introduces dark current, increasing noise levels and resulting to low detectivity and high NEP. Nevertheless, PC SLG-based PDs have a fast temporal response [158], making the suitable for applications requiring fast photodetection.

A way to increase the photoresponse of SLG based PDs is to utilize the photogating effect [fig. 2.1(b)]. There are two different implementations of this mechanism. In the first one, trapping centers are created in graphene itself (e.g. by introducing electron trapping centers and by creating a bandgap in graphene through band structure engineering [160]), trapping one of the two type of carriers. In the second implementation, e-h pair generation occurs in nanoparticles, charge traps or molecules in the vicinity of graphene. Afterwards, one type of carrier is transferred onto graphene (e.g. by applying a bias voltage), while the opposite polarity carriers remain on the nanoparticles, molecules or traps [161–164]. This creates a photoinduced gating, with the free carrier-type being recirculated on graphene between a source and a drain electrode. Utilizing a high-mobility conductor, such as graphene, and long trapping times, the photocunductive gain in PG configurations can be as high as 10^8, leading to impressive responsivities in the order of $\sim 10^7$ A/W [161]. However, this gain originates from very long trapping times of the carriers, reaching even ~ 1 s [165], resulting in slow operation speeds, typically with a cutoff frequency $f_{\text{cutoff}} \ll$ MHz [44].

While PC and PG PDs rely on external bias voltage to induce photocurrent, the photovoltaic (PV) effect [fig. 2.1(c)] is based on the built-in electric field developed in *p-n* junctions [166, 167] or graphene-semiconductor Schottky junctions [168]. Graphene/Si Schottky junctions [168] are a popular platform to exploit PV effect using graphene [168–178]. The built-in electric field developed in Si is used to separate the photoexcited e-h pairs[fig. 2.1(c)], so PV PDs can operate in unbiased conditions. However, the application of a bias voltage is often used to drive the photocarriers out of the junction more rapidly, lowering the temporal response. This, however, can increase dark current, leading to a lower detectivity and higher NEP. In general, PV PDs can have a responsivity exceeding 1 A/W , with high detectivity in the order $D^* \sim 10^{12}$ cm Hz$^{0.5}$ W^{-1} at $\sim$ ms response times [173, 175]. Faster ($\sim$ GHz) configurations have been reported, but with the responsivity dropping in the ~ 100 mA/W regime and detectivity $\sim 10^{11}$ cm Hz$^{0.5}$ W^{-1} [176]. However, PV PDs are inherently limited by the semiconductor bandgap ($E_{g,\text{Si}} \approx 1.1$ eV [20]), limiting their operation in the visible (VIS) and near-infrared (NIR) regime.

The spectral response of graphene/Si Schottky PDs can be pushed beyond Si bandgap by utilizing the internal photoemission (IPE) effect [fig. 2.1(d)]. In this mechanism, light is absorbed in graphene and photoexcited carriers can be injected above the Schottky barrier height (Φ_B), given that incoming photons have enough energy to overcome this barrier. Even though this configuration is again spectrally limited by Φ_B, it enables photodetection

beyond Si bandgap, up to $\approx 2\mu$m [179], including the technologically important band of 1.55μm [153]. Several works have studied the IPE-enabled graphene/Si Schottky configuration [153,180–182], resulting to responsivities in the mA/W regime, detectivities in the order of $\approx 10^7$ cm Hz$^{0.5}$ W^{-1} with speeds potentially reaching the GHz regime [126,153].

All of the above PD mechanisms are, one way or another, spectrally limited, rendering them suitable for photodetection in the VIS up to MWIR spectral regime. Graphene based hot-carrier-assisted PDs [fig. 2.1(e) – 2.1(g)] on the other hand, utilize graphene's ultrabroadband absorption, fast carrier thermalization and slow carrier cooling [64], to realize spectrally-unlimited photodetection, extending up to the THz regime [24]. Hot-carrier-assisted PDs involve the generation of photocarriers through light absorption. However, since e-h pair generation is not necessary for their operation, both intraband and interband transitions can contribute to this process, resulting to a broad spectral response. Photocarriers subsequently thermalize with the surrounding carriers, generating a hot-carrier distribution. This procedure, realized by e-e scattering, is ultrafast and very effective in graphene [183, 184], making the latter an ideal materials platform for this type of PDs. Consequently, the local or global carrier distribution can have several effects on transport properties, which can be utilized to generate an electrical readout. For example, in the photothermoelectric (PTE) effect [fig. 2.1(f)] a gradient in electronic temperature generates a photovoltage, through the Seebeck effect, resulting in photocurrent generation. In bolometric (BOL) effect [fig. 2.1(e)] the increased electronic temperature results to a reduction in electrical conductivity, which can be detected through the appliance of an external voltage. Furthermore, the excess thermal energy of the hot-carriers can be utilized to enable their injection over a potential barrier, e.g. enabling photo-thermionic emission (PTh) over the Schottky barrier [fig. 2.1(g)] of graphene/semiconductor Schottky junctions, even for photon energies below both the Si bandgap and the barrier height Φ_B.

Specifically, the bolometric effect, as discussed, utilizes the temperature-induced mobility reduction in graphene, to detect the decrease in channel conductivity by applying a bias voltage. Numerous studies have reported high performance graphene-based bolometers [185–188], capable of detecting radiation up to the THz regime, at cryogenically cooled operation temperatures. At room temperature, however, BOL PDs have lower performance (responsivities < 0.1 A/W) and typically a slow temporal response [189, 190]. The reduced performance is expected since BOL PDs rely on conductivity change with increasing temperature, $\Delta\sigma/\Delta T_e$, which is larger at high doping levels and low temperatures [191].

Another promising graphene-based photodetection platform are the photothermoelectric (PTE) PDs [fig. 2.1(f)]. In PTE PDs light absorption generates a local hot-carrier distribution having an asymmetric temperature gradient ∇T_e. If this temperature gradient overlaps with regions having different Seebeck coefficients, e.g. by introducing a lateral p-n junction, a photovoltage is created through the Seebeck effect [64]. This photovoltage acts as an electromotive force, leading to photocurrent generation. Since the potential difference in PTE is inherently generated by the hot-carriers arising from light absorption, there is no need for application of an external bias. This lowers the power consumption and eliminates dark current contribution in the noise of PTE PDs. Moreover, PTE is a broadband photodetection platform, with graphene-based PTE photodetectors reported from MIR [67] up to the THz regime [66, 192]. PTE PDs have responsivities in the ~ 100 mA/W regime, with NEP down to few pW/Hz$^{0.5}$, detectivity in the $10^6 - 10^7$ cm Hz$^{0.5}$ W^{-1} and ultrafast response in the order of few ns [66, 67]. Recent studies have shown that the performance of PTE PDs can be improved even further, under proper device design and

optimization, with potential responsivity in the $\sim$ A/W regime at $\sim$ 100 GHz operation speed at zero bias [68].

Finally, hot-carrier-assisted PDs can be realized utilizing the photo-thermionic emission (PTh) configuration [fig. 2.1(g)]. In this mechanism, low energy photons are absorbed in graphene, redistributing their energy in the carrier bath, resulting in a hot carrier distribution. Hot carriers in the high energy tail of this Fermi-Dirac distribution can utilize their excess thermal energy to overcome an energy barrier, e.g. in SLG/Si Schottky junctions [71] or other SLG heterostructures [65, 70, 193]. Responsivity in the order of $\sim$ 10 mA/W with an ultrafast ($\sim$ GHz) temporal response has been reported for graphene-based PTh photodetection [65]. The performance and optimization of PTh SLG/Si Schottky junction PDs will be analyzed in detail on the following chapters.

2.1.3 State-of-the-art photodetectors

From the above it is clear that realizing graphene-based PDs with high response, large sensitivity, broadband operation and fast temporal response simultaneously, while operating at room temperature, is not an easy task. Current SOTA IR detector technology utilizes low ($<$ 0.4 eV) bandgap semiconductors such as HgCdTe [23, 194] or III-V compounds (e.g. InSb, InAs [195]) with detectivities almost reaching the ideal photodetection operation when cryogenically cooled. The performance of these PDs remains high even at RT, surpassing SLG-based PDs performances up to date [194]. However, the ever growing demand for PDs co-integrated with supporting circuitry (e.g. drivers, amplifiers and processors) on the same Si chip requires CMOS compatibility. HgCdTe and III-IV platforms are not compatible with standard CMOS processes because of cross contamination and dopant redistribution effects [196–198], requiring separate manufacturing, followed by complex bonding and assembling processes [199]. Moreover, their fabrication involves growth techniques such as metal-organic chemical vapor deposition or molecular beam epitaxy, which are not only incompatible with Silicon monolithic integration but high cost as well [197, 200]. Finally, PDs based on HgCdTe or III-V compounds have a cutoff wavelength at $\approx$ 10 μm due to their finite bandgap [198].

In terms of responsivity, graphene PDs holds the record with $\approx 10^6 - 10^8$ A/W in the VIS up to SWIR part of the spectrum [161] utilizing a hybrid graphene - quantum dot platform with trapped carriers. However, due to the long lifetime of carrier trapping, the aforementioned PDs have a very long response time ($<$ 10 Hz) rendering them unfit for applications requiring fast photodetection. PDs in longer wavelengths utilize nanostructures (fig. 2.3) [201] (e.g. colloidal quantum dots, nanowires, quantum wells) along with III-V compounds, graphene or other 2D materials (e.g. black phosphorus [202]) with responsivities up to $\approx$ 10 A/W. For example, a recent study demonstrated graphene-based PDs, in a platform utilizing gold-patched graphene nanostripes, resulting in 11.5 A/W responsivity at 20 μm with ultrafast operation speed exceeding 50 GHz [203]. Moreover, graphene-based PDs utilizing the PTE effect have been demonstrated in the MWIR [67] and THz [66] spectral regimes, with responsivities in the order of $\approx$ mA/W and ultrafast ($\approx$ 20 ns) response times.

SOTA performances regarding detectivity (fig. 2.4) are achieved by HgCdTe PDs [155, 194], with $D^* \approx 10^9 - 10^{10}$ cm Hz$^{0.5}$ W^{-1} for wavelengths up to $\approx$ 6 μm at $\approx$ 100 ns temporal response for PV HgCdTe PDs [204] and $D^* \approx 10^7 - 10^8$ cm Hz$^{0.5}$ W^{-1} for wavelengths up to $\approx$ 10 μm with $\approx$ 10 ns temporal response for PC HgCdTe PDs [204]. The above cutoff wavelengths can be extended up to $\approx$ 13μm if the above PDs are cryo-

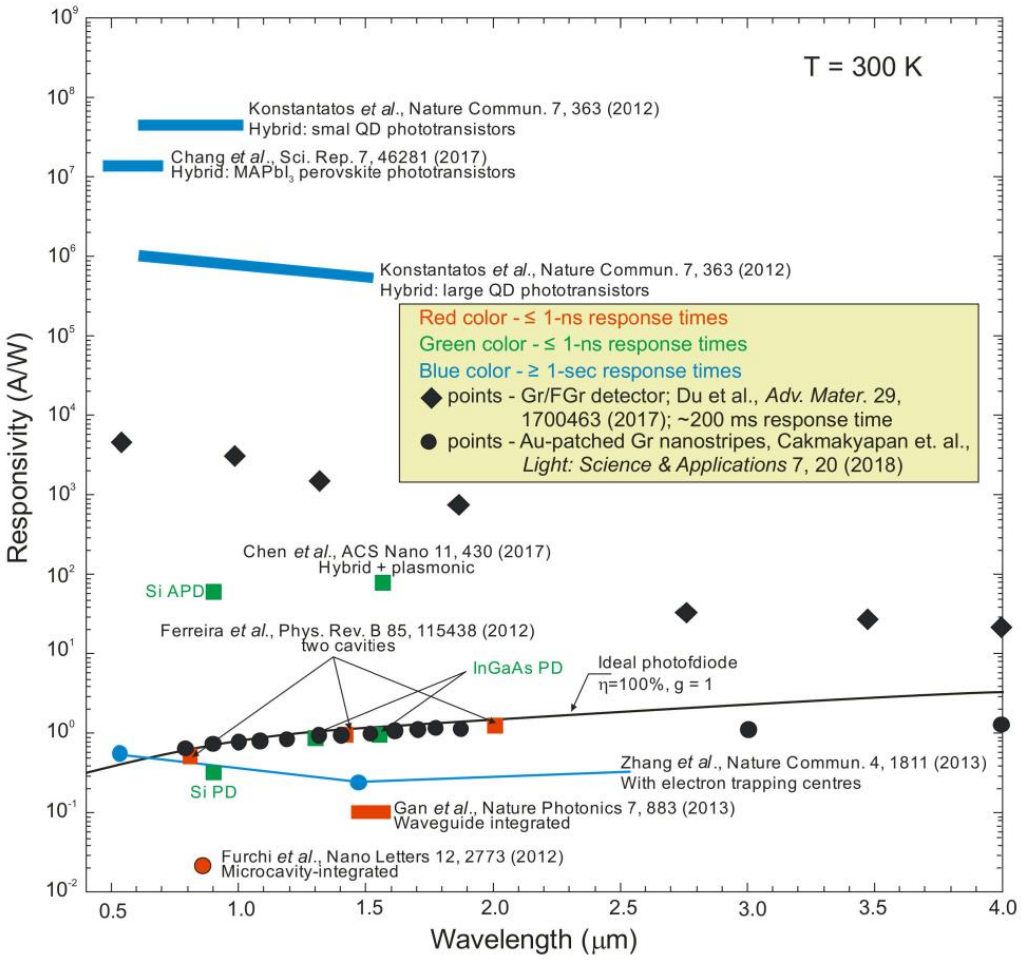

Figure 2.2: Graphene-based photodetectors spectral responsivity up to SWIR compared with commercially available devices. Temporal response ≤ 1 ns is depicted using red and green colors while blue corresponds to temporal response ≥ 1 sec. Commercial PDs are marked in green. Figure adopted from ref. [194].

genically cooled [204]. Graphene-based PTE PDs with D^* in the mid-10^6 cm Hz$^{0.5}$ W^{-1} and $\approx$ 10 ns response time have been reported in the 6-7 μm regime [67] while $D^* \approx 10^8$ cm Hz$^{0.5}$ W^{-1} with a 50 GHz temporal response has also been reported, with response up to ≈ 20 μm [203].

Although graphene-based PDs currently have lower performances when compared to SOTA commercially available devices, they are fully compatible with Si and CMOS technology while their operation can be extended beyond MWIR, up to LWIR and THz regimes. Furthermore, recent developments and ongoing research on large-scale fabrication methods and scalability are expected to lower manufacturing cost significantly. As a result, graphene and 2D materials based PDs are expected to become a PD platform highly competitive with existing IR detection technologies.

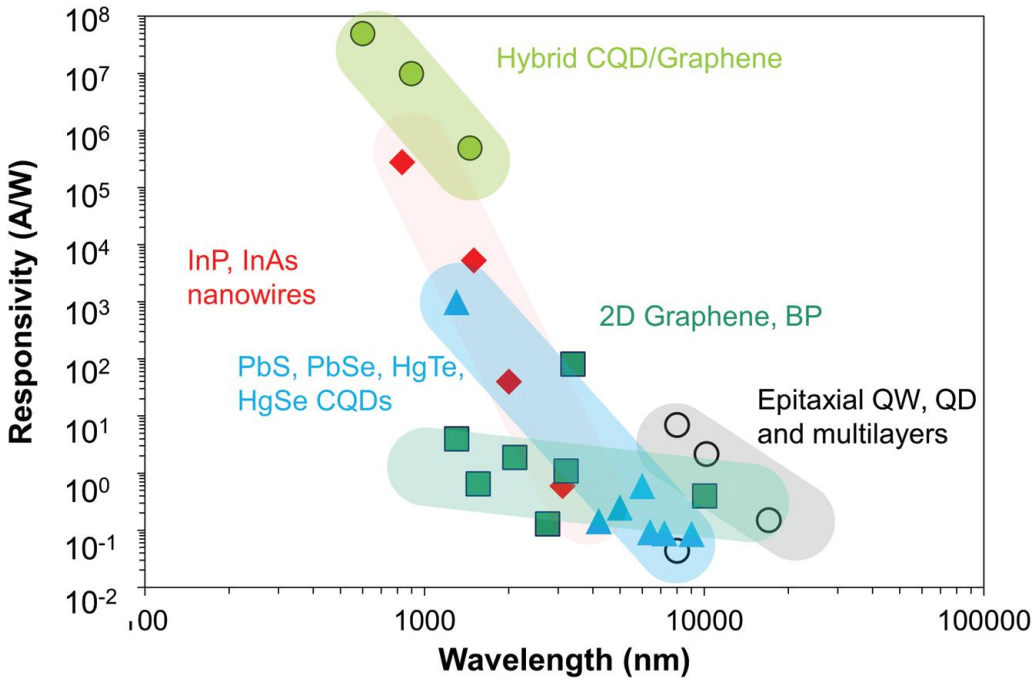

Figure 2.3: Responsivity of various PD platforms based on nanostructured materials across the infrared part of the spectrum. Figure adopted from ref. [201].

2.2 Optical modulators

Optical modulators are one of the key components of optoelectronic devices, since they are used to modulate (i.e. vary the fundamental characteristics of) an optical carrier signal, propagating in free space or in an optical waveguide, upon an external electronic, photonic or other input [207–209]. Modulators operating in free-space configuration are crucial for pulse-shaping applications [147, 148], light-radars [145], ranging systems [210, 211] and free-space optical communications [142–144, 212], while they are expected to play an important role in emerging 5G and 6G technologies [213]. Graphene is an appealing material for realizing optical modulators, given its electrostatically tunable optical response and ultrafast carrier dynamics, on top of its CMOS/Si compatibility and broadband optical absorption. As a result, an extensive amount of research has been carried out regarding graphene-based optical modulators [24, 214–219], with performances competitive with SOTA technology in both SWIR [217] and THz spectral regimes [24, 219].

2.2.1 Modulation performance metrics

Some of the key figure of merits that characterize a modulator's performance are modulation depth (MD), insertion loss (IL) and modulation frequency (MF).

Modulation depth

MD is given by the relative change between the maximum and minimum value of the varying optical readout (e.g. reflectance R or transmittance T) during modulation. It can

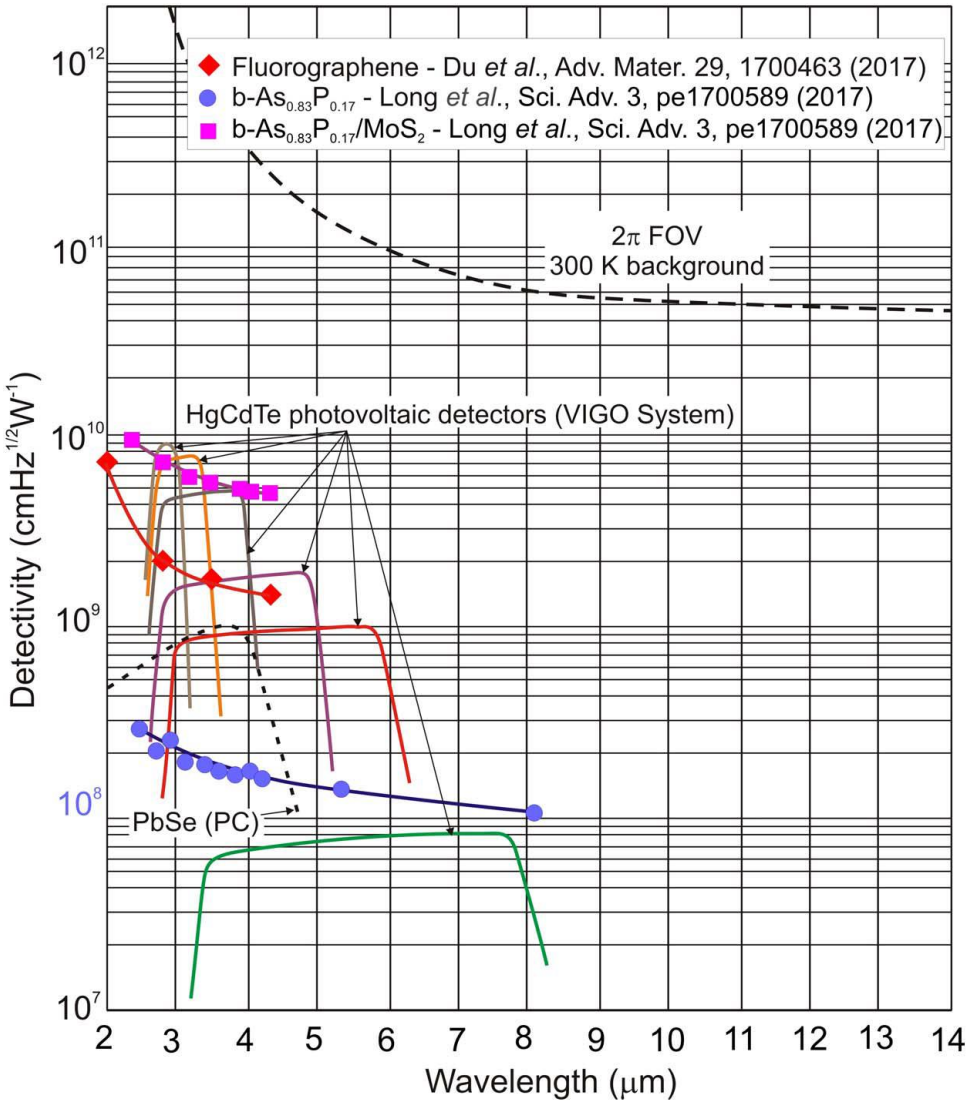

Figure 2.4: Spectral detectivity curves of HgCdTe PDs and PbSe photoconductor at RT. Detectivity of black arsenic [205] and fluorographene [206] PDs are shown in the same graph, the later acquired at 77 K. Figure adopted from ref. [155].

be expressed either as a percentage:

$$\mathrm{MD}[\%] = 100\,\frac{R_{\max} - R_{\min}}{R_{\max}} \left(\text{or } 100\,\frac{T_{\max} - T_{\min}}{T_{\max}}\right) \tag{2.8}$$

or using decibel units:

$$\mathrm{MD}[\mathrm{dB}] = 10\log_{10}\frac{R_{\max}}{R_{\min}} \left(\text{or } 10\log_{10}\frac{T_{\max}}{T_{\min}}\right) \tag{2.9}$$

Insertion loss

IL of an optical modulator is also a significant figure of merit, since it is directly related with the modulator's energy efficiency. IL quantifies the loss of the input optical signal at

the *on* state of an optical modulator. It can also been expressed as a percentage:

$$\mathrm{IL}[\%] = 100\,(1 - R_{\max}) \;\; (\text{or } 100\,[1 - T_{\max}]) \tag{2.10}$$

or in decibel units:

$$\mathrm{IL}[\mathrm{dB}] = -10\log_{10}(R_{\max}) \;\; (\text{or } -10\log_{10}[T_{\max}]) \tag{2.11}$$

Modulation frequency

Of great importance is a modulator's MF, i.e. the speed at which it is able to vary the optical readout between the *on* and *off* state. If an electrical signal is used as input, usually MF is limited by the RC time constant of the involved circuitry. Another limitation could be related to the optics-limited operating frequency (e.g. in the case of a cavity integrated modulator), although this frequency is usually much higher than the RC cutoff frequency, only affecting MF in all-optical modulators [218].

2.2.2 Graphene-based modulation mechanisms

Optical modulators can be categorized in many different ways. Regarding the attribute of light that they modulate, they can be distinguished in amplitude, phase, polarization or wavelength modulators. A different categorization can be made depending on the operating principle of an optical modulator. Thereafter, optical modulators can be differentiated in all-optical [218, 220] electro-optic [221, 222], magneto-optic [223], acousto-optic [224, 225], thermo-optic [226] modulators and so on. Finally, depending on the material optical property that is modulated, modulators can be categorized in absorptive and refractive modulators. For the former, the absorption coefficient (i.e. the imaginary part of the refractive index) is varied. In the case of graphene, this can be done by varying the Fermi-level via electrostatic gating [218,220] [i.e. electro-absorption modulation, fig. 2.5(a)] using a typical silicon on insulator substrate [227], an electrolyte substrate [228] or even resonant optical cavities [229]. This approach, however has operational speeds limited by the parasitic resistance and capacitance of the electronic circuit. A way to overcome this bottleneck is to utilize an all-optical modulation scheme, where a pump light signal is used to control the probe light [218]. In graphene this can be done by hot-carrier-induced changes in optical conductivity, originating from the absorption of an input pulse [64, 80] [fig. 2.5(b)].

Finally, refractive modulators vary the real part of the refractive index, e.g. utilizing the Kerr effect [230], thermal modulation of the refractive index, or using electrostatic gating. The later, referred to as electro-refractive modulators, are often used as a Mach-Zehnder interferometer in integrated schemes [209]. It should be noted that often the modulation scheme induces changes in several optical properties simultaneously, e.g. by varying the chemical potential in a graphene-based electro-absorption modulator, both the real and the imaginary part of the refractive index are modulated.

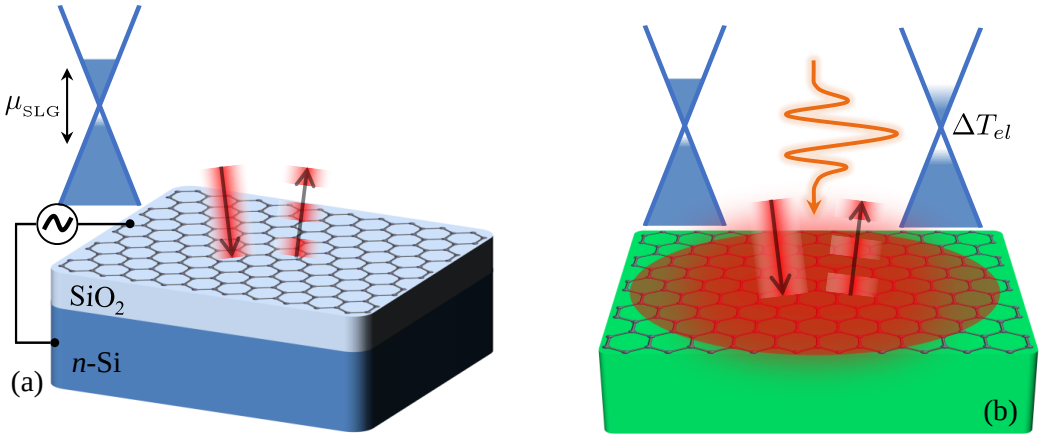

Figure 2.5: Schematic of graphene-based optical modulation schemes. (a) Electro-optic modulation. The ability to control graphene's Fermi-level, hence its optical properties, via electrostatic gating is utilized to modulate the reflectance or transmittance of a device by applying an alternating electrical input signal. (b) Hot-carrier induced absorption modulation. In this all-optical modulation scheme, hot-carrier induced changes in graphene's optical conductivity, originating from an ultrafast incoming light pulse, are exploited to modulate graphene's optical response in the same or in a different frequency of the incoming light.

The above mechanisms have been exploited in a variety of studies to utilize graphene-based optical modulators ranging from VIS [228], to IR [221,222,231,232] up to the THz part [227,233,234] of the electromagnetic spectrum.

2.2.3 State-of-the-art optical modulators

Optical modulation in SWIR, especially around $\lambda = 1550$ nm, is crucial for free-space optical communications and optical interconnects. At this wavelength propagation losses in fog [143] and humid conditions [235] are minimized due to lower absorption and scattering compared to lower wavelengths. Interconnect with telecommunication systems is optimal at this spectral regime, since at 1550 nm optical fibers present a reduced light absorption [236]. Moreover, with the ever expanding use of optical interconnects, eye safety is an important issue. Since the outer layer of the human eye (cornea) absorbs light at 1550 nm [143], it does not allow it to be focused on the retina and cause damage in human eyesight.

Electro-optic modulation is the preferable method for realizing SOTA optical modulators, since it allows for interconnection with mature circuitry technology [15]. Naturally, CMOS compatibility is desired for these devices. However, Si is not a suitable material platform to realize electro-optic modulators, since it does not have a strong electro-optic response. Even though alternative modulation schemes have been proposed, e.g. thermo-optic effect [237] or micro-electromechanical (MEMS) devices [238], they are limited to low speed applications. A workaround towards efficient and high-speed electro-optical modulation is the integration of Si alongside other materials with strong electro-optic effects, e.g. Si/Ge heterostructures [239] or graphene [221].

A popular approach to realize CMOS compatible electro-optic modulation is to utilize the quantum-confined Stark effect in germanium (Ge) quantum wells (QW) [240, 241]. Since in free-space operation the optical interaction length is limited, a QW based electro-absorptive modulator is usually fabricated in conjunction with a resonant cavity to achieve high performance modulation. Typically, this is done using asymmetric Fabry-Perot cavities using epitaxial distributed Bragg reflectors [242, 243]. This approach has been employed in both Si/Ge QWs [244, 245] as well as III-IV compound heterostructures [246] leading to fast, high performance electro-optic modulators operating in the SWIR regime. A recent study proposed the use of multiple *p-n* junctions subwavelength gratings, in an all Si configuration, to realize transmission modulation in a free-space device. Their calculations predicted MD up to 19 dB with a 10 GHz MF for 1550 nm [247].

Graphene, with its electrically tunable optical response [25] is an ideal platform for the realization or electro-optic modulators. As in the case of QWs, resonant cavities are also employed in graphene-based free space optical modulators, to enhance SLG light absorption and increase the modulation performance. Gao *et. al.* [248] demonstrated the use of a graphene/boron nitride heterostructure integrated with a silicon photonic crystal nanocavity, to achieve MD ~ 3.2 dB with a MF of 1.2 GHz at 1550 nm. Sun *et. al.* [249] combined a high-contrast grating with graphene and by varying the voltage applied to the latter managed to modulate the reflection at 1550 nm with a 11 dB MD with speeds up to ~ 0.8 GHz. On a similar approach, Gan *et. al.* [250] studied an electro-optic modulator in reflection mode, consisting of graphene on high-contrast nanocavity, with a 10 dB MD at 1 GHz MF and with low loses (IL ~ 1.3 dB) for a resonant wavelength of 1570 nm. Finally, Yu *et. al.* [229] showcased the possibility of using graphene on asymmetric Fabry-Perot cavities, using distributed Bragg reflectors, to modulate the transmission of their proposed device, by varying the electrostatic gating in graphene. Their calculation concluded that up to 15 dB MD at 5 GHz MF is possible, in a configuration that can be tuned for operation from the VIS up to the SWIR part of the spectrum. The performances of the aforementioned devices, regarding electro-optic modulation in free-space operation at SWIR are summarized in table 2.1.

It should be noted that the review presented in this section is focused in free-space configuration of modulators operating in the technologically important SWIR regime. Free-space graphene-based modulators with high performances have been reported up to the MWIR [251, 252] and THz regimes [24, 80, 227, 233, 234]. Moreover, a lot of studies have reported graphene-based modulators with ultrafast response and high performance in waveguide-integrated schemes [217, 253–256].

Material Platform	Operation Wavelength (nm)	If measured	MD (dB)	IL (dB)	MF (GHz)	Ref. and year
Si/Ge QWs	1429	Yes	3.5	3.7	3.5	[244], 2012
Si/Ge QWs	1471	Yes	10	1.3	4	[245], 2013
GaInAsP–AlInAs QWs	1550	Yes	10	1.0	> 0.01	[246], 2005
Si *p-n* junctions	1550	No	19	\	10	[247], 2017
Graphene/BN	1550	Yes	3.2	\	1.2	[248], 2015
Graphene	1550	Yes	11	\	0.78	[249], 2016
Graphene	1570	Yes	10	1.3	1	[250], 2013
Graphene	700 – 1550	No	15	< 5	5	[229], 2015

Table 2.1: State-of-the-art values for optical modulators operating in free-space configuration in the SWIR. The columns, from left to right, report the platform of the optical active material, the operation wavelength, if the study was experimental or theoretical, modulation depth, insertion loss, modulation frequency and finally the reference and the year of each study.

Chapter 3

Graphene theoretical background

In this chapter, the theoretical foundation of graphene's optoelectronic properties is reviewed. An extensive layout regarding graphene's electronic, optical and thermal properties, along with the description of graphene/semiconductor junctions is presented. The concepts developed in the following chapter are the basis upon which the self-consistent model that was used to study graphene-based optoelectronic devices in this thesis was built.

3.1 Electronic properties

Graphene consists of a planar sheet of carbon atoms arranged in a 2D hexagonal lattice. Each carbon atom forms four bonds with its neighboring atoms. Three of them are strong σ-bonds, arising from the hybridization of the $2s$, $2p_x$ and $2p_y$ orbitals of each carbon atom. The σ-bonds, which lay in the plane of the hexagonal lattice, are responsible for graphene's extraordinary mechanical properties [40]. The remaining p_z orbitals of each carbon atom, perpendicular to the hexagonal lattice plane, overlap to create the π and π^* bands below and above the lattice plane respectively. These π and π^* bands dominate graphene's bandstructure in lower energies and the delocalized electrons in them are responsible for graphene's electronic and optical properties [53].

3.1.1 Lattice and band structure

Single layer graphene's (SLG) lattice structure is depicted in fig. 3.1(a). It consists of two interpenetrating triangular Bravais sub-lattices, that together form a hexagonal honeycomb structure [26]. The unit cell consists of one atom of each sub-lattice, labeled as C_1 and C_2 respectively. Given the carbon-carbon bond length $\alpha_{\text{c-c}} = 1.42\,\text{Å}$ [257, 258], the lattice vectors can be found:

$$\begin{aligned} \mathbf{a}_1 &= \frac{\alpha_{\text{c-c}}}{2}\left(3, \sqrt{3}\right) \\ \mathbf{a}_2 &= \frac{\alpha_{\text{c-c}}}{2}\left(3, -\sqrt{3}\right) \end{aligned} \tag{3.1}$$

while the nearest-neighbor vectors are given by:

$$\begin{aligned}\boldsymbol{\delta}_1 &= \frac{\alpha_{\text{c-c}}}{2}\left(1, \sqrt{3}\right)\\ \boldsymbol{\delta}_2 &= \frac{\alpha_{\text{c-c}}}{2}\left(1, -\sqrt{3}\right)\\ \boldsymbol{\delta}_3 &= \alpha_{\text{c-c}}\left(-1, 0\right)\end{aligned} \tag{3.2}$$

The reciprocal lattice has also a hexagonal structure and the first Brillouin zone is defined by the reciprocal lattice vectors:

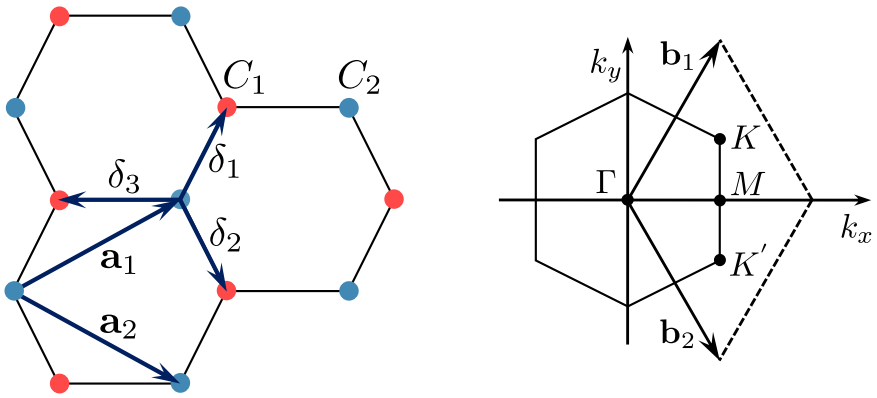

(a) (b)

Figure 3.1: (a) Graphene's lattice structure. The sub-lattices C_1 (red) and C_2 (blue) are shown along with the lattice vectors $\mathbf{a}_1$, $\mathbf{a}_2$ and the nearest neighbor vectors $\boldsymbol{\delta}_1$, $\boldsymbol{\delta}_2$, $\boldsymbol{\delta}_3$. (b) Graphene's reciprocal lattice and first Brillouin zone along with the reciprocal lattice vectors $\mathbf{b}_1$, $\mathbf{b}_2$ and the high-symmetry points K, $K^{'}$, M and Γ.

$$\begin{aligned}\mathbf{b}_1 &= \frac{2\pi}{3\alpha_{\text{c-c}}}\left(1, \sqrt{3}\right)\\ \mathbf{b}_2 &= \frac{2\pi}{3\alpha_{\text{c-c}}}\left(1, -\sqrt{3}\right)\end{aligned} \tag{3.3}$$

A schematic representation of the Brillouin zone, which includes several high symmetry points, is depicted in fig. 3.1(b).

At lower energies ($\lesssim$ 10 eV), the bandstructure of graphene can be accurately described using the tight-binding approximation and assuming only nearest-neighbors interactions [26, 53, 258]. In this case, the energy dispersion is given by [258]:

$$\begin{aligned}E(k_x, k_y) = \pm\, t \Bigg[1 + 4\cos\left(\frac{3\alpha_{\text{c-c}}k_x}{2}\right)\cos\left(\frac{\sqrt{3}\alpha_{\text{c-c}}k_y}{2}\right)\\ + 4\cos^2\left(\frac{\sqrt{3}\alpha_{\text{c-c}}k_y}{2}\right)\Bigg]^{1/2}\end{aligned} \tag{3.4}$$

where $t \approx 2.8$ eV is the nearest-neighbor hopping energy [53] and the $-$ $(+)$ sign corresponds to the π bonding (π^* anti-bonding) band. Equation 3.4 is plotted in fig. 3.2(a). At the six corners of the Brillouin zone, the valence and conduction bands meet each other. Only two of these points are nonequivalent (due to the two different sub-lattices), labeled as K/K' and referred to as Dirac points. Their position also defines the zero energy reference point, which is commonly referred to as charge neutrality point (CNP). For undoped, pristine SLG and zero temperature, the Fermi level resides at the Dirac points, making graphene a zero-gap semi-metal [33].

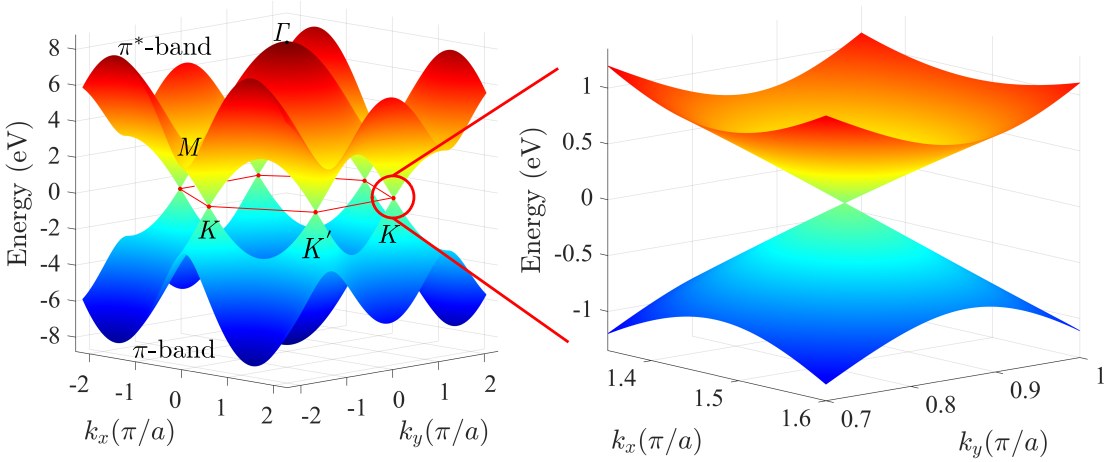

Figure 3.2: (a) Graphene's energy dispersion as described by eq. 3.4 (b) Linear energy dispersion for low energies ($\lesssim 1$ eV) around the CNP as described by eq 3.5.

Equation 3.4 can be expanded around CNP for small wavevectors (corresponding to energies up to ~ 1 eV), yielding the linear low energy dispersion relation [26]:

$$\epsilon(\mathbf{k}) = \pm\frac{3t\alpha_{\text{c-c}}}{2}\,|\mathbf{k}| = \pm\hbar v_{F,\text{SLG}}\,|\mathbf{k}| \tag{3.5}$$

with $\hbar$ the reduced Planck constant and $v_{F,\text{SLG}} \approx c/300 \approx 10^6$ m/s the SLG Fermi velocity [26, 53]. Equation 3.5 resembles a Dirac Hamiltonian for massless Dirac fermions, moving with a velocity $v_{F,\text{SLG}}$ [31, 33]. Within this low energy regime, conduction and valence bands have a conical shape [fig. 3.2(b)], with the Fermi surface scaling linearly with energy. This linear dispersion is unique in graphene, in contrast to conventional semiconductors which are described by parabolic dispersion relationships [27]. The resultant density of states is proportional to energy [53]:

$$\nu(\epsilon) = \frac{g_s g_v}{2\pi(\hbar v_{F,\text{SLG}})^2}\,|\epsilon| \tag{3.6}$$

with $g_s = g_v = 2$ the spin and valley degeneracies respectively. The charge density at zero temperature can be found by integrating eq. 3.6:

$$n(\epsilon) = \int_0^{\epsilon} \nu(\epsilon)d\epsilon = \frac{\epsilon^2}{\pi(\hbar v_{F,\text{SLG}})^2} \tag{3.7}$$

from which the SLG Fermi level $E_{F,\text{SLG}}$ can be correlated to the charge density:

$$E_{F,\text{SLG}} = \text{sgn}(n)\ \hbar v_{F,\text{SLG}}\sqrt{\pi\,|n|} \tag{3.8}$$

where $n > 0$ for electrons and $n < 0$ for holes.

3.1.2 Doping graphene via electrostatic gating

One of the most appealing properties of graphene, regarding optoelectronic applications, is the ability to control $E_{F,\mathrm{SLG}}$ using a gate voltage [28]. Given graphene's gapless nature, $E_{F,\mathrm{SLG}}$ can be tuned continuously from *n* to *p* doping [31] by injection of electrons or holes (eq. 3.8). By applying a potential difference across SLG and a metal (or a doped semiconductor), separated by a dielectric with thickness d and dielectric constant ϵ_r, charge Δn is induced in SLG, described by a simple capacitor model [28]:

$$\Delta n = \frac{C_g V_g}{e} = \frac{\epsilon_0 \epsilon_r V_g}{ed} \tag{3.9}$$

where C_g is the gate capacitance, ϵ_0 the vacuum permittivity and e the electron charge. A common configuration for electrostatic doping of graphene, initially demonstrated by Novoselov and Geim [28], is the usage of SiO_2 as backgate dielectric, on top of a doped Si substrate [fig. 3.3]. Electrostatic gating not only allows for the $E_{F,\mathrm{SLG}}$ control in an easy

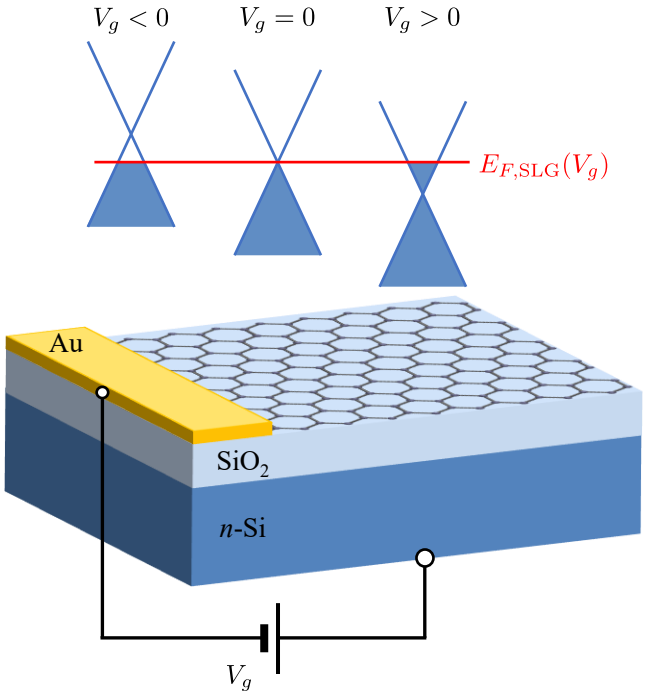

Figure 3.3: Schematic representation of graphene electrostatic doping. A common configuration, with a SiO_2 backgate dielectric on top of a *n*-doped Si substrate is depicted. The top inset illustrates the changes in $E_{F,\mathrm{SLG}}$ in respect to the applied bias, assuming the ideal case of pristine SLG, i.e. $E_{F,\mathrm{SLG}} = 0$ at $V_g = 0$.

and convenient way, it is also a fully reversible and non-destructive method to achieve this. Combining eqs. 3.8 - 3.9, $E_{F,\mathrm{SLG}}$ can be correlated to the applied voltage:

$$E_{F,\mathrm{SLG}}(V_g) = \hbar v_{F,\mathrm{SLG}} \sqrt{\frac{\pi \epsilon_0 \epsilon_r V_g}{ed}} \tag{3.10}$$

Note that the inset of fig. 3.3 illustrates the ideal case where $E_{F,\mathrm{SLG}} = 0$ for $V_g = 0$. If graphene is extrinsically doped (e.g. due to charge transfer from a substrate or fabrication procedure), a gate voltage V_g must be applied to reach CNP.

Apart from the configuration of fig. 3.3, alternative implementations can be carried out for electrostatic doping, considering the target application. For example, in THz applications it is a common technique to use porous polymeric substrates containing ionic liquid electrolytes to implement electrostatic gating [55, 56, 228, 259, 260].

3.1.3 Equilibrium chemical potential

$E_{F,\mathrm{SLG}}$ sets the net SLG charge density at zero carrier temperature ($T_{e,\mathrm{SLG}} = 0$). Assuming n-doped SLG, at $T_{e,\mathrm{SLG}} = 0$ the electron and hole densities are:

$$n_{e,\mathrm{SLG}}\left(E_{F,\mathrm{SLG}}, 0\right) = \frac{E_{F,\mathrm{SLG}}^2}{\pi\left(\hbar v_{F,\mathrm{SLG}}\right)^2}, \; n_{h,\mathrm{SLG}}\left(E_{F,\mathrm{SLG}}, 0\right) = 0 \tag{3.11}$$

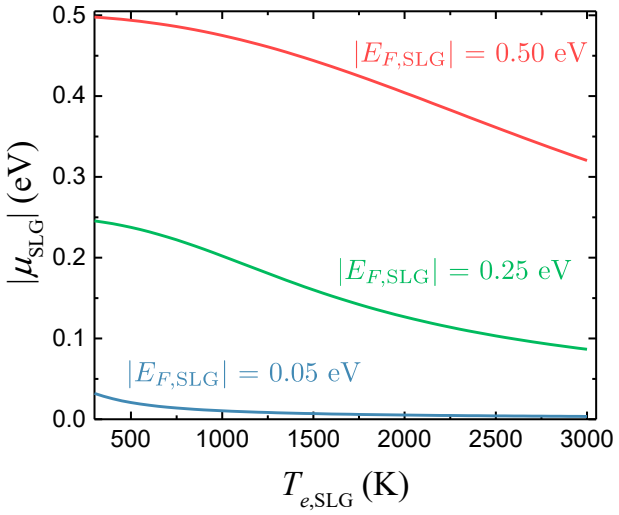

Figure 3.4: Equilibrium chemical potential $|\mu_{\mathrm{SLG}}|$ calculated using eqs. 3.12 and 3.13 as a function of carrier temperature $T_{e,\mathrm{SLG}}$ for $|E_{F,\mathrm{SLG}}| = 0.50$ eV (red line), 0.25 eV (green line) and 0.05 eV (blue line). Positive (negative) values of $E_{F,\mathrm{SLG}}$ and μ corresponds to n-doped (p-doped) SLG.

At $T_{e,\mathrm{SLG}} > 0$ and thermodynamic equilibrium, i.e. same temperature $T_{e,\mathrm{SLG}}$ for electrons in the conduction band and holes in the valence band, the individual charge carrier concentrations increase, due to thermal excitation from the valence to the conduction band, but the net charge remains constant:

$$n_{e,\mathrm{SLG}}\left(\mu_{\mathrm{SLG}}, T_{e,\mathrm{SLG}}\right) - n_{h,\mathrm{SLG}}\left(\mu_{\mathrm{SLG}}, T_{e,\mathrm{SLG}}\right) = \frac{E_{F,\mathrm{SLG}}^2}{\pi\hbar^2 v_{F,\mathrm{SLG}}^2} \tag{3.12}$$

with μ_{SLG} the equilibrium chemical potential ($\mu > 0$ for n-doping and $\mu < 0$ for p-doping).

The temperature-dependent carrier densities are given by [64, 261]:

$$\begin{aligned} n_{e,\mathrm{SLG}}\left(\mu_{\mathrm{SLG}}, T_{e,\mathrm{SLG}}\right) &= \int_0^\infty \nu(\epsilon) f_{FD}\left(\epsilon; \mu_{\mathrm{SLG}}, T_{e,\mathrm{SLG}}\right) d\epsilon \\ n_{h,\mathrm{SLG}}\left(\mu_{\mathrm{SLG}}, T_{e,\mathrm{SLG}}\right) &= \int_0^\infty \nu(\epsilon) f_{FD}\left(\epsilon; -\mu_{\mathrm{SLG}}, T_{e,\mathrm{SLG}}\right) d\epsilon \end{aligned} \tag{3.13}$$

with $f_{FD}(\epsilon; \mu_{\mathrm{SLG}}, T_{e,\mathrm{SLG}}) = \{\exp[(\epsilon - \mu_{\mathrm{SLG}})/(k_B T_{e,\mathrm{SLG}})] + 1\}^{-1}$ the Fermi - Dirac distribution and $\nu(\epsilon)$ the electronic density of states given by eq. 3.6. The chemical potential μ_{SLG} can be determined self-consistently, upon inserting eqs. 3.13 in eq. 3.12. It is apparent that higher $T_{e,\mathrm{SLG}}$ leads to lower $|\mu_{\mathrm{SLG}}|$, as dictated by the charge conservation, while $\mu_{\mathrm{SLG}} \equiv E_{F,\mathrm{SLG}}$ as $T_{e,\mathrm{SLG}} \to 0$ (fig. 3.4).

3.1.4 Transport properties

By varying the charge density, one can also modulate the SLG DC conductivity $\sigma_{\mathrm{DC,SLG}}$. In reality, however, the conductivity never vanishes, even at the CNP. This is because of a minimum conductivity $\sigma_{\mathrm{min,SLG}} \sim 4e^2/h$ arising from the quantum mechanical interpretation of carriers near the CNP at low ($n < 10^{11}\mathrm{cm}^{-2}$) carrier densities [262, 263]. Moreover, in most cases even the above value of $\sigma_{\mathrm{min,SLG}}$ cannot be reached. That is because the charge density never completely vanishes, at least locally, due to electron-hole charge puddles caused by disorder in the form of charge impurities [264]. Typical values for the residual local charge density fluctuations near the CNP at SiO_2 supported graphene are in the range $n_{\mathrm{min,SLG}} \sim 10^{10} - 10^{12}$ cm^{-2} [263, 265]. Taking $n_{\mathrm{min,SLG}}$ into account, the SLG dc conductivity is given by:

$$\sigma_{\mathrm{DC,SLG}} = n_{\mathrm{min,SLG}}\, e\, \mu_{q,\mathrm{SLG}} \left(1 + \frac{n}{n_{\mathrm{min,SLG}}}\right) \tag{3.14}$$

where $n = n_{e,\mathrm{SLG}} + |n_{h,\mathrm{SLG}}|$ the total SLG carrier concentration and $\mu_{q,\mathrm{SLG}}$ is the SLG carrier mobility. The latter has values that depend on the fabrication process and configuration. Ultra-high mobilities in room temperature, in the order of $\mu_{q,\mathrm{SLG}} \sim 2 \times 10^5$ cm^{2}V^{-1}s^{-1} have been reported for suspended graphene [266], while values up to $\sim 1.4 \times 10^5$ cm^{2}V^{-1}s^{-1} have been measured for SLG encapsulated in hexagonal boron nitride [267]. In the case of graphene suspended on a SiO_2 substrate, the mobility is limited by long-range Coulomb scattering with charge impurities [263] and is expected to be always reduced to values $\mu_{q,\mathrm{SLG}} < 4 \times 10^4$ cm^{2}V^{-1}s^{-1} [268].

Finally, the charge puddles affect the value of SLG quantum capacitance $C_{q,\mathrm{SLG}}$ [269, 270]. The later is given by [269]:

$$C_{q,\mathrm{SLG}} = \frac{2e^2}{\hbar v_{F,\mathrm{SLG}}\sqrt{\pi}} \left(n + |n_{\mathrm{min,SLG}}|\right)^{1/2} \tag{3.15}$$

and, depending on its value and the given configuration, one might need to add its contribution to eq. 3.10 to get accurate results for $E_{F,\mathrm{SLG}}(V_g)$. However, in typical SiO_2/Si gating configurations, its contribution is negligible compared to the junction capacitance and can safely be ignored [270].

3.1.5 Electronic heat capacity

The electronic heat capacity is an important electronic property, since it dictates carrier heating, upon illumination with a light source, as well as their subsequent cooling. By definition, it is given by the temperature derivative of the carriers' total internal energy $U_{\mathrm{SLG}}(\mu_{\mathrm{SLG}}, T_{e,\mathrm{SLG}})$ [64, 261]:

$$c_{e,\mathrm{SLG}}(\mu_{\mathrm{SLG}}, T_{e,\mathrm{SLG}}) = \frac{\partial U_{\mathrm{SLG}}(\mu_{\mathrm{SLG}}, T_{e,\mathrm{SLG}})}{\partial T_{e,\mathrm{SLG}}} = \\ = \frac{\partial}{\partial T_{e,\mathrm{SLG}}} \int_0^\infty \nu(\epsilon)\, \epsilon\, \left[f_{FD}\left(\epsilon; \mu_{\mathrm{SLG}}, T_{e,\mathrm{SLG}}\right) + f_{FD}\left(\epsilon; -\mu_{\mathrm{SLG}}, T_{e,\mathrm{SLG}}\right) \right] d\epsilon \tag{3.16}$$

where the first (second) term in the integral of eq. 3.16 accounts for electron (hole) internal energy. $c_{e,\mathrm{SLG}}$ can also be calculated using numerical approximations. At the non-degenerate limit, i.e., $\mu_{\mathrm{SLG}} \ll k_B T_{e,\mathrm{SLG}}$, $c_{e,\mathrm{SLG}}$ can be approximated by [271]:

$$c_{e,\mathrm{SLG}} \mid_{\mu_{\mathrm{SLG}} \ll k_B T_{e,\mathrm{SLG}}} = \frac{18\zeta(3)}{\pi \left(\hbar v_{F,\mathrm{SLG}}\right)^2} k_B^3 T_{e,\mathrm{SLG}}^2 \tag{3.17}$$

where $\zeta(3) \approx 1.202$ is the Apéry's constant. For $\mu_{\mathrm{SLG}} \ll k_B T_{e,\mathrm{SLG}}$, the approximate relation of $c_{e,\mathrm{SLG}}$ scales with $T_{e,\mathrm{SLG}}^2$. On the other hand, at the degenerate limit, i.e., $\mu_{\mathrm{SLG}} \gg k_B T_{e,\mathrm{SLG}}$, the approximate solution of $c_{e,\mathrm{SLG}}$ scales linearly with $T_{e,\mathrm{SLG}}$ following [272]:

$$c_{e,\mathrm{SLG}} \mid_{\mu_{\mathrm{SLG}} \gg k_B T_{e,\mathrm{SLG}}} = \frac{\pi^2}{3} \nu(E_{F,\mathrm{SLG}}) k_B^2 T_{e,\mathrm{SLG}} \tag{3.18}$$

Figure 3.5 plots both the exact solution as well as the two approximations for $c_{e,\mathrm{SLG}}$. Assuming small initial Fermi level, e.g. $E_{F,\mathrm{SLG}} = 0.05$ eV as for fig. 3.5(a), the approximation for the non-degenerate case (eq. 3.17) follows the exact solution of eq. 3.16 for a wide range for temperatures. For highly doped SLG [e.g., $E_{F,\mathrm{SLG}} = 0.50$ eV as for fig. 3.5(b)] on the other hand, the approximation considering the degenerate limit (eq. 3.18) results in better agreement with the full solution, but only up to certain carrier temperature of $T_{e,\mathrm{SLG}} \approx 700$ K. In this thesis the aim is to model graphene-based devices' temporal dynamics as the carrier temperature increases, e.g. during illumination, for a wide range of $E_{F,\mathrm{SLG}}$. Thus, in all calculations the exact solution described by eq. 3.16 was used.

Note that the record-low values of the electronic heat capacity of graphene [64, 273], in the order of $\lesssim 1$ nJ cm^{-2} K^{-1}, make it an ideal candidate for optoelectronic applications based on "hot" (thermalized) carriers, since one can achieve significant temperature rise using low power excitation.

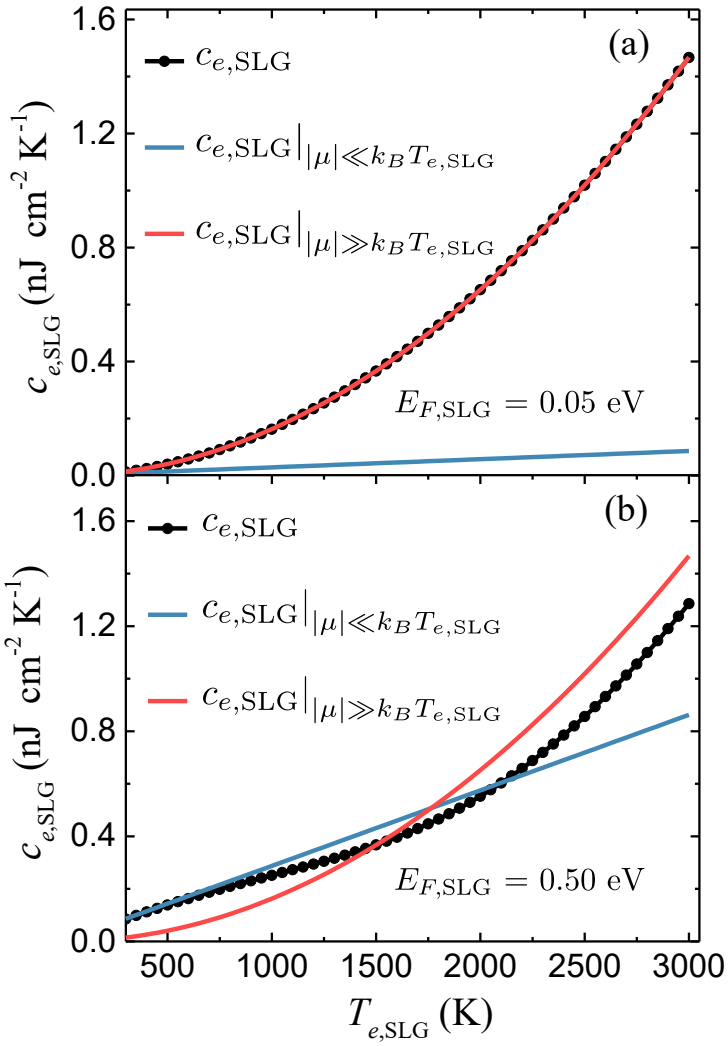

Figure 3.5: Electronic heat capacity calculated using eq. 3.16 (black dotted line), eq. 3.17 (red line) and eq. 3.18 (blue line) as e function of carrier temperature $T_{e,\mathrm{SLG}}$ assuming initial Fermi level (a) $E_{F,\mathrm{SLG}} = 0.05$ eV and (b) $E_{F,\mathrm{SLG}} = 0.50$ eV.

3.2 Optical properties

Graphene possesses unique optical properties, making it an appealing material for the development of optoelectronic applications. Among these properties are the SLG broadband absorption, owing to its gapless nature, across the visible and IR part of the spectrum [42] and the SLG tunable optical conductivity through the control of $E_{F,\mathrm{SLG}}$ [25, 208].

3.2.1 Optical conductivity

Graphene's optical response is governed by its optical conductivity $\sigma^{\mathrm{opt}}_{\mathrm{SLG}}$. The latter can be distinguished in two terms, one for intraband and one for interband transitions:

$$\sigma^{\mathrm{opt}}_{\mathrm{SLG}}(\omega;\mu,T_{e,\mathrm{SLG}}) = \sigma^{\mathrm{opt}}_{\mathrm{intra,SLG}}(\omega;\mu,T_{e,\mathrm{SLG}}) + \sigma^{\mathrm{opt}}_{\mathrm{inter,SLG}}(\omega;\mu,T_{e,\mathrm{SLG}}) \tag{3.19}$$

These are calculated using the Kubo formula [57, 274] yielding:

$$\sigma^{\mathrm{opt}}_{\mathrm{intra,SLG}} = \frac{ie^2}{\pi\hbar^2\Omega}\int_0^\infty \epsilon\left[\frac{\partial f_{FD}(-\epsilon;\mu,T_{e,\mathrm{SLG}})}{\partial\epsilon} - \frac{\partial f_{FD}(\epsilon;\mu,T_{e,\mathrm{SLG}})}{\partial\epsilon}\right]d\epsilon \tag{3.20}$$

for the intraband and:

$$\sigma^{\mathrm{opt}}_{\mathrm{inter,SLG}} = \frac{ie^2\Omega}{\pi\hbar^2}\int_0^\infty \left[\frac{f_{FD}(-\epsilon;\mu,T_{e,\mathrm{SLG}}) - f_{FD}(\epsilon;\mu,T_{e,\mathrm{SLG}})}{\Omega^2 - 4\left(\frac{\epsilon}{\hbar}\right)^2}\right]d\epsilon \tag{3.21}$$

for the interband term. In the above equations $\Omega = \omega + i\tau^{-1}_{\mathrm{opt}}$, where τ_{opt} is the free electron relaxation time related to charge carrier mobility in SLG [47] (see discussion below).

Figure 3.6 plots $\sigma^{\mathrm{opt}}_{\mathrm{SLG}}$ as calculated from eq. 3.19. The plot considers both the case of $T_{e,\mathrm{SLG}} = 0$ K (dashed lines) as well as three cases of finite $T_{e,\mathrm{SLG}} > 0$ (solid lines). For $\hbar\omega \geq 2\,|\mu_{\mathrm{SLG}}|$, the real part of $\sigma^{\mathrm{opt}}_{\mathrm{SLG}}$ converges to the universal frequency-independent value $\sigma_0 = e^2/4\hbar$ [42], characteristic for SLG Dirac fermions [263]. At this spectral regime, $\sigma^{\mathrm{opt}}_{\mathrm{SLG}}$ is dominated by interband transitions. This can be understood by the schematic representation of a photon absorption event depicted in fig. 3.7. Interband transitions for photons with energies $\hbar\omega \lesssim 2\,|\mu_{\mathrm{SLG}}|$ are not allowed, given energy and momentum conservation, since the conduction band is already occupied (rightmost arrows in fig. 3.7). This restriction for interband conductivity, commonly referred to as Pauli blocking, is lifted only for $\hbar\omega \gtrsim 2\,|\mu_{\mathrm{SLG}}|$ (leftmost arrows in fig. 3.7), where the interband term dominates yielding the universal value σ_0. The transition between the interband and intraband regimes has a step-like profile, exactly at $\hbar\omega = 2\,|\mu_{\mathrm{SLG}}|$, for $T_{e,\mathrm{SLG}} = 0$ K. A smearing is observed for finite $T_{e,\mathrm{SLG}}$ values. The broadening around $\hbar\omega = 2\,|\mu_{\mathrm{SLG}}|$ is enlarged for greater $T_{e,\mathrm{SLG}}$ (fig. 3.6). Eventually at $\hbar\omega \lesssim 2\,|\mu_{\mathrm{SLG}}|$ $\sigma^{\mathrm{opt}}_{\mathrm{SLG}}$ becomes minimum, resulting in the transparency regime.

For $\hbar\omega \ll 2\,|\mu_{\mathrm{SLG}}|$, graphene's optical conductivity is dominated by free carrier absorption, described by the intraband term as for eq. 3.20 (middle curved arrows in fig. 3.7). The latter, given that $k_B T_{e,\mathrm{SLG}} \ll \mu_{\mathrm{SLG}} \sim E_{F,\mathrm{SLG}}$, can be described by a Drude-like expression [275, 276]:

$$\sigma^{\mathrm{opt}}_{\mathrm{intra,SLG}} \approx \frac{ie^2}{\pi\hbar^2}\frac{\mu_{\mathrm{SLG}}}{\omega + i\tau^{-1}_{\mathrm{opt}}} \tag{3.22}$$

In this intraband dominated regime, spanning from mid-wavelength infrared (MWIR) up to the THz part of the spectrum, $\sigma^{\mathrm{opt}}_{\mathrm{SLG}}$ strongly depends on τ_{opt}. The latter depends on both

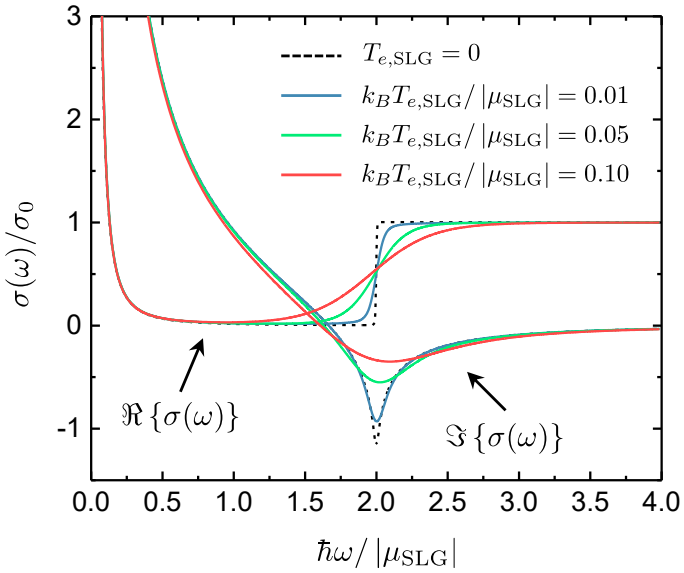

Figure 3.6: Real and imaginary parts of graphene's optical conductivity (eq. 3.19), normalized to the universal value $\sigma_0 = e^2/4\hbar$, for $T_{e,\mathrm{SLG}} = 0$ (dashed line) and $T_{e,\mathrm{SLG}} > 0$ (solid lines) as a function of photon wavelength. The above calculations ware performed assuming $E_{F,\mathrm{SLG}} = 0.25$ eV and a constant $\tau_{\mathrm{opt}} = 200$ fs.

SLG quality (i.e., contaminants, defects, wrinkles, and non-uniformities) as well as the substrate on which SLG is placed and the interface quality [47, 277]. In the degenerate limit ($\mu_{\mathrm{SLG}} \gg k_B T_{e,\mathrm{SLG}}$), fixed values can be assumed for τ_{opt}, ranging from 10 - 300 fs [47]. Since τ_{opt} cannot be directly measured, it can be correlated with carrier mobility through [277, 278]:

$$\mu_{q,\mathrm{SLG}} = e\tau_{\mathrm{opt}} v_{F,\mathrm{SLG}}^2 / E_{F,\mathrm{SLG}} \tag{3.23}$$

which can be easily extracted from resistivity measurements [266–268].

On the other hand, at elevated carrier temperatures (e.g., due to light absorption), if one is interested to calculate $\sigma_{\mathrm{SLG}}^{\mathrm{opt}}$ in the intraband dominated regime, the carrier energy dependence of τ_{opt} must be considered [263, 279–282]. Free carrier energy-depended scattering is usually described considering two main mechanisms [263, 279–282]; short-range scattering at disorder sites and long-range scattering at Coulomb impurities. For the former, which is dominant in suspended or encapsulated graphene, acquired by mechanical exfoliation, the energy dependence of τ_{opt} is given by [263, 279]:

$$\tau_{\mathrm{opt}}(\epsilon) = \frac{4\hbar^3 v_{F,\mathrm{SLG}}^2}{n_d V_0^2 \epsilon} = \frac{\beta}{\epsilon} \tag{3.24}$$

where n_d is the short-range scattering impurity concentration and V_0 the strength of the short-ranged disorder potential [263]. For this scattering regime, τ_{opt} turns out to be inversely proportional to carrier energy. The proportionality constant β in eq. 3.24 depends on n_d and V_0 and can be readily extracted from experiments upon conductivity measurement at room temperature (RT), i.e., $\beta = \tau_{\mathrm{opt}}(E_{F,\mathrm{SLG}})\, E_{F,\mathrm{SLG}}$ [280–282]. The second

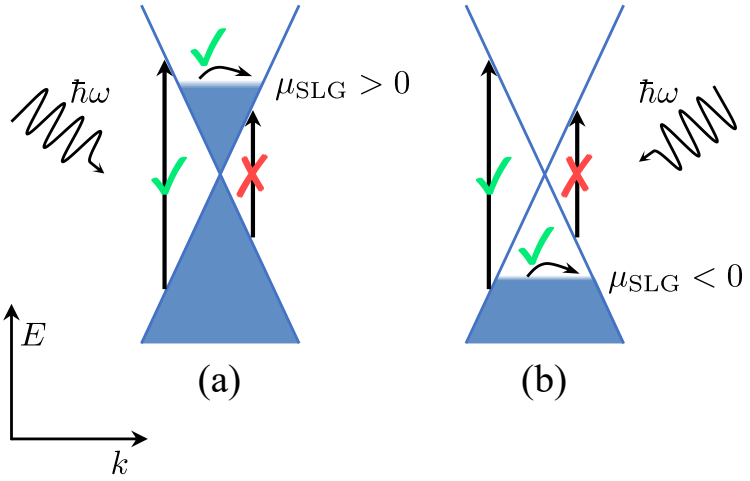

Figure 3.7: Schematic representation of an intraband (middle arrows), allowed interband (leftmost arrows) and Pauli blocked interband (rightmost arrows) transition for (a) *n*-doped and (b) *p*-doped graphene.

mechanism, long-range Coulomb scattering on ionized impurities, is dominant on CVD-grown graphene supported by a substrate [263, 279–282]. In this scenario, the energy-dependent τ_{opt} is given by:

$$\tau_{\text{opt}}(\epsilon) = \frac{\hbar}{\pi^2}\frac{\epsilon_{sub}^2}{e^4}\frac{1}{n_i}\epsilon = \gamma\epsilon \tag{3.25}$$

where n_i is the ionized-impurity concentration and ϵ_{sub} the background dielectric constant [263, 279]. In this case, τ_{opt} is proportional to carrier energy, while the proportionality constant γ can be extracted from conductivity measurements at RT, as for the case of the short-range scattering mechanism, i.e. $\gamma = \tau_{\text{opt}}(E_{F,\text{SLG}})/E_{F,\text{SLG}}$ [280–282]. Depending on the given configuration, eq. 3.24 or eq. 3.25 can be inserted in eqs. 3.19 - 3.20 to accurately calculate $\sigma_{\text{SLG}}^{\text{opt}}$.

Conversely, in the visible (VIS) up to MWIR part of the spectrum, where graphene's optical conductivity is interband dominated as discussed above, $\sigma_{\text{SLG}}^{\text{opt}}$ is independent of the τ_{opt} values [283].

The optical absorption of suspended SLG is determined by the real part of $\sigma_{\text{SLG}}^{\text{opt}}$ [57]:

$$\alpha_{\text{SLG}}^{\text{sus}} = \frac{\Re\left\{\sigma_{\text{SLG}}^{\text{opt}}\right\}}{\epsilon_0 c} \tag{3.26}$$

where ϵ_0 and c is the vacuum permittivity and the speed of light in vacuum respectively. Interestingly, in VIS up to MWIR where $\sigma_{\text{SLG}}^{\text{opt}}$ has the universal value $\sigma_0 = e^2/4\hbar$, SLG absorption turns out to be $\alpha_{\text{SLG}}^{\text{sus}} = e^2/(4\hbar\epsilon_0 c) = \pi\alpha \approx 2.3\,\%$, where $\alpha = e^2/(4\pi\hbar\epsilon_0 c)$ the fine-structure constant [42].

The photon energy for transition from intraband to interband dominated $\sigma_{\text{SLG}}^{\text{opt}}$, i.e., $\hbar\omega = 2\,|\mu_{\text{SLG}}|$, can be modulated in a convenient and reversible manner using electrostatic gating. For experimentally achievable $E_{F,\text{SLG}}$ values, in the range of ≈ 50 meV up to ≈ 1 eV, this transition falls in the MWIR to VIS part of the spectrum. The ability to manipulate SLG optical conductivity in this manner, sets the scene for a large variety of graphene-based optoelectronic applications.

3.2.2 Dielectric function and refractive index

Having determined the optical conductivity, graphene's dielectric function is given by [284, 285]:

$$\epsilon_{\mathrm{SLG}}(\omega;\mu,T_{e,\mathrm{SLG}}) = \epsilon_{\infty,\mathrm{SLG}} + \frac{i\sigma^{\mathrm{opt}}_{\mathrm{SLG}}(\omega;\mu,T_{e,\mathrm{SLG}})}{\epsilon_0\,\omega d_{\mathrm{SLG}}} \tag{3.27}$$

where $\epsilon_{\infty,\mathrm{SLG}} = 5.7$ is the frequency independent part of the dielectric function at high frequencies [285] and $d_{\mathrm{SLG}} = 0.335$ nm is the SLG thickness [286, 287]. Finally, graphene's

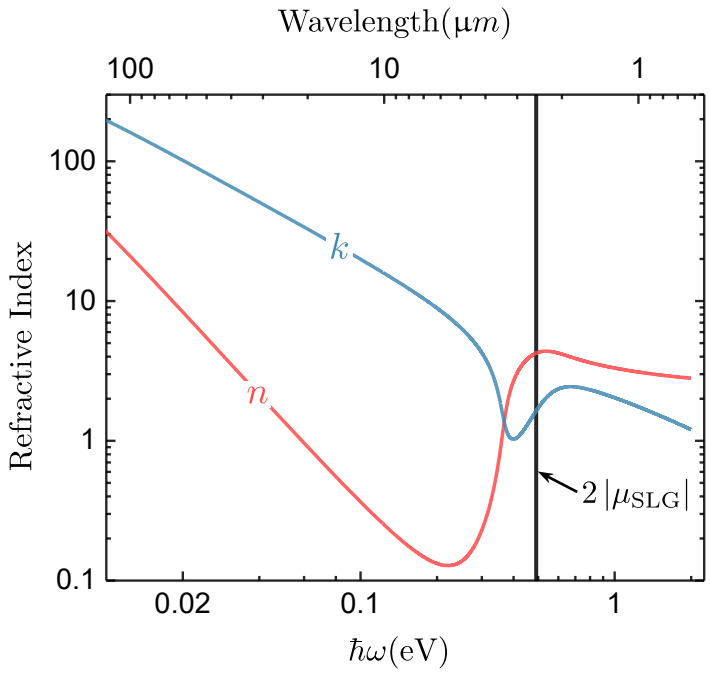

Figure 3.8: Real (red) and imaginary (blue) part of graphene's refractive index as a function of photon energy (bottom axis) and wavelength (top axis). The vertical black line marks the photon energy $\hbar\omega = 2\,|\mu_{\mathrm{SLG}}|$, below which interband transitions are Pauli blocked.

complex refractive index:

$$\widetilde{n}_{\mathrm{SLG}} = n + ik \tag{3.28}$$

can be calculated via eq. 3.27 [288]:

$$\begin{aligned} \Re\{\epsilon_{\mathrm{SLG}}\} &= n^2 - k^2 \\ \Im\{\epsilon_{\mathrm{SLG}}\} &= 2nk \end{aligned} \tag{3.29}$$

Figure 3.8 plots graphene's complex refractive index from the VIS up to the FIR part of the spectrum, assuming $|E_{F,\mathrm{SLG}} = 0.25|$ eV and a fixed value for the free carrier relaxation time $\tau_{\mathrm{opt}} = 200$ fs. The vertical black line marks the position of $\hbar\omega = 2\,|\mu_{\mathrm{SLG}}|$, around which the transition from intraband-dominated to interband-dominated optical conductivity occurs.

3.3 Graphene plasmonics

Graphene is an ideal platform for the realization of surface plasmon polaritons (SPP). SPP, which can be regarded as the collective plasma (free charge carrier) oscillations of a conductor, are bound electromagnetic waves propagating in a metal-dielectric interface [fig. 3.9(b)]. These modes allow for subwavelength optics and strong electromagnetic field confinement, useful for a plethora of applications. SPP in graphene [fig. 3.9(b)] can lead to enhanced SLG light absorption [289–295] (especially when combined with the critical coupling scheme, described in Appendix A) which is crucial for developing optoelectronic applications.

An immediate advantage of using graphene over conventional metal plasmonics, is the ability to control the former's charge density, e.g. with electrostatic gating. Additionally, graphene's 2D nature renders it an ideal platform for the realization of plasmonic applications, with unprecedented spatial field confinement and low losses, when compared to conventional metal-based plasmonics [59–63].

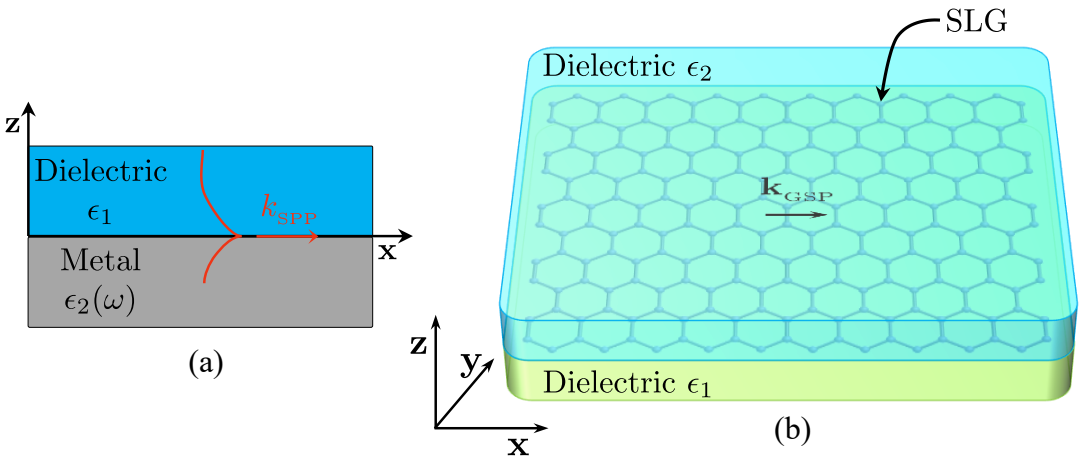

Figure 3.9: (a) SPP propagating in a metal-dielectric interface. The red lines qualitatively show the field profile (b) SPP bound on SLG surface, sandwiched between two dielectrics.

3.3.1 Surface Plasmons on metal-dielectric interfaces

Before the description of graphene plasmonics, it is instructive to introduce the concept of SPP in the conventional metal-dielectric platform. In this section, a brief overview of their key aspects is presented. A complete description of SPP can be found in literature in a variety of reviews [296–298] and textbooks [299, 300].

Let us assume the simple configuration of a dielectric-metal interface as for fig. 3.9(a). The dielectric is characterized by a positive dielectric constant $\epsilon_1 > 0$ whereas for the metal a Drude-like dielectric function is assumed, i.e.:

$$\epsilon_2(\omega) = \epsilon_\infty - \frac{\omega_p^2}{\omega^2 + i\omega\tau^{-1}} \tag{3.30}$$

where ω_p is the plasma frequency, ϵ_∞ the dielectric constant at high frequencies ($\omega \gg \omega_p$) and τ is the relaxation time of the free carriers [299]. Bound wave solutions can be

acquired for TM polarization [299] with their electric and magnetic fields given by:

$$\begin{aligned}\mathbf{E}(\mathbf{r},t) &= (E_{j,x}\,\mathbf{x} + E_{j,z}\,\mathbf{z})\,e^{-\kappa_j|z|}e^{i(k_{\text{SPP}}x-\omega t)}\\ \mathbf{B}(\mathbf{r},t) &= B_{j,y}\,\mathbf{y}\,e^{-\kappa_j|z|}e^{i(k_{\text{SPP}}x-\omega t)}\end{aligned} \tag{3.31}$$

where the index $j = 1, 2$ identifies the medium, as for 3.9(a), and k_{SPP} is the SPP wavevector propagating along the x-axis. The wave vector κ_j, perpendicular to the surface, is given by:

$$\kappa_j = \sqrt{k_{\text{SPP}}^2 - \epsilon_j\omega^2/c^2} \tag{3.32}$$

The continuity of the electric and magnetic fields tangential components result to a relationship of the form [299]:

$$\frac{\epsilon_1}{\kappa_1(k_{\text{SPP}},\omega)} + \frac{\epsilon_2(\omega)}{\kappa_2(k_{\text{SPP}},\omega)} = 0 \tag{3.33}$$

From eq. 3.33 one can deduce that SPP can only exist in the interfaces of materials with opposite signs of the real part of their permittivities, e.g., in insulator-metal interfaces, where $\epsilon_1 > 0$ and $\Re\{\epsilon_2(\omega)\} < 0$. Inserting 3.32 in 3.33, the SPP dispersion relationship is given by:

$$k_{\text{SPP}} = \frac{\omega}{c}\sqrt{\frac{\epsilon_1\epsilon_2(\omega)}{\epsilon_1 + \epsilon_2(\omega)}} \tag{3.34}$$

The dispersion relationship 3.34, regarding SPP on a Ag/Si interface, is plotted in fig. 3.10(a). The dielectric response of Ag is extracted from the experimental data of ref. [301], while for Si a dielectric constant of $\epsilon_{\text{Si}} = 3.42$ is assumed. Note that due to their bound nature, SPP dispersion curve lies to the right side of the light lines [fig. 3.10(a)] of air (green line) and Si (red line). Therefore, special phase matching techniques are required to excite them (e.g., gratings, prisms or other nanostructures). The SPP dispersion approaches the characteristic surface plasmon frequency [299] $\omega_{sp} \approx 2.3$ eV at a finite value of wavevector k_{SPP}. Above this frequency there are also solutions, but they do not correspond to SPP [299].

3.3.2 Graphene surface plasmon polaritons

SPP can be realized in SLG sandwiched between two dielectrics (including the case of the top dielectric being air) as for 3.9(b). Again, the main aspects of SPP on graphene are briefly highlighted and the reader is referred to the extensive reviews [59–62] and textbooks [63] in literature for a more complete description. The derivation of dispersion relationship for SPP on SLG is acquired in a similar way as for the metal-dielectric SPP case, with the difference that surface conductivity of graphene must be accounted for, when applying the boundary conditions at the graphene-dielectric interfaces [302], i.e.:

$$\frac{\epsilon_1}{\kappa_1(k_{\text{GSP}},\omega)} + \frac{\epsilon_2}{\kappa_2(k_{\text{GSP}},\omega)} + i\frac{\sigma_{\text{SLG}}^{\text{opt}}}{\omega\epsilon_0} = 0 \tag{3.35}$$

with k_{GSP} being the graphene surface plasmon (GSP) wavevector, and the index $j = 1, 2$ accounting for the dielectric constants of the mediums below and above SLG respectively, as for fig. 3.9(b). In the MWIR up to THz spectral regime, $\sigma_{\text{SLG}}^{\text{opt}}$ is dominated by intraband

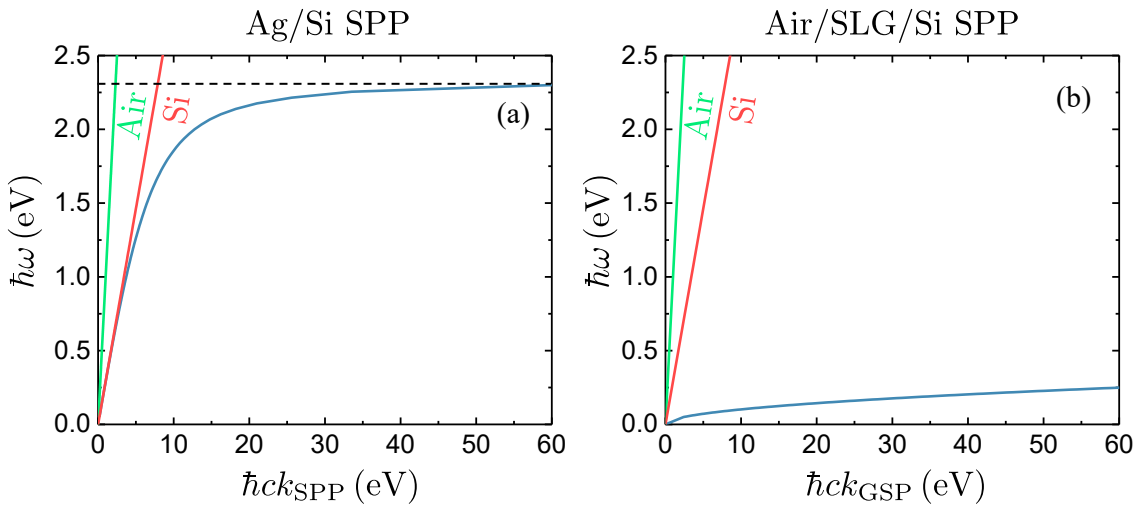

Figure 3.10: (a) Dispersion of SPP in Ag/Si interface. The data for Ag dielectric function were extracted from ref. [301]. The green (red) curves correspond to the light lines of air (Si). The SPP solutions converge to the characteristic frequency $\omega_{SP} \approx 2.3$ eV. (dashed line). (b) Dispersion relationship of SPP, assuming SLG on Si, $E_{F,\rm SLG} = 0.45$ eV and $\tau_{\rm opt} = 200$ fs. The green (red) curves correspond to the light lines of air (Si).

transitions and can be described using the Drude-like eq. 3.22, given that $E_{F,\rm SLG} \gg T_{e,\rm SLG}$ and $E_{F,\rm SLG} \gg \hbar\omega$. Plugging 3.22 in 3.35, the dispersion relationship for GSP is given by:

$$k_{\rm GSP} = \frac{\pi\hbar^2\epsilon_0\epsilon_r}{e^2 E_{F,\rm SLG}}\omega^2\left(1+\frac{i}{\omega\tau_{\rm opt}}\right) \tag{3.36}$$

with $\epsilon_r = \epsilon_1 + \epsilon_2$. Equation 3.36 is plotted in fig. 3.10(b), assuming $E_{F,\rm SLG} = 0.45$ eV and a constant $\tau_{\rm opt} = 200$ fs. The much greater confinement of SLG SPP is clear, since their dispersion curve lies much further than the light lines of air (green) and Si (red), when compared to the Ag/Si SPP case [3.10(b)].

One way to quantify wave localization on SPP is to compare the free space wavelength λ to the surface plasmon wavelength $\lambda_{\rm SPP} \equiv 1/(2\pi k_{\rm SPP})$ by taking their ratio. Losses, i.e., plasmon decay due to scattering of charge carriers, can also be quantified by taking the ratio of the real to the imaginary part of the plasmon wavevector. Figure 3.11 plots these quantities for the Ag/Si SPP [fig. 3.11(a)] as well as for the GSP case [fig. 3.11(b)]. It is clear that GSP have lower loses and greater wave localization compared to conventional SPP in metal-dielectric interfaces. Note that only the simplest configuration of a metal-dielectric interface has been reviewed here; there are more complex configurations (e.g., metal-dielectric-metal or dielectric-metal-dielectric interfaces) which also support SPP, with better performance compared to the simple interface case. Nevertheless, none of the above has the advantages of GSP, namely low losses and strong localization, atop of the tunability offered by graphene [59–63].

3.3.3 Plasmonics on graphene nanoribbons

In the previous section, it has already been stressed that special phase matching techniques are required to excite SPP, since the latter are bound surface waves with their dispersion

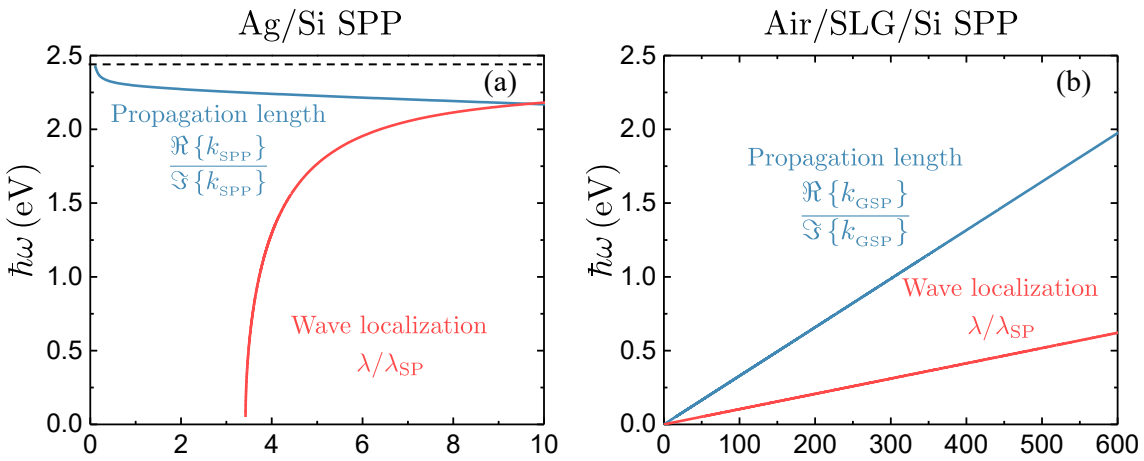

Figure 3.11: Propagation length and wave localization for (a) SPP in Ag/Si interface (b) GSP on air/Si interface, assuming $E_{F,\mathrm{SLG}} = 0.45$ eV and $\tau_{\mathrm{opt}} = 200$ fs.

curve lying below the light line. One way to achieve this phase matching, without resorting to gratings or prisms, is to exploit scattering from metallic nanoparticles [285,303,304] or atomic force microscope tips [305, 306] to excite GSP. An additional, straightforward way to achieve phase matching, is to use nanostructured SLG itself as a scattering platform. The latter can be achieved using either graphene nanodisks [307–312] or graphene nanoribbons [313–320]. In the contexts of this thesis, we will focus on graphene nanoribbons (GNR).

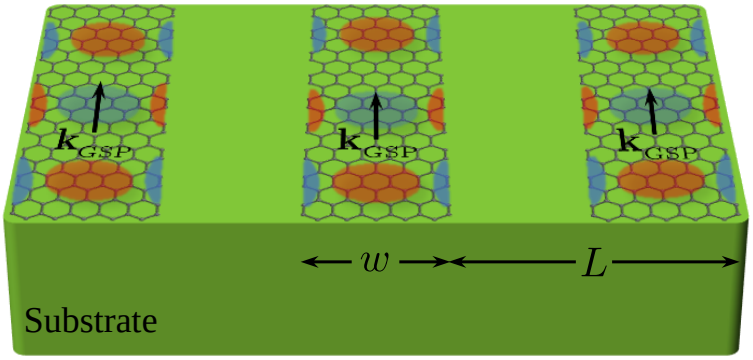

Figure 3.12: Schematic representation of a commonly used periodic graphene ribbon array with width w and period L for the excitation of GSP, where $L = 2w$.

A common GNR configuration [313–320] consists of a periodic array of graphene ribbons, having width w and period L, placed on a substrate, as for fig. 3.12. The GSP resonances in the ribbons approximately satisfy:

$$w \sim n\,\lambda_{\mathrm{GSP}}/2 \tag{3.37}$$

where n is an integer and $\lambda_{\mathrm{GSP}} = 2\pi/\Re\{k_{\mathrm{GSP}}\}$. That is, a half-integer number of GSP wavelengths must fit in the ribbon width [317–320]. Plugging eq. 3.36 in 3.37 and taking

into account that the later turns into an equality if the geometric features of a given configuration are taken into account (e.g. w/L ratio), the resonant wavelength of the GSP on a GNR array is given by:

$$\lambda = \eta \frac{2\pi\hbar c}{e} \sqrt{\frac{1}{n} \frac{w}{E_{F,\mathrm{SLG}}} \epsilon_r \epsilon_0} \tag{3.38}$$

The prefactor η accounts for the hybridization and redshift of plasmons in neighboring GNRs [317–319], where $\eta \to 0$ for large ($w/L \to 0$) GNR separations. η can also be affected by SPP-cavity interactions, e.g., in the case of a substrate terminated with a metallic backmirror, in order to enhance the plasmonic resonance [321]. In eq. 3.38 the integer n corresponds to the plasmonic resonance order, e.g. for $n = 1$ the lowest energy (bipolar) resonance emerges [317, 319]. Furthermore, from eq. 3.38 it turns out that using GNR arrays, one has further degrees of freedom for tuning the plasmonic resonance, i.e. the dielectric environment ϵ_r, the width w and the rest geometric parameters (w/L ratio, possible use of a Fabry-Perot cavity) that determine η. The above, however, are chosen at the fabrication stage and cannot be reversibly altered during operation, in contrast to electrostatic gating. The latter can be used to tune $E_{F,\mathrm{SLG}}$ and bring the plasmonic resonance in the desired wavelength.

The use of GNR can be exploited to enhance light absorption on graphene. Depending on the configuration, up to 100 % light absorption in graphene can be achieved [289, 322] in a straightforward, easy to fabricate and tunable configuration.

3.4 Photocarrier dynamics

In this section graphene's carrier dynamics upon light absorption are addressed. First, the ultrafast thermalization of photoexcited graphene carriers is briefly discussed. Next, the carrier heat dissipation channels, via electron-phonon collisions, are presented. Lastly, the rate equations that govern carriers' temporal dynamics upon illumination are formulated, to accurately describe graphene photoexcitation.

3.4.1 Carrier heating

At finite temperature $T_{e,\mathrm{SLG}}$ and thermodynamic equilibrium, graphene's carrier distribution is given by eq. 3.13, with a common temperature and chemical potential for both electrons and holes. The total energy density of the electronic system is then given by:

$$\mathcal{E}_{eq} = \int_0^\infty \epsilon\, \nu(\epsilon) \left[f_{FD}\left(\epsilon; \mu_{\mathrm{SLG}}, T_{e,\mathrm{SLG}}\right) + f_{FD}\left(\epsilon; -\mu_{\mathrm{SLG}}, T_{e,\mathrm{SLG}}\right) \right] d\epsilon \tag{3.39}$$

If the electronic system is excited with an energy density F_{in}, the conservation of energy dictates:

$$\mathcal{E}_{eq} + F_{in} = \mathcal{E}_{hot} \tag{3.40}$$

where $\mathcal{E}_{hot}$ is characterized by "hot" Fermi-Dirac distributions at an increased temperature $T_{e,\mathrm{SLG}}$. Carrier thermalization occurs via Coulomb carrier-carrier scattering, where carriers exchange energy and momentum, and is typically concluded within tens of fs [64, 183, 184, 323, 324]. This thermalization leads to broadened a Fermi-Dirac distributions of graphene carriers, accompanied with a lowering of the chemical potential, as dictated by the charge conservation (eq. 3.12). Both the broadening and the μ_{SLG} lowering

have been observed experimentally [325] and have a crucial impact on graphene's optical and electronic properties, as we will see in the following chapters.

At this point, it is instructive to briefly discuss the physical mechanisms that lead to the efficient and ultrafast thermalization of graphene carriers. This thermalization can occur within a single band ($|E_{F,\mathrm{SLG}}| \gg k_B T_{e,\mathrm{SLG}}$, intraband thermalization) or across both the valence and conduction bands ($|E_{F,\mathrm{SLG}}| \ll k_B T_{e,\mathrm{SLG}}$, interband thermalization). For typical semiconducting materials there are two main carrier-carrier processes; impact ionization and Auger recombination [20]. In the former, a high-energy electron passes its energy to another, lower energy electron, which is excited from the valence to the conduction band. The latter is the reverse process, where a high energy electron is degraded from the conduction to the valence band. These processes lead to an increase, in the case of impact ionization, or decrease, in the case of Auger recombination, of the carrier density. In graphene, the same processes can occur, especially in the case of interband thermalization [184]. There are also analogous effects taking place across a single band [326], i.e. in intraband thermalization [327]. In this case, the total carrier density remains constant but the hot carrier density, i.e. the density of carriers with energy above the chemical potential, is increased. The intraband impact ionization process is usually referred to in literature as impact excitation [326,328]. It should be noted that in graphene the impact ionization and impact excitation processes are favored compared to Auger recombination [183,324,329], leading to efficient carrier heating.

Let us assume that high energy carriers have been created, e.g. by absorbing a photon with energy $\hbar\omega > 2E_{F,\mathrm{SLG}}$. In this case, high energy carriers will be created at $\pm\hbar\omega/2$ around the Dirac point. During impact excitation, i.e. $E_{F,\mathrm{SLG}} \gg k_B T_{e,\mathrm{SLG}}$, these high energy carriers redistribute their energy via inelastically scattering events to other carriers in the Fermi sea, which gain kinetic energy. Secondary hot carriers are created, thus the impact excitation leads to hot carrier multiplication. In each scattering event, the initially high-energy carrier exchanges an amount of energy $\Delta\epsilon$ with a carrier within the Fermi sea. This $\Delta\epsilon$ follows a distribution that peaks around $E_{F,\mathrm{SLG}}$ [326]. Subsequently, an initial high-energy carrier can lead to the creation of multiple hot carriers during its cascade, leading to multiple hot carrier generation per absorbed photon. In the interband thermalization regime i.e., $E_{F,\mathrm{SLG}} \ll k_B T_{e,\mathrm{SLG}}$, impact excitation occurs in a similar manner, leading to "real" carrier multiplication, where multiple free carriers can be created per absorbed photon [329].

So far the case of interband photoexcitation has been considered, i.e. $\hbar\omega > 2E_{F,\mathrm{SLG}}$. For intraband photoexcitation, where $\hbar\omega < 2E_{F,\mathrm{SLG}}$, the carrier thermalization processes are similar. The intraband excitation leads to acceleration of free carriers, which will then redistribute the energy they gained across the Fermi sea, within the same ultrafast timescale of tens of fs [325]. There have been several studies that demonstrate the efficient carrier heating using intraband photoexcitation, in both MWIR [66] and THz spectral regimes [280,282,330].

3.4.2 Non-equilibrium photoexcited carriers

In the previous section, it was assumed that during thermalization electrons in the conduction band and holes in the valence band are described by a common temperature $T_{e,\mathrm{SLG}}$ and chemical potential μ_{SLG}. However, non-thermal distributions have been observed for tens of femtoseconds after illumination, in the case of interband photoexcitation ($\hbar\omega > 2E_{F,\mathrm{SLG}}$) [183,184,323,325,331]. During this short time, the electrons in the

conduction band and the holes in the valence band are described by two different chemical potentials, labeled $\mu_{c,\mathrm{SLG}}$ and $\mu_{v,\mathrm{SLG}}$ respectively. The lifetime of these non-thermal distributions has been measured using ultrafast pump-probe spectroscopy [184] and calculated using analytical and numerical methods [183], yielding a value $\tau_{e-e} \sim 20$ fs. In order to calculate $\mu_{c,\mathrm{SLG}}$ and $\mu_{v,\mathrm{SLG}}$, one needs to account for the non-equilibrium photoexcited carrier density $\delta_{n,\mathrm{SLG}}$ stemming from interband transitions. Knowing $\delta_{n,\mathrm{SLG}}$, one can solve for the non-equilibrium chemical potentials according to [261]:

$$\begin{aligned} n_{e,\mathrm{SLG}}\left(\mu_{c,\mathrm{SLG}}, T_{e,\mathrm{SLG}}\right) &= n_{e,\mathrm{SLG}}\left(\mu_{\mathrm{SLG}}, T_{e,\mathrm{SLG}}\right) + \delta_{n,\mathrm{SLG}} \\ n_{h,\mathrm{SLG}}\left(\mu_{v,\mathrm{SLG}}, T_{e,\mathrm{SLG}}\right) &= n_{h,\mathrm{SLG}}\left(\mu_{\mathrm{SLG}}, T_{e,\mathrm{SLG}}\right) + \delta_{n,\mathrm{SLG}} \end{aligned} \tag{3.41}$$

where μ_{SLG} is the equilibrium chemical potential, calculated from eq. 3.13. For interband photoexcitation, where $\delta_{n,\mathrm{SLG}} \neq 0$, all the quantities that depend on μ_{SLG}, e.g. eqs. 3.19-3.21, eq. 3.16 et.c., must instead be calculated using $\mu_{c,\mathrm{SLG}}$ for electrons and $\mu_{v,\mathrm{SLG}}$ for holes respectively.

It has been shown that for intraband photoexcitation ($\hbar\omega < 2E_{F,\mathrm{SLG}}$), a single broadened Fermi-Dirac distribution is directly established [325], i.e. $\delta_{n,\mathrm{SLG}} = 0$.

3.4.3 Hot carrier cooling in graphene

After their ultrafast thermalization, graphene's hot carriers will eventually dissipate their excess energy through several cooling channels [64]. These include electron-phonon (e-ph) scattering [58,183,184,323,332] as well as diffusive cooing, where carriers cool down by in-plane heat diffusion on graphene, out of the initially heated spot [64,66,68]. In the context of this thesis, only the first mechanism will be considered, since uniform illumination (hence thermalization) of graphene is assumed in all of the studied configurations.

There have been numerous studies addressing the e-ph cooling of graphene hot carriers, finding it to occur within a $\sim$ ps timescale [58, 64, 65, 183, 184, 323, 332–335]. The heat current density from thermalized carriers to the phonon bath is derived in this section, explicitly accounting for electron-optical phonon and electron acoustic-phonon supercollisions. Note that yet another cooling pathway may arise from the coupling of hot carriers to substrate phonons [336]. However, this pathway becomes important only when a polar substrate is used [64], e.g. SiO_2. Moreover, the contribution of this cooling pathway is even greater when a substrate hosting hyperbolic phonon modes, e.g. hexagonal-Boron Nitride, is used [337–339]. In this thesis, non-polar substrates were utilized (e.g. Si, ionic liquids) for all the hot-carrier relevant schemes. Thus, the cooling pathway through coupling to substrate phonons can safely be neglected [64].

Cooling through optical-phonon scattering

Graphene has two degenerate optical phonon branches (longitudinal and transverse) at the Γ point of the Brillouin zone, both with energies $\Omega_\Gamma = 196$ meV [340–342], corresponding to the G-peak of graphene's Raman spectrum, which induce intra-valley transitions [343]. Moreover, there is a degenerate phonon branch in the K point of the Brillouin zone, with energy $\Omega_K = 161$ meV [340–342], corresponding to the D-peak of graphene's Raman spectrum. K phonon modes, induce inter-valley carrier scattering, where carriers are scattered from the K to the $K^{'}$ valley and the other way around [343]. Both Γ and K phonon modes have the same functional dependence on their respective frequencies and lattice temperature [333]. This arises from the fact that even though the phonons at

K point have double the electron-phonon coupling constant when compared to those in the Γ point [333, 344], the latter are doubly degenerate [333, 343, 345]. The thermal current density due to the above phonon modes can be extracted by employing a Boltzmann collision integral within the Fermi golden rule approximation [345–347]:

$$J_{op}(\mu_{\mathrm{SLG}}, T_{e,\mathrm{SLG}}, T_{l,\mathrm{SLG}}) = \sum_i \left\{ \frac{9\hbar\Omega_{i,SLG}^3 \left(\gamma_0^{'}\right)^2}{\pi(\hbar v_{F,SLG})^4 \rho_{SLG}} \times \left[N\left(\frac{\Omega_{i,SLG}}{k_B T_{e,SLG}}\right) - N\left(\frac{\Omega_{i,SLG}}{k_B T_{l,SLG}}\right) \right] \mathcal{F}(\mu_{SLG}, T_{e,SLG}) \right\} \tag{3.42}$$

In eq. 3.42, $T_{l,\mathrm{SLG}}$ is graphene's lattice temperature, $\rho_{SLG} = 7.6 \times 10^{-7}$ Kg/m^2 the SLG mass density [49,348,349], $\gamma_0^{'} \sim 40$ eV/nm the derivative of the nearest-neighbor coupling amplitude (hopping integral) γ_0 with respect to SLG bond length [345], $N(x) = [e^x - 1]^{-1}$ the Bose distribution and the integral $\mathcal{F}$ is given by [345, 346]:

$$\mathcal{F}(\mu_{SLG}, T_{e,SLG}) = \int_{-\infty}^{\infty} |x(1-x)| \left\{ f[\Omega_i(x-1)] - f(\Omega_i x) \right\} dx \tag{3.43}$$

The summation in eq. 3.42 is performed accounting for both phonon branches, i.e., for $\Omega_\Gamma = 196$ meV and $\Omega_K = 161$ meV.

Cooling through acoustic-phonon scattering via disorder-assisted supercollisions

Normal (momentum-conserving) acoustic phonon scattering is suppressed in graphene, due to its small Fermi surface [328, 348]. As a result, this weak cooling pathway results to slow relaxation times, in the order of $\sim$ ns [346, 350] and can safely be neglected [71,351–353]. However, heat dissipation via the carrier-acoustic phonon pathway can take in place in graphene through disorder-assisted supercollisions [328, 351–353]. These consist of three-body collisions between carriers, phonons and impurities in SLG lattice [328, 351, 353]. With momentum-conserving collisions to acoustic phonons constrained by SLG's small Fermi surface and optical phonon energies ($\Omega_\Gamma = 196$ meV, $\Omega_K = 161$ meV) $\gg k_B T_{e,\mathrm{SLG}}$ for $T_{e,\mathrm{SLG}}$ below a few hundred K, which makes carrier-optical phonon scattering insufficient at lower temperatures, disorder-mediated scattering can potentially dominate e-ph cooling using the entire thermal distribution of phonons [353] and leading to energy dissipation $\sim k_B T_{l,\mathrm{SLG}}$ per scattering event [351]. Disorder-assisted supercollisions are modeled assuming disordered short-range scatterers with a mean free path l. The supercollision thermal current is calculated using [328, 351–353]:

$$J_{sc}(\mu_{c,\mathrm{SLG}}, \mu_{v,\mathrm{SLG}}, T_{e,\mathrm{SLG}}, T_{l,\mathrm{SLG}}) = \gamma_{sc} \left(T_{e,\mathrm{SLG}}^3 - T_{l,\mathrm{SLG}}^3 \right) \tag{3.44}$$

with the prefactor γ_{sc} given by:

$$\gamma_{sc} = \frac{9.62 D_{\mathrm{SLG}}^2 k_B^3}{2\rho_{\mathrm{SLG}} s_{\mathrm{SLG}}^2 \hbar k_{F,\mathrm{SLG}} l} \frac{4\left(n_{e,\mathrm{SLG}} + n_{h,\mathrm{SLG}} + 2\delta_{n,\mathrm{SLG}}\right)}{\pi \left(\hbar v_{F,\mathrm{SLG}}\right)^4} \tag{3.45}$$

with $n_{e,\mathrm{SLG}}$ ($n_{h,\mathrm{SLG}}$) the e (h) concentration, $\delta_{n,\mathrm{SLG}}$ the non-equilibrium carrier density and $k_{F,\mathrm{SLG}}\, l$ the disorder parameter [328, 351–353], defined as the product of SLG Fermi wavevector $k_{F,\mathrm{SLG}}$ and mean free path l for short-range scatterers. The latter is inversely proportional to the concentration of impurities [353]. D_{SLG} is the deformation potential

for supercollision scattering, i.e. the effective potential associated with lattice deformation upon disorder-mediated acoustic phonon emission. Literature values are between 10 and 30 eV [49, 348, 351, 352, 354]. Here, it is set at an intermediate value of 20 eV [71, 328, 351, 352]. In eq. 3.45, s_{SLG} is the sound velocity in SLG, with theoretical [328, 336, 343, 349, 350] and experimental [49, 348, 352, 353] values ranging from 10^4 m/s to 2×10^4 m/s. Here, a value of $s_{\text{SLG}} = 1.5\times10^4$ m/s is assumed, in agreement with theoretical predictions accounting for both transverse and longitudinal acoustic phonons [343]. Equation 3.44 was initially derived [351] at the degenerate limit, i.e. $\mu_{\text{SLG}} \gg k_B T_{e,\text{SLG}}$. In this thesis, its use is extended in higher temperatures $T_{e,\text{SLG}}$ by accounting for all the available carriers for scattering, i.e. $n_{e,\text{SLG}}$, $n_{h,\text{SLG}}$ as well as $\delta_{n,\text{SLG}}$ (eq. 3.45).

It is an open debate whether e-ph scattering is dominated by J_{op} or J_{sc} [328, 333, 351–353]. For high quality graphene (e.g $\mu_{q,\text{SLG}} > 10^4\,\text{cm}^2\text{V}^{-1}\text{s}^{-1}$, typically encountered in suspended SLG or graphene encapsulated within other 2D materials [267, 333]) J_{op} is expected to dominate the e-ph cooling pathway [333]. However, in the case of graphene with higher impurity concentration (e.g. $\mu_{q,\text{SLG}} \leq 10^4\,\text{cm}^2\text{V}^{-1}\text{s}^{-1}$), as for the case of graphene supported by a conventional dielectric substrate (e.g., SiO_2) [268] or nanostructured graphene [321, 355], J_{sc} can dominate the e-ph cooling channel [352, 353]. For large-scale SLG, with $\mu_{q,\text{SLG}} \sim 10^4\ \text{cm}^2\text{V}^{-1}\text{s}^{-1}$, assigning a mean free path $l \sim 200$ nm brings the J_{op} and J_{sc} cooling powers roughly at the same level, assuming $\mu_{\text{SLG}} \lesssim 0.2$ eV and $T_{e,\text{SLG}} \sim 300$ K, in which case the optical-phonon pathway is suppressed, as discussed above.

An effective "instantaneous" cooling time can be assigned to each e-ph pathway, as for:

$$\tau_{\text{eff}}^{i} = \frac{c_{e,\text{SLG}}\,\Delta T}{J_i} \tag{3.46}$$

where $c_{e,\text{SLG}}$ is the SLG carriers' heat capacity, $\Delta T \equiv T_{e,\text{SLG}} - T_{l,\text{SLG}}$ and the index i stands either for solely optical-phonon or only supercollision scattering. Figure 3.13 plots this effective cooling time, as a function of carrier temperature $T_{e,\text{SLG}}$ for different $E_{F,\text{SLG}}$ values. For simplicity, the non-equilibrium photoexcited carrier density is assumed $\delta_{n,\text{SLG}} = 0$ (i.e. intraband photoexcitation is assumed) and the SLG lattice temperature is considered fixed at $T_{l,\text{SLG}} = 300$ K. From fig. 3.13(a) it is clear that the optical-phonon cooling pathway is insufficient at RT and low $E_{F,\text{SLG}}$, since in these cases there is a big mismatch between carriers' and optical-phonon energies. For $E_{F,\text{SLG}} > 200$ meV, both optical phonon branches are active even at RT, which is manifested by the lower values of τ_{eff}^{op} (hence larger J_{op}). At high $T_{e,\text{SLG}}$, above a few thousand K, a large fraction of graphene carriers are thermalized and τ_{eff}^{op} converges to a single value, irrespective of the initial $E_{F,\text{SLG}}$. The results for this effective cooling time in the case of supercollision scattering, on the other hand, is somewhat different. The values at RT are roughly at the same level, no matter the initial $E_{F,\text{SLG}}$. For increasing $T_{e,\text{SLG}}$, the cooling times converge to a single value, as for the case of carrier-optical phonon scattering.

To get the combined contribution of the above cooling pathways, one can use eq. 3.46, with the denominator $J_{\text{e-ph}} \equiv J_{op} + J_{sc}$ or simply add the individual cooling times using a simple Matthiessen-type rule [356], i.e.:

$$\tau_{\text{eff}}^{-1} = \left(\frac{1}{\tau_{\text{eff}}^{op}} + \frac{1}{\tau_{\text{eff}}^{sc}}\right) \tag{3.47}$$

The total e-ph effective cooling time is plotted in fig. 3.14 as a function of $T_{e,\text{SLG}}$, for the same $E_{F,\text{SLG}}$ values and assumptions (i.e., fixed $T_{l,\text{SLG}} = 300$ K, $\delta_{n,\text{SLG}} = 0$, $l = 200$ nm)

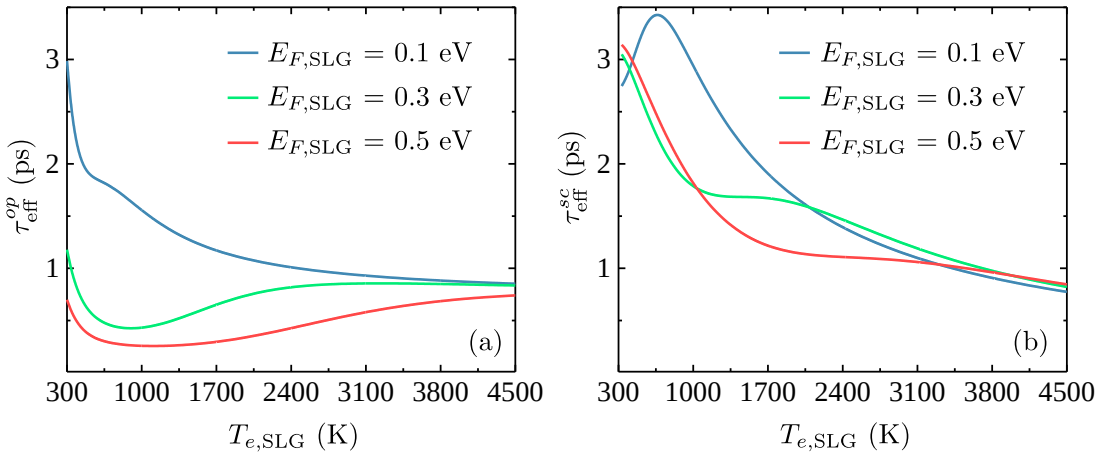

Figure 3.13: Effective "instantaneous" cooling carrier-phonon times as a function of carrier temperature $T_{e,\mathrm{SLG}}$, assuming constant $T_{l,\mathrm{SLG}} = 300$ K, for different $E_{F,\mathrm{SLG}}$ values. Panel (a) plots the effective cooling time accounting solely for carrier-optical phonon scattering and (b) accounting solely for disorder-assisted supercollision scattering, with a mean free path $l = 200$ nm. In both cases any additional effects arising from non-equilibrium photoexcited carriers are for simplicity neglected (i.e. $\delta_{n,\mathrm{SLG}} = 0$).

as for fig. 3.13. As expected, the total τ_{eff} depends on $E_{F,\mathrm{SLG}}$, with lower values of the latter resulting to less effective cooling, in perfect agreement with recent reports [333]. τ_{eff} eventually converges to a single value at higher $T_{e,\mathrm{SLG}}$, where the majority of SLG carriers are thermalized, irrespective of the initial $E_{F,\mathrm{SLG}}$. This value, however, can deviate drastically from the respected value in RT, especially in the case of low $E_{F,\mathrm{SLG}}$. Consequently, one has to explicitly account for the individual cooling thermal current densities J_{op} and J_{sc} and their temperature dependence, to reliably capture graphene's response during $T_{e,\mathrm{SLG}}$ temporal evolution. The assignment of a single, temperature independent τ_{eff}, however, can be used in the case that the examined $T_{e,\mathrm{SLG}}$ rise is small, i.e. $\Delta T \ll T_{l,\mathrm{SLG}} \sim 300$ K, leading to reliable results [66, 68].

As a final remark, it should be noted once more that in the above a fixed $T_{l,\mathrm{SLG}}$ was assumed. For a more accurate description of $T_{e,\mathrm{SLG}}$ evolution, the effect of graphene's lattice temperature rise should be accounted for, as discussed in the following section.

3.4.4 Light absorption and carrier dynamics

In this section the equations that describe graphene's temporal dynamics upon photoexcitation are derived. These dynamics are summarized qualitatively in fig. 3.15, assuming interband photoexcitation. Specifically, carrier distributions are plotted assuming $E_{F,\mathrm{SLG}} = 0.15$ eV, $\hbar\omega = 0.4$ eV and $T_{e,\mathrm{SLG}} = 900$ K upon thermalization, well within the range of carrier temperatures studied in this thesis. Following interband absorption, non-equilibrium photoexcited carriers are created at $\pm\hbar\omega/2$ in respect to CNP [3.15(b)]. These thermalize through e-e scattering in an ultrafast timescale $\tau_{e-e} = 20$ fs [183, 184], leading to a carrier distribution at an elevated $T_{e,\mathrm{SLG}}$ [3.15(c)]. The thermalized distribution

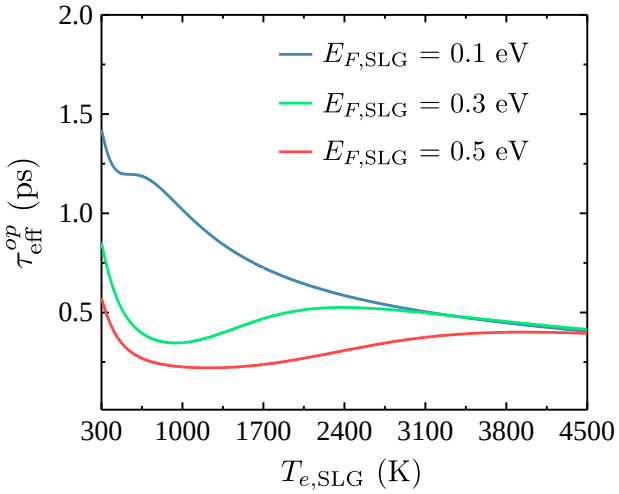

Figure 3.14: Total effective "instantaneous" cooling carrier-phonon time as a function of carrier temperature $T_{e,\rm SLG}$, assuming constant $T_{l,\rm SLG} = 300$ K, for different $E_{F,\rm SLG}$ values. Both optical-phonon as well as supercollision scattering are accounted for, while for the latter a mean free path $l = 200$ nm is assumed. Any additional effects arising from non-equilibrium photoexcited carriers are for simplicity neglected (i.e. $\delta_{n,\rm SLG} = 0$).

eventually cools down, through e-ph scattering, at a ps timescale [3.15(d)], as described in the previous section.

The fast ($\sim$ 20 fs) thermalization of graphene's carriers and their slow ($\sim$ ps) cooling with phonon-modes allows for the description of carrier temporal dynamics using a two temperature-model [64, 65], where $T_{e,\rm SLG}$ and $T_{l,\rm SLG}$ are described by two different rate equations. For illumination by a pulsed light source with power density $P_{in}(t)$, these rate equations become:

$$c_{e,\rm SLG}\frac{\partial T_{e,\rm SLG}}{\partial t} = \alpha_{\rm SLG}P_{in}(t) - J_{e-ph} \tag{3.48}$$

for graphene's carriers temperature $T_{e,\rm SLG}$ and

$$c_{l,\rm SLG}\frac{\partial T_{l,\rm SLG}}{\partial t} = J_{e-ph} - \Gamma_{\rm SLG-sub}(T_{l,\rm SLG} - T_0) \tag{3.49}$$

for graphene's lattice temperature $T_{l,\rm SLG}$. In eq. 3.48 $c_{e,\rm SLG} \equiv c_{e,\rm SLG}(\mu, T_{e,\rm SLG}, \delta_{n,\rm SLG})$ is SLG electronic heat capacity, $\alpha_{\rm SLG} \equiv \alpha_{\rm SLG}(T_{e,\rm SLG}, \delta_{n,\rm SLG})$ graphene's optical absorbance (acquired for a given configuration via TMM or FDTD simulations, as described in the following chapters) and $J_{e-ph} \equiv J_{op}(\mu_{\rm SLG}, T_{e,\rm SLG}, T_{l,\rm SLG}) + J_{sc}(\mu_{c,\rm SLG}, \mu_{v,\rm SLG}, T_{e,\rm SLG}, T_{l,\rm SLG})$ the electron-to-phonon thermal current density due to optical phonon and disorder-assisted supercollision scattering. J_{e-ph} is dissipated into the phonon bath, consequently it is included in the right hand side of eq. 3.49. In the left hand side of eq. 3.49, $c_{l,\rm SLG}$ is graphene's lattice heat capacity. The latter was extracted from experiments in ref. [357] and found to scale linearly with lattice temperature, for $T_{l,\rm SLG}$ up to $\sim$ 600 K. The data from ref. [357] were used to extract $c_{l,\rm SLG}$ using a linear parametrization, as for:

$$c_{l,\rm SLG} = -1.4 \times 10^{-5} + 1.9 \times 10^{-6}\, T_{l,\rm SLG} \left[\frac{\rm J}{\rm m^2 K}\right] \tag{3.50}$$

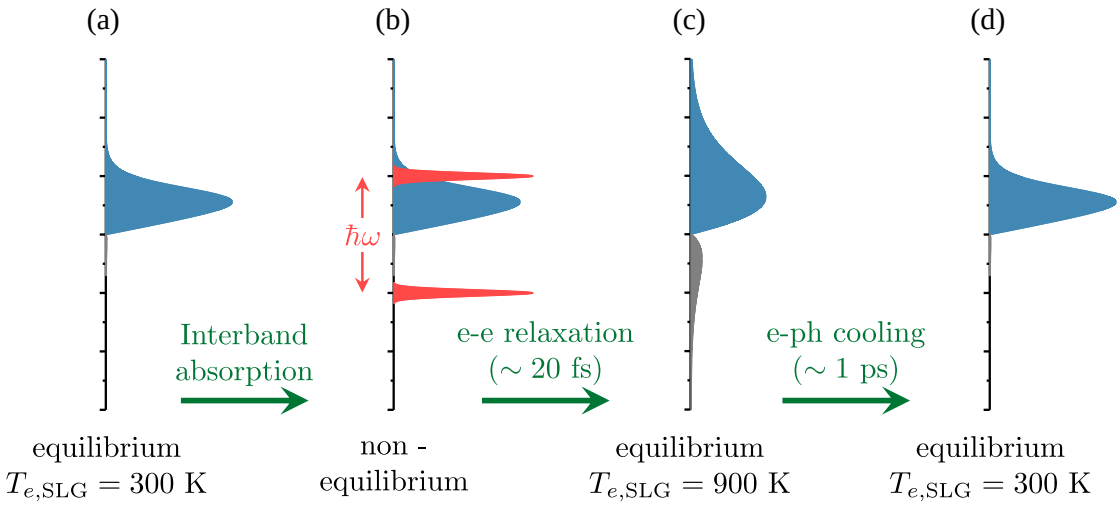

Figure 3.15: SLG carrier distribution assuming $E_{F,\mathrm{SLG}} = 0.15$ eV. (a) before photoexcitation at $T_{e,\mathrm{SLG}} = 300$ K, (b) just after illumination, assuming excitation with photons' energy $\hbar\omega = 0.4$ eV, with the red peaks denoting non-equilibrium photoexcited carriers, (c) after hot carriers relax into a Fermi-Dirac distribution at an elevated $T_{e,\mathrm{SLG}} = 900$ K, (d) after e-ph relaxation, cooled back to RT.

This yields $c_{l,\mathrm{SLG}} \sim$ three orders of magnitude larger than $c_{e,\mathrm{SLG}}$. As a result, graphene's lattice remains at relatively low temperatures (~ 500 K), compared to carriers' temperatures, even for fairly high values (few thousands K) of the latter.

The thermal energy accumulated in graphene's lattice is dissipated to ambient air (in the case of freestanding graphene) or to a substrate (in the case of supported graphene) with a rate $\Gamma_{\mathrm{SLG-sub}}$, while it also depends on $T_{l,\mathrm{SLG}}$ and substrate's (or ambient, in the case of suspended graphene) temperature T_0. The values of $\Gamma_{\mathrm{SLG-sub}}$, for graphene supported by a substrate, have been explored in numerous studies, usually found in the range of $10 - 1000$ MW m^{-2} K^{-1} [357–359]. The interfacial thermal conductivity between SLG and a supporting substrate has been addressed considering various substrates [360], the latter having bulk thermal conductivities, κ, ranging several orders of magnitude (e.g. $\kappa \sim 1$ W/m K for SiO_2 while $\kappa \sim 300$ W/m K for SiC [360]). Interestingly, the interfacial thermal conductivity with graphene has been reported to not have the same amplitude dispersion, e.g. a value of ~ 100 MW m^{-2} K^{-1} was extracted for SiO_2 substrate and ~ 1000 MW m^{-2} K^{-1} for SiC substrate in ref. [360]. Naturally, these values can be affected by the roughness of graphene/substrate contact. In the context of this thesis, for the studied configurations where carrier heating is relevant and for graphene supported by Si, a conservative value of $\Gamma_{\mathrm{SLG-sub}} \sim 20$ MW m^{-2} K^{-1} is assumed, in line with values reported in literature for similar configurations [359].

For a complete and accurate description of temperature dynamics, the non-equilibrium photoexcited carrier density $\delta_{n,\mathrm{SLG}}$ should also be accounted for, in the case if interband photo-excitation. The temporal evolution of $\delta_{n,\mathrm{SLG}}$ is calculated by an additional rate equation [261]:

$$\frac{\partial \delta_{n,\mathrm{SLG}}}{\partial t} = \frac{P_{in}(t)\, a_{\mathrm{inter,SLG}}}{\hbar\omega} - \frac{\delta_{n,\mathrm{SLG}}}{\tau_{e-e}} \tag{3.51}$$

where $\tau_{e-e} = 20$ fs [183, 184] the time for carriers to relax into a thermal distribution time via e-e scattering, $\hbar\omega$ the excitation photon energy (assuming $\hbar\omega \geq 2E_{F,\text{SLG}}$) and $a_{\text{inter,SLG}}$ the interband portion of SLG absorption. Since the total α_{SLG} is proportional to $\Im\{\epsilon_{SLG}\}$ [285] (i.e., to $\Re\{\sigma^{\text{opt}}_{\text{SLG}}\}$), the interband contribution to optical absorption is determined by:

$$a_{\text{inter,SLG}} = \alpha_{\text{SLG}} \frac{\Re\left\{\sigma^{\text{opt}}_{\text{inter,SLG}}\right\}}{\Re\left\{\sigma^{\text{opt}}_{\text{intra,SLG}} + \sigma^{\text{opt}}_{\text{inter,SLG}}\right\}} \tag{3.52}$$

The three coupled rate equations 3.48 – 3.51 can be used to acquire the temporal evolution of graphene's carrier dynamics upon illumination by a pulsed source. If the duration of the pulse is longer than all the timescales involved (i.e. $\tau_{\text{pulse}} \gg \tau_{e-e}, \tau_{\text{e-ph}}$) or in the case of continuous-wave (CW) illumination, these rate equations can be solved for the quasi-CW case. Equation 3.48 becomes:

$$\alpha_{\text{SLG}} P_{in} = J_{e-ph} \tag{3.53}$$

This implies an equilibrium condition, so that the deposited power in the electronic system $J_{in} \equiv \alpha_{\text{SLG}} P_{in}$ is equal to the power removed from the graphene's carriers and into the phonon bath J_{e-ph}. Since both α_{SLG} and J_{e-ph} are $T_{e,\text{SLG}}$ dependent, eq. 3.53 must be solved self-consistently. The two remaining rate equations, in the quasi-CW case become:

$$T_{l,\text{SLG}} = T_0 + \Gamma^{-1}_{\text{SLG}-\text{sub}} J_{e-ph} \tag{3.54}$$

for lattice temperature and:

$$\delta_{n,\text{SLG}} = \frac{\tau_{e-e}\, a_{\text{inter,SLG}}\, P_{in}}{\hbar\omega} \tag{3.55}$$

for the non-equilibrium photoexcited carrier density $\delta_{n,\text{SLG}}$, respectively. Since both sides of eq. 3.54 (eq. 3.55) are $T_{l,\text{SLG}}$ ($T_{e,\text{SLG}}$) dependent, self-consistent iterations are also required to calculate them in the quasi-CW case.

Figure 3.16 depicts a flowchart of the self-consistent algorithm used throughout this thesis to solve eq. 3.53 - 3.55. This algorithm begins by assuming an arbitrary pair of $T_{e,\text{SLG}} - P_{in}$ and then calculates all the relevant parameters (i.e. α_{SLG}, $\delta_{n,\text{SLG}}$, $T_{l,\text{SLG}}$ et.c) to conclude in a certain J_{e-ph} value. The convergence criterion, for a steady state to be reached, is that the input pair of values leads to the condition $\alpha_{\text{SLG}} P_{in} = J_{e-ph}$, where the incoming and outgoing power to the electronic system is the same. In the following chapters the agreement of this self - consistent treatment with the rate equations 3.48 – 3.51 will be explored.

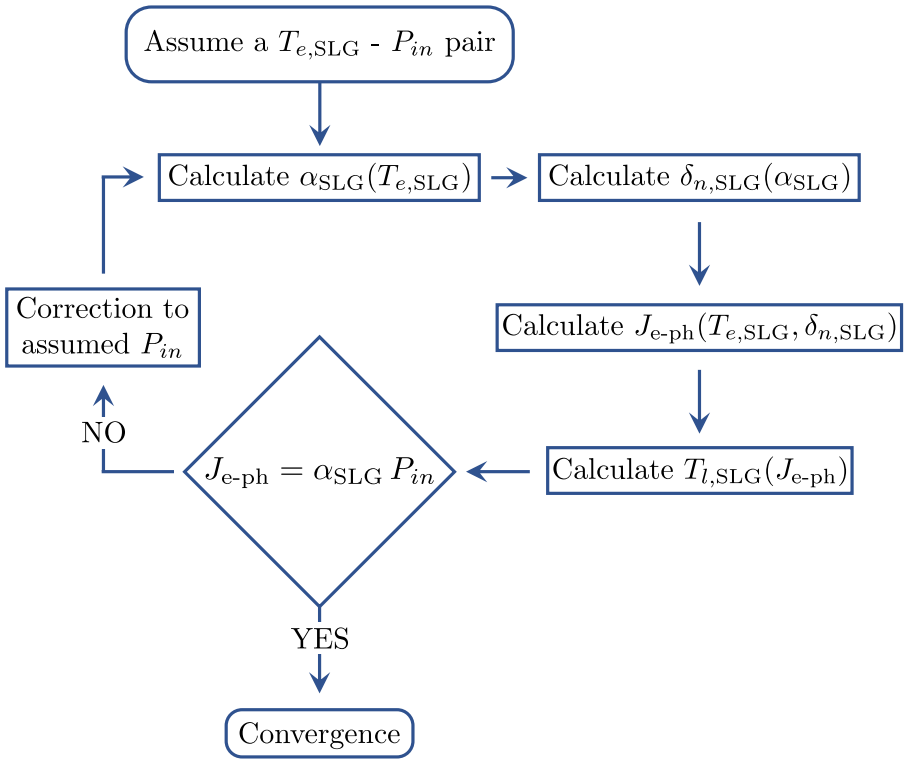

Figure 3.16: Flowchart of the self-consistent algorithm developed for the solution of the quasi-CW equations 3.53 – 3.51. Converged is achieved when the initially assumed $T_{e,\mathrm{SLG}}$ – P_{in} pair leads to the equilibrium condition $J_{e-ph} = J_{in}$, where $J_{e-ph} \equiv J_{op} + J_{sc}$ and $J_{in} \equiv \alpha_{\mathrm{SLG}} P_{in}$.

3.5 Graphene-semiconductor Schottky diodes

Given its 2D nature, physical and chemical properties, SLG can be integrated with existing semiconducting technologies to develop next-generation optoelectronic devices [361]. Graphene can be combined with 2D [362] or 3D [112, 168, 363] semiconducting materials to form junctions with rectifying characteristics, behaving as excellent Schottky diodes [168]. It has been reported that graphene heterostructures can lead to the development of graphene-based photodetection applications [44, 126, 169, 364] and solar-cells [365, 366]. However, the graphene-based Schottky junction is somewhat different from the conventional metal-semiconductor junction. The biggest difference, in the case of graphene-based Schottky junctions, is the tunable Schottky barrier height , arising from the small density of states in graphene [168]. Thus, special treatment is needed for the description of Schottky heterostructures based on graphene, to accurately describe them and develop applications based on them. In the context of this thesis, we assume Schottky junctions formed between SLG and Si. In the following sections we derive the necessary relationships for the description of Schottky barrier formation as well as the photocurrent calculation across these junctions.

3.5.1 Schottky barrier formation

In this section the physics of the Schottky contact between graphene and Si are reviewed and the modeling approach for such configurations is described. Let us consider a SLG

with electron affinity (energy difference between SLG charge neutrality point and vacuum level) $\chi_{\text{SLG}} = 4.5$ eV [367] (theoretical value, experiments put it between 4.2eV and 5 eV, depending on metal contacts and fabrication [368]) and initial (i.e. before contact) p-doping at Fermi level $E'_{F,\text{SLG}} < 0$ [fig. 3.17(a)].

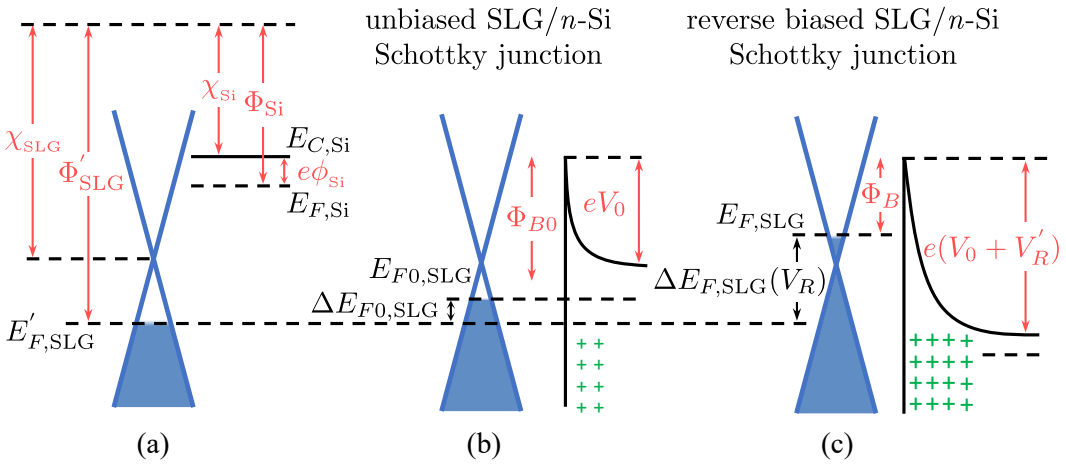

Figure 3.17: (a) Schematic energy levels of SLG and Si before they form a junction. (b-c) Schematic energy levels and junction formation in (b) unbiased and (c) reverse biased junctions.

This SLG is assumed in contact with n-type Si [fig. 3.17(b)]. The Si work-function is $\Phi_{\text{Si}} = \chi_{\text{Si}} + e\phi_{\text{Si}}$, where $\chi_{\text{Si}} = 4.05$ eV is the electron affinity in Si [168], $e\phi_{\text{Si}} = E_{C,\text{Si}} - E_{F,\text{Si}}$ is the energy difference between the conduction band $E_{C,\text{Si}}$ and the Fermi level $E_{F,\text{Si}}$ in Si and e is the electron charge. $e\phi_{\text{Si}} = k_B T_{\text{Si}} \ln\left(\frac{N_{C,\text{Si}}}{N_{d,\text{Si}}}\right)$, where $N_{C,\text{Si}} = 2.8 \times 10^{19}$ cm^{-3} is the effective density of states in the conduction band of Si [20], $N_{d,\text{Si}}$ [cm^{-3}] is the Si doping concentration, k_B is the Boltzmann constant and T_{Si} is the electronic temperature in Si. Throughout this work, T_{Si} is set to $T_{\text{Si}} = 300$ K (given to the larger heat capacitance of Si compared to SLG [357]). The dopant concentration $N_{d,\text{Si}}$ will be varied, depending on the studied configuration, as will be discussed in the following chapters.

The workfunction of SLG (before contact with Si) is $\Phi'_{\text{SLG}} = \chi_{\text{SLG}} - \mu'_{\text{SLG}}$, where μ'_{SLG} is the equilibrium chemical potential of the suspended SLG. Upon contact [fig. 3.17(b)], since $\Phi_{\text{Si}} < \Phi'_{\text{SLG}}$ electrons will flow from Si to SLG elevating its Fermi level to $E_{F0,\text{SLG}}$ (thermodynamic equilibrium, i.e., $E_{F0,\text{SLG}}$ constant across the junction [168,369,370]) and workfunction to Φ_{SLG}. At finite $T_{e,\text{SLG}}$, this corresponds to a SLG chemical potential $\mu_{0,\text{SLG}}$ ($\mu_{0,\text{SLG}} < 0$, p-doped; $\mu_{0,\text{SLG}} > 0$, n-doped). Assuming no $E_{F,\text{SLG}}$ pinning [371] and neglecting surface-states effects [168, 372], the energy balance in thermodynamic equilibrium gives a built-in voltage V_0 [168]:

$$eV_0 = \Phi_{\text{SLG}} - \Phi_{\text{Si}} \tag{3.56}$$

and a zero bias Schottky barrier height [168]:

$$\Phi_{B0} = eV_0 + e\phi_{\text{Si}} \tag{3.57}$$

The electrons transferred from Si to SLG, leave a space region in Si depleted from carriers. The depleted charge, in the zero bias case, is given within the depletion approximation by [168, 369]:

$$Q_{D,\mathrm{Si}} = eN_{d,\mathrm{Si}}\chi_{d,\mathrm{Si}} = \sqrt{2e\epsilon_{\mathrm{Si}}N_{d,\mathrm{Si}}\left(V_0 - k_BT_{\mathrm{Si}}/e\right)} \tag{3.58}$$

where $\chi_{d,\mathrm{Si}}$ is the depletion region width, $\epsilon_{\mathrm{Si}} = 11.7\,\epsilon_0$ is the dielectric permittivity of Si [20] and ϵ_0 the vacuum permittivity. The same amount of charge is accumulated in SLG ($Q_{D,\mathrm{SLG}} = -Q_{D,\mathrm{Si}}$), shifting $E'_{F,\mathrm{SLG}}$ to $E_{F0,\mathrm{SLG}}$.

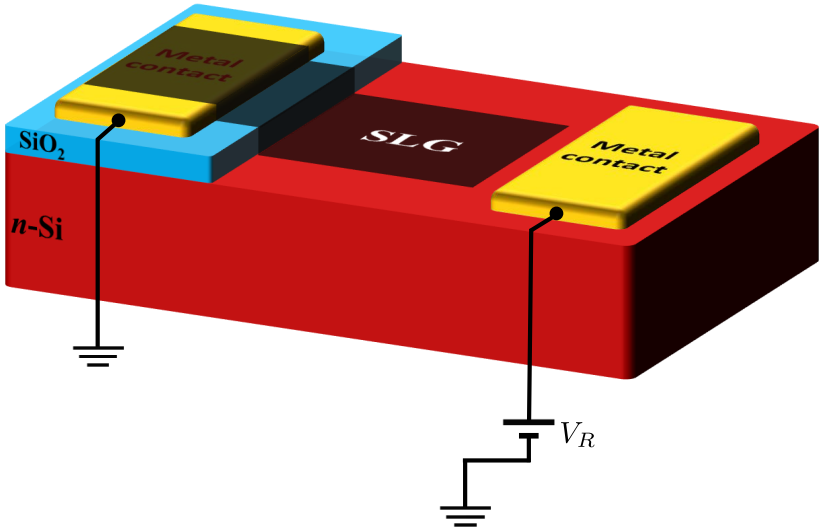

Figure 3.18: Schematic representation of reverse-biased SLG/*n*Si Schottky junction.

In SLG Schottky junctions, the SBH depends on μ_{SLG} [168]. Therefore, if the device is reverse-biased [373, 374] with external voltage V_R (positive potential to Si, as for fig. 3.18), e will flow into SLG changing its Fermi level to $E_{F,\mathrm{SLG}} = E_{F0,\mathrm{SLG}} + \Delta E_{F,\mathrm{SLG}}$, where $\Delta E_{F,\mathrm{SLG}}$ is the bias induced Fermi level shift. V_R will be distributed between SLG and Si, i.e. $|V_R| = |\Delta E_{F,\mathrm{SLG}}/e| + |V'_R|$, where V'_R is the reverse bias voltage drop in the Si depletion region, resulting in energy band bending $|e(V_0 + V'_R)|$ [369, 370, 375]. To calculate $E_{F,\mathrm{SLG}}$, μ_{SLG} and the reduced SBH Φ_B when the device is reverse-biased, we consider that the electrical charge transferred across the junction results in a change of depletion region charge, $\Delta Q_{D,\mathrm{Si}} > 0$ due to V'_R [168, 369, 375, 376]:

$$\begin{aligned}\Delta Q_{D,\mathrm{Si}} = &\sqrt{2e\epsilon_{\mathrm{Si}}N_{d,\mathrm{Si}}\left(V_0 + V'_R - \frac{k_BT_{\mathrm{Si}}}{e}\right)} - \\ &\sqrt{2e\epsilon_{\mathrm{Si}}N_{d,\mathrm{Si}}\left(V_0 - \frac{k_BT_{\mathrm{Si}}}{e}\right)}\end{aligned} \tag{3.59}$$

The same charge is accumulated in SLG ($\Delta Q_{\mathrm{SLG}} = -\Delta Q_{D,\mathrm{Si}} < 0$) and causes $\Delta E_{F,\mathrm{SLG}}$, i.e. $\Delta Q_{\mathrm{SLG}} = e(n_{\mathrm{SLG}} - n_{0,\mathrm{SLG}})$, where $n_{\mathrm{SLG}} = E^2_{F,\mathrm{SLG}}/(\pi\hbar^2 v^2_{F,\mathrm{SLG}})$ is the e concentration associated with $E_{F,\mathrm{SLG}}(\mu_{\mathrm{SLG}})$ [57], $n_{0,\mathrm{SLG}}$ is the initial e concentration in SLG associated with $E_{F0,\mathrm{SLG}}(\mu_{0,\mathrm{SLG}})$. Combining the above, we get a transcendental equation [369, 370,

375]:

$$s_F E_{F,\mathrm{SLG}}^2 - s_{F0} E_{F0,\mathrm{SLG}}^2 = \sqrt{\Gamma\left(\chi_{\mathrm{SLG}} - \Phi_{\mathrm{Si}} - \mu_{\mathrm{SLG}} + e|V_R'| - k_B T_{\mathrm{Si}}\right)} - \sqrt{\Gamma\left(\chi_{\mathrm{SLG}} - \Phi_{\mathrm{Si}} - \mu_{0,\mathrm{SLG}} - k_B T_{\mathrm{Si}}\right)} \tag{3.60}$$

where $\Gamma = 2\epsilon_{\mathrm{Si}} N_{d,\mathrm{Si}} \pi^2 \hbar^4 v_{F,\mathrm{SLG}}^4 e^{-2}$, $s_{F,F0} = \mathrm{sign}(E_{F,\mathrm{SLG}}, E_{F0,\mathrm{SLG}})$. For $T_{e,\mathrm{SLG}} \to 0$, where $\mu_{\mathrm{SLG}} \equiv E_{F,\mathrm{SLG}}$, eq. 3.60 can be solved algebraically, but for finite $T_{e,\mathrm{SLG}}$ it needs to be treated using a self-consistent algorithm [369].

In both unbiased and reverse-biased cases, the built-in potential V_0 depends on the depletion charge, which is itself V_0-dependent. Consequently, self-consistent iterations are required to calculate V_0, $E_{F,\mathrm{SLG}}$ and μ_{SLG}. A flowchart of the algorithm that was used throughout this thesis to treat the SLG/Si Schottky junctions and calculate all the relevant parameters, is depicted in fig. 3.19. An initial value for V_0 is assumed and then the depletion charge, arising from this assumption, is extracted. This charge, which is transferred to SLG, is used to calculate $E_{F,\mathrm{SLG}}$ and μ_{SLG}. Finally, the latter is used to calculate the resulting built-in potential, through eq. 3.56. If the extracted potential V_0' matches the initially assumed value V_0, convergence is achieved. Otherwise, a correction to the initial condition about V_0 is made and the whole procedure is repeated. Having calculated V_0, $E_{F,\mathrm{SLG}}$ and μ_{SLG}, the SBH in the reverse-biased case is given by:

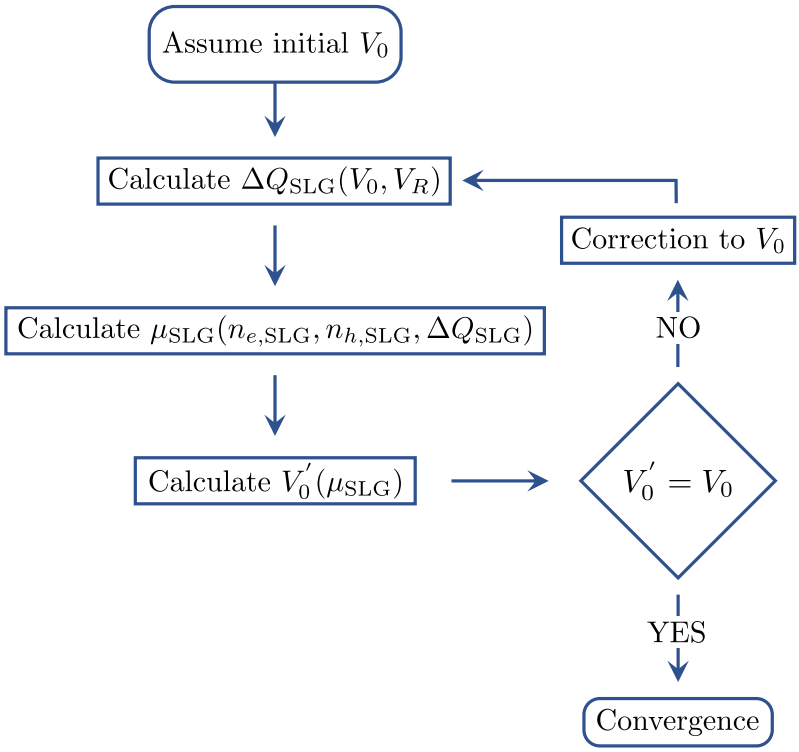

Figure 3.19: Flowchart of the self-consistent algorithm developed to calculate built-in potential V_0, Fermi level $E_{F,\mathrm{SLG}}$ and chemical potential μ_{SLG} on a SLG/Si Schottky junction.

$$\Phi_B = eV_0 + e\phi_{\mathrm{Si}} \tag{3.61}$$

It should be noted that several additional effects can also modify the SBH, such as image force barrier lowering [168, 377] (i.e. the Schottky effect) and Schottky barrier inhomogeneity [168, 377], but for simplicity are neglected in the context of this thesis.

Equations 3.56 – 3.61 can also be used in the case of graphene – *p*-doped Si (*p*-Si) Schottky junctions, with minor modifications. For *p*-Si, the workfunction of the later must be calculated using:

$$\Phi_{\text{Si}} = \chi_{\text{Si}} + E_{g,\text{Si}} - e\phi_{\text{Si}} \tag{3.62}$$

where $E_{g,\text{Si}} = 1.1$ ev is the Si bandgap [20] and $e\phi_{\text{Si}}$ now corresponds to the difference between Si Fermi level, $E_{F,\text{Si}}$, and its valence band, $E_{V,\text{Si}}$. In the case of *p*-Si, this difference is now given by $e\phi_{\text{Si}} = k_B T_{\text{Si}} \ln\left(\frac{N_{V,\text{Si}}}{N_{a,\text{Si}}}\right)$, where $N_{V,\text{Si}} = 1.04 \times 10^{19}$ cm^{-3} the effective density of states in Si valence band [20] and $N_{a,\text{Si}}$ the Si acceptor concentration. Moreover, $N_{d,\text{Si}}$ must be replaced with $N_{a,\text{Si}}$ in eqs. 3.58 and 3.59 as well as in the prefactor Γ of eq. 3.60. For graphene – *p*-Si Schottky junctions, $\Phi_{\text{Si}} > \Phi'_{\text{SLG}}$, so that holes are transferred from Si to graphene, both at the unbiased as well as in the reverse bias case (i.e., negative potential to *p*-Si). As a result, Si is depleted from holes, and its depletion region has a negative charge. Apart from the aforementioned changes, eqs. 3.56 – 3.61 hold true and the same self-consistent algorithm discussed above is used to treat them.

To validate the methods described in this section, the configuration presented in ref. [369] was reproduced using the equations and the algorithm described above. In [369], graphene was initially (i.e. before contact) *p*-doped, with a carrier concentration $n'_{h,\text{SLG}} \approx 3.5 \times 10^{12}$ cm^{-2}. This SLG was then put in contact with *p*-Si, the latter having a dopant concentration $N_{a,\text{Si}} = 3 \times 10^{16}$ cm^{-3}. After the appliance of a reverse bias, SBH was experimentally determined [369] and the SBH modification as a function of the applied bias was extracted. The results, as reported in ref. [369], are depicted in fig. 3.20 using blue dots and the calculations, performed with the algorithm as described above, are plotted using a red dashed line. The calculations agree perfectly with the reported values, providing confidence for the robustness of the methods used to calculate SBH throughout this thesis.

Finally, it should be noted than when modeling graphene/Si Schottky junctions assuming reverse bias application, special caution must be taken to not overcome the reverse bias breakdown potential. The latter, in the case of Si, is given by [20]:

$$V_R^{\text{BD}} = \frac{\epsilon_{\text{Si}} E_{cr}}{2eN} \tag{3.63}$$

where E_{cr} is the critical breakdown field [20]:

$$E_{cr} = \frac{4 \times 10^5}{1 - \frac{1}{3}\log_{10}\left(\frac{N}{10^{16}}\right)} \text{ [V / cm]} \tag{3.64}$$

and $N \equiv N_{d,\text{Si}}$ $(N_{a,\text{Si}})$ for *n*-doped (*p*-doped) Si.

3.5.2 Photocurrent across the Schottky junction

Graphene semiconductor Schottky diodes are typically fabricated using moderately doped semiconductors, with dopant concentrations $N \leq 5 \times 10^{17}$ cm^{-3} [168]. In these configurations, assuming low energy illumination, i.e., energy photons below both the semiconductor bandgap and SBH, photo-thermionic emission (PTh), i.e. the emission of thermally

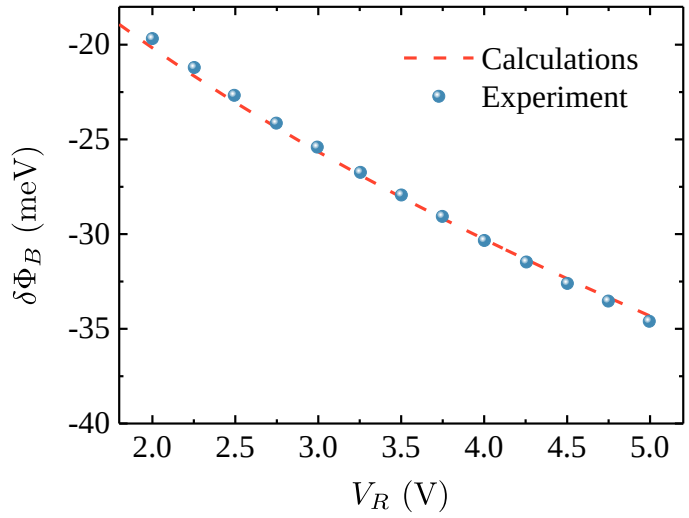

Figure 3.20: Comparison for the SBH modification upon reverse bias appliance between calculations performed with the algorithm described in this section (red dashed line) and experimental values from ref. [369].

excited carrier across SBH, is the main mechanism of photocurrent generation [168]. Alternative transport mechanisms, e.g., thermionic field emission (TFE) [168,378] and field emission (FE) [168,378], which include tunneling through the barrier, could potentially contribute to the photocurrent. However, for $N \leq 3 \times 10^{17}$ cm^{-3} and $T_{e,\mathrm{SLG}} >$ RT, examined in this thesis, PTh is the dominating mechanism [168], prevailing over TFE and FE as well as over additional mechanisms such as electron diffusion in the depletion region [168,379]. Indeed, refs. [65,168,372] showed that PTh can accurately reproduce the I-V characteristics across a SLG/Si Schottky junction. It should also be noted that due to the absence of electronic temperature gradients on SLG for the studied platforms, photo-thermoelectric effects [66,68] are not expected to contribute to the photocurrent.

For given $T_{e,\mathrm{SLG}}$, T_{Si} and Φ_B, the thermionic current density across a SLG/Si Schottky junction can be calculated using the Landauer transport formalism [168,372]:

$$J_{el} = -\frac{e}{\tau_{\mathrm{inj}}} \int_{-\infty}^{\infty} \nu(\epsilon)\mathcal{T}(\epsilon)\mathcal{D}f(\epsilon)\, d\epsilon \tag{3.65}$$

where τ_{inj} is the effective injection rate of charge carriers from SLG to Si [65, 168, 362, 372, 380, 381] and will be discussed in the following section. In eq. 3.65 $\mathcal{D}f(\epsilon) \equiv f_{FD}\left(\epsilon;\mu_{\mathrm{SLG}},T_{e,\mathrm{SLG}}\right) - f_{FD}\left(\epsilon;\mu_{\mathrm{Si}},T_{\mathrm{Si}}\right)$, $\mathcal{T}(\epsilon)$ is the transmission probability of charge carriers from SLG to Si over Φ_B. For simplicity, a heaviside step function is assumed for the latter, as for $\mathcal{T}(\epsilon) = \Theta\left(\epsilon - \Phi_B^{\mathrm{CNP}}\right)$ [168,372], with Φ_B^{CNP} the SBH measured from CNP.

There is also a corresponding thermionic thermal current density (J_{th}), since the transporting electrons carry energy $\epsilon - \mu_{\mathrm{SLG}}$ across the junction [71]:

$$J_{th} = \frac{1}{\tau_{\mathrm{inj}}} \int_{-\infty}^{\infty} \nu(\epsilon)(\epsilon - \mu_{\mathrm{SLG}})\mathcal{T}(\epsilon)\mathcal{D}f(\epsilon)\, d\epsilon \tag{3.66}$$

This thermal current will contribute to cooling and must be added in the right hand side of eq. 3.48 (or in the right hand side of eq. 3.53 , if quasi-CW illumination is assumed)

when SLG/Si Schottky junctions are modeled. However, the carriers injected across SBH, are transferred in Si directly, not interacting with graphene's phonon bath. Consequently, while J_{th} must be taken into account for carrier cooling, it does not add thermal energy into the phonon bath and must not be accounted for in the right hand side of eq. 3.49 (or eq. 3.54, assuming the quasi-CW case).

At low $T_{e,\mathrm{SLG}}$ ($k_B T_{e,\mathrm{SLG}} \ll \Phi_B$), eq. 3.65 can be solved analytically, resulting in the ideal diode equation [65, 372]:

$$J_{el} = \mathcal{A}^*_{2d} \left[\mathcal{R}(T_{\mathrm{Si}}) e^{eV_R/k_B T_{\mathrm{Si}}} - \mathcal{R}(T_{e,\mathrm{SLG}}) \right] \tag{3.67}$$

where $\mathcal{A}^*_{2d} = 2ek_B^2 / \left(\tau_{\mathrm{inj}} \pi \hbar^2 v^2_{F,\mathrm{SLG}}\right)$ and:

$$\mathcal{R}(T) = e^{\frac{\mu_{\mathrm{SLG}}}{k_B T}} T^2 \left(\frac{\Phi_B^{\mathrm{CNP}}}{k_B T} + 1 \right) e^{\frac{-\Phi_B^{\mathrm{CNP}}}{k_B T}} \tag{3.68}$$

For $T_{e,\mathrm{SLG}} = T_{\mathrm{Si}} = T$ this simplifies to the Richardson equation [20]:

$$J_{el} = J_0 [\exp(eV/k_B T) - 1] \tag{3.69}$$

with the reverse saturation current:

$$J_0 = \mathcal{A}^*_{2d} T^2 \left(\frac{\Phi_B^{\mathrm{CNP}}}{k_B T} + 1 \right) e^{-\Phi_B/k_B T} \tag{3.70}$$

A similar analytical expression can be derived for the thermionic thermal current density across the junction (corresponding to eq. 3.66):

$$J_{th} = \mathcal{A}^*_{th} \left[\mathcal{R}_{th}(T_{e,\mathrm{SLG}}) - \mathcal{R}_{th}(T_{\mathrm{Si}}) e^{\frac{eV_R}{k_B T_{\mathrm{Si}}}} - \mathcal{R}'_{th}(T_{e,\mathrm{SLG}}) + \mathcal{R}'_{th}(T_{\mathrm{Si}}) e^{\frac{eV_R}{k_B T_{\mathrm{Si}}}} \right] \tag{3.71}$$

where $\mathcal{A}^*_{th} = 2 / \left(\tau_{\mathrm{inj}} \pi \hbar^2 v^2_{F,\mathrm{SLG}}\right)$ and

$$\mathcal{R}_{th}(T) = e^{\frac{\mu_{\mathrm{SLG}}}{k_B T}} k_B^3 T^3 \left[\left(\frac{\Phi_B^{\mathrm{CNP}}}{k_B T} \right)^2 + \frac{2\Phi_B^{\mathrm{CNP}}}{k_B T} + 2 \right] e^{-\frac{\Phi_B^{\mathrm{CNP}}}{k_B T}} \tag{3.72}$$

$$\mathcal{R}'_{th}(T) = e^{\frac{\mu_{\mathrm{SLG}}}{k_B T}} k_B^2 T^2 \mu_{\mathrm{SLG}} \left(\frac{\Phi_B^{\mathrm{CNP}}}{k_B T} + 1 \right) e^{-\frac{\Phi_B^{\mathrm{CNP}}}{k_B T}} \tag{3.73}$$

Figure 3.21 compares the current densities calculated using Landauer transport formalism (eqs. 3.65, 3.66) and the extracted analytical relationships (eqs. 3.67, 3.71), as a function of $T_{e,\mathrm{SLG}}$. For these calculations $E'_{F,\mathrm{SLG}} = 0.15$ eV was assumed, contacted with *n*-Si ($N_{d,\mathrm{Si}} = 10^{16}$ cm^{-3}) resulting to a SBH $\Phi_B = 0.3$ eV at room temperature. The carrier injection time was set to $\tau_{\mathrm{inj}} = 30$ ps [372]. The two curves slightly diverge for $T_{e,\mathrm{SLG}} > 2000$ K. The overall agreement validates the simplified diode equations for low ($k_B T_{e,\mathrm{SLG}} \ll \Phi_B$) temperatures. However, since a wide range of SBH and $T_{e,\mathrm{SLG}}$ will be examined in this thesis, the exact solutions of eqs. 3.65, 3.66 are used in the following chapters.

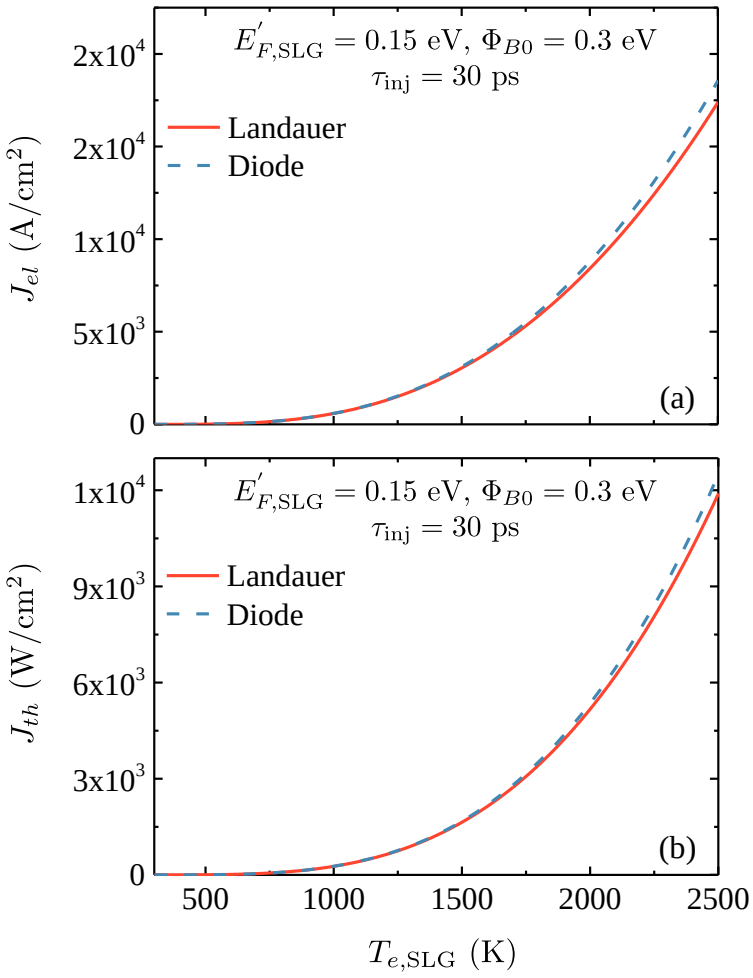

Figure 3.21: (a) Electrical and (b) thermal current densities across a SLG/Si Schottky junction. Calculations preformed using Landauer transport (red solid) and diode equations (blue dashed) assuming $E'_{F,\mathrm{SLG}} = 0.15$ eV and $\tau_{\mathrm{inj}} = 30$ ps.

3.5.3 The carrier injection time

In this section, the carrier injection time across a SLG/Si Schottky interface is discussed. Its effect on the performance of graphene-based Schottky diodes is crucial, as will become apparent in the following chapters.

τ_{inj} is a phenomenological parameter characterizing the rate at which charge carriers are injected from SLG into Si, across the SLG/Si interface [168, 372]. Its value depends on various fundamental and/or device aspects, such as SLG quality [168, 372], Schottky interface quality [65, 369, 376, 382], momentum conservation/relaxation of charge carriers upon injection over the Schottky barrier [362, 380, 381], Ohmic contact interfaces [168, 372, 383], as well as $E_{F,\mathrm{SLG}}$ and $T_{e,\mathrm{SLG}}$ [362, 380, 381].

It remains an open question of how low τ_{inj} can be achieved at the SLG/Si interface. E.g., $\tau_{\mathrm{inj}} \sim 0.11$ ps was extracted for SLG/*n*-Si Schottky junctions in [380] and ~ 50 ps for Schottky/*n*-Si Schottky junctions in [372] using Cr/Au contacts, the latter dropping to ~ 0.13 ps if Pd metal contacts are used instead [372, 383]. A theoretical es-

timation of a lower bound for τ_{inj} [381], using the Fermi liquid theory for doped SLG [381] ($|E_{F,\text{SLG}}| \gg k_B T_{e,\text{SLG}}$) and the Dirac liquid theory for intrinsic SLG ($|E_{F,\text{SLG}}| \ll k_B T_{e,\text{SLG}}$) [381], derived minimum values $\tau_{\text{inj}} \sim \hbar |E_{F,\text{SLG}}|/(k_B T_{e,\text{SLG}})^2$ for the former and $\tau_{\text{inj}} \sim \hbar/(k_B T_{e,\text{SLG}}) \sim 0.025$ ps at RT for the latter.

For a qualitative comparison to the bulk case, we note that for metal/*n*-Si Schottky junctions, the Richardson constant is $\mathcal{A}^*_{3d} = 112\,\text{cm}^{-2}\text{K}^{-2}$ [168]. In the Landauer transport formalism for 2d systems, the effective Richardson constant is:

$$\mathcal{A}^*_{2d} = 2ek_B^2 / \left(\tau_{\text{inj}} \pi \hbar^2 v_{F,\text{SLG}}^2\right) \left(\Phi_B^{\text{CNP}} / k_B T_{e,\text{SLG}}\right) \tag{3.74}$$

as discussed in the previous section. For $\Phi_B^{\text{CNP}} = 0.45$ eV, corresponding to SLG/*n*-Si Schottky junctions and RT, $\mathcal{A}^*_{2d}$ reaches the $\mathcal{A}^*_{3d}$ value for $\tau_{\text{inj}} \sim 0.03$ ps. This is close to the lower limits of τ_{inj} estimated in [381].

During the following chapters of this thesis, in the configurations regarding SLG/Si Schottky junctions, the device performance will be considered as a function of τ_{inj}.

Chapter 4

Computational tools

In this chapter the computational tools that are used throughout this thesis are presented. Initially, the methods for extracting the optical response of the studied structures, i.e. transfer matrix method and finite difference time domain, are discussed. Next, the computational methods for handling rate equations and numerical integrations in the simulation framework developed in this thesis are briefly highlighted.

4.1 Transfer Matrix Method

Transfer Matrix Method (TMM) [384, 385] is an efficient tool for analyzing the propagation of light through a stratified optical medium, i.e. a multilayer stack with arbitrary thicknesses and optical constants (fig. 4.1). The main idea of TMM is the correlation of the electric and magnetic fields at a certain position with their respected values at different positions, through a 2x2 matrix, called the transfer matrix. The latter is the combination two different kinds of matrices: the interface matrix, which associates the fields across a material interface, and the propagation matrix, which represents the propagation a plane wave across a homogeneous medium. After the derivation of the transfer matrix, the reflection and transmission coefficients of a multilayer stack can be evaluated. Moreover, it is possible to extract the absorptivity of each individual absorptive layer of the stack [386, 387].

Nevertheless, TMM has also its drawbacks. To begin with, being a frequency domain method, it can only be used to extract the response of a given structure for one wavelength at a time. This, however, can be compensated by the fact that the overall calculation is very fast. Consequently, one can get the response for a broad spectrum simply by repeating the calculation for each individual wavelength. Maybe the most strict limitation of TMM is that it assumes all the layers isotropic and infinite in the plane perpendicular to the direction of propagation (x-y plane in fig. 4.1). As a result, the layers that are modeled have to be wide enough to avoid errors due to this assumption. Additionally, TMM is not able to incorporate geometric features in the x-y plane, at least in the implementation adopted here, making it essentially a 1D technique. In the following chapters, methods to overcome this limitation, in graphene-based configurations, will be explored.

4.1.1 Interface matrix

Let us assume the elementary case of an interface between two adjacent materials with complex refractive indices n_j and n_{j+1}. In the general case, one may have waves incoming from both directions. A schematic of the relevant plane waves, for the simple case of

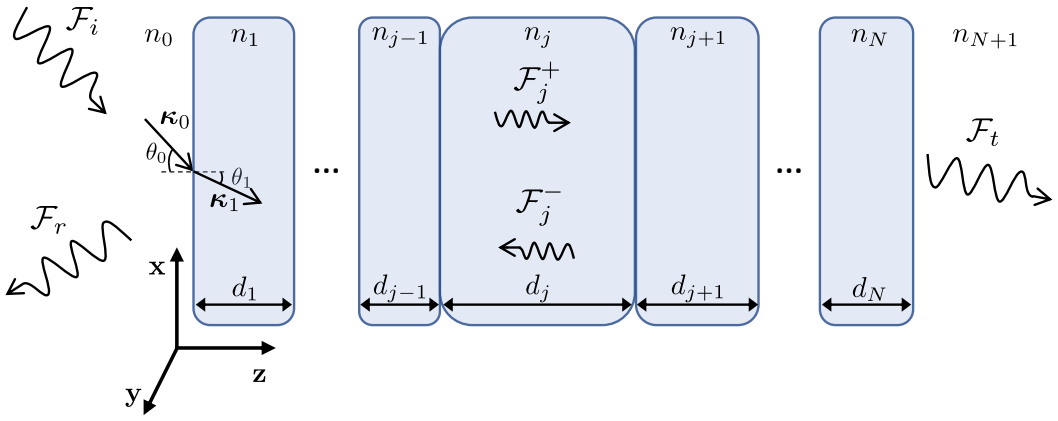

Figure 4.1: A multilayer stack consisting of N slabs, with thicknesses d_j and complex refractive indices n_j. An incident plane wave ($\mathcal{F}_i$) is assumed, incoming from the semi-infinite medium with n_0 at an angle θ_0. This results to a reflected ($\mathcal{F}_r$) and a transmitted ($\mathcal{F}_t$) wave, through the multilayer stack. At each individual j layer, there are plane to be waves traveling in both $+\boldsymbol{z}$ ($\mathcal{F}_j^+$) as well as at the $-\boldsymbol{z}$ directions ($\mathcal{F}_j^-$).

normal incidence, is depicted in fig. 4.2 for (a) TE and (b) TM polarization. Naturally, the outgoing waves at each side of the interface will be a superposition of the reflected amplitude of one of the incoming waves with the transmitted amplitude of the opposite incoming wave. The electric field amplitudes at each side of the interface can be correlated, by enforcing the boundary conditions for **E** and **H** right at the interface [384, 385]:

$$\begin{pmatrix} E_{j+1}^+ \\ \\ E_{j+1}^- \end{pmatrix} = \mathcal{I}_{j,j+1}^{TE/TM} \begin{pmatrix} E_j^+ \\ \\ E_j^- \end{pmatrix} \tag{4.1}$$

where $\widetilde{I}_{j,j+1}^{TE/TM}$ is the interface matrix for the transition of the material j to the adjacent slab $j+1$. This matrix depends on wave polarization. For the TE case, the interface matrix is:

$$\mathcal{I}_{j,j+1}^{TE} = \frac{1}{2} \begin{pmatrix} 1 + \dfrac{n_j cos\theta_j}{n_{j+1} cos\theta_{j+1}} & 1 - \dfrac{n_j cos\theta_j}{n_{j+1} cos\theta_{j+1}} \\ 1 - \dfrac{n_j cos\theta_j}{n_{j+1} cos\theta_{j+1}} & 1 + \dfrac{n_j cos\theta_j}{n_{j+1} cos\theta_{j+1}} \end{pmatrix} \tag{4.2}$$

where n_j, n_{j+1} the complex refractive indices and θ_j, θ_{j+1} the propagation angles at the respected slabs. The transition matrix in the case of TM polarization becomes:

$$\mathcal{I}_{j,j+1}^{TM} = \frac{1}{2} \begin{pmatrix} \dfrac{n_j}{n_{j+1}} + \dfrac{cos\theta_j}{cos\theta_{j+1}} & \dfrac{n_j}{n_{j+1}} - \dfrac{cos\theta_j}{cos\theta_{j+1}} \\ \dfrac{n_j}{n_{j+1}} - \dfrac{cos\theta_j}{cos\theta_{j+1}} & \dfrac{n_j}{n_{j+1}} + \dfrac{cos\theta_j}{cos\theta_{j+1}} \end{pmatrix} \tag{4.3}$$

Assuming incidence from a slab with index n_0 at an angle θ_0, as for fig. 4.1, it can easily be derived, using Snell's law, that the propagation angle at each layer j is given by $\cos\theta_j = \sqrt{1 - \left(\frac{n_0}{n_j}\right)^2 \sin^2\theta_j}$.

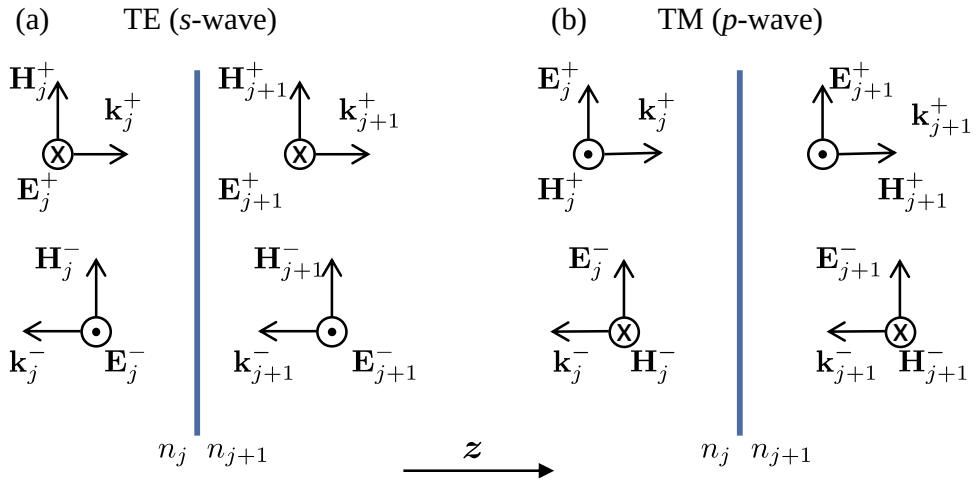

Figure 4.2: Plane wave transmission through an interface between two adjacent materials with refractive indices n_j, n_{j+1}. The general case, with waves traveling in both $+\boldsymbol{z}$ and $-\boldsymbol{z}$ directions at each side of the interface is assumed. (a) TE and (b) TM wave polarizations are depicted, for the simple case of normal incidence.

4.1.2 Propagation matrix

Let us now consider the propagation of light through a homogeneous medium with index n_j and thickness d_j. Once again, inside this layer we assume a wave traveling in the $+\boldsymbol{z}$ direction, with amplitude E_j^+, and one traveling in the $-\boldsymbol{z}$ direction, with amplitude E_j^-. After the propagation through this layer, the light accumulates a phase factor $\phi_j \equiv \boldsymbol{z} \cdot \mathbf{k} = 2\pi n_j d_j \cos\theta_j / \lambda$, where λ the wavelength of the propagating plane wave. The amplitudes of the respected waves after propagation through a layer with index n_j and thickness d_j ($E_{z+d_j}^{\pm}$) are correlated to the ones at its origin ($E_z^{\pm}$) through:

$$\begin{pmatrix} E_{z+d_j}^+ \\ \\ E_{z+d_j}^- \end{pmatrix} = \mathcal{P}_j \begin{pmatrix} E_z^+ \\ \\ E_z^- \end{pmatrix} \tag{4.4}$$

where the matrix $\mathcal{P}_j$ is called propagation matrix and is given by:

$$\mathcal{P}_j = \begin{pmatrix} e^{\phi_j} & 0 \\ 0 & e^{-\phi_j} \end{pmatrix} \tag{4.5}$$

The propagation matrix does not depend on wave polarization.

4.1.3 Transfer matrix of a multilayer stack

After deriving the matrices to describe the transition across individual slabs as well as the propagation of light through them, one can derive the total transfer matrix for a multilayer stack consisting of N arbitrary layers, such as the one depicted in fig 4.1. Assuming light incoming from the semi-infinite material with n_0 having an amplitude $E_i \equiv 1$ and exiting at the semi-infinite material with n_{N+1}, where no light incoming from the $N+1$ layer is considered, the amplitudes of incident ($E_i \equiv 1$), reflected (E_r) and transmitted (E_t) waves

are associated through:

$$\begin{pmatrix} E_t \\ 0 \end{pmatrix} = \mathcal{M} \begin{pmatrix} 1 \\ E_r \end{pmatrix} = \begin{pmatrix} M_{11} & M_{12} \\ M_{21} & M_{22} \end{pmatrix} \begin{pmatrix} 1 \\ E_r \end{pmatrix} \tag{4.6}$$

where the total transfer matrix $\mathcal{M}$ is the product of the ensemble of transition and propagation matrices that describe the whole multilayer stack:

$$\mathcal{M} = \mathcal{I}_{N,N+1}^{TE/TM} \mathcal{P}_N \mathcal{I}_{N-1,N}^{TE/TM} \cdots \mathcal{I}_{1,2}^{TE/TM} \mathcal{P}_1 \mathcal{I}_{0,1}^{TE/TM} \tag{4.7}$$

4.1.4 Reflection and Transmission coefficients

Equation 4.6 can be rewritten as:

$$\begin{aligned} E_t &= M_{11} + M_{12} E_r \\ 0 &= M_{21} + M_{22} E_r \end{aligned} \tag{4.8}$$

The reflection (R) and transmission (T) coefficients are defined as:

$$R = |E_r / E_i|^2 \tag{4.9}$$

and

$$T = \left(\frac{n_{N+1}\, cos\theta_{N+1}}{n_0\, cos\theta_0} \right) |E_t / E_i|^2 \tag{4.10}$$

Using eqn. 4.6, the reflection and transmission coefficients of the whole multilayer stack as:

$$R = \left| -\frac{M_{21}}{M_{22}} \right|^2 \tag{4.11}$$

and

$$T = \left(\frac{n_{N+1}\, cos\theta_{N+1}}{n_0\, cos\theta_0} \right) \left| \frac{\det \mathcal{M}}{M_{22}} \right|^2 \tag{4.12}$$

4.1.5 Absorption of lossy layers

Supposing that the multilayer structure under consideration includes lossy layers, the total absorption of the whole stratified medium is simply:

$$A = 1 - R - T \tag{4.13}$$

If one is interested in the absorption of the j^{th} layer, this can be acquired by:

$$A_j = S_{j-1} - S_{j+1} \tag{4.14}$$

where S_{j-1}, S_{j+1} are the radiative fluxes of electromagnetic energy through the previous and next layer correspondingly, in respect to the j^{th} layer.

In order to get the radiative flux through an arbitrary layer j, both the forward ($\mathcal{F}_j^+$) and the backward ($\mathcal{F}_j^-$) traveling plane waves through this layer must be accounted for, as for fig. 4.1. The amplitudes of the forward ($E_j^+ \equiv \mathcal{A}_j$) and backward ($E_j^- \equiv \mathcal{B}_j$) waves at any layer j can be easily derived using the interface and propagation matrices, as discussed in the previous section. The radiative flux is then given by [386, 387]:

$$S_j = \mathfrak{Re} \left\{ \frac{n_j\, cos\theta_j}{n_1\, cos\theta_1} \right\} \left(|\mathcal{A}_j|^2 - |\mathcal{B}_j|^2 \right) - 2\, \mathfrak{Im} \left\{ \frac{n_j\, cos\theta_j}{n_1\, cos\theta_1} \right\} \mathfrak{Im} \left\{ \mathcal{A}_j\, \mathcal{B}_j^* \right\} \tag{4.15}$$

4.2 Finite Difference Time Domain

4.2.1 Outline of the finite difference time domain method

Finite difference time domain (FDTD) is a versatile numerical method for simulating the optical response of complex structures. FDTD aims for the explicit solution of the time domain Maxwell curl equations. At the heart of the method lies the Yee algorithm, established by K. S. Yee in 1966 [388]. In this context, both space and time are discretised. Space is divided into box-shaped cells, commonly referred to as Yee cells, which are smaller than the minimum wavelength of interest and fine enough to accurately describe any arbitrary geometry of the studied configuration. Time is quantized into small timesteps, corresponding to the time that light needs to travel from one cell to another. Figure 4.3 shows a schematic of a Yee cell, where the electric field components are staggered on the edges of each cell and the magnetic field components on its faces. In this configuration every **E** field component is surrounded by four circulating **H** field components and vice versa. With this spatial discretization, the Maxwell's curl equation are inherently satis-

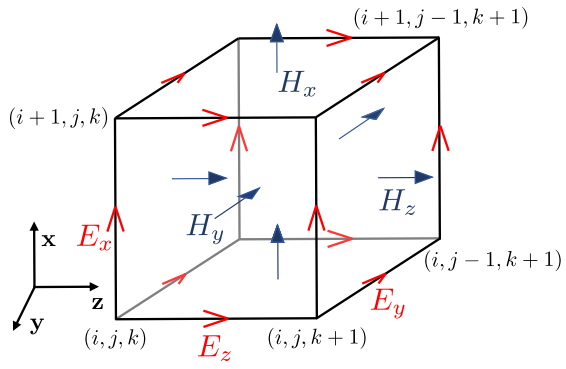

Figure 4.3: Schematic representation of a box-shaped Yee cell, with the **E** field components placed on the edges and **H** field components on the faces.

fied, while the space derivatives in these equations can be calculated using second-order accurate central differences. Moreover, the continuity of **E** and **H** fields are inherently maintained across material interfaces parallel to any of the coordinate axis. Finally, the placement of the **E** and **H** fields in Yee cell and the central difference operations implicitly enforces both Gauss's laws of electromagnetism, leading to a divergence-free mesh in the absence of electric and magnetic charges [389].

Additionally, the Yee formulation centers **E** and **H** fields in time (fig. 4.4). Doing so, it allows for the time derivatives of Maxwell's curl equations to also be solved using second-order accurate central differences. **H** field computations are performed at a certain timestep, for all the simulated region, using **E** field data from the preceding timestep. Afterwards, they are stored in memory and are used for the **E** field calculation at the next timestep. This method, commonly referred to as leapfrog time-stepping, is continued until the simulation converges and the calculation is concluded. The leapfrog time-stepping is non-dissipative, i.e. numerical waves traveling across the Yee mesh do not decay due to spurious non physical artifacts, adding to the robustness of the method.

This discretization, however, also has its drawbacks. Numerical dispersion, i.e. the frequency dependent difference between the phase velocity of a numerically propagated wave from the physical velocity of a light wave, is an inherent property of the FDTD

algorithm and can potentially limit its accuracy. A workaround to compensate these errors is to use a fine mesh for the spatial grid, typically 20 - 30 times smaller than the shortest wavelength considered in the simulation setup.

Moreover, in order to keep the algorithm stable, a certain relation between spatial grid size and timestep must be satisfied. An extensively large time step can result to numerical instability, which can cause the computed values of the fields to spuriously increase without limit during the leapfrog time-stepping. To avoid this, for a certain cell size ($\Delta x,\ \Delta y,\ \Delta z,$) the timestep Δt must satisfy the so-called Courant stability criterion:

$$u_{max}\Delta t \leq \left(\frac{1}{\Delta x^2 + \Delta y^2 + \Delta z^2}\right)^{1/2} \tag{4.16}$$

with u_{max} the maximum phase velocity within the model.

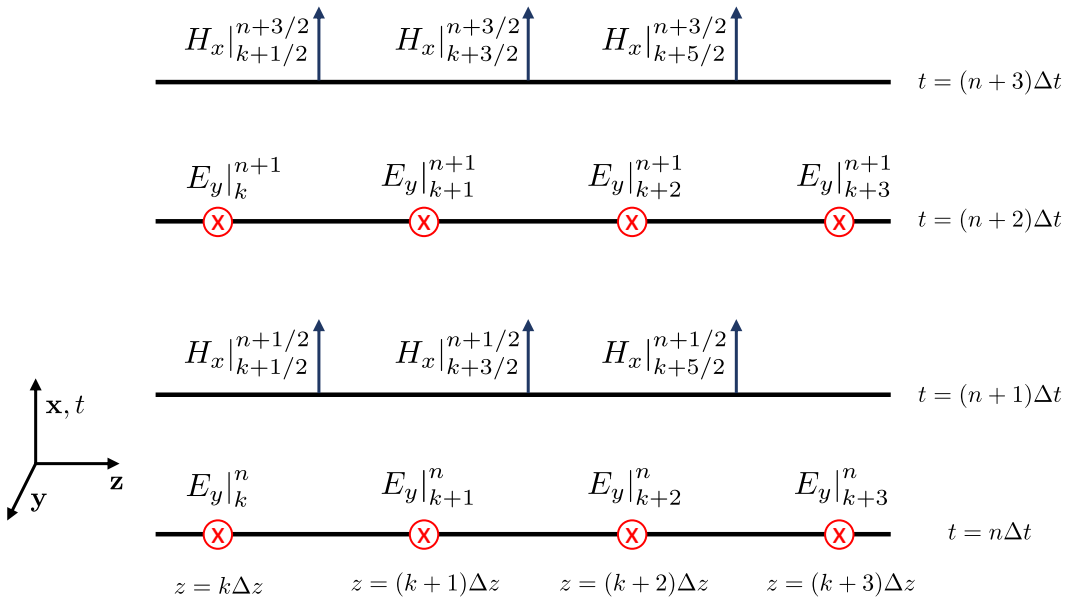

Figure 4.4: 1D Yee grid, demonstrating the discretization in space and time, allowing for the use of central differences for both space and time derivatives.

4.2.2 Advantages and limitations

The main advantages of the FDTD method are a direct consequence of the Yee algorithm:

- Unlike frequency domain methods, FDTD allows one to obtain the response of a system in a wide frequency range with a single simulation run, since it treats Maxwell equations in the time domain. This is particularly useful in broadband applications or in applications where the resonant frequencies are unknown.
- Given that the Courant stability criterion is satisfied, the method is extremely stable. Moreover, computer round-off errors are suppressed, given the central - difference approach of the Yee algorithm.
- Since the fields are numerically propagated across the simulation region, with the curl Maxwell's equations solved explicitly, the method is free of spurious solutions.

- FDTD allows for the accurate modeling of dispersive and non-linear media, enabling the study of a wide variety of phenomena associated with linear or non-linear dielectric and magnetic structures. Additionally, FDTD can treat any arbitrary geometry, given that the grid discretization is fine enough to accurately describe small geometric features.
- With FDTD one can obtain all of the electromagnetic field components, which is very useful in plasmonic applications, where all the electromagnetic field components are relevant.

The main drawbacks of the FDTD method are:

- The inherent numerical dispersion of the Yee formulation, as discussed above. This drawback can be compensated by applying a finer mesh grid. This treatment, however, comes with a larger demand of computational resources.
- Since the method demands an adequately simulation time for the calculation to converge, it demands long computational times for the simulation of high-Q structures, in which the energy dissipates slowly.
- As mentioned above, the approximation of a complex geometry, with geometrical details much smaller than the wavelength of interest, can be challenging for FDTD. In this case, a finer mesh can substantially increase the computation time. Nevertheless, these drawbacks can be alleviated using advanced meshing techniques, e.g. conformal meshing [389, 390].

4.2.3 The Yee algorithm

In this section a brief outline regarding the implementation of the FDTD method is presented. Maxwell's curl equations are:

$$\nabla \times \mathbf{E} = -\mu \partial_t \mathbf{H} \tag{4.17}$$

$$\nabla \times \mathbf{H} = \epsilon_0 \epsilon_\infty \partial_t \mathbf{E} + \partial_t \mathbf{P}_D + \sum_{j=1}^{N} \partial_t \mathbf{P}_j \tag{4.18}$$

where ∂_t denotes the partial time derivatives. Material dispersion is taken into account assuming a Drude - Lorentz model for the dielectric function, although additional dispersive models (e.g. Debye, Plasma frequency model et.c.) can be incorporated in the method [389, 391]. For the dispersion implementation, FDTD can utilize time-domain auxiliary differential equations (ADE) for Drude ($\mathbf{P}_D$) and each Lorentz ($\mathbf{P}_j$) polarization terms. The dielectric function, in the context of Drude - Lorentz model, is given by [288]:

$$\epsilon(\omega) = \epsilon_\infty - \frac{\omega_p^2}{\omega^2 + i\omega\gamma_D} + \sum_{j=1}^{N} \frac{\Delta\epsilon_j \Omega_j^2}{\Omega_j^2 - \omega^2 - i\Gamma_j} \tag{4.19}$$

where ϵ_∞ is the frequency-independent value of the dielectric function, the second term is the Drude free electron contribution and the third term contains N Lorentz oscillators corresponding to interband transitions. In the Drude term ω_p and $1/\gamma_D$ are free electron plasma frequency and relaxation time respectively. For the Lorentz terms, $\Delta\epsilon$ denotes

oscillator strength, Ω the transition frequency and Γ the decay rate of each oscillator. Equation 4.19 must be Fourier - transformed in order to acquire the ADEs in the time domain [389, 391]:

$$\partial_t^2 \mathbf{P}_D + \gamma_D \partial_t \mathbf{P}_D = \omega_p^2 \epsilon_0 \mathbf{E} \tag{4.20}$$

$$\partial_t^2 \mathbf{P}_j + \Gamma_j \partial_t \mathbf{P}_j + \Omega_j^2 \mathbf{P}_j = \Delta\epsilon_j \Omega_j^2 \epsilon_0 \mathbf{E} \tag{4.21}$$

The key step for a robust implementation in the FDTD method is to express eqns. 4.20 and 4.21 using central differences, i.e.:

$$\partial_x \mathcal{F} \equiv \delta_x^c \{\mathcal{F}\} = \frac{\mathcal{F}(x + \Delta x/2) - \mathcal{F}(x - \Delta x/2)}{\Delta x} \tag{4.22}$$

in order to be time-stepped in sync with Maxwell's curl equations. With a few algebraic manipulations, we can write 4.20 using 4.22 [391]:

$$\mathbf{P}_D^{n+1} = c_{1,D}\mathbf{P}_D^n + c_{2,D}\mathbf{P}_D^{n-1} + c_{3,D}\mathbf{E}^n \tag{4.23}$$

where the superscript n indicates the time $n\Delta t$ at which each quantity is calculated, assuming a timestep Δt. The prefactors $c_{1,D}$, $c_{2,D}$ and $c_{3,D}$ for the Drude term are given by:

$$\begin{aligned} c_{1,D} &= \frac{4}{\Delta t \gamma_D + 2} \\ c_{2,D} &= \frac{\Delta t \gamma_D - 2}{\Delta t \gamma_D + 2} \\ c_{3,D} &= \frac{2\epsilon_0 \Delta t^2 \omega_p^2}{\Delta t \gamma_D + 2} \end{aligned} \tag{4.24}$$

In the same manner, eqn. 4.21 within the context of 4.22 becomes [391]:

$$\mathbf{P}_j^{n+1} = c_{1,L}\mathbf{P}_j^n + c_{2,L}\mathbf{P}_j^{n-1} + c_{3,L}\mathbf{E}^n \tag{4.25}$$

where the prefactors $c_{1,L}$, $c_{2,L}$ and $c_{3,L}$ for Lorentz oscillators are given by:

$$\begin{aligned} c_{1,L} &= \frac{4 - 2\Delta t^2 \Omega_j^2}{\Delta t \Gamma_j + 2} \\ c_{2,L} &= \frac{\Delta t \Gamma_j - 2}{\Delta t \Gamma_j + 2} \\ c_{3,L} &= \frac{2\epsilon_0 \Delta t^2 \Delta\epsilon_j^2 \Omega_j^2}{\Delta t \Gamma_j + 2} \end{aligned} \tag{4.26}$$

For the derivation of Maxwell's curl equations using the central difference scheme, let us assume the simple case of 1D Yee grid, as for fig. 4.4, with TE polarized light propagating across the z direction. Equations 4.17 and 4.18 become:

$$(\nabla \times \mathbf{E})_y = -\mu \partial_t H_x \Rightarrow \partial_z E_y = \mu \partial_t H_x \tag{4.27}$$

$$\begin{aligned} (\nabla \times \mathbf{H})_x = \epsilon_0 \epsilon_\infty \partial_t E_y + \partial_t P_D + \sum_{j=1}^{N} \partial_t P_j \Rightarrow \\ \partial_z H_x = \epsilon_0 \epsilon_\infty \partial_t E_y + \partial_t P_D + \sum_{j=1}^{N} \partial_t P_j \end{aligned} \tag{4.28}$$

respectively, where isotropic polarization for both Drude and Lorentz terms is assumed. Applying the central difference approximation in 4.27, the update equation for the x-component of the **H** field is given by:

$$H_x|_{k+1/2}^{n+1/2} = H_x|_{k+1/2}^{n-1/2} + \frac{\Delta t}{\mu \Delta x}\left(E_y|_{k+1}^{n} - E_y|_{k}^{n}\right) \tag{4.29}$$

where the notation $\mathcal{F}(k\Delta z, n\Delta t) \equiv \mathcal{F}|_k^n$ is used. Using eqn. 4.29 one can compute the **H** field component at timestep $n + 1/2$, given its value in the preceding timestep and the **E** field components in its adjacent grid points at timestep n. This procedure is repeated for the whole simulation region and the **H** field components values are stored in memory. Using these values, the **E** field components are then evaluated, after applying the central difference scheme in eqn. 4.28:

$$\begin{aligned} E_y|_k^{n+1} = E_y|_k^n - \frac{1}{\epsilon_0 \epsilon_\infty}\left(P_D|_k^{n+1} - P_D|_k^n\right) - \frac{1}{\epsilon_0 \epsilon_\infty}\sum_{j=1}^{N}\left(P_j|_k^{n+1} - P_j|_k^n\right) \\ + \frac{\Delta t}{\epsilon_0 \epsilon_\infty \Delta z}\left(H_x|_{k+1/2}^{n+1/2} - H_x|_{k-1/2}^{n+1/2}\right) \end{aligned} \tag{4.30}$$

where P_D and P_j values are calculated using eqns. 4.23- 4.25. The **E** components from the above calculation are stored, and will be used for the **H** field calculation, at the next timestep, using eqn. 4.29. The Yee algorithm caries on at this leapfrog time-stepping, until the convergence criteria of the simulation are reached, at which point the computation stops. The update equations for the TM polarization as well as the ones for the 2D and the full 3D Yee grid are derived in a similar manner and can be found in any FDTD textbook [389, 392–394].

At the beginning of the simulation all fields are set to zero. Although a variety of different electromagnetic sources are available in FDTD [389,393], in the scope of this thesis the plane wave source was used. Plane wave sources numerically inject laterally-uniform electromagnetic energy from one side of the simulation region using a time-domain pulse. The time dependency of the incident pulse is selected in order to include all the frequencies of interest.

Upon simulation termination, the values of all the time-domain field components are known in the whole simulation region. To get the frequency dependent values, the time-domain results simply have to be Fourier-transformed. After that, any information about the optical response can be extracted, e.g. the power flow through a cross section S of the computational grid can be obtained by integrating the Poynting vector across the surface S.

4.2.4 Boundary conditions

FDTD algorithm solves for the electromagnetic response of a given structure at a finite numerical lattice. As a result, special treatment must be taken at the termination of this lattice. Without any boundary conditions, Yee's formulation treats the simulation region as surrounded by a perfect electric conductor, leading to spurious reflections. To avoid non-physical solutions, the lattice must be truncated at its edges, extending it to infinity and numerically simulate an unbound volume. This can be achieved by either absorbing boundary conditions (ABC) or periodic boundary conditions (PBC).

In ABCs an absorbing medium surrounds the simulation region, in the directions that free space needs to be simulated. This absorbing medium should ideally absorb all electromagnetic radiation at every frequency incoming from every angle. Early implementation of ABCs used a lossy, impedance-matched medium to achieve this goal [389]. However, their performance was poor for non-normal incident angles. A more effective solution introduced by Berenger [395]. Berenger's implementation, called the perfectly matched layer (PML), was based on splitting the field components in Maxwell's equations and showed better performance [395]. This solution proved to be very effective and is the basis of the modern PML techniques, used in FDTD as well as in other numerical methods. Nevertheless, despite the fact that PML is reflection-free in continuous space, the discretised nature of FDTD method, where PML are implemented as a multi-layer medium can result in spurious reflections. Later studies re-implemented PMLs as a uniaxial medium [396] . Although this method accomplished better performance than the original implementation by Berenger [395], they performed poorly in absorbing evanescent modes that had long time interactions with the PMLs. The above problems with evanescent modes inside the PML layers were alleviated by introducing the complex frequency shifted PMLs [397]. An efficient implementation, based on stretched - coordinate formulation [398], called the convolutional PML is one of the most effective ABCs to date. During this thesis, FDTD simulations were performed using the commercial FDTD solver *FDTD Solutions* by Lumerical Inc. [399]. Stretched coordinate PMLs, based on the work by Gedney and Zhao [400], were used as ABCs in all simulations.

If the studied structure is periodic across an axis, it is more efficient to simulate only on unit cell and apply periodic boundary conditions (PBS) along the axis of periodicity. In non-periodic directions, ABCs can be used to truncate the lattice, as described above. Let us assume a periodic structure in $x-y$ directions. In this case, all scalar field components $\mathcal{F}$ succumb to Floquet-Bloch theorem [401]:

$$\mathcal{F}(x+d_x, y+d_y, z) = \mathcal{F}(x, y, x)\exp[i(k_x x + k_y y)] \tag{4.31}$$

with d_x, d_y the unit cell dimensions and k_x, k_y the incident plane wave's wavevector components. Using eqn. 4.31 in FDTD algorithm demands for complex values of all the field components, with all the incident plane waves having the same k_x and k_y. Under oblique incidence, this means that we are restricted to single frequency simulations. Under normal incidence considered in this thesis, however, $k_x = k_y = 0$, thus the incident time-domain pulse can consist of an ensemble of frequencies, enabling efficient broadband FDTD simulations. In this case, FDTD software simply copy the fields calculated at one side of the periodic axis and inject them on the opposite one.

4.2.5 Implementing Graphene in FDTD

Modeling SLG using the FDTD method can be challenging, given the 2D nature of the former. In conventional FDTD algorithms, materials are inserted in the simulation through their volumetric permittivity, as described in the previous sections. The dispersion of graphene optical properties are based on its surface conductivity, described by the Kubo formula (eq. 3.19). Moreover, given the infinitesimal thickness of SLG, a very fine mesh is required for its simulation using FDTD. For applications in IR, or even longer wavelengths, the simulated devices can have dimensions spanning several μm, resulting to a huge amount of Yee cells to be computed, which require large computational resources.

There are two basic approaches in order to overcome these obstacles and efficiently simulate SLG with FDTD.

The first approach associates graphene's surface conductivity to an equivalent volumetric permittivity. SLG is modeled through this uniaxial anisotropic permittivity, assuming it has a finite thickness. This method, however, assumes SLG thickness equal to the grid spacing normal to SLG surface. Even though this thickness is larger than graphene's actual thickness of ~ 0.335 nm, it should be kept relatively small (in the few nm range) in order to produce accurate results [402].

The second approach describes SLG as a 2D surface through a charged surface boundary condition applied only to a fraction of Yee cells, e.g. those adjacent to the graphene layer. This surface boundary condition is of the form of:

$$\mathbf{n} \times \left({}^{1}\mathbf{H} - {}^{2}\mathbf{H}\right) = \sigma_{\text{SLG}}\mathbf{E} \tag{4.32}$$

where $\mathbf{n}$ is the unit vector normal to SLG surface, ${}^{1}\mathbf{H}$ and ${}^{2}\mathbf{H}$ the magnetic fields in each side of SLG surface, σ_{SLG} the SLG surface conductivity and $\mathbf{E}$ the tangent electric field [403,404]. This is an efficient and elegant approach which alleviates the need for extreme space and time discretization.

The Lumerical FDTD solver [399], used alongside the simulation framework developed in this thesis, implements graphene as a 2D conducting surface, following the second approach. Doing so, efficient simulations are carried out, where the computation is concluded within few minutes using a personal computer, even for a fine grid meshing of 1 nm.

4.3 4th order Runge-Kutta method

The temporal response of the graphene-based devices studied in this thesis can be obtained by a set of three coupled rate equations (eqs. 3.48 – 3.51). These equations are often used in conjunction with TMM, where a large number of calculations are needed to a obtain a broadband result. Moreover, they are included in self-consistent iterations, which often need to be computed several times until convergence is achieved. It is thus necessary to treat them using an efficient manner. To do so, the 4^{th} order Runge - Kutta method [405,406] (4RK) is used throughout this thesis. 4RK is an explicit iterative method, widely used in temporal discretization. Let us assume the initial value problem:

$$\frac{\partial y}{\partial t} = f(t, y),\ y(t_0) = y_0 \tag{4.33}$$

where the function f and the initial values $t_0,\ y_0$ are known. Given a timestep $\Delta t > 0$, the value of y can be approximated by:

$$\begin{aligned} y_{n+1} &= y_n + \frac{\Delta t}{6}(k_1 + 2k_2 + 2k_3 + k_4) \\ t_{n+1} &= t_n + \Delta t \end{aligned} \tag{4.34}$$

for $n = 1,\ 2,\ 3\ldots$ with:

$$\begin{aligned} k_1 &= f\left(t_n, y_n\right) \\ k_2 &= f\left(t_n + \frac{\Delta t}{2}, y_n + \Delta t\frac{k_1}{2}\right) \\ k_3 &= f\left(t_n + \frac{\Delta t}{2}, y_n + \Delta t\frac{k_2}{2}\right) \\ k_4 &= f\left(t_n + \Delta t, y_n + \Delta t k_3\right) \end{aligned} \tag{4.35}$$

That is, the value y_{n+1} is given by the preceding value y_n plus the weighted average of four increments, each one the product of the time interval Δt and an estimated slope k, with added weight to the mid-point slopes. Being a fourth-order method, 4RK has a total accumulation error in the order of $\mathcal{O}(\Delta t^4)$ [405] and can give good approximate solutions without the need for extremely small discretization, in contrast to other numerical methods for ordinary differential equations, e.g. Euler's method [405].

4.4 Composite Simpson's rule

SLG properties, e.g. carrier density (eq. 3.13), heat capacity (eq. 3.16), optical conductivity (eq. 3.19) et.c., are obtained through numerical integrations. These integrations are included in self-consistent loops, as discussed in the previous section. Consequently, their calculations, regarding the systems studied in this thesis, needed to be done in a robust and efficient way. The algorithms developed during this thesis implemented the composite Simpson's rule [405] to handle the necessary numerical integrations. In this context, for an interval $[a, b]$ splitted in n sub-intervals, the integral of a function $f(x)$ is given by:

$$\int_a^b f(x)dx \approx \frac{\Delta x}{3}\left[f(a) + 4\sum_{j=1}^{n/2} f(x_{2j-1}) + 2\sum_{j=1}^{n/2-1} f(x_{2j}) + f(b)\right] \tag{4.36}$$

with $\Delta x = (b-a)/n$ and $x_j = a + j\Delta x$. Composite Simpson's rule can handle integrands that are not smooth in the integration interval, e.g. integrands that are highly oscillatory in the given interval. Moreover, it does not need a fine discretization of the interval for the calculation to converge. Since the integrals we are interested in this study are usually calculated over infinite or semi-infinite intervals, the following change of variables were used to numerically compute them:

$$\int_{-\infty}^{+\infty} f(x)dx = \int_{-1}^{+1} f\left(\frac{u}{1-u^2}\right)\frac{1+u^2}{(1-u^2)^2}\,du \tag{4.37}$$

for the integrals over infinite intervals and:

$$\begin{aligned} \int_a^{+\infty} f(x)dx &= \int_0^1 f\left(a + \frac{u}{1-u}\right)\frac{du}{(1-u)^2} \\ \int_{-\infty}^{a} f(x)dx &= \int_0^1 f\left(a - \frac{1-u}{u}\right)\frac{du}{u^2} \end{aligned} \tag{4.38}$$

for the integrals over semi-infinite intervals.

Chapter 5

Electro-absorption modulator in a mobility-independent graphene-loaded Bragg resonator

Deep and fast electro-optic modulation is critical for high-speed near infrared signal processing. We combine the electro-absorption tunability of graphene with the high-Q resonance of a Bragg-based Fabry-Perot resonator at $\lambda = 1550$ nm and show that $\sim 100\%$ free-space signal modulation at small insertion loss and GHz speed can always be achieved independently of graphene quality (i.e., mobility), provided that the device operates in the reflection mode and is tuned in critical coupling with graphene. Remarkably, the critical coupling mechanism produces a higher extinction ratio for lower graphene mobility. We use practical considerations to optimize the device architecture and operation as a function of graphene mobility. With a small modification, this scheme can be turned into a very sensitive acousto-absorption modulator with an extinction ratio of $\sim 30\,\mathrm{dB/\AA}$ or an index sensor with a sensitivity of 10^7 % RIU. These designs can be extended throughout the infrared spectrum by appropriate material selection and scaling of layer dimensions.

This chapter is based on:

➤ **S. Doukas**, A. Chatzilari, A. Dagkli, A. Papagiannopoulos and E. Lidorikis, *Deep and fast free-space electro-absorption modulation in a mobility-independent graphene-loaded Bragg resonator*, Appl. Phys. Lett. 113, 011102 (2018), https://doi.org/10.1063/1.5030699

5.1 Introduction

Optical modulation in SWIR is crucial for a variety of applications, as discussed in chapter 2. Graphene, with its electrically tunable conductivity [53] and fast carrier relaxation time ($\sim$ ps) [183, 184] is posed to make important contributions on this field [25, 45, 112, 117, 407]. Graphene based SWIR modulation [217] has been demonstrated in both waveguide-integrated [253–256] and free space [222, 248–250, 408] configurations. In the latter case, up to $\sim$ 11 dB modulation depth at $\sim$ GHz modulation frequency (MF) has been demonstrated [249, 250].

Graphene absorption is highly tunable within the VIS - SWIR range via electrostatic gating, being $\sim 2.3\,\%$ [42] when air suspended and $2.3/n\,\%$ when embedded in a dielectric of index n [285], given that $\hbar\omega > E_{F,\mathrm{SLG}}$, i.e. with allowed interband transitions, where Fermi level $E_{F,\mathrm{SLG}}$ is determined by the electrostatic doping. At $\hbar\omega < E_{F,\mathrm{SLG}}$ graphene's absorption is significantly reduced due to Pauli blocking, as discussed in detail in chapter 3. Transitioning across the Pauli blocking point is relatively sharp for high quality graphene (i.e. high carrier mobility and long free carrier relaxation time τ_{opt}) but smooths up as τ_{opt} gets shorter. In any case, however, because of the overall weak graphene absorption ($< 2.3\,\%$), it is imperative that graphene light interaction is enhanced by the use of a resonator structure, such as an optical cavity [222, 249, 408] and/or plasmonics [59–63].

Numerical simulations predict that free-space modulators consisting of graphene integrated with a Bragg-type resonator can reach MDs $\sim 100\,\%$, with low insertion loss (IL) and $\sim$ GHz MFs [229, 409], promising great opportunities in free-space SWIR (or MWIR - THz [409]) modulation. In these studies, however, a particular hypothesis for graphene quality (i.e. carrier mobility and free carrier relaxation time τ_{opt}) is adopted and the device architecture is optimized accordingly. Besides being problematic for devices operating in transmission mode (as we will show), since low graphene mobility will drastically reduce MD and increase IL, graphene quality consistency issues without a systematic understanding and design strategy around them can potentially turn into show-stoppers. In this study, it is shown that a graphene-loaded Bragg resonator device operating in reflection mode can always be dynamically tuned into critical coupling [410, 411] (i.e. total absorption) irrespective of graphene quality, ensuring systematically large MD ($\sim 100\,\%$, >30 dB extinction ratio), low IL ($<$ 1 dB), and high MF ($>$ 1 GHz). Practical considerations are assumed to optimize the device architecture and operation as a function of graphene mobility. Moreover, with a small modification, the scheme designed in this chapter can be turned into a very sensitive acousto-absorption modulator with an extinction ratio of $\sim$ 30 dB/Å or an index sensor with a sensitivity up to 10^7 % RIU. All the consideration and designs studied in this chapter for $\lambda = 1550$ nm can also be extended throughout the IR spectrum by appropriately choosing the materials involved and scaling their dimensions.

5.2 Device layout

The studied device consists of an asymmetrical Bragg cavity, shown in fig. 5.1(a), comprised of 3 periods of a Si/SiO_2 bilayer in either side with an Au mirror on the back. The layer thicknesses are $d_{\mathrm{Si}} = 113.3$ nm and $d_{\mathrm{SiO_2}} = 265.4$ nm corresponding to quarter-wave layers at $\lambda = 1550$ nm for refractive indices $n_{\mathrm{Si}} = 3.42$ and $n_{\mathrm{SiO_2}} = 1.46$ respectively. The central cavity consists of a SiO_2 double layer with a single layer graphene (SLG) in between. Graphene's permittivity is modeled via the Kubo formula (eq. 3.27) at room temperature using $\tau_{\mathrm{opt}} = 200$ fs and assuming that it can be electrostatically doped by in-

terrogating the bottom doped Si layer (assuming all other Si layers intrinsic), as depicted in fig. 5.1(a). The dielectric strength of SiO_2 $\sim 10^7$ V/cm [412] and the layer thickness $d_{SiO_2} = 265.4$ nm restrict gating to an upper limit of $V_g^{\max} = 265.4$ V. Assuming zero internal graphene doping at zero gating, graphene's Fermi level is given by:

$$E_{F,\mathrm{SLG}} = \hbar v_{F,\mathrm{SLG}} \sqrt{\frac{\epsilon_0 \epsilon_{SiO_2} \pi V_g}{e d_{SiO_2}}} \tag{5.1}$$

where $v_{F,\mathrm{SLG}} = 10^6$ m/S is the Fermi velocity of electrons in graphene and $\epsilon_{SiO_2} = 3.9$ [412] the gate dielectric constant. This enforces an upper limit on Fermi level $E_{F,\mathrm{SLG}}^{\max} = 0.54$ eV. Note, however, that this is a limiting case; $E_{F,\mathrm{SLG}}^{\max}$ can be much higher considering that graphene usually has an initial doping [413–415] and/or that one can use a high-k dielectric, e.g., HfO_2 with $\epsilon_{HfO_2} = 25$ [416]. Furthermore, a single highly doped ($N_{d,\mathrm{Si}} = 10^{20}$ cm^{-3}) *n*-Si gate layer is considered, with its absorption taken into account through a Drude model for its dielectric function [417, 418]:

$$\epsilon_{\mathrm{Si}} = n_{\mathrm{Si}}^2 \left[1 - \frac{\omega_p^2}{\omega^2 + i\omega\tau_{\mathrm{Si}}^{-1}} \right] \tag{5.2}$$

where $\hbar\omega_p = \hbar n_{\mathrm{Si}}^{-1} \sqrt{N_{d,\mathrm{Si}}\, e^2/\epsilon_0\, m^*} \cong 0.21$ eV, $m^* = 0.26\, m_e$, $\tau_{\mathrm{Si}} = m^* \mu_{\mathrm{Si}}/e \cong 200$ fs and $\mu_{\mathrm{Si}} = 1350$ cm^{2}V^{-1}s^{-1} [20]. As an estimate this corresponds to an absorption coefficient $\alpha = 4\pi\kappa/\lambda \cong 42$ cm^{-1}, where $\kappa = \Im\mathrm{m}\left\{\sqrt{\epsilon_{\mathrm{Si}}}\right\}$, with single pass absorption $1 - \exp(-\alpha d_{\mathrm{Si}}) \cong 0.05$ %. This is much smaller than graphene's single pass absorption of $2.3/n_{SiO_2} \cong 1.5$ % and considering that the Si layer is not inside the central cavity, it can be assessed that its effect is going to be relatively small. For completeness, however, all calculations are with Si absorption taken into account. Finally, the Au mirror at the bottom ensures that there is no transmitted wave. It should be noted that the approach adopted here is valid for any alternative choice of materials comprising the Bragg stacks.

The system reflection under normal incidence is calculated by employing the Fresnel equations with the transfer matrix method (section 4.1) and plotted in fig. 5.1(b) for two different SLG doping levels. There exists a critical doping level $E_{F,\mathrm{SLG}}^{\mathrm{c}}$ for which the reflection at $\lambda = 1550$ nm is practically zero. It should be noted that in the absence of transmission, this means perfect absorption, a condition also called critical coupling [410, 411, 419–421] (see also Appendix A). At any other doping level, the reflection becomes finite and generally close to 1, yielding a MD of $\sim 100\%$. The studied device is essentially a single port system, given the negligible transmission imposed by the backmirror. In this case, there is always a perfect absorption (critical coupling) condition as can be seen by inspection of the general single-port coupled-mode formulation for absorption [422] (see also eq. A.3 in Appendix A):

$$A = \frac{4\gamma_a \gamma_d}{(\omega_0 - \omega)^2 + (\gamma_a + \gamma_d)^2} \tag{5.3}$$

where ω_0 is the cavity resonance frequency, γ_a the total absorption rate of the system, and γ_d the decay rate of the cavity. In our case, absorption is provided by the graphene layer, the Au mirror in the back and the *n*-Si gate below graphene. At resonance ($\omega = \omega_0$), we achieve critical coupling when the absorption rate matches the cavity decay rate ($\gamma_a = \gamma_d$). So, for any given cavity, there is always a critical absorptivity of its elements which will promote perfect absorption. It is interesting to note that deviating in any way

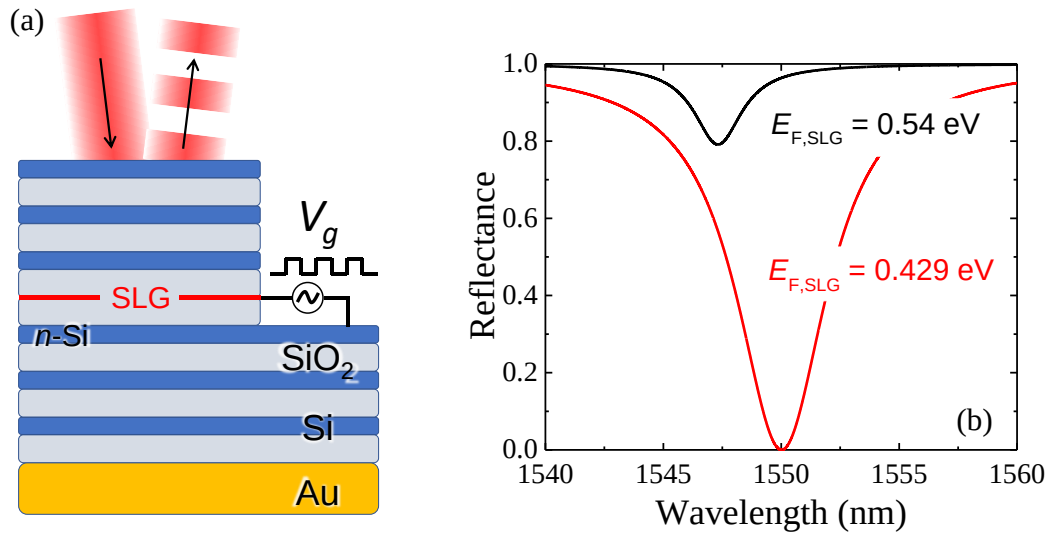

Figure 5.1: Schematic of the proposed device with three Si/SiO_2 periods on either side of the cavity. (b) Reflectance of the device in (a) for graphene electrostatic doping 0.429 (red) and 0.54 eV (black).

from this condition reduces the overall absorption. That is, we have the (maybe) counter-intuitive result that for a cavity with a small decay rate (i.e., high quality factor Q), we may need to reduce the absorptivity of the cavity elements in order to increase the overall absorption. Graphene is a particularly promising material towards this direction as its internal absorptivity can be easily controlled and fine-tuned by electrostatic gating.

Tunability of the studied configuration towards critical coupling is explored in figs. 5.2(a) and 5.2(b), where the total and constituent absorption as a function of graphene doping are plotted. We distinguish two cases, where the Au mirror is in direct contact with a Si layer [fig. 5.2(a)] or with a SiO_2 layer [fig. 5.2(b)], as shown by schematics in the inset. It should be noted that because the resonant wavelength shifts as we dope graphene, and to facilitate our discussion on critical coupling, for each different doping level, the wavelength range is scanned and the point of maximum total absorption is plotted. We find that the simple change in Au mirror contact (Si or SiO_2) imposes dramatic changes between the two absorption graphs. Specifically, in the case of direct contact with Si, the Au mirror exhibits higher absorption compared to the other case. Simply, at $\lambda = 1550$ nm, the Au refractive index is $n_{\text{Au}} = 0.51 + 10.7i$ [423], and its single-pass absorption under normal incidence is $A_{\text{Au}} = 1 - R_\infty$, where the semi-infinite reflectance is $R_\infty = |n_{\text{diel}} - n_{\text{Au}}|^2 / |n_{\text{diel}} + n_{\text{Au}}|^2$. Thus, the absorptivity in the Si/Au interface is 5.4%, about 2.2 times larger compared to 2.5% of the SiO_2/Au interface. Consequently, the required SLG absorptivity for critical coupling should be about 2.2 times lower in the Si-terminated case, as is indeed shown in figs. 5.2(a) and 5.2(b). The lower Au absorptivity in SiO_2/Au implies larger room for tunability by graphene. Also, working in the reflection mode, the largest contrast is obtained in the SiO_2/Au case between critically coupled graphene and highly doped graphene. Thus, the optimal configuration is with the smallest index dielectric (i.e., SiO_2) in contact with the Au mirror.

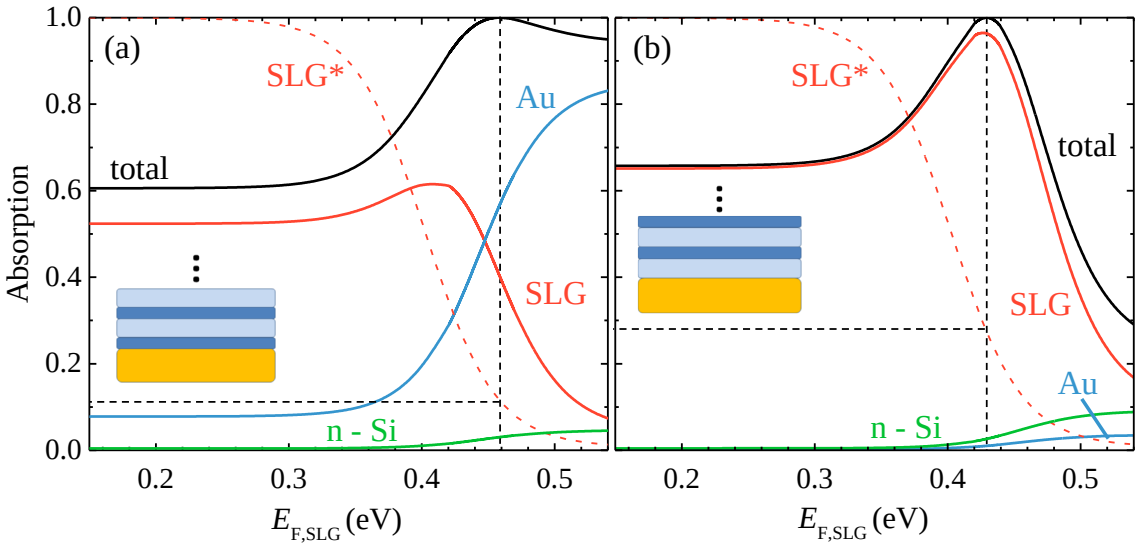

Figure 5.2: The absorption in each constituent as a function of graphene doping for a device having the Au mirror in contact with (a) Si and (b) SiO_2. The red dashed line marked as SLG* is the normalized absorptivity of suspended graphene.

5.3 Effect of graphene quality

For evaluating device performance we use MD and IL (either in percentage or in dB units), as they were defined in section 2.2.1. The maximum reflectance (R_{max}) is obtained at the highest graphene doping (i.e., at $E_{F,\text{SLG}} = 0.54$ eV) and the minimum reflectance (R_{min}) at critical coupling. The latter varies depending on the structure and graphene quality. In fig. 5.3(a), we plot the modulation depth as a function of detuning $\delta E_F = E_{F,\text{SLG}} - E^{\text{c}}_{F,\text{SLG}}$ from the critical coupling condition, i.e., the detuning of R_{min}. Extremely large values can be obtained, provided that we can tune the graphene Fermi level with enough accuracy. Given the natural limitations to this, we explore the more realistic condition of having a tolerance in the applied gate voltage. In particular, the $E_{F,\text{SLG}} = 0.429$ eV doping needed for critical coupling [see fig. 5.2(b)] results from an applied voltage $V_g^c = 166$ V, according to eq. 5.1. A tolerance of $\mathcal{D}E_{F,\text{SLG}} = 1$ meV [dotted lines in fig. 5.3(a)] corresponds to $\mathcal{D}V_g = 0.8$ V, or a variation of $\sim 0.5\%$, while a $\mathcal{D}E_{F,\text{SLG}} = 10$ meV tolerance [full width of fig, fig. 5.3(a)] corresponds to $\mathcal{D}V_g$ of $\sim 5\%$. The minimum reflectance is then calculated as:

$$\langle R_{\text{min}} \rangle = (\mathcal{D}E_{F,\text{SLG}})^{-1} \int R(\epsilon) d\epsilon \tag{5.4}$$

where the integration is performed within $\mathcal{D}E_{F,\text{SLG}}$ around the $E^{\text{c}}_{F,\text{SLG}}$ value. For high quality graphene with $\tau_{\text{opt}} = 200$ fs, the modulation depth is $\langle \text{MD} \rangle = 6.5 \times 10^4$ and 6.7×10^2 for 0.5% and 5% gating tolerances respectively.

The calculation is repeated for smaller relaxation times τ_{opt} (corresponding to lower graphene mobilities according to eq. 3.23). For example, fig. 5.3(a) also plots MD for $\tau_{\text{opt}} = 10$ fs (i.e. $\mu_{q,\text{SLG}} \cong 210$ cm^{2}V^{-1}s^{-1}) found at critical doping $E^{\text{c}}_{F,\text{SLG}} = 0.475$ eV (for comparison, for $\tau_{\text{opt}} = 200$ fs and $E^{\text{c}}_{F,\text{SLG}} = 0.429$ eV the carrier mobility is $\mu_{q,\text{SLG}} \cong 4660$ cm^{2}V^{-1}s^{-1}). While the peak value remains the same, there is a wider response curve for lower τ_{opt}, resulting in a larger averaged modulation depth $\langle \text{MD} \rangle$. This is actually a

quite consistent trend, as shown in fig. 5.3(b) where $\langle \text{MD} \rangle$ is plotted as a function of τ_{opt} for both 0.5% and 5% tolerances. An almost three-fold increase in the modulation depth is observed when lower quality graphene is assumed. This is a remarkable result that significantly loosens graphene quality and fabrication requirements. To understand its origins, in fig. 5.4(a) the Fermi level of graphene required to achieve critical coupling as a function of τ_{opt} is plotted. It should be noted that higher doping is required for lower τ_{opt}. In fig. 5.4(b) the absorptivity of graphene at $\lambda = 1550$ nm suspended in SiO_2 is plotted, as a function of Fermi level. This is given by $A_{\text{SLG}} = 2\pi d_{\text{SLG}} \epsilon_2 / n_{\text{SiO}_2} \lambda$, where $d_{\text{SLG}} = 0.335$ nm is the effective graphene thickness and $\epsilon_2 (\omega, E_{F,\text{SLG}})$ the imaginary part of graphene dielectric function (eq. 3.27). In order to keep the graphene absorptivity constant as we

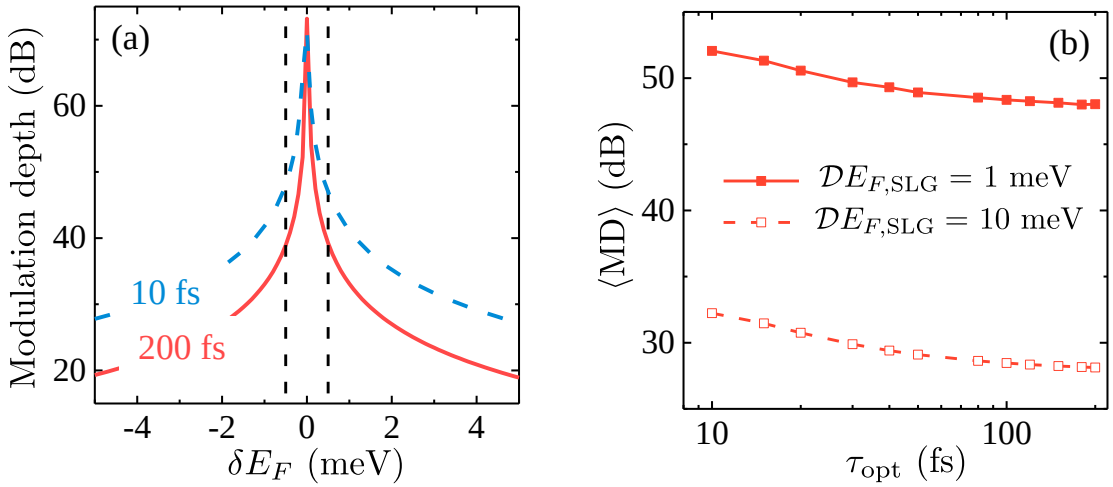

Figure 5.3: (a) Modulation depth MD for the device shown in fig. 5.1(a) as a function of detuning $\delta E_F = E_{F,\text{SLG}} - E^{\text{c}}_{F,\text{SLG}}$ from R_{min}.(b) $\langle \text{MD} \rangle$ as a function of electron relaxation time assuming two values of tolerance on electrostatic doping.

reduce τ_{opt}, we indeed need to increase the doping. What determines then the magnitude of $\langle \text{MD} \rangle$ is the derivative of absorptivity with doping, i.e., $\partial A_{\text{SLG}} / \partial E_{F,\text{SLG}}$, which is plotted in fig. 5.4(c). The two vertical lines mark $\tau_{\text{opt}} = 200$ fs and $\tau_{\text{opt}} = 10$ fs critical absorptivity, showing about a threefold decrease in the slope for the latter case. However, the above result is not generic but rather specific to the requirements of the studied device. As seen in fig. 5.4(c), there are doping levels where $\partial A_{\text{SLG}} / \partial E_{F,\text{SLG}}$ is smaller for the high quality graphene. If critical coupling had occurred at these doping levels (e.g. had we started with another device layout), then the high quality graphene would appear as the champion.

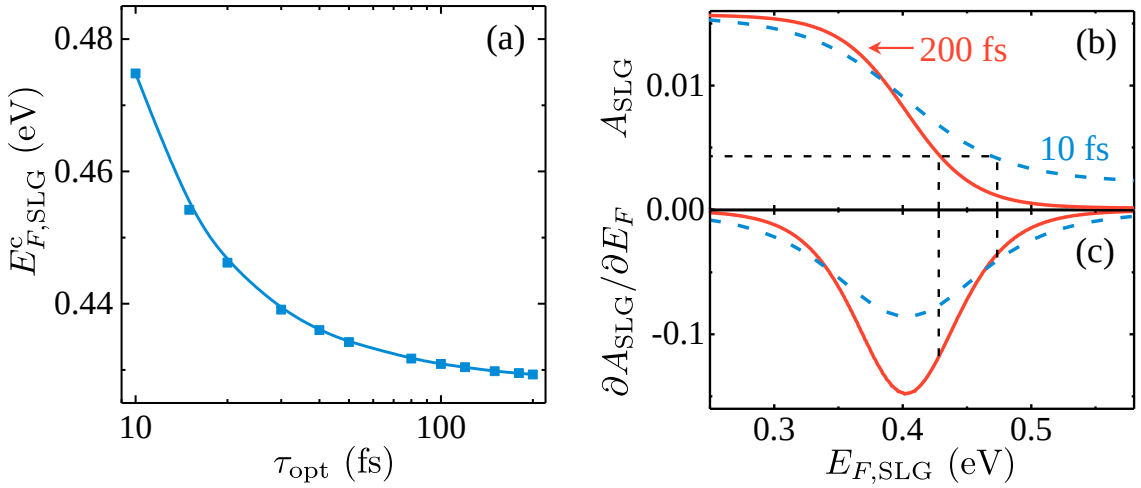

Figure 5.4: (a) Critical Fermi level $E^{c}_{F,SLG}$ for achieving critical coupling. (b) Graphene absorptivity for $\tau_{opt} = 200$ fs (solid red) and $\tau_{opt} = 10$ fs (dashed blue). (c) Absorption derivative in respect to Fermi level for the two relaxation times above.

5.4 Effect of device layout

To explore the effect of device layout, the number of Bragg periods is varied. In fig. 5.5, three different configurations with 2, 3, and 4 periods of Si/SiO_2 bilayers are evaluated, marked as R2, R3, and R4. In the R2 configuration, because of the much higher γ_d, high internal absorptivity was needed and thus the Si/Au configuration [as in fig. 5.2(a)] was used. In the R4 configuration, it is $E^{c}_{F,SLG} > E^{max}_{F,SLG}$ for $\tau_{opt} < 50$ fs, so the analysis was limited for $\tau_{opt} \geq 50$ fs. This is expected since a low absorption rate γ_a is needed to match the low decay rate γ_d of the R4 configuration. This, however, requires large doping levels $E^{c}_{F,SLG} > E^{max}_{F,SLG}$ for low τ_{opt} values, as is evident from fig. 5.4(b).

For comparison, the results for a similar modulator (a symmetric one without the Au back mirror) operating in the transmission mode (with 4, 5, and 6 Bragg periods, marked T4, T5, and T6) are shown as well in fig. 5.5. In this case, $\langle MD \rangle$ deteriorates quickly with reduced graphene mobility. This behavior is expected since such a device requires graphene to be fully transparent in the *on* state for maximum response. This is in contrast to the proposed modulator in the reflection mode, which shows enhanced performance for lower quality graphene. It should be noted that in fig. 5.5(a) the calculation was performed assuming a 0.5% tolerance in gate voltage and the curves should be lowered by ~ 20 dB for 5% tolerance.

Adding Si/SiO_2 bilayers on both sides improves the modulation depth in the transmission mode because of a lower T_{min} in the *off* state. This, however, carries a major drawback as it also leads to an increase in the device's insertion loss as seen in fig. 5.5(b). In the reflection mode, in contrast, adding Si/SiO_2 bilayers only slightly reduces the modulation depth [because of a narrower R_{min}, see fig. 5.3(a)] and also significantly decreases the insertion loss. A 3-Si/SiO_2 bilayer system in the reflection mode overall outperforms all the other examined devices in all the desired figure of merits, even with a 5% tolerance in gate voltage and, most importantly, without any restrictions on graphene quality.

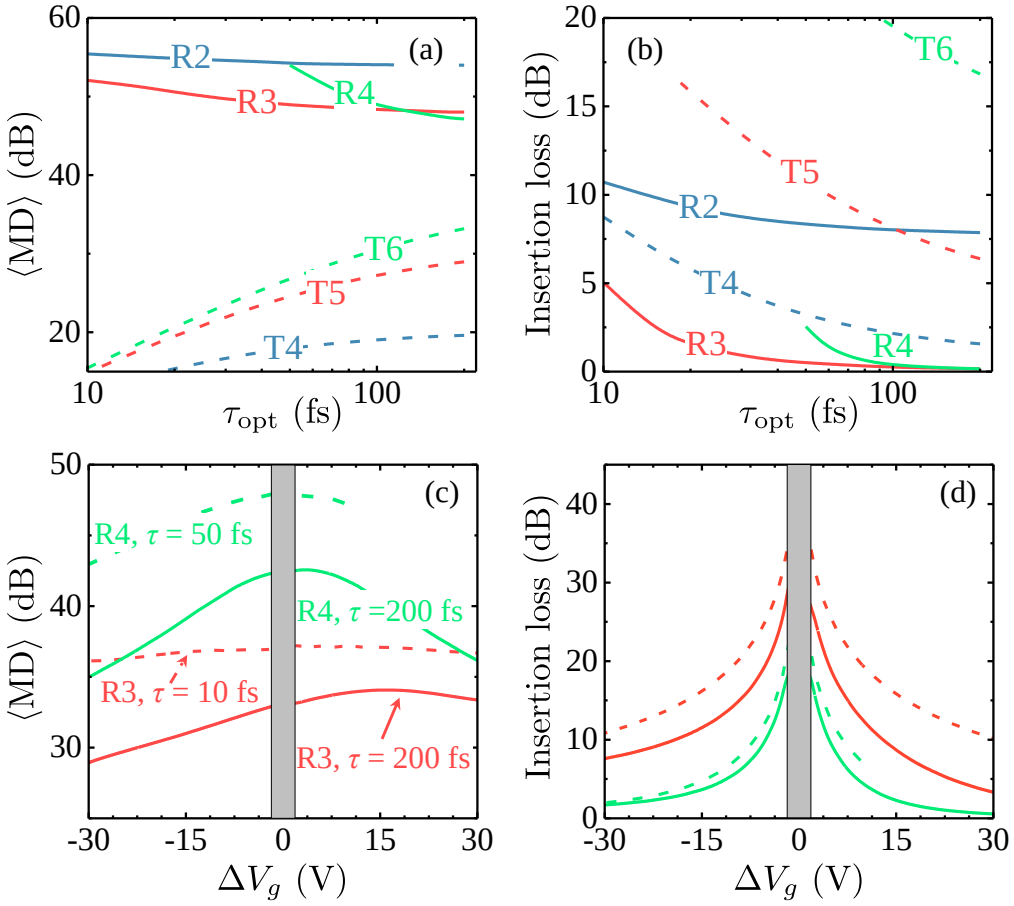

Figure 5.5: (a) ⟨MD⟩ and (b) IL for 3 reflective devices consisting of 2, 3, and 4 Bragg periods on each side (R2, R3, and R4) and 3 transmitting devices consisting of 4, 5, and 6 Bragg periods on each side (T4, T5, and T6). (c) ⟨MD⟩ and (d) IL vs voltage swing $\left(\Delta V_g = V_g - V_g^c\right)$ for the R3 and R4 devices. A swing-dependent tolerance $\mathcal{D}V_g = \Delta V_g/10$ was used for ⟨MD⟩. Vertical gray bars at $\Delta V_g \sim 0$ denote the region where even the calculation becomes impractical due to the excessive IL.

5.5 Modulation frequency

The modulation frequency of the studied device may be limited by the photon lifetime inside the optical cavity and the resistance-capacitance (RC) time constant of the electrostatic gating circuit. The optics limited frequency is given by [229]:

$$f_{\text{opt}} = \frac{c}{2L\, n_{\text{SiO}_2} Q} \tag{5.5}$$

where c/n_{SiO_2} is the speed of light in the dielectric, $2L = 1060$ nm is the roundtrip length of the cavity (the middle 2 SiO_2 layer in our case), and Q the cavity quality factor defined as $Q = \omega_0/\Delta\omega$, where ω_0 is the cavity mode resonant frequency the $\Delta\omega$ the full-width-at-half-maximum (FWHM) of the resonance. For the case of 3 bilayers, we find $Q \sim 325$ and $f_{\text{opt}} \sim 600$ GHz. The electronics-limited operating frequency is however much smaller, defined by [153]:

$$f_{\text{el}} = \frac{1}{2\pi R_{el} C} \tag{5.6}$$

where R_{el} is the system's Ohmic resistance and $C = \epsilon_0 \epsilon_{SiO_2} A/d_{SiO_2}$ its capacitance. For a $A = 50 \times 50 \mu m^2$ square area (covering a typical optical beam size), the capacitance is estimated $C = 0.33$ pF. SLG resistance can be approximated using $R_{SLG} = n_{e,SLG} e \mu_{q,SLG}$, with the carrier density $n_{e,SLG}$ given by eq. 3.8 for a given $E_{F,SLG}$ and the mobility $\mu_{q,SLG}$ by eq. 3.23 for a given $E_{F,SLG}$ $-$ τ_{opt} pair. These yield $R_{SLG} \sim 0.1$ kΩ and $R_{SLG} \sim 1.8$ kΩ for the $\tau_{opt} = 200$ fs and $\tau_{opt} = 10$ fs cases respectively. The *n*-Si contribution is $R_{Si} = (d_{Si} N_{d,Si} e \mu_{Si})^{-1} \sim 4\ \Omega \ll R_{SLG}$. Thus, it is safe to assume $R_{el} \cong R_{SLG}$, which results in $f_{el} \sim 5$ GHz and $f_{el} \sim 0.3$ GHz respectively. Apparently, higher quality graphene and/or smaller device footprint can lead to even higher MF.

Cycling through large potentials (e.g., between 166 V and 265 V) at GHz frequencies is of course impractical. To better reflect a realistic proposal, a variable tolerance $\mathcal{D}V_g = \Delta V_g/10$ is adopted and figs. 5.5(c) and 5.5(d) plot the performance as a function of a voltage swing $\Delta V_g = V_g - V_g^c$, where V_g is the potential used to drive the system away from critical coupling (V_g can be either lower or higher than V_g^c). For the R3 device, both the $\tau_{opt} = 200$ fs and $\tau_{opt} =$ fs cases are shown, while for the R4 device, we show the $\tau_{opt} = 200$ fs and $\tau_{opt} = 50$ fs cases (note that for the latter case, $E_{F,SLG}^{max} = 0.54$ eV limit is reached for $\Delta V_g = 10$ V). Excellent performance is obtained regarding the modulation depth in both cases, even for the smallest voltage swings, but at the expense of high insertion losses. However, at slightly larger voltage swings, the insertion loss becomes small for the R4 device. Overall, high MD (> 30 dB) at low IL (< 1 dB) at GHz MF is possible with voltage swings below 30 V.

5.6 Acousto-optic modulation - refractive index sensing

We have shown that the smallest deviation from critical coupling has a major consequence in the device reflection. This fact can be exploited to design a sensitive acousto-optic modulator. We separate the Au mirror from the rest of the device by a distance x, creating a secondary cavity as seen in the inset of fig. 5.6(a). For every distance x, we tune the graphene Fermi level into its corresponding critical coupling value $E_{F,SLG}^c$ and plot in fig. 5.6(a) the total absorption as a function of mirror separation x and wavelength. A strong anti-crossing behavior is found at around $x \sim 700$ nm due to interference between the SiO_2 cavity and the mirror cavity, making up for an extremely sensitive response. We pick $x_0 = 735$ nm, where perfect absorption is observed for $\lambda =$1550 nm and plot in fig. 5.6(b) $\langle$MD$\rangle$ (assuming $\mathcal{D}V_g = 0.5\%$; gating is fixed in this case and thus easily tuned to high accuracy) as a function of mirror deflection $\delta x = x - x_0$. Strong reflections for increasing δx make up for very high $\langle$MD$\rangle$ values. For example, a tiny $\delta x = 1$ Å results in a massive increase in reflectance $R = 10^3 \langle R_0 \rangle$ corresponding to a sensitivity of ~ 30 dB/Å, with the drawback, however, of small overall reflection and large IL.

By the same token, a small change in the refractive index inside the mirror cavity will also produce a measurable change in reflectance. Since the optical length is nx, $\delta n/n = \delta x/x$ will produce the same $\delta R/R$. Using the numbers of fig. 5.6(b), we estimate an index sensitivity of the order of 10^7 % RIU. It should be noted that these high sensitivities are independent of graphene mobility, as seen in fig. 5.6(b), because the only requirement is to find the appropriate $E_{F,SLG}^c$ to tune into critical coupling.

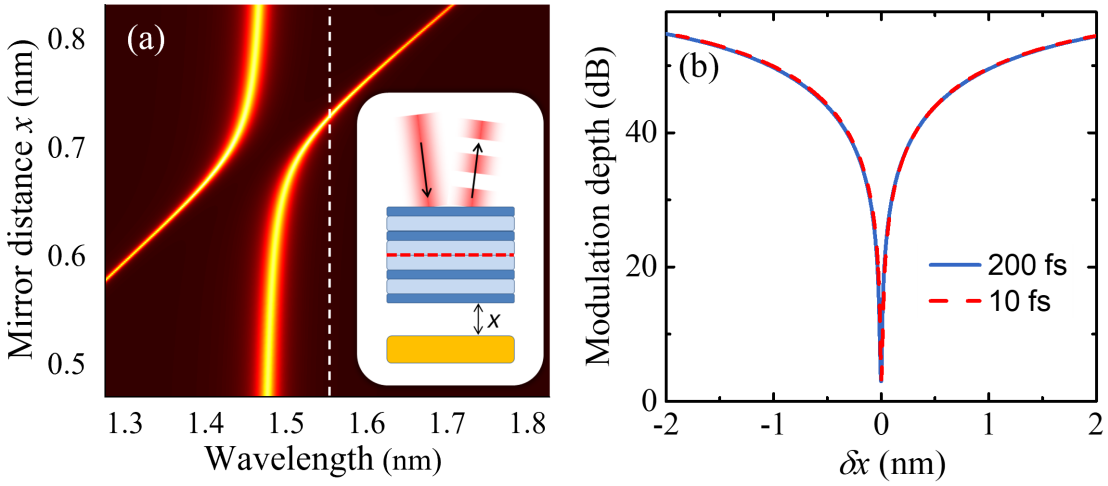

Figure 5.6: (a) Overall absorption vs mirror separation x and wavelength. The inset schematic shows the device configuration. The color scale is from 0 to 1. (b) $\langle \mathrm{MD} \rangle$ as a function of detuning from critical separation x_0.

5.7 Conclusions

In conclusion, it is shown that critical coupling is a versatile tool in achieving deep and fast optical modulation. A graphene-loaded Bragg resonator device operating in the reflection mode can always be tuned into critical coupling irrespective of graphene quality. The key to this is our ability to fine tune the graphene electrostatic doping in order to match the cavity decay and absorption rates, without having to alter the device architecture. This scheme consistently yields a large modulation depth (~ 100 %) at small insertion loss and GHz modulation frequencies even when graphene electron relaxation time falls to 10 fs. This mechanism can in addition be extended to include other operation formats, such as a sensitive acousto-absorption modulator (~ 30 dB/Å) or a sensitive index sensor ($\sim 10^7$ % RIU). All considerations and designs studied here for $\lambda = 1550$ nm can also be extended throughout the IR spectrum by appropriately choosing the materials and scaling their dimensions: device area $A \sim \lambda^2$ and gate oxide thickness $d_{ox} \sim \lambda$, and so, capacitance $C \sim \lambda$; graphene critical doping $E^{\mathrm{c}}_{F,\mathrm{SLG}} \sim \lambda^{-1}$ and thus $n_{e,\mathrm{SLG}} \sim \lambda^{-2}$ and $\mu_{q,\mathrm{SLG}} \sim \lambda$ resulting to $R_{\mathrm{SLG}} \sim \lambda$; *n*-Si thickness $d_{\mathrm{Si}} \sim \lambda$ and resistivity $R_{\mathrm{Si}} \sim \lambda^{-1} N^{-1}_{d,\mathrm{Si}}$ and so, to keep a constant ratio with R_{SLG} one can use $N_{d,\mathrm{Si}} \sim \lambda^{-2}$. Overall, the above yield a scaling law MF$\sim \lambda^{-2}$. MD and IL only depend on achieving critical coupling, and so, they weakly depend on the operating wavelength as long as we avoid IR-absorbing dielectrics (e.g., SiO_2 for $\lambda > 7$ μm due to its optical phonon modes). Au mirror absorption decreases with λ, while free carrier absorption in *n*-Si scales approximately as $d_{\mathrm{Si}} \Im\mathrm{m}\{\epsilon_{\mathrm{Si}}\}/\lambda$, i.e., as $d_{\mathrm{Si}} \omega_p^2 / \omega^3 \lambda \sim N_{d,\mathrm{Si}} \lambda^3$, and by using the $N_{d,\mathrm{Si}} \sim \lambda^{-2}$ noted above, one finds that free carrier absorption in *n*-Si scales as $\sim \lambda$, which as shown earlier will remain small within the IR spectrum. So, all these material absorption variations will not alter anything more than the exact gate voltage needed to achieve critical coupling, showcasing the versatility of this mechanism. Regarding the gate voltage, it shown in this chapter that the swing from the critical value can be small, in the order ~ 30 V, to reliably achieve high MF. Both the absolute value and the variation from the critical voltage can be much lower than the

values extracted here ($V_g^c = 166$ V) if ionic gating [55, 56, 259, 260] is used instead of the popular dielectric/Si configuration. This would reduce power consumption and potentially could lead to even higher MF.

Chapter 6

Thermionic graphene/silicon Schottky infrared photodetectors

Optical communications, imaging, and biomedicine require efficient detection of infrared radiation. Growing demand pushes for the integration of such detectors on chips. It is a challenge for conventional semiconductor devices to meet these specs due to spectral limitations arising from their finite band gap, as well as material incompatibilities. Single layer graphene (SLG) is compatible with complementary metal-oxide-semiconductor (CMOS) Si technology, while its broadband (UV to THz) absorption makes the SLG/Si junction a promising platform for photodetection. Here we model the thermionic operation of SLG/Si Schottky photodetectors, considering SLG's absorption, heat capacity, and carrier cooling dependence on temperature and carrier density. We self-consistently solve coupled rate equations involving electronic and lattice temperatures, and nonequilibrium carrier density under light illumination. We use as an example the infrared photon energy of 0.4 eV, below the threshold for direct photoemission over the Schottky barrier, to study the photo-thermionic response as a function of voltage bias, input power, pulse width, electronic injection, and relaxation rates. We find that device and operation parameters can be optimized to reach responsivities competitive with the state of the art for any light frequency, unlike conventional semiconductor-based devices. Our results prove that the SLG/Si junction is a broadband photodetection platform.

This chapter is based on:

➤ **S. Doukas**, P. Mensz, N. Myoung, A. C. Ferrari, I. Goykhman and E. Lidorikis, *Thermionic graphene/silicon Schottky infrared photodetectors*, Phys. Rev. B 105, 115417 (2022), https://doi.org/10.1103/PhysRevB.105.115417

6.1 Introduction

Light detection in the MWIR spectral regime is key to a number of applications, as discussed in chapter 2. Current SOTA semiconductor technology, however, does not include a platform being all together high performance, broadband and CMOS compatible (see section 2.1.3). A simple, yet promising, broadband CMOS-compatible approach is the SLG/Si Schottky junction [44, 125, 126, 168]. SLG/semiconductor (SLG/SC) Schottky diodes [25, 43, 44, 168, 372, 375, 382, 424, 425] with rectifying electrical characteristics have been explored for PDs using free-space [65, 70, 71, 153, 169–176, 178–182, 426] and guided-mode configurations [74, 123, 125, 427].

A SLG/SC Schottky PD has three modes of operation for photocurrent generation:

- *photovoltaic* (PV) [169–176, 178, 426], where photons with energy $\hbar\omega > E_{g,\mathrm{Si}}$ (SC bandgap) are absorbed by the SC creating electron-hole (e-h) pairs, which then split under the internal field in the depletion region.

- *internal photoemission* (IPE) [153, 179–182], in which sub-bandgap $\hbar\omega < E_{g,\mathrm{Si}}$ photons are absorbed in SLG to yield photoexcited carriers with sufficient energy to overcome the Schottky barrier at the SLG/SC interface and emit into the SC.

- *photo-thermionic* (PTh) [65, 70, 71, 381, 428], where low-energy photons (below both SC bandgap and Schottky barrier) absorbed in SLG yield photoexcited carriers, without sufficient energy to overcome the Schottky barrier directly. Instead, they multiply [183, 329, 429] and thermalize due to e-e scattering [183, 184, 430–432] resulting in an increased SLG electronic temperature, $T_{e,\mathrm{SLG}}$ [64, 183, 184, 323, 324]. These thermalized hot carriers in SLG are long-lived due to their slow cooling ($\sim$ few ps) through phonon modes [64, 65, 184, 261, 323, 327, 352, 433, 434] raising the prospects for achieving high enough $T_{e,\mathrm{SLG}}$ to gain thermal energy for thermionic emission [64, 65, 71] (photocurrent) over the Schottky barrier.

In contrast to the first two regimes (PV, IPE) where the spectral response of SLG/SC Schottky PDs is limited by $E_{g,\mathrm{Si}}$ and Schottky barrier height (SBH, Φ_B) [153, 169–176, 178–182, 426], PTh enables low energy ($\hbar\omega < 2\Phi_B$) multispectral photodetection [65, 71, 381] owning to SLG broadband absorption [42, 57]. The lower density of states in SLG [53] compared to bulk metals, leads to SLG Fermi level ($E_{F,\mathrm{SLG}}$) shifts upon doping [270], enabling the control of the SBH beyond the "classical" Schottky effect [20, 371] of barrier lowering [20, 168], by application of an external electric field via gating [435] and/or a reverse voltage bias [369, 373, 436]. This electrical tuning of SBH provides an extra degree of freedom for optimizing the PTh response in SLG/SC PDs, and also allows to reach $\sim 100\,\%$ optical absorption in SLG when the device is integrated into an optical cavity [410, 421, 437, 438], by adjusting SLG's absorption (i.e. optical loss) towards the critical coupling [410, 411, 421] condition (loss rate equal to cavity decay rate, as discussed in the previous chapter and appendix A). Thus, SLG/SC Schottky PDs are a promising material platform for photodetection across multiple MWIR spectral bands.

Ref. [65] reported SLG/SC Schottky PDs in the PTh regime. In SLG/WSe_2/SLG Schottky PDs (with WSe_2 thicknesses from $\sim$ 2 to 40nm), the transition between PV and PTh was demonstrated, with a strong reduction in generated photocurrent, as well as a superlinear dependence on input power, the latter being a manifestation of thermal activation of carriers over the SBH. While it is common that the photocurrent is strongly reduced in

the PTh regime (compared to IPE or PV) [65,171,178,439], it is not clear if this reduction is due to fundamental PTh limitations, or to improper device architecture and operation conditions. A theoretical understanding of photocurrent in the SLG/SC Schottky PTh domain is thus needed if one is to explore and optimize the PD operation parameters and performance.

Here, a self-consistent framework is developed to investigate the performance metrics, such as responsivity and detectivity, of SLG/Si Schottky PDs under IR illumination in the PTh regime and optimize them by exploring different device architectures (cavity integration) and operation parameters (reverse bias, input power, carrier injection time, etc). PDs where SLG is integrated inside a dielectric Bragg cavity are considered and it is shown that, by tuning the cavity to the critical coupling condition, almost total light absorption in SLG can be achieved, even for SLG nanoribbons of reduced surface coverage. This corresponds to SLG absorption density > 100 %, i.e., absorption cross-section larger than the geometrical cross-section, resulting in a higher $T_{e,\mathrm{SLG}}$ compared to that for full SLG coverage at 100 % absorption.

The coupled rate equations of $T_{e,\mathrm{SLG}}$ (eq. 3.48), lattice temperature $T_{l,\mathrm{SLG}}$ (eq. 3.49), and non-equilibrium carrier density $\delta_{n,\mathrm{SLG}}$ (eq. 3.51) are self-consistently solved, to obtain, using the Landauer formalism, the PD PTh response (eq. 3.65) as a function of input optical power, optical pulse duration, applied bias and charge injection/relaxation rates, taking into account the phonon-mediated (eq. 3.42), disorder-assisted (eq. 3.44) and thermionic-injection (eq. 3.66) cooling processes. Realistic considerations are implemented about all device aspects, such as mobility, input power density, reverse bias and doping. It is shown that, under appropriate combinations of the above, the PD external responsivity and specific detectivity can in principle reach $\sim$ 1A/W and $\sim$ 10^7 cm $\mathrm{Hz}^{0.5}$ W^{-1}, comparable with graphene-based state-of-the-art performances reported in MWIR [43, 44]. When combined with the SLG broadband absorption and fast electron dynamics, our results imply similarly sensitive and fast photodetection in other spectral bands, e.g., LWIR (8 - 15 μm) and FIR ($>$ 15 μm). The methods and conclusions derived in this study are applicable to any PTh SLG/SC Schottky PD configuration, providing a comprehensive framework for the SLG/SC Schottky junction as a photodetection platform throughout the IR. Our approach can be implemented in commercial simulators to create key software modules for designing graphene-based free-space photonic devices and integrated circuits.

6.2 Background and implementation

6.2.1 Graphene-Silicon Schottky junction

The methods described in section 3.5 are used to model the SLG/Si Schottky junction. Graphene is assumed in contact with a *n*-doped Si substrate, the latter having a dopant concentration $N_{d,\mathrm{Si}} = 10^{16}$ cm^{-3}, unless stated otherwise. SLG and Si workfunctions and electron affinities are assumed as for section 3.5 (see fig. 3.17). Si electronic temperature is set at $T_{e,\mathrm{Si}} = 300$ K throughout this chapter, given the large heat capacity of the latter compared to graphene [20]. Equations 3.56 - 3.61 are used to determine graphene's Fermi level and chemical potential, built-in voltage in Si depletion region and Schottky barrier height (SBH) at zero (Φ_{B0}) or reverse bias (Φ_B), after SLG/Si contact, using the self-consistent algorithm depicted in fig. 3.19. Figure 6.1(a) plots the calculated SLG chemical potential at RT after junction formation, assuming different values for graphene

Fermi level prior to the contact ($E'_{F,\mathrm{SLG}}$), as a function of the applied reverse bias V_R. For the configuration studied in this chapter, reverse bias breakdown is expected at $\sim$ 51 V, according to eq. 3.63, so V_R values up to 25 V are assumed to be safely applied. The calculated SBH values are plotted in fig. 6.1(b), as a function of reverse bias, for the same initial Fermi level values considered in fig. 6.1(a). These results are well within SBH values reported in the literature [168, 439]. The developed algorithm can inherently handle $E_{F,\mathrm{SLG}}$ transitioning from *p* to *n* doping upon reverse bias application. This algorithm (fig. 3.19) is used throughout this chapter to extract $E_{F,\mathrm{SLG}}$, μ_{SLG} and SBH during illumination and photodetection operation of the studied devices. Finally, it should be noted that even

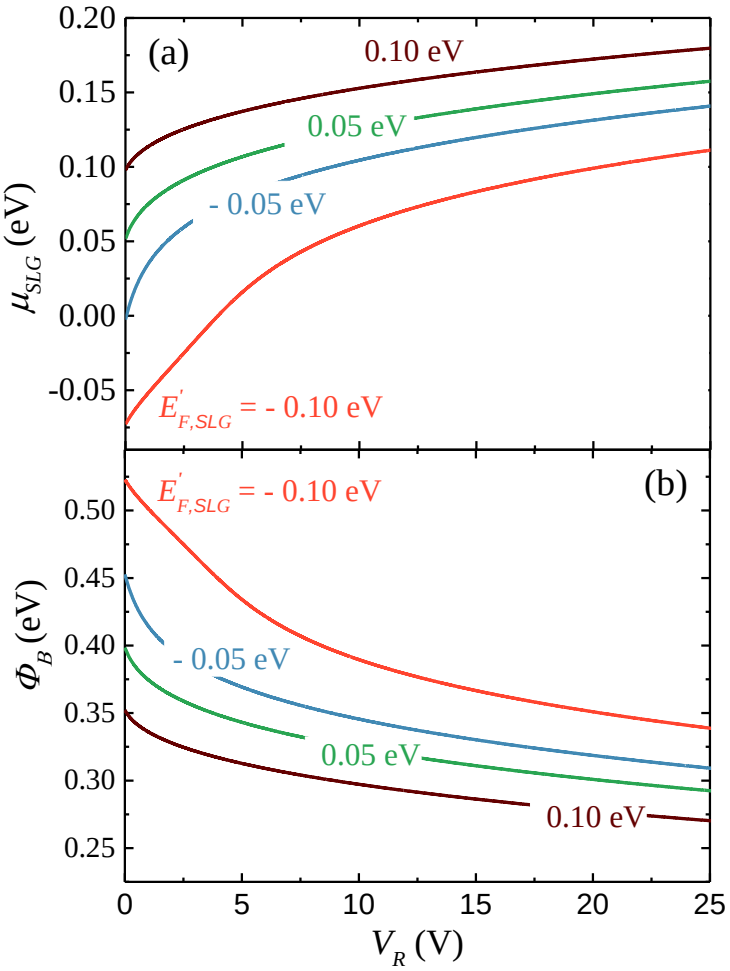

Figure 6.1: (a) Chemical potential μ_{SLG} and (b) Schottky barrier Φ_B as a function of reverse bias V_R and initial (i.e., before contact) SLG Fermi level $E'_{F,\mathrm{SLG}}$.

though the results of fig. 6.1 are acquired in thermodynamic equilibrium, in the rest of the chapter temperature induced and photoexcited carriers' contributions are taken into account in the self-consistent solution depicted in fig. 3.19 to extract SBH. This is done by replacing μ_{SLG} in eqs. 3.56 - 3.61 with $\mu_{c,\mathrm{SLG}}\left(E_{F,\mathrm{SLG}}; T_{e,\mathrm{SLG}}, \delta_{n,\mathrm{SLG}}\right)$, since here we consider SLG contacted with *n*-doped Si (e.g. $\mu_{v,\mathrm{SLG}}$ should instead be used if *p*-doped Si was assumed).

6.2.2 Carrier dynamics upon illumination in SLG/Si Schottky junctions

We assume photon energies in the thermionic regime $\hbar\omega/2 < \Phi_B^{\text{CNP}}$, where $\Phi_B^{\text{CNP}} = \chi_{\text{SLG}} - \chi_{\text{Si}} = 0.45$ eV is the SBH with reference to the charge neutrality point (CNP), but with allowed interband transitions in SLG, i.e. $\hbar\omega/2 > E_{F,\text{SLG}}$. These cases involve photon energies below the Si bandgap ($\hbar\omega < 1.1$ eV [20]), so that absorption occurs only in SLG. Figure 6.2 presents the calculated charge density distributions (eq. 3.13) for SLG following IR absorption at $\hbar\omega = 0.4$ eV. To demonstrate this concept, we assume, without loss of generality, $E_{F,\text{SLG}} = 0.15$ eV (a wider range of $E_{F,\text{SLG}}$ will be discussed later). The interband transitions create hot e-h at energies $\pm\hbar\omega/2$ with respect to the CNP [fig. 6.2(c)]. Since $\hbar\omega/2 < \Phi_B^{\text{CNP}}$, these non-equilibrium carriers do not have enough energy to overcome the Schottky barrier. Thus, within a time scale τ_{e-e} they relax, due to e-e collisions [65, 183, 184, 261, 323], into an equilibrium *e* bath at some elevated $T_{e,\text{SLG}}$ (fig. 6.2(d), assuming $T_{e,\text{SLG}} = 900$ K at equilibrium, consistent with values found in our simulations). As a result, the tail of the Fermi-Dirac distribution extending above the SBH gets enlarged, enabling thermionic emission. In pulsed optical operation, the *e* bath eventually cools down to RT by electron-phonon (e-ph) scattering within a picosecond (ps) time-scale τ_{e-ph} [183, 184, 352, 433, 434] [fig. 6.2(c)].

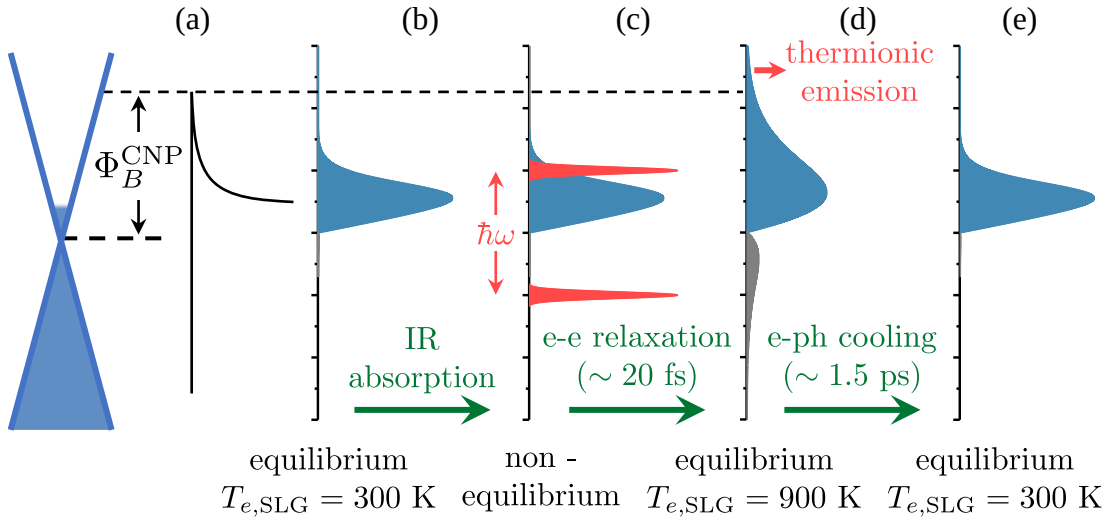

Figure 6.2: (a) Schematic of energy levels in SLG/Si Schottky junctions. (b) SLG carrier distribution assuming $\hbar\omega = 0.4$ eV, $E_{F,\text{SLG}} = 0.15$ eV at $T_{e,\text{SLG}} = 300$ K, (c) just after pulse absorption, with red peaks denoting nonequilibrium carriers, (d) after photoexcited carriers relax into a hot Fermi-Dirac distribution at $T_{e,\text{SLG}} = 900$ K, (e) after cooling back to RT.

To describe $T_{e,\text{SLG}}$ dynamics, a two-temperature model is used, as described in section 3.4.4. Temporal evolution of $T_{e,\text{SLG}}$ is acquired using eq. 3.48, with the addition of J_{th} (eq. 3.66) in its right-hand side, accounting for the thermionic thermal current in SLG/Si Schottky junctions studied here. The SLG lattice temperature is given by eq. 3.49, while $\Gamma_{\text{SLG-Si}} \sim 20$ MW m^{-2} K^{-1} is assumed for the transfer rare of thermal current from SLG to Si, the latter considered to have a constant RT. Finally, non-equilibrium photoexcited carriers are taken into account via eq. 3.51, assuming a e-e relaxation time $\tau_{e-e} = 20$

fs [183, 184]. The three coupled rate equations 3.48, 3.49 and 3.51 are time integrated using the 4^{th} order Runge-Kutta (4RK) method (section 4.3), self-consistently including all the relevant temperature dependent parameters to yield SLG carrier dynamics upon pulsed illumination:

- Light absorption in SLG $\alpha_{\text{SLG}} \equiv \alpha_{\text{SLG}}\left(\mu_{c,\text{SLG}}, \mu_{v,\text{SLG}}, T_{e,\text{SLG}}\right)$ is calculated using the Transfer Matrix Method (TMM, section 4.1). For this purpose, graphene's optical conductivity is calculated using eq. 3.19, to acquire graphene's dielectric function (eq. 3.27) and subsequently graphene's complex refractive index (eq. 3.28), which is then used as input in TMM. For $\sigma_{\text{SLG}}^{\text{opt}}$ calculation, one needs to determine a value for the free carrier relaxation time τ_{opt}. For 0.4 eV photon energy the SLG absorption is dominated by interband transitions because $2\left|E_{F,\text{SLG}}\right| < \hbar\omega$. For these, τ_{opt} contribution is small (since it mainly affects intraband absorption as discussed in section 3.2.1). For the $E_{F,\text{SLG}}$ values considered here, we estimate that the change in α_{SLG} when varying τ_{opt} between 100 and 300 fs is $< 1\%$ at RT. Elevated temperatures will result in μ_{SLG} lowering, driving graphene deeper within the interband dominated regime, where the τ_{opt} contribution is even smaller. Thus, for simplicity, we set a constant value of $\tau_{\text{opt}} = 200$ fs.

- Carrier cooling due to scattering with graphene's optical phonons (J_{op}) is calculated as discussed in section 3.4.3 using eq. 3.42, accounting for both optical phonon branches, the one corresponding to the K point of the Brillouin zone and the doubly-degenerate phonon branch corresponding to the Γ point of graphene's Brillouin zone.

- Disorder-assisted supercollision cooling (J_{sc}) is calculated as discussed in section 3.4.3 using eq. 3.44. For the latter, we assume a mean free path for short-range scatterers $l = 200$ nm, unless stated otherwise. This brings J_{sc} roughly at the same level of J_{op} for the $E_{F,\text{SLG}}$ values examined in this chapter. Since it is an open debate whether e-ph scattering is dominated by J_{sc} or J_{op} [333], a wide range of mean free path l values will be examined later in this chapter.

- Thermionic thermal current across the Schottky junction (J_{th}) is calculated using eq. 3.66, as discussed in section 3.5.2. J_{th} is added in the right hand side of eq. 3.48. However, since it transfers thermal energy to the Si substrate and not in graphene's lattice, it is not included in the left hand side of eq. 3.49, which accounts for graphene lattice's heating. As we will see in the rest of this chapter, J_{th} strongly depends on carrier injection time τ_{inj} (section 3.5.3) and, depending on the latter's value, it can dominate carrier cooling [64, 71], surpassing both J_{op} and J_{sc} contributions.

- Temperature dependent electronic heat capacity ($c_{e,\text{SLG}}$) is calculated using eq. 3.16.

- SLG lattice heat capacity $c_{l,\text{SLG}}$ is calculated using eq. 3.50.

- Finally, non-equilibrium photoexcited carrier density $\delta_{n,\text{SLG}}$ is calculated as described in section 3.4.4 using eq. 3.51.

Putting all of the above together and solving the 3 coupled rate equations using 4RK method, we can get the temporal evolution of graphene's carrier dynamics.

Moreover, if the pulse duration is longer than all the timescales involved (i.e., τ_{e-e}, τ_{e-ph} and τ_{inj}), a quasi-cw solution is possible. This can be done using eq. 3.53 - 3.55 (with

the addition of J_{th} in the right hand side of eq. 3.53 to account for thermionic thermal current, as discussed above). However, since both hand sides of these equations depend on each other (e.g., in eq. 3.53 α_{SLG}, J_{eph} as well as J_{th} depend on $T_{e,\text{SLG}}$, while $T_{e,\text{SLG}}$ depends itself from J_{eph}, J_{th} and α_{SLG}) a self-consistent treatment is needed (fig. 3.16) for the quasi-cw approach. In what follows, we will see under which circumstances the quasi-cw solution is valid, yielding the same results with the full 4RK temporal solution.

6.2.3 Critical coupling, geometrical focusing and giant graphene absorption density

The interband absorption in suspended SLG is 2.3% [42] and it decreases to 0.46% when SLG is transferred on Si due to the Fresnel reflections at the air-substrate interface [285]. This is a severe limitation for any SLG PD. An improvement is needed so to enforce the optical power to be fully absorbed in SLG. Integrating a SLG/Si thermionic PD in an optical cavity can result in $\sim 100\,\%$ absorption of incident light by SLG [410,411,421,437, 438]. To achieve this, the same strategy as in chapter 5 is followed, integrating the studied PD in one-port asymmetric Bragg cavities, exploiting the critical coupling mechanism (Appendix A). For a fixed cavity geometry with predefined (fixed) decay rate γ_d, critical coupling can be achieved by tuning $E_{F,\text{SLG}}$ (thus SLG absorption and, consequently, the total absorption rate γ_a) using reverse bias across the junction.

We assume an asymmetric Bragg cavity as depicted in the inset of fig. 6.3(a), consisting of $N = 2$ periods of Si/SiO_2 layers on either side, with an Au mirror on the back. SLG is sandwiched between a SiO_2 and a *n*–doped Si layer of double thickness compared to the Bragg layers. The Bragg layer thicknesses are $d_{\text{Si}} = 226.6$ nm and $d_{\text{SiO}_2} = 530.7$ nm following the quarter-wave rule for the target $\hbar\omega = 0.4$ eV, using the refractive indices $n_{\text{Si}} = 3.42$ [20] and $n_{\text{SiO}_2} = 1.46$ [20]. The Au back mirror has a thickness $d_{\text{Au}} = 100$ nm and complex refractive index $n_{\text{Au}} = 1.73 + 19.2i$ at $\hbar\omega = 0.4$ eV [423]. Only the Si layer beneath SLG is doped, while the other Si layers are assumed to be intrinsic. The doped Si layer contribution to the optical absorption is also considered using a Drude model (eq. 5.2) for its dielectric function [417,418]. SLG is assumed to be covering an area equal to the diffraction limit ($S_0 = \lambda^2/\pi \sim 10^{-7}$ cm^2).

We get the SLG optical absorption under normal incidence by employing the Fresnel relations using TMM (section 4.1), with SLG permittivity given by eq. 3.27. Figure 6.3(a) plots the total absorption spectrum, as calculated using the TMM (red curve), assuming $E_{F,\text{SLG}} = 0.15$ eV, $T_{e,\text{SLG}} = 300$ K and SLG effective thickness $d_{\text{SLG}} = 0.335$ nm.

Further validation of these calculations is established using the FDTD method (section 4.2) to get the total absorption of the exact same layout (blue curve in fig. 6.3(a)). FDTD simulations were performed using the commercial FDTD solver Lumerical [399]. A 2D computational cell was used, assuming semi-infinite extension (i.e., much larger than the considered wavelengths and all the rest geometrical features) across the $y-$axis (transverse direction), periodic boundary conditions along the $x-$axis and PML absorbing boundary conditions along the $z-$axis. SLG is inserted in the FDTD simulations as a surface boundary (see section 4.2.5), with its surface conductivity acquired from eq. 3.19. The mesh-grid size of the computational cell is set to 1 nm (in both x and z axis) and the whole structure is illuminated by a plane wave under normal incidence. The calculations yield almost perfect agreement between TMM and FDTD (fig. 6.3(a)), with a difference $< 0.1\%$ regarding the resonant wavelength, possibly arising from the fact that SLG is inserted in TMM with a finite thickness while in FDTD as an infinitesimally thin surface

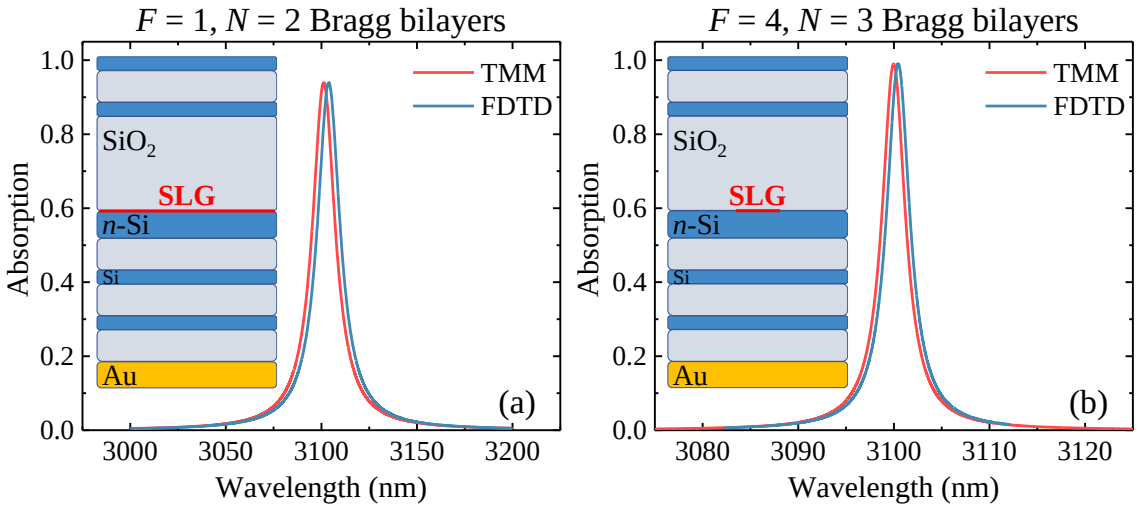

Figure 6.3: Absorption spectra of the SLG/Si PD integrated in asymmetric Bragg cavities, consisting of (a) 2 and (b) Bragg bilayers. TMM (red) and FDTD (blue) simulations are shown in each graph for the corresponding configuration assuming $E_{F,\mathrm{SLG}} = 0.15$ eV. The inset schematic depicts the layout studied in each case. (a) For $N = 2$ Si/SiO_2 Bragg bilayers an inverse surface coverage ratio $F = 1$ is assumed. (b) For $N = 3$ Si/SiO_2 Bragg bilayers $F = 4$ is used.

boundary. In both cases, total absorption reaches $\sim 100\%$, with almost all of it occurring in graphene. The designed Bragg cavity lead to almost total light absorption in graphene for all the $E_{F,\mathrm{SLG}}$ values ($|E_{F,\mathrm{SLG}}| \lesssim 0.15$ eV) considered here.

Figure 6.4(a) plots light absorption in SLG and each constituent as a function of $E_{F,\mathrm{SLG}}$ for $\hbar\omega = 0.4$ eV, calculated using TMM. Exploiting the asymmetric Bragg configuration, $> 90\%$ light absorption in graphene is achieved for all the $E_{F,\mathrm{SLG}}$ values considered in this study. This allows for almost perfect absorption even in nanostructured (e.g., nanoribbons of subwavelength width) SLG partially covering the PD illuminated area.

Perfect absorption in a partially covered SLG area means that the absorption per unit SLG area is inversely proportional to its coverage fraction. This can be quantified by defining the SLG inverse surface coverage ratio:

$$F = \frac{S_0}{S} \tag{6.1}$$

as the ratio of the diffraction limited area $S_0 = \lambda^2/\pi \sim 10^{-7}$ cm^2 over the SLG geometrical cross-section S (within S_0). In this configuration, the absorption density, defined as the ratio of absorption cross-section to SLG geometrical cross-section, can be up to $\sim 100\,\% \times F$. This is equivalent to light focusing within a spot below the diffraction limit. We term this mechanism *geometrical focusing*. The increased absorption density will lead to increased $T_{e,\mathrm{SLG}}$, thus increased thermionic emission across the Schottky junction. By patterning SLG into ribbons, the absorption rate γ_a of the cavity is reduced. A straightforward way to reduce the decay rate of the cavity γ_d and reestablish critical coupling conditions is adding more Bragg layers. Adding a third Bragg period (inset schematic of fig. 6.3(b)) will also lead to sharper resonance, e.g., a quality factor $Q \sim 235$ is extracted for 2 Bragg periods and $Q \sim 1050$ for 3 Bragg periods. The ~ 4.5 increase in Q means an equal decrease in cavity decay rate γ_d. Consequently, to restore critical coupling conditions graphene's absorptivity must be reduced by the same amount. Indeed,

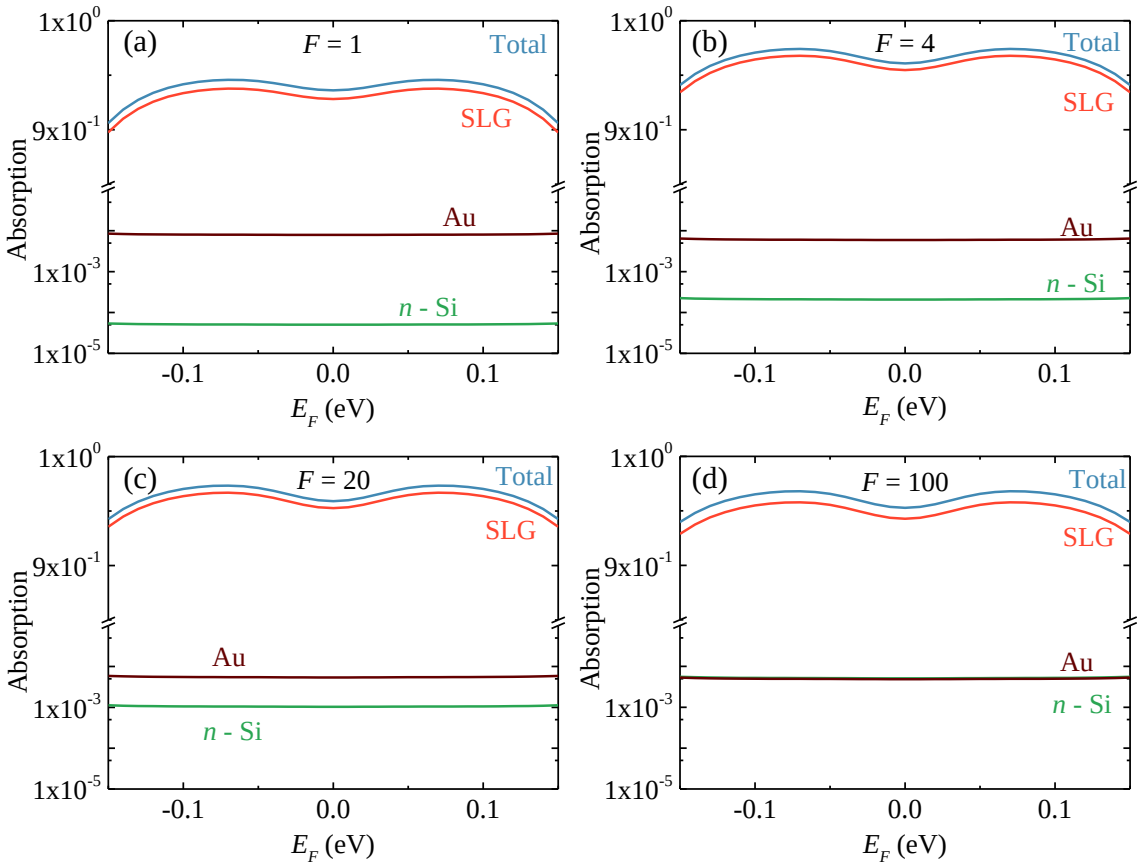

Figure 6.4: Absorption of SLG and each constituent as a function of $E_{F,\mathrm{SLG}}$ for $\hbar\omega$= 0.4 eV at RT calculated using TMM for (a) $F = 1$ and (b) $F = 4$ (c) $F = 20$ and (d) $F = 100$ inverse surface coverage ratios.

FDTD simulations with SLG covering 25 % of the computational cell (i.e., $F = 4$, inset schematic of fig. 6.3(b)) reveal that critical coupling is restored in the configuration with $N = 3$ Bragg bilayers [blue curve in fig. 6.3(b)].

However, FDTD has inherent difficulties in simulating high Q configurations, as discussed in section 4.2, requiring long computational times. For example, a TMM calculation (for the whole spectrum) regarding the configuration of fig. 6.3(a) is concluded within $\sim$ 1 sec while the same calculation using FDTD requires $\sim$ 1 minute. Simulating the higher Q cavity of fig. 6.3(b) leads to an $\sim$ 1 hour simulation, using FDTD in a personal computer, since longer time is needed for energy dissipation inside the computational cell. On the other hand, TMM (at least its implementation in the context of this thesis, as described in section 4.1), is essentially a 1D method, unable to account for the reduced SLG $x-$dimension and the increased F. Nevertheless, we can effectively simulate the reduced surface coverage of SLG that we need to study here, by reducing its effective thickness d_{SLG} inserted in the TMM algorithm. In this context, a reduced surface coverage by a factor of F and the subsequent reduction in SLG absorption is simulated reducing d_{SLG} by the same amount. Indeed, following this strategy, fig. 6.3(b) plots the calculated total absorption for $N = 3$ Bragg bilayers using the TMM (red curve), yielding almost identical results with the FDTD method (blue curve), in which graphene covers a 25% of the $x-$dimension. The implementation using TMM instead of FDTD is crucial, since the PD optical response needs to be calculated several times during time-integration

using 4RK or during the self-consistent iterations using the quasi-cw algorithm described in fig. 3.16. This would be impractical with FDTD, even for $F = 1$.

Having established an efficient way to extract the PD optical response at reduced surface coverage, we can keep adding Bragg bilayers to further increase the absorption density. For $F = 4$, 20, 100 we use 3, 4, and 5 Bragg bilayers respectively. Absorption in SLG in these cases can be up to $\sim 95\%$ 6.4 while absorption density is enhanced by a factor of F. In what follows we will see how this effects the PD performance.

6.2.4 Photocurrent across the junction and carrier injection time

For the configuration studied in this chapter, with Si dopant concentration $N_{d,\mathrm{Si}} \leq 10^{17}$ cm^{-3} and $T_{e,\mathrm{SLG}} \geq 300$ K, the photo-thermionic emission (PTh) is the dominant photocurrent generation mechanism, as discussed in section 3.5.2. Having determine $T_{e,\mathrm{SLG}}$, μ_{SLG} and SBH, the electronic and thermal thermionic currents across the Schottky junction are calculated using eqs. 3.65 and 3.66 respectively, employing the Landauer formalism. Both J_{el} and J_{th} strongly depend on τ_{inj} value, which is a phenomenological parameter characterizing the rate at which charge carriers are injected from SLG into Si, across the SLG/Si interface (section 3.5.3). In the rest of this chapter we assume τ_{inj} values between the two extremes reported up to date (0.13 ps $\lesssim \tau_{\mathrm{inj}} \lesssim$ 30 ps) [372, 380, 383], and study its effect on PD performance. An exception to this convention is made in fig. 6.8, where we consider τ_{inj} down to the fs regime to study its effect on PD operation and account for possible future experimental improvements.

6.3 Results and discussion

In the rest of this chapter we implement the model described above and evaluate the PD performance in respect to all the different operation parameters, using the metrics defined in section 2.1.1.

6.3.1 Temporal evolution of carriers upon illumination of a simple SLG/Si junction

We first consider the elementary case of SLG on a *n*-Si substrate (i.e., no Bragg cavities involved) illuminated by a 1.5 ps pulse at $\lambda = 3.1\,\mu$m ($\hbar\omega = 0.4$ eV) at peak power $P_{in} = 10^8$ W/cm^2 (fluence $\sim 150\,\mu$J/cm^2, enough to create observable thermal effects). Equations 3.48- 3.51 are time-integrated using 4RK as described above. We assume: $\tau_{e-e} = 20$ fs, $\tau_{\mathrm{opt}} = 200$ fs, $\tau_{\mathrm{inj}} = 30$ ps, $l = 200$ nm resulting in supercollision disorder parameter $k_{F,\mathrm{SLG}}\, l \sim 50$, and $E'_{F,\mathrm{SLG}} = 0.15$ eV before contact, giving rise to $\Phi_{B0} = 0.30$ eV at zero voltage bias, a value commonly found in SLG/Si heterojunctions [168, 439]. Figure 6.5 plots all the dynamics within and after the pulse duration. In fig. 6.5(a), $T_{e,\mathrm{SLG}}$ reaches ~ 1200 K and decays slowly back to RT within a ps timescale, as dictated by e-phonon scattering. It should be noted that graphene's lattice temperature rise is much lower, in the order of ~ 10 K, given the $\sim$ three orders of magnitude larger $c_{l,\mathrm{SLG}}$ compared to $c_{e,\mathrm{SLG}}$ (section 3.4.4). In fig. 6.5(b) the fractional changes of SLG absorption, thermal capacity and chemical potential are shown, with baseline values $\alpha_{\mathrm{SLG}} = 0.0041$, $c_{e,\mathrm{SLG}} = 2.34 \times 10^{-11}$ J cm^{-2} K^{-1}, $\mu_{\mathrm{SLG}} = 0.15$ eV.

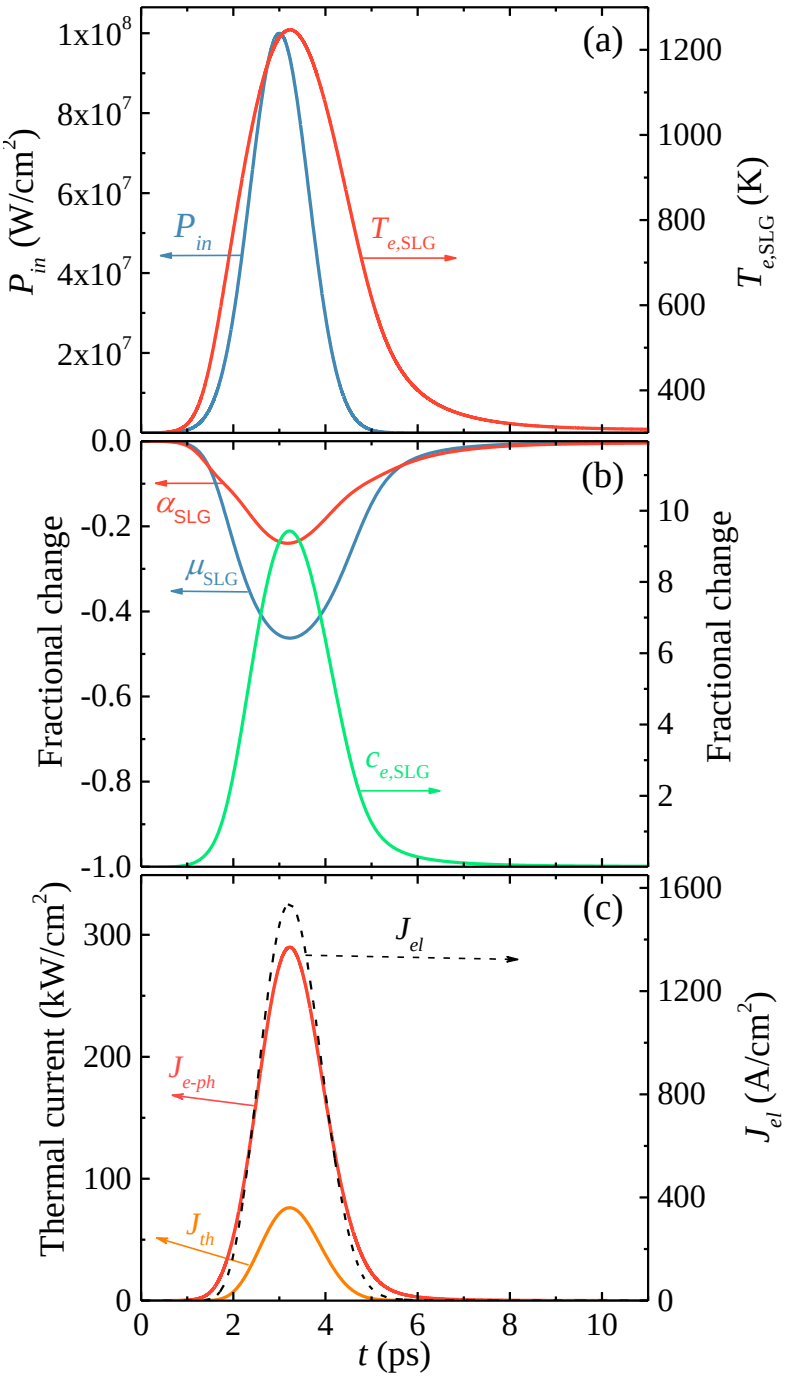

Figure 6.5: Temporal response of an unbiased SLG/Si Schottky PD illuminated by a 1.5 ps pulse with $\lambda = 3.1$ µm at peak power 10^8 W/cm^2. $E'_{F,\mathrm{SLG}} = 0.15$ eV, $k_{F,\mathrm{SLG}}l \sim 50$, $\tau_{e-e} = 20$ fs, $\tau_{\mathrm{opt}} = 200$ fs, $\tau_{\mathrm{inj}} = 30$ ps. (a) incident power and $T_{e,\mathrm{SLG}}$, (b) fractional change of chemical potential, absorption, and thermal capacitance, (c) thermal (left axis) and electronic (right) current densities.

A critical parameter is $c_{e,\mathrm{SLG}}$, whose sharp increase with temperature (about one order of magnitude at $T_{e,\mathrm{SLG}} \sim 1200$ K) limits the achievable $T_{e,\mathrm{SLG}}$. By comparison, the SLG absorption reduction $\sim 20\%$ at peak $T_{e,\mathrm{SLG}} \sim 1200$ K is less severe. Figure 6.5(c) also shows the thermal (J_{e-ph}, J_{th}, left axis) and electrical (J_{el}, right axis) currents created. In fig. 6.5, cooling is dominated by J_{e-ph} while J_{th} is negligible. This is due to the

imbalance between cooling and injection times: $\tau_{e-ph} \sim 1$ ps and τ_{inj} =30 ps, which leads to ineffective hot carrier injection across the Schottky barrier and $J_{e-ph} \gg J_{th}$. Later in this chapter, different carrier injection times (1 fs $\leq \tau_{\text{inj}} \leq$30 ps) and the cross-over between the two cooling regimes (i.e. J_{e-ph} vs J_{th}) will be explored.

6.3.2 Quasi-CW approximation limit

Having determine J_{el} across the junction, the external responsivity R_{ext} (eq. 2.4) can be calculated as discussed in section 2.1.1. Note that up to now, we assume no reverse bias applied in the PD, thus the dark current density is $J_d = 0$. To test the effect of pulse duration on PD peak responsivity (R_{peak}), defined as the peak R_{ext} during the pulse duration, and to define a quasi-cw approximation limit, fig. 6.6 plots the normalized responsivity R_{peak}/R_{CW} (where R_{CW} is the external responsivity under the quasi-cw approximation) at fixed power $P_{in} = 10^7$ W/cm^2 as a function of pulse duration for different τ_{inj}. The other simulation parameters are as in fig. 6.5. For $\tau_{\text{inj}} > 1$ ps, the cooling is dominated by e-ph scattering, and the quasi-cw approximation is valid only for pulse duration $>$ 10 ps. On the other hand, the sub-ps pulses cannot be described by a quasi-cw approximation for any τ_{inj}. In the rest of this chapter long ($>$ 10 ps) pulses/CW-illumination is assumed and PD response is acquired using the self-consistent algorithm of fig. 3.16.

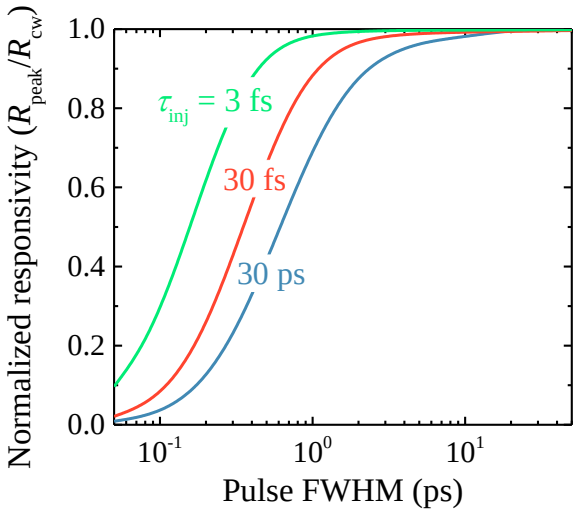

Figure 6.6: $R_{\text{peak}}/R_{\text{CW}}$ at $P_{in} = 10^7$ W/cm^2 as a function of pule duration and τ_{inj}.

6.3.3 Bragg cavity integration and geometrical focusing

We next consider a SLG/*n*-Si Schottky PD integrated into an asymmetric Bragg cavity at critical coupling (fig. 6.3 inset schematics) to allow $\sim$ 100 % SLG optical absorption as discussed in section 6.2.3. We first consider the PD area equal to the diffraction limit $S_0 = \lambda^2/\pi \sim 10^{-7}$ cm^2 fully covered by SLG (i.e., $F = 1$).

Figure 6.7 plots the calculated R_{ext} as a function of P_{in} for quasi–cw illumination ($\tau_{e-e} = 20$ fs, $\tau_{\text{opt}} = 200$ fs, $\tau_{\text{inj}} = 30$ ps, $\Phi_{B0} = 0.3$ eV, $k_{F,\text{SLG}}\, l \sim 50$). At low input powers ($P_{in} < 10^2$ W/cm^2 down to the noise equivalent power level [eq. 2.5]), J_{el} is linear with P_{in}, so the PD exhibits a linear dynamical range (LDR, i.e. the power range

of constant R_{ext}) over five decades for 10^{-3} W/cm^2 $< P_{in} <$ 10^2 W/cm^2. At higher $P_{in} > 10^2$ W/cm^2 the PD response becomes nonlinear, and R_{ext} increases exponentially by almost three orders of magnitude. In this range, a substantial rise in $T_{e,\mathrm{SLG}}$ leads to exponentially enhanced thermionic emission across the Schottky barrier, as also evident from the Richardson equation [168], i.e. $J_{el} \propto \exp\left[-q\Phi_B/(k_B T_{e,\mathrm{SLG}})\right]$ (see also section 3.5.2, eq. 3.67). R_{ext} reaches its maximum at a certain P_{in}, beyond which it declines. This decline is understood as a combination of several factors occurring as $T_{e,\mathrm{SLG}}$ increases: i) the exponential term saturates (i.e., when $k_B T_{e,\mathrm{SLG}}$ becomes comparable to SBH), ii) the SLG absorption drops, iii) the SLG thermal capacitance increases significantly [see fig. 6.5(b)] requiring increasingly larger input power to achieve the same $T_{e,\mathrm{SLG}}$ increase. Therefore, $T_{e,\mathrm{SLG}}$ and J_{el} continue to rise with increased P_{in}, but at a progressively slower, sub-linear rate, resulting in the R_{ext} drop. In our discussion, P_{in} is still below the threshold where SLG saturable absorption [440, 441] starts to dominate and becomes a limiting factor to the PD performance. Finally, the effect of the τ_{inj} value is evident, since in fig. 6.7(a), $\tau_{\mathrm{inj}} = 30$ ps leads to R_{ext} in the order of $\sim$ mA/W, while $\tau_{\mathrm{inj}} = 0.13$ ps results in $R_{ext} \sim$ A/W [fig. 6.7(b)]. If the SLG electrode is nanostructured [e.g. ribbons narrower than

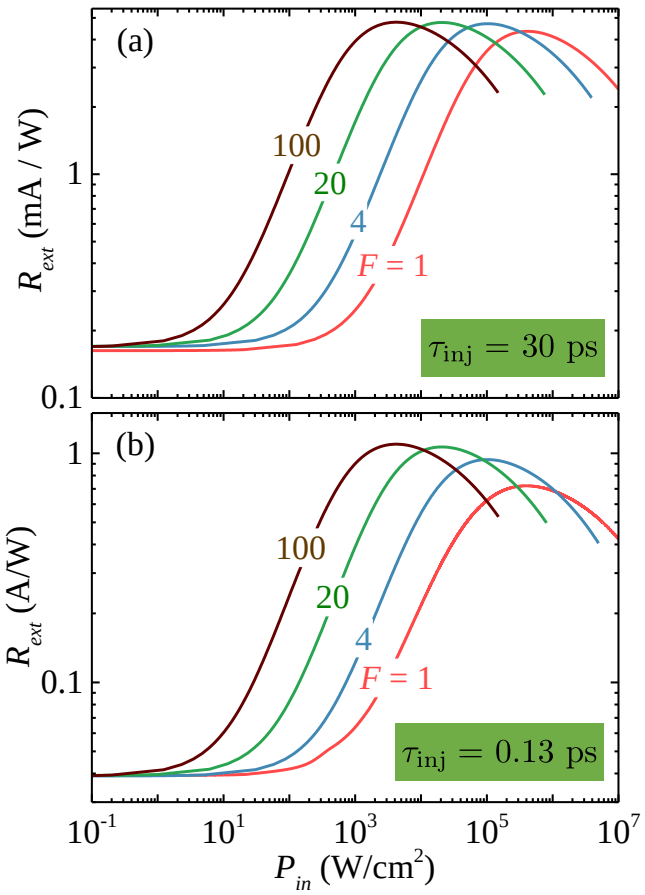

Figure 6.7: R_{ext} for $F = 1, 4, 20, 100$ as a function of P_{in} for (a) $\tau_{\mathrm{inj}} = 30$ ps and (b) $\tau_{\mathrm{inj}} = 0.13$ ps. Note that in (a) R_{ext} is in mA/W while in (b) in A/W.

$\lambda/2$, fig. 6.3(b)], its spatially averaged absorptivity will decrease (assuming no resonant phenomena, such as plasmons become active), but critical coupling conditions can still be met if the cavity decay rate is reduced to match the new total absorption rate, as shown in section 6.2.3. Figure 6.7 plots the resulting R_{ext} for SLG reduced below the diffraction

limit for $F = 4, 20, 100$. As more multilayer periods are added to achieve critical coupling, the corresponding absorption densities increase by a factor F, giving rise to higher $T_{e,\text{SLG}}$. At the same time the SLG/Si contact area is proportionally smaller, limiting the overall current across the junction. As a result, if light absorption in SLG remains constant with increasing F, R_{ext} values will remain the same, but observed at smaller input power, reduced by a factor F. In fig. 6.7 a slight increase in R_{ext} is observed for $F > 1$, arising from slightly larger SLG light absorption in these cases [fig. 6.4]. This increase in absorption originates from the fact that critical coupling conditions are not perfectly met for $F = 1$ and $E_{F,\text{SLG}}$ values considered here (i.e., $\gamma_a \approx \gamma_d$). A better match of cavity decay rate γ_d and absorption rate γ_a is achieved for $F > 1$ values, leading to increased SLG light absorption, hence higher R_{ext}. This effect is more profound on the $\tau_{\text{inj}} = 130$ fs case fig. 6.7(b). Overall, in the configuration considered here, patterning SLG in ribbons lower than S_0 lead to R_{ext} peak values achieved at input powers reduced by at least a factor of F.

6.3.4 Effect of carrier injection time

Next, the effect of τ_{inj} on PD performance is considered. Figure 6.8(a) plots the normalized J_{e-ph} and J_{th} as a function of τ_{inj} for different P_{in}. We assume $F = 1$ and fixed 100% SLG absorption, to isolate the effect of τ_{inj} on PD performance. While $\tau_{\text{inj}} \sim 0.13$ ps is the lowest value reported to-date [372, 380, 383], we anticipate that future studies may do better, so we extend our work into the ~ 10 fs regime. The cross-over between phonon-dominated ($J_{e-ph} > J_{th}$) and thermionic-dominated ($J_{e-ph} < J_{th}$) cooling regimes is observed in all cases [fig. 6.8(a)], but at a different τ_{inj}, depending on P_{in}. For larger P_{in}, $T_{e,\text{SLG}}$ increases, leading to enhanced thermionic cooling, and the cross-over point is shifted to the higher τ_{inj}. For $\tau_{\text{inj}} > 1$ ps, cooling is e-ph dominated even for large P_{in}. The corresponding $T_{e,\text{SLG}}$ and R_{ext} are shown in fig. 6.8(b). $R_{ext} \sim 1$ A/W is achievable for τ_{inj} in the sub-ps regime. A smaller τ_{inj} results in lower NEP and higher D^* [fig. 6.8(c)]. In the limit of $\tau_{\text{inj}} \sim 10$ fs, $D^* > 10^7 \text{cm}\,\text{Hz}^{0.5}\,\text{W}^{-1}$, values typical in SLG based IPE PDs [153, 179], thus indicative of the potential competitiveness of the PTh configuration, the latter being additionally spectrally unlimited in contrast to IPE.

Overall, lower τ_{inj} lead to better PD performance, both in terms of R_{ext} and D^*, while τ_{inj} value determines the dominant carrier cooling mechanism (i.e., J_{e-ph} or J_{th}).

6.3.5 Effect of initial Fermi level and zero bias Schottky height

These results impose an upper limit for thermionic emission in SLG/Si Schottky PDs for a given SBH. The latter depends on the initial $E_{F0,\text{SLG}}$ upon contact and the applied reverse bias V_R, which both affect Φ_B and the leakage (dark) current. For $V_R = 0$, Φ_{B0} depends on SLG Fermi level before contact $E'_{F,\text{SLG}}$ and *n*-Si dopant concentration $N_{d,\text{Si}}$, having a lower limit $\Phi_{B0}^{min} \approx e\phi_{Si}$ (eq. 3.57) depending on $N_{d,\text{Si}}$ (assuming the ideal case of no charges and Fermi level pinning at the interface).

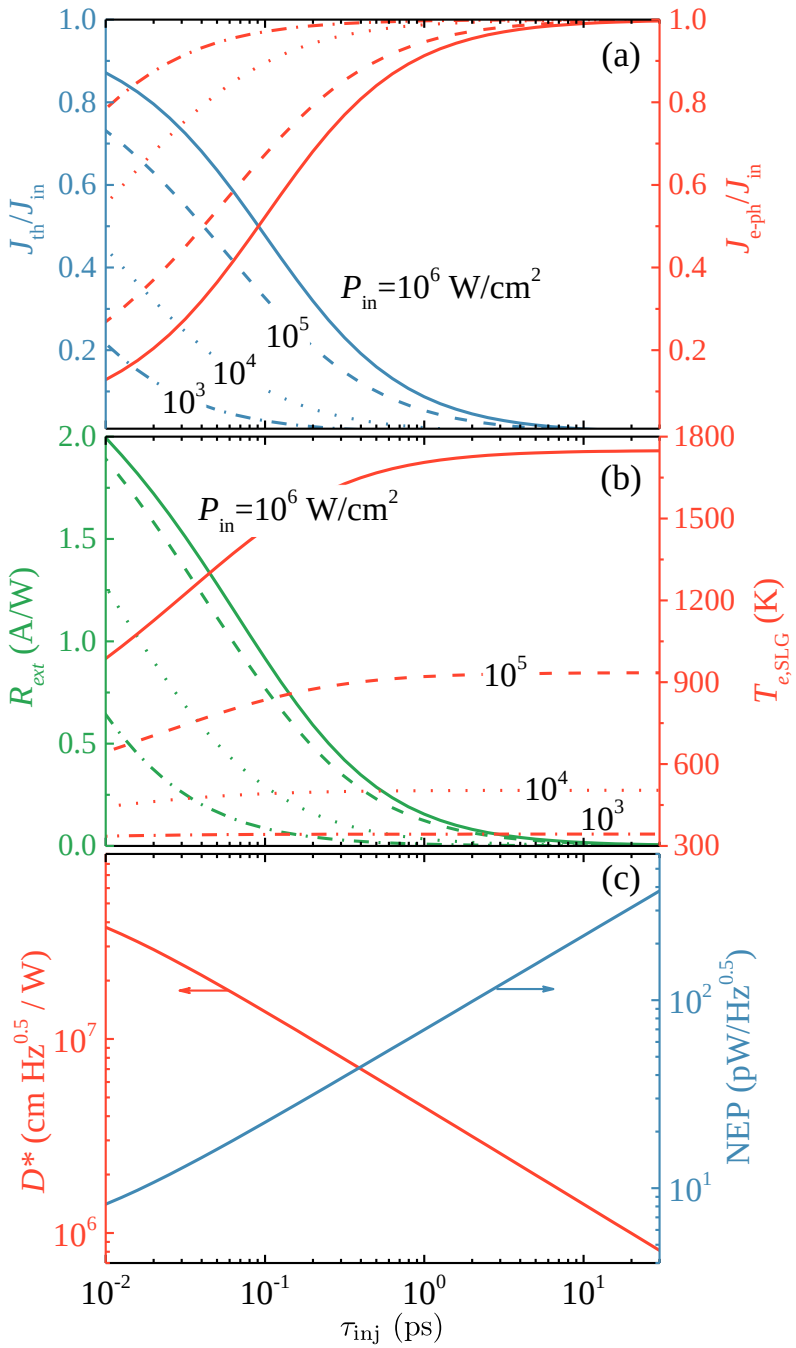

Figure 6.8: Performance under CW operation as a function of τ_{inj} (a) Thermal currents, (b) $T_{e,\text{SLG}}$ and R_{ext} (c) D^* and NEP. All calculations assume $\Phi_{B0} = 0.3$ eV at $V_R = 0$, $\tau_{e-e} =$ 20 fs, $k_{F,\text{SLG}}\, l \sim 50$, $F = 1$ and 100 % SLG absorption. In (a) and (b) continuous, dash, dot and dash-dot lines correspond to $P_{in} = 10^6$, 10^5, 10^4 and 10^3 W/cm^2 respectively.

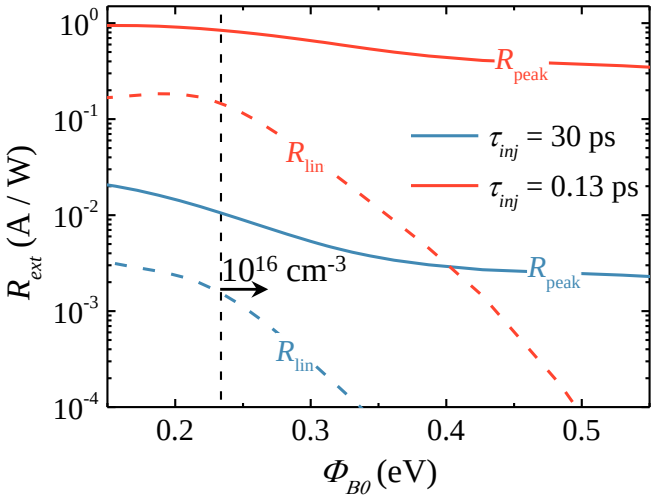

Figure 6.9: Peak (solid) and linear regime (dashed) R_{ext} as a function of Φ_{B0} for $\tau_{\text{inj}} =$ 30 ps (blue) and $\tau_{\text{inj}} = 0.13$ ps (red). Vertical dashed lines denote the limiting SBH values accessible depending on $N_{d,\text{Si}}$.

Figure 6.9 plots the linear regime responsivity R_{lin} (at low input power, P_{in} <10^2 W/cm^2) and peak responsivity R_{peak} (e.g., derived at $P_{in} > 10^5$ W/cm^2 for $F = 1$) as a function of Φ_{B0}. We consider two cases for τ_{inj}; 30 ps and the lower bound of 0.13 ps. The span of possible SBH achievable for different $N_{d,\text{Si}}$ is denoted in fig. 6.9 by a vertical dashed line (e.g., $\Phi_{B0}^{min} = 235$ meV and 150 meV for $N_{d,\text{Si}} = 10^{16}$ and 3×10^{17} cm^{-3} respectively). $R_{lin} > 0.1$ A/W is reached for $\tau_{\text{inj}} = 0.13$ ps at $\Phi_{B0} < 0.25$ eV even in the linear (low power) regime. R_{lin} and R_{peak} plateau at lower SBH for both τ_{inj}. This is due to more efficient cooling at higher $E_{F0,\text{SLG}}$ (i.e., lower Φ_{B0}). This behavior is more pronounced in the linear regime ($T_{e,\text{SLG}} < 310$ K), where a peak at $\Phi_{B0} \sim 0.2$ eV is obtained for $\tau_{\text{inj}} = 0.13$ ps. Such behavior is expected when the thermionic cooling becomes dominant in combination with Pauli blocking at $E_{F0,\text{SLG}} > 0.2$ eV ($\Phi_{B0} <$ 0.25 eV). The latter contrasts with the high $T_{e,\text{SLG}} > 800$ K case, where Pauli blocking is suppressed by the thermally excited carriers and decreasing $\mu_{c,\text{SLG}}$ [see fig. 6.5(b)]. For $\tau_{\text{inj}} = 30$ ps cooling is phonon-dominated and does not result in a performance drop by further increasing $E_{F0,\text{SLG}}$.

6.3.6 Photodetection performance under reverse bias

SBH can also be controlled by V_R. The dependence of SBH on V_R is plotted in fig. 6.1(b). Figure 6.10 plots R_{peak} as a function of V_R for different Φ_{B0}. We consider the two cases $\tau_{\text{inj}} = 30$ ps and 0.13 ps assuming, for simplicity, τ_{inj} independent of V_R. For $\tau_{\text{inj}} = 30$ ps, R_{peak} is limited to the mA/W range. For $\tau_{\text{inj}} = 0.13$ ps, $R_{\text{peak}} \sim 1$ A/W can be reached. Higher $E_{F0,\text{SLG}}$ and/or V_R both contribute to SBH lowering, thus higher R_{peak}. In fig. 6.10 the slope changes at $V_R = 4$ V for Φ_{B0} =0.52 eV and at $V_R = 21$ V for $\Phi_{B0} = 0.58$ eV. This is attributed to SLG transitioning from *p* to *n* as V_R increases (for $\Phi_{B0} \leq 0.45$ eV SLG is already n-doped at $V_R = 0$) and $E_{F,\text{SLG}}$ shifts from valence to conduction band via the CNP. During this transition, the rate of μ_{SLG} variation with V_R changes due to the smaller density of states around the CNP [see also fig. 6.1(a)]. As an additional remark, we note that peak R_{peak} values of fig. 6.10 are observed in different $T_{e,\text{SLG}}$ for each distinct configuration. $T_{e,\text{SLG}}$ values resulting in maximum R_{peak} as for fig. 6.10 are found in the

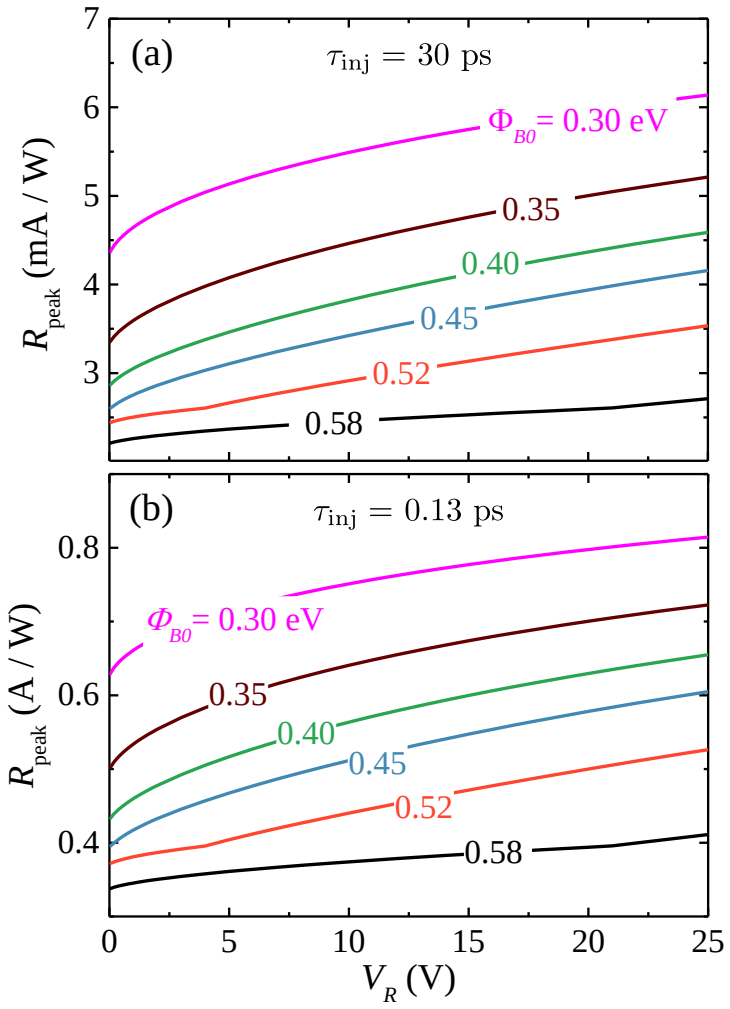

Figure 6.10: R_{peak} as a function of V_R for τ_{inj} (a) 30 ps and (b) 0.13 ps (τ_{inj} assumed independent of bias).

range $1000\,\text{K} \lesssim T_{e,\text{SLG}} \lesssim 1500\,\text{K}$. The corresponding lattice temperature $T_{l,\text{SLG}}$ in these cases is in the order of ~ 400 K, much lower than graphene's melting point of $T_{m,\text{SLG}} \sim 4500$ K [442], indicating that CW illumination can safely be applied even for the high power densities considered here.

Figure 6.11 plots D^* as a function of V_R for different Φ_{B0}. D^* strongly depends on the PD noise level. In our calculations, we consider shot and thermal (Johnson) noise contributions. Shot noise is proportional to the PD current (eq. 2.1), whilst thermal noise is inversely proportional to the diode resistance (eq. 2.2). At low V_R, the PD dark (leakage) current is reduced, and the Schottky junction resistance is increased, so that the total noise figure decreases and D^* is expected to grow for $V_R \to 0$. Figure 6.11(a) shows that this is valid only for *n*-doped SLG (e.g. $\Phi_{B0} = 0.3$,0.35,0.4 eV). In contrast, when the SLG/Si Schottky contact results in *p*-doped SLG (e.g. $\Phi_{B0} = 0.52$, 0.58 eV) D^* increases with V_R. This is interpreted as follows: for *p*-doped SLG, a larger V_R increase both photo- and dark currents (thus noise levels), but at the same time shifts $E_{F,\text{SLG}}$ towards the CNP, weakening both e-optical phonon and supercollision-assisted heat dissipation channels (eqs. 3.42 - 3.45), while making the SBH lowering effect more profound [fig. 6.1(b)], resulting in enhanced R_{ext}.

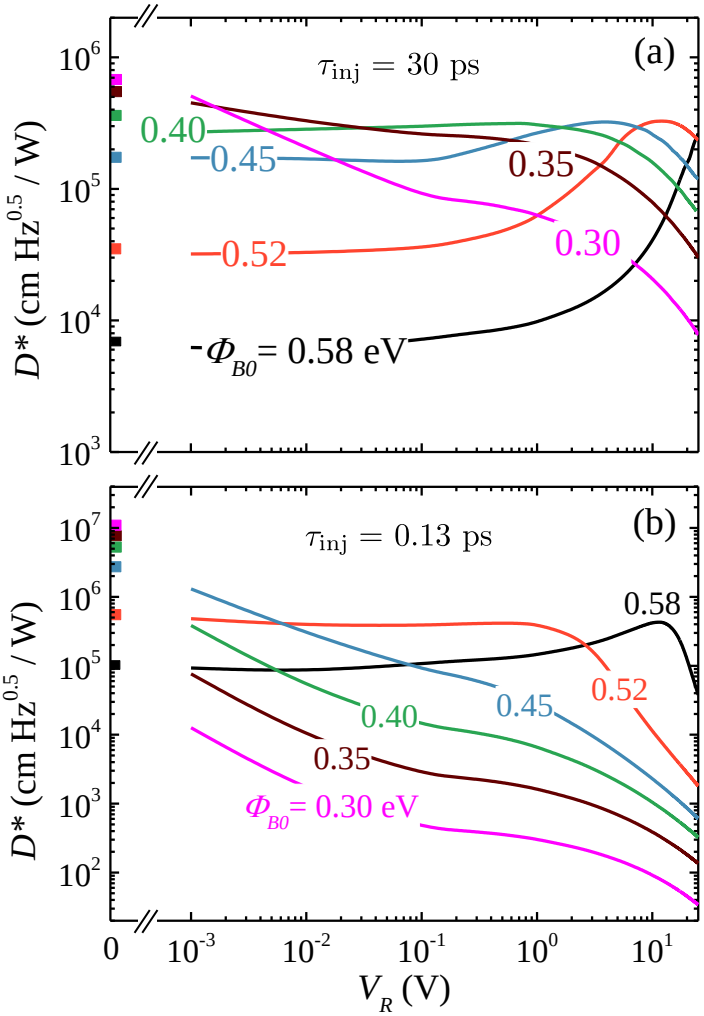

Figure 6.11: D^* as a function of V_R for different Φ_{B0} for τ_{inj} = (a) 30ps and (b) 0.13ps (τ_{inj} assumed independent of bias).

To better understand this, let us consider the response of *n*SLG and *p*SLG PDs at the lowest input power, i.e. at NEP level, under reverse bias. For both cases, V_R leads to an increased $E_{F,\text{SLG}}$, thus lower SBH. This is more profound in the *p*SLG case because of the reduced charge density as one approaches the Dirac point. Also, in the *n*SLG case the total number of carriers available for SC cooling as well as the ability for e-optical phonon scattering is increased with V_R, while in *p*SLG the additional e transfer from Si to SLG will lead (initially) to a reduced number of carriers and scattering due to optical phonon, thus reduced cooling. Both these effects lead to increased R_{ext} with V_R in the *p*SLG case and reduction in the *n*SLG case, as shown in the D^* graphs of fig. 6.11. After D^* peaks in the *p*SLG case, further increase in V_R leads to R_{ext} reduction, for the same reasons it reduces in *n*SLG. A critical factor determining the peak position, is the point at which thermionic cooling mechanism becoming dominant. Figure 6.12 compares the two cooling channels (e-ph and thermionic) as a function of V_R for two $E'_{F,\text{SLG}}$, assuming input power at the NEP level. We verify that in *n*SLG thermionic cooling is always dominant (except close to $V_R = 0$) while in *p*SLG a cross over is found for $V_R \sim 22$ V. Thus, the combined counteracting phenomena described above lead to an initially increase in D^* with V_R in the *p*SLG/*n*Si. For *n*SLG/*n*Si all V_R values lead to lower D^*. This is more profound in the high injection time scenario, since for low $\tau_{\text{inj}} = 0.13$ ps thermionic cooling is more

important than e–ph cooling.

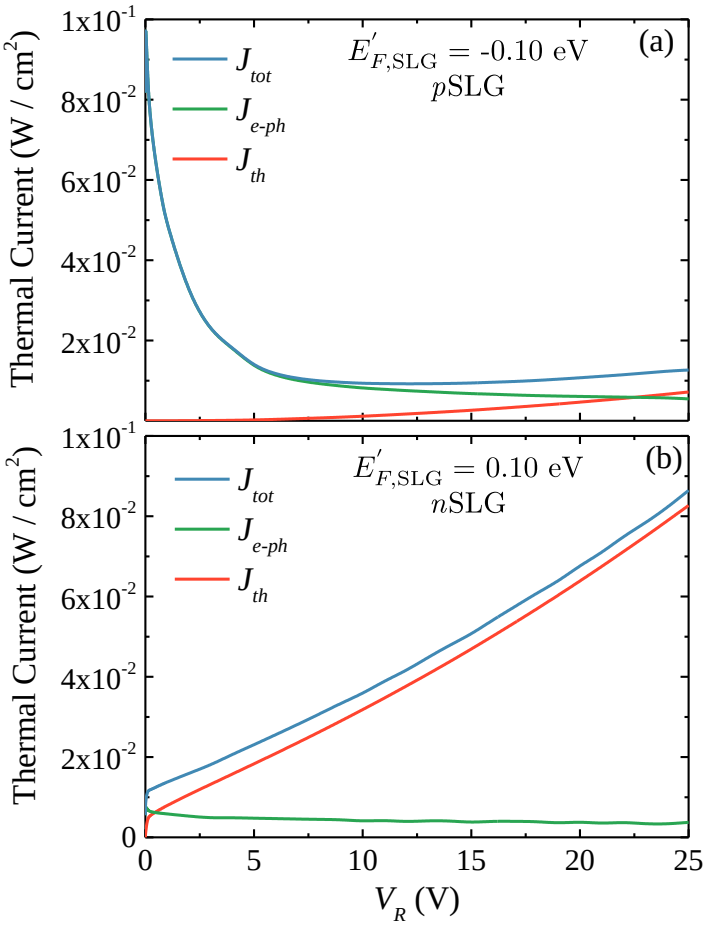

Figure 6.12: Thermionic (red), e-ph (green) and total (blue) thermal currents for $\tau_{\mathrm{inj}} = 30$ ps for initially (a) pSLG ($E'_{F,\mathrm{SLG}} = -0.10$ eV; Φ_{B0} =0.52 eV) and (b) nSLG ($E'_{F,\mathrm{SLG}} =$ 0.10 eV; $\Phi_{B0} = 0.35$ eV).

Overall, the effect of V_R on D^* depends on $E_{F,\mathrm{SLG}}$ relative to Si: it will enhance D^* when the initial $E_{F,\mathrm{SLG}}$ and $E_{F,\mathrm{Si}}$ are of opposite sign, but it will severely reduce it in the opposite case. R_{ext}, on the other hand, always increases with V_R, as shown in figs. 6.9 and 6.10.

6.3.7 Effect of supercollision scattering strength

Another important factor affecting R_{peak} is $k_{F,\mathrm{SLG}}\, l$, related to supercollision cooling J_{sc} (eqs. 3.44 - 3.45), with $k_{F,\mathrm{SLG}} = \sqrt{\pi n^*_{\mathrm{SLG}}}$, where n^*_{SLG} is the free carrier concentration associated with SLG doping. Figure 6.13 shows the R_{peak} dependence on $k_{F,\mathrm{SLG}}\, l$ for $\Phi_{B0} =$ 0.3 eV (by varying l) for the two representative τ_{inj} and the two extremes of V_R. In the slow τ_{inj} regime (e.g. 30 ps), where cooling is dominated by e-ph scattering, as $k_{F,\mathrm{SLG}}\, l \to 0$, supercollision cooling is enhanced and becomes dominant (surpassing e-optical phonon scattering and thermionic cooling). This leads to a drop in R_{peak}. As $k_{F,\mathrm{SLG}}\, l$ increases, e.g., for lower density of defects, supercollision scattering is suppressed. At a certain point the e-optical phonon scattering becomes dominant, and R_{peak} plateaus, as $k_{F,\mathrm{SLG}}\, l$ increases further. For the fast τ_{inj} (e.g. 0.13 ps), cooling is dominated by the thermionic heat flow

(J_{th}) from SLG to Si, resulting in large R_{peak}, but this quickly deteriorates as $k_{F,\text{SLG}}\, l \to 0$ and supercollision cooling is enhanced.

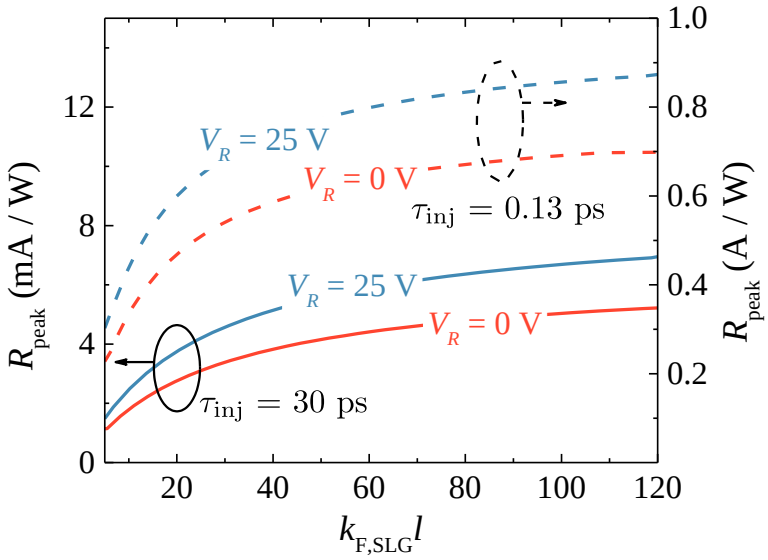

Figure 6.13: R_{peak} as a function of $k_{F,\text{SLG}}\, l$ assuming $\Phi_{B0} = 0.3$ eV. Red lines for $V_R = 0$ V, blue lines for $V_R = 25$ V. Solid lines are calculated for $\tau_{\text{inj}} = 30$ ps and dashed for $\tau_{\text{inj}} = 0.13$ ps. The calculations were performed assuming l varying from 10 to 400 nm.

6.3.8 Wavelength dependence of photodetector response

We now investigate the wavelength dependence of our thermionic PD platform. Fig. 6.14 plots the SLG absorption, as calculated through TMM, within the MWIR regime in the range of $\hbar\omega$ = 0.38-0.42 eV. The Bragg cavities (composed by Bragg mirrors with $N = 2$ Si/SiO_2 repetitions each) are scaled for each target wavelength, based on the methods described in section 6.2.3. For simplicity, we restrict our analysis to the case of $F = 1$ and $E_{F,\text{SLG}} = 0.15$ eV. Almost total light absorption in graphene can be achieved, as can be seen from the continuous lines in fig. 6.14. The dashed lines correspond to the calculated SLG absorption using $N = 3$ Bragg bilayers for each mirror. In the latter case, the decay rate of the cavity is reduced, critical coupling conditions are not met, and SLG absorption decreases to $\sim$ 70 %.

Figure 6.15(a) plots the SLG absorption as a function of photon energy, from quasi-cw calculations. We assume $E'_{F,\text{SLG}} = 0.15$ eV, $F = 1$, $\tau_{e-e} = 20$ fs, $\tau_{\text{opt}} = 200$ fs, $\tau_{\text{inj}} = 0.13$ ps, $\Phi_{B0} = 0.3$ eV, $k_{F,\text{SLG}}\, l \sim 50$ for both $N = 2$ and $N = 3$ Bragg bilayers. Dashed lines correspond to the absorption at the linear regime (low input power, $T_{e,\text{SLG}} \sim 301$ K) and solid lines for input power corresponding to the peak of R_{ext} (high input power, $T_{e,\text{SLG}} \sim$ 1200 K). We observe that at lower $\hbar\omega$, SLG absorption is reduced in both cases, due to Pauli blocking, resulting in a reduced SLG absorption rate and broken critical coupling conditions. This behavior is more profound in the linear regime, since at R_{peak} the high $T_{e,\text{SLG}}$ allows for SLG absorption even within Pauli blocking ($\hbar\omega < 0.3$ eV). Nonetheless, we can compensate for the reduced SLG absorption rate by adding a third Bragg bilayer, thus reducing the cavity decay rate. In this case, critical coupling conditions are restored in these lower photon energies.

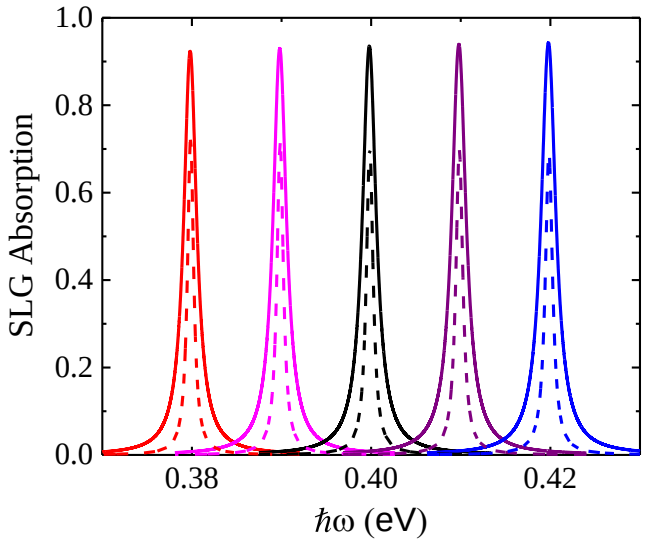

Figure 6.14: SLG absorption as a function of $\hbar\omega$ at RT for $E_{F,\mathrm{SLG}}$= 0.15 eV and $F = 1$. The calculations are performed assuming $N = 2$ (solid) and $N = 3$ (dashed) Si/SiO_2 Bragg bilayers in each mirror.

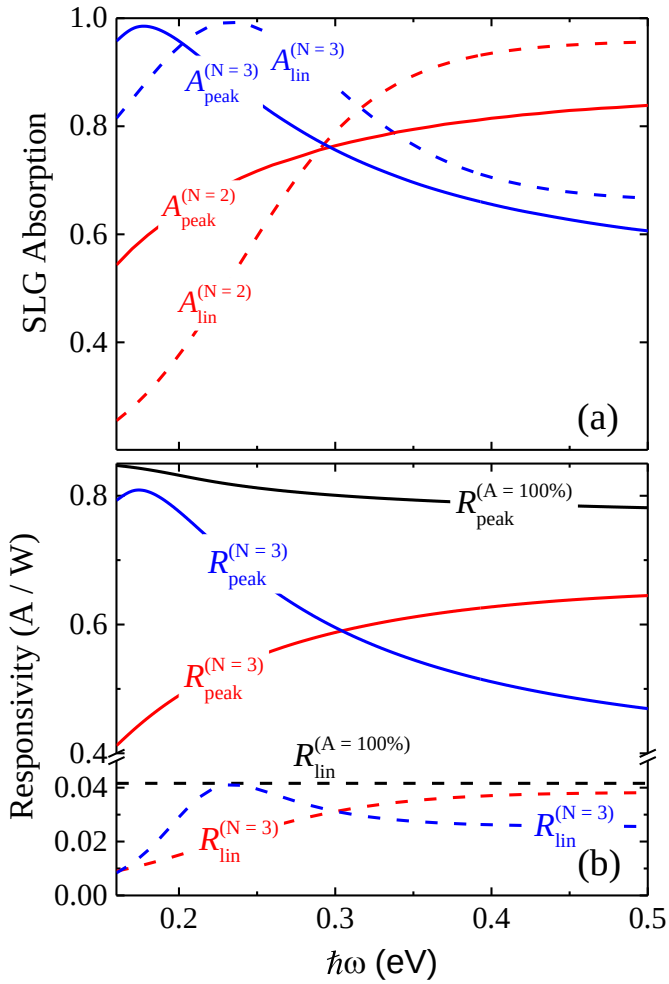

Figure 6.15: (a) SLG absorption and (b) R_{ext} as a function of $\hbar\omega$. Solid lines correspond to peak R_{ext} and dashed lines to the low power (linear) regime. In (b) black lines correspond to the limiting case, where 100 % SLG absorption is assumed. For each wavelength, the Bragg layer thicknesses were scaled accordingly.

Figure 6.15(b) plots R_{ext} as a function of $\hbar\omega$, in the linear regime (dashed lines) and at its peak (solid lines). As expected, the R_{ext} trend follows that of SLG absorption. The black lines, labeled with $R^{(A=100\%)}$, show the limiting case of 100 % SLG absorption, irrespective of photon wavelength. In the linear regime, $R_{\text{lin}}^{(A=100\%)}$ is flat, as expected, while in the non–linear regime we observe a slight decrease with increasing photon energy. This is due to the photo-excited non-equilibrium carries: for the same input power, a higher number of photons are absorbed at lower $\hbar\omega$. As a result, a higher non-equilibrium carrier density is involved in these cases (eq. 3.55), resulting to a higher $\mu_{c,\text{SLG}}$ (eq 3.41). Since SLG is contacted with *n*Si, the higher $\mu_{c,\text{SLG}}$ will lead to reduced SBH Φ_B and thus a slightly increased thermionic emission for lower $\hbar\omega$.

These results show that our methods and conclusions are applicable throughout the MWIR spectrum. By exploiting the critical coupling mechanism, it is possible to design PDs with optimal response at the desired wavelength. A large variety of tunability options are available, by combining $E_{F,\text{SLG}}$, number of Bragg bilayers and materials used in Bragg cavities.

6.3.9 Temporal response and photodetection frequency

Finally, we estimate the limiting factors defining the time response of the studied PD platform. These are: 1) τ_{tr}, the transit time of charge carriers across the depletion zone; 2) τ_{RC}, the charge/discharge RC time constant of the diode/circuit combination; 3) τ_{ph}, the photon lifetime inside the optical cavity. The overall time response is thus limited by [176]:

$$\tau = \sqrt{\tau_{tr}^2 + \tau_{RC}^2 + \tau_{ph}^2} \tag{6.2}$$

1. τ_{tr} can be estimated as [20, 153]:

$$\tau_{tr} = \chi_d / v_{sat,\text{Si}} \tag{6.3}$$

where χ_d is the depletion region width and $v_{sat,\text{Si}} = 10^7$ cm/s the carrier saturation velocity in Si [20]. The depletion region varies with V_R and initial SLG doping, i.e., $\chi_d \propto \left(V_0 + V_R^{'}\right)^{0.5}$ (eqs. 3.58 - 3.59), where $V_R^{'}$ is the reverse bias induced voltage drop in Si depletion region (section 3.5.1). χ_d ranges from 150 nm (at V_R=0) up to the fully depleted *n*Si layer thickness d_{Si}, i.e. $\chi_d = d_{\text{Si}} = 453$ nm. These values bring τ_{tr} between 1.5 and 4.5 ps, with the corresponding transit-time limited cutoff frequency $f_{tr} = (2\pi\tau_{tr})^{-1} \sim$ 35-100 GHz.

2. Electronics limited frequency, arising from parasitic RC effects, is given by:

$$f_{RC} = (2\pi R_{el} C_{tot})^{-1} \tag{6.4}$$

$R_{el} = R_s + R_c$ is the sum of the series and contact resistances respectively. R_s has two contributions, one due to *n*Si and one due SLG and C_{tot} the total capacitance of the Schottky junction. The Si resistance is calculated as $R_{\text{Si}} = (d_{\text{Si}}\, N_{d,\text{Si}}\, e\mu_{\text{Si}})^{-1} \sim$ 10 kΩ assuming $N_{d,\text{Si}} = 10^{16}$ cm^{-3} with the electron mobility in Si $\mu_{\text{Si}} = 1350$ cm^2/Vs [20]. For SLG, we use $R_{\text{SLG}} = (\sigma_{dc,\text{SLG}})^{-1}$ where $\sigma_{dc,\text{SLG}}$ is the DC conductivity of SLG (eq. 3.14), assuming a minimum charge puddle concentration $n_{\text{min,SLG}} \sim 10^{12}$ cm^{-2} and $\mu_{q,\text{SLG}} \sim 10^4$ cm^{2}V^{-1}s^{-1} for the SLG mobility. R_{SLG} is estimated to be $\sim$ 0.1-1 kΩ, depending on $E_{F,\text{SLG}}$, V_R and $T_{e,\text{SLG}}$. For the contact resistance, we assume $R_c \sim 1$ k$\Omega \cdot \mu$m [67, 383, 443]. The total capacitance is

$C_{tot}^{-1} = C_j^{-1} + C_{q,\text{SLG}}^{-1}$ with $C_j = S_0\,\epsilon_0\,\epsilon_{\text{Si}}/\chi_d$ the junction capacitance and $C_{q,\text{SLG}}$ the SLG quantum capacitance (eq. 3.15). The latter, given the assumed $n_{\text{min,SLG}}$, is estimated in the order of$\sim 1\ \mu$F/cm^2 [269], almost two orders of magnitude above C_j. It is thus safe to assume $C_{tot} \sim C_j$. Considering all the above ranges, we find $f_{RC} \sim$ 1-10 GHz. This can be increased using a higher Si doping and/or reducing C_j by geometrical focusing. For example, $f_{RC} \sim 100$ GHz is estimated if $N_{d,\text{Si}} = 10^{17}$ cm^{-3} is used. On the other hand, $F \gg 1$ will eventually impose an upper limit in the temporal response, due to the required high–Q optical cavities.

3. The optics-limited f_{opt} frequency is given by [229]:

$$f_{opt} = c/(n2LQ) \tag{6.5}$$

$2L$ is the cavity roundtrip length (the middle nSi and SiO_2 layers) and c/n the speed of light inside this cavity. Since the latter consists of two different materials we get:

$$L = c\left(\frac{1}{n_{\text{SiO}_2} d_{\text{SiO}_2}} + \frac{1}{n_{\text{Si}} d_{\text{Si}}}\right) \tag{6.6}$$

where $d_{\text{SiO}_2} \sim 1.06$ μm and $d_{\text{Si}} \sim 0.45$ μm are the thicknesses of the two middle layers. The quality factor, Q is defined as:

$$Q = \frac{\omega_0}{\Delta\omega} \tag{6.7}$$

with ω_0 the cavity resonant frequency and $\Delta\omega$ the FWHM of the resonance. We find $Q \sim 235$ for $F = 1$ and $Q \sim 21000$ for $F = 100$. Depending on the chosen configuration (i.e. geometrical focusing), f_{opt} ranges from 10 GHz (for $F = 100$) up to 1 THz (for $F = 1$).

As expected, the time response limitations are mainly imposed by τ_{RC}, bringing overall operation frequencies in the range of 1-100 GHz, depending on configuration selection.

6.4 Conclusions

In this study the electrical, optical and thermal properties of graphene, described in chapter 3, where put together in a self-consistent simulation framework. Using this framework, the temporal response (using the 4RK method) or CW operation (using the self-consistent algorithm depicted in fig. 3.16) of graphene-based devices can be simulated. Modeling devices with the methods developed here, include all carrier dynamics and account for realistic full-device representations, enabling the design and optimization of novel graphene-based optoelectronics schemes.

Regarding the specific PD platform studied in this chapter, the physical behavior and performance limits of SLG/Si Schottky IR PDs operating in the thermionic regime were assessed. We described the PD operation under realistic conditions for all relevant parameters, e.g., Schottky barrier height [168, 439], carrier injection time [372, 380] and graphene quality/supercollision cooling strength [333, 351]. Moreover, the transition between thermionic dominated and e-ph dominated cooling regimes [71], and its effect on PD operation, was described in detail for both biased and unbiased cases. Exploiting Bragg cavities configurations and the critical coupling mechanism, introduced in chapter

5, it is shown that the *geometrical focusing* scheme, outlined in section 6.2.3, can lead to R_{peak} responsivities achieved at lowered input powers, if SLG in nanopatterned and Bragg cavities are designed accordingly.

Overall, R_{ext} up to $\sim$ 1 A/W is achievable in the nonlinear (high-power) regime, R_{ext} $\sim$ 100 mA/W in the linear (low power) regime, while D^* peaks at $\sim 10^7$ cmHz$^{0.5}$/W with a five decades linear dynamic range at low ($< 10^2$ W/cm^2) input powers. The temporal response of the PD platform studied here is in the order of $\sim$ 1 - 10 GHz, with the potential to reach even $\sim$ 100 GHz if highly doped Si is used or the *geometrical focusing* configuration is utilized. These performance metrics are comparable to IPE configurations but at a spectrally unlimited scheme, since the results and conclusions derived here are general and applicable throughout the MWIR, if the architecture length scale is appropriately adjusted to the corresponding wavelength. Consequently, the proposed PTh PD platform is promising for multispectral detection at ambient conditions using CMOS compatible hybrid SLG-Si technology.

Chapter 7

Electrical detection of graphene plasmons for mid-infrared photodetection and chemical sensing

Electrical detection of graphene plasmons is important for developing mid-infrared photodetection and sensing applications based on graphene. Here, we theoretically investigate a configuration based on graphene nanoribbons on silicon, forming a series of Schottky junctions. We calculate the heating up of charge carriers in graphene, following plasmon decay, and their thermionic emission across the junctions leading to the generation of photocurrent. We extract an external responsivity up to $\approx$ 110 mA/W with a corresponding noise equivalent power $\approx$ 190 pW/Hz$^{0.5}$, specific detectivity $D^* \approx 4 \times 10^6$ cm Hz$^{0.5}$ W^{-1}, and response time $\approx$ 12 ns. We further demonstrate how this platform can be used for developing label free chemical sensors, utilizing surface enhanced infrared absorption, where the analyte presence is directly monitored by the photocurrent change. The methods and conclusions derived in this work are applicable throughout the infrared spectrum, where graphene plasmons can be realized

This chapter is based on:

➤ **S. Doukas**, P. Sharma, I. Goykhman and E. Lidorikis,
Electrical detection of graphene plasmons for mid-infrared photodetection and chemical sensing: A computational study,
Appl. Phys. Lett. 121, 051103 (2022),
https://doi.org/10.1063/5.0093981

7.1 Introduction

Surface plasmon polaritons (SPP) in single layer graphene [59–63] are a promising platform for light detection [69, 444–447], optical modulation [251, 448, 449] and sensing applications [450–455]. SLG-SPPs are gate-tunable throughout the MWIR [305, 306, 313], sensitive to chemical doping [456], and exhibit high spatial field confinement [59, 320, 450, 457]. The latter is a result of significant momentum mismatch between SLG-SPP and free-space light [60, 63], which however, also renders the light in-coupling to SLG-SPPs inefficient due to momentum conservation [60, 63]. Techniques to match momenta and increase in-coupling efficiency include SNOM assisted scattering [305, 306], scattering from metallic-nanoparticles [285, 303, 304], and nanostructured SLG, e.g. in the form of nanodisks [307–312] or nanoribbons [313–316, 318, 319].

Detection of SLG-SPPs is typically done optically and is indirect, i.e., by spectral measurements of the reflected and transmitted light [310–313, 315, 449–452], followed by post-processing and simulation to identify and subtract background absorption and peaks coming from other device elements such as metallic antennas, Fabry-Perot cavities, et.c. An electrical measurement technique yielding direct information on SLG-SPP excitation, however, would be ideal for reasons both fundamental (understanding of the excitation and decay mechanisms) and practical (clear distinction between SLG-SPPs and other device resonances, avoidance of bulky optics). There have been several studies addressing electrical detection of SLG-SPPs. In all of them, the elevated SLG electronic temperature at plasmonic resonance is utilized to induce and harvest a photocurrent [69, 445–447]. One approach involves the photo-thermoelectric effect [445]. In ref. [445] R_{ext} of 20 mA/W was measured at zero bias, with a calculated NEP of 400 pW/Hz$^{0.5}$. Another approach involves the temperature-induced changes in SLG conductivity [69, 446, 447]. However, this requires electrically biasing SLG, which introduces significant dark current noise. A further bottleneck is also related to the weak temperature dependence of SLG conductivity [458], especially in CVD graphene where carrier transport is dominated by defects and grain boundaries [459, 460]. As a result, the measured R_{ext} in ref. [69] was found in the order of $R_{ext} \approx 10\,\mu\text{A/W}$. An improvement, utilizing the conductivity change due to elevated SLG carrier temperature mechanism, was reported in ref. 447, using graphene disk plasmonic resonators (GDPR) [446, 447] connected with graphene nanoribbons [447] (GNR), whereby the GDPRs generate hot carrier population via plasmon resonant absorption and thermalization, while carrier transport is thermally activated along the GNRs. This work resulted in measuring $R_{ext} \approx 16$ mA/W [447], with a measured NEP ≈ 1.3 nW/Hz$^{0.5}$, and a theoretical lower limit [447] of NEP calculated at ≈ 460 pW/Hz$^{0.5}$. This approach, however, still requires voltage-biased SLG as well as the fabrication of complex nanostructures and molecular junctions.

In this chapter an unbiased SLG/Si Schottky junction configuration operating in the thermionic regime is designed and theoretically investigated, as a platform for electrical detection of SLG-SPPs. A periodic array of SLG-GNR on top of a *p*-doped silicon substrate (*p*-Si) is assumed, forming a series of SLG/Si Schottky contacts, where graphene plasmon resonance frequency scales with nanoribbon width and graphene Fermi level $E_{F,\text{SLG}}$ (section 3.3.3). The absorbed optical power in GNR, promoted by SPPs excitation, leads to a thermalized hot carrier gas in SLG [445–447, 461], which in turn creates photocurrent via thermionic emission across the SLG/Si junction, as discussed in the previous chapter. The theoretical framework that was developed in chapter 6 for inter-band optical excitations in SLG, with photons energy $\hbar\omega > 2E_{F,\text{SLG}}$, is extended

to the intra-band absorption process at longer wavelengths (i.e. at Pauli blocking regime $\hbar\omega < 2E_{F,\mathrm{SLG}}$). It is demonstrated that GNR-SPPs based Schottky junctions can produce significant photocurrent. Specifically, using optimized device geometry and realistic operational parameters, an external responsivity $R_{ext} \approx 110$ mA/W is calculated, with NEP ≈ 190 pW/Hz$^{0.5}$. Furthermore, we demonstrate this electrical detection scheme in a chemical sensing application, utilizing the surface enhanced infrared absorption (SEIRA) technique [321,450–454,462–464], using toluene [465] as an analyte paradigm. The sensing device architecture and operational parameters are optimized, and we explore its detection and sensitivity limits.

7.2 Photodetection layout and FDTD simulations

The studied configuration consists of a periodic GNR array of width w and period L placed on top of a p-Si substrate ($N_{A,\mathrm{Si}} = 10^{17}$ cm^{-3}), forming a series of Schottky contacts, as depicted in Fig. 7.1(a). We assume the GNRs to be p-doped, as is common in CVD fabricated graphene [466,467], and, for simplicity, a fixed $w/L = 0.5$ ratio. The structure is supplemented by an Au backmirror at distance d_{Si}, to form a Fabry-Perot cavity and enhance GNR light absorption [321, 449, 450]. The lowest energy (bipolar) GNR-SPP resonant wavelength can be calculated by eq. 3.38. By adjusting $E_{F,\mathrm{SLG}}$ and/or w, the GNR-SPP resonance can be tuned within the application desired wavelength range. For the specific study, targeting at plasmonic resonance in the 13-15 μm, assuming $w = 40$ nm (more w values will also be explored) the required $E_{F,\mathrm{SLG}}$ lies in the range of ~ 0.30 - 0.4 eV. To determine the exact resonant wavelength, extract the absorption spectrum and optimize the mirror distance d_{Si} for maximum light absorption in graphene, FDTD simulations were performed, using the commercial software Lumerical [399].

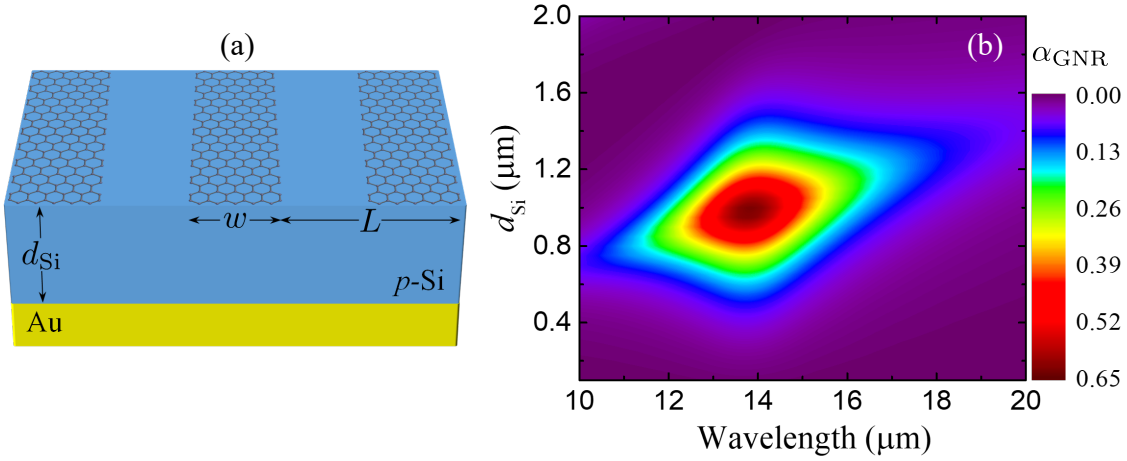

Figure 7.1: (a) Schematic of the periodic GNR array of width w and period L on top of p-Si, separated by distance d_{Si} by an Au backmirror. (b) SLG absorption colormap as a function of wavelength and p-Si thickness d_{Si}.

FDTD simulations were carried out using a 2D computational cell [assuming semi-infinite y-direction (transverse) dimensions] with periodic boundary conditions along the

x-axis and absorbing boundary conditions (perfectly matched layer, PML) along the z-axis, and a mesh grid size of 1 nm. SLG was inserted in Lumerical software as a 2D boundary, with its surface conductivity modeled using the Kubo formula (eq. 3.19), assuming $E_{F,\mathrm{SLG}} \approx 0.36$ eV. The free carriers relaxation time in SLG, τ_{opt}, depends on $E_{F,\mathrm{SLG}}$ and is related to carrier mobility $\mu_{q,\mathrm{SLG}}$ via eq. 3.23. Typically, τ_{opt} is in the order of $\sim$ 100 fs [47] for polycrystalline CVD graphene. For nanopatterned GNR examined here, however, τ_{opt} is assumed to be w-limited [355], i.e., $\tau_{\mathrm{opt}} = w/v_{F,\mathrm{SLG}} = 40$ fs, a limitation arising from carrier scattering at the edge of the ribbons. This yields mobility $\mu_{q,\mathrm{SLG}} \approx 1000$ cm^{2}V^{-1}s^{-1}, similar to what expected for defected and/or nanostructured SLG [321, 355]. The *p*-Si ($N_{a,\mathrm{Si}} = 10^{17}$ cm^{-3}) substrate's optical response was modeled assuming a Drude model, as described in the previous chapters, using eq. 5.2, but with $m^* = 0.38m_e$, and $\mu_{h,\mathrm{Si}} = 450$ cm^{2}V^{-1}s^{-1} [20] the Si hole mobility instead, since here we consider *p*-doped Si. The Au backmirror's optical response was modeled using data from ref. 423. The configuration of fig. 7.1(a) is illuminated using a plane wave source under normal incidence and the calculated GNR absorption colormap is plotted in 7.1(b), as a function of wavelength and mirror separation d_{Si}. A maximum SLG absorption $\sim$ 65 % at $\approx$ 14 μm was calculated, at optimum $d_{\mathrm{Si}} = 1$ μm.

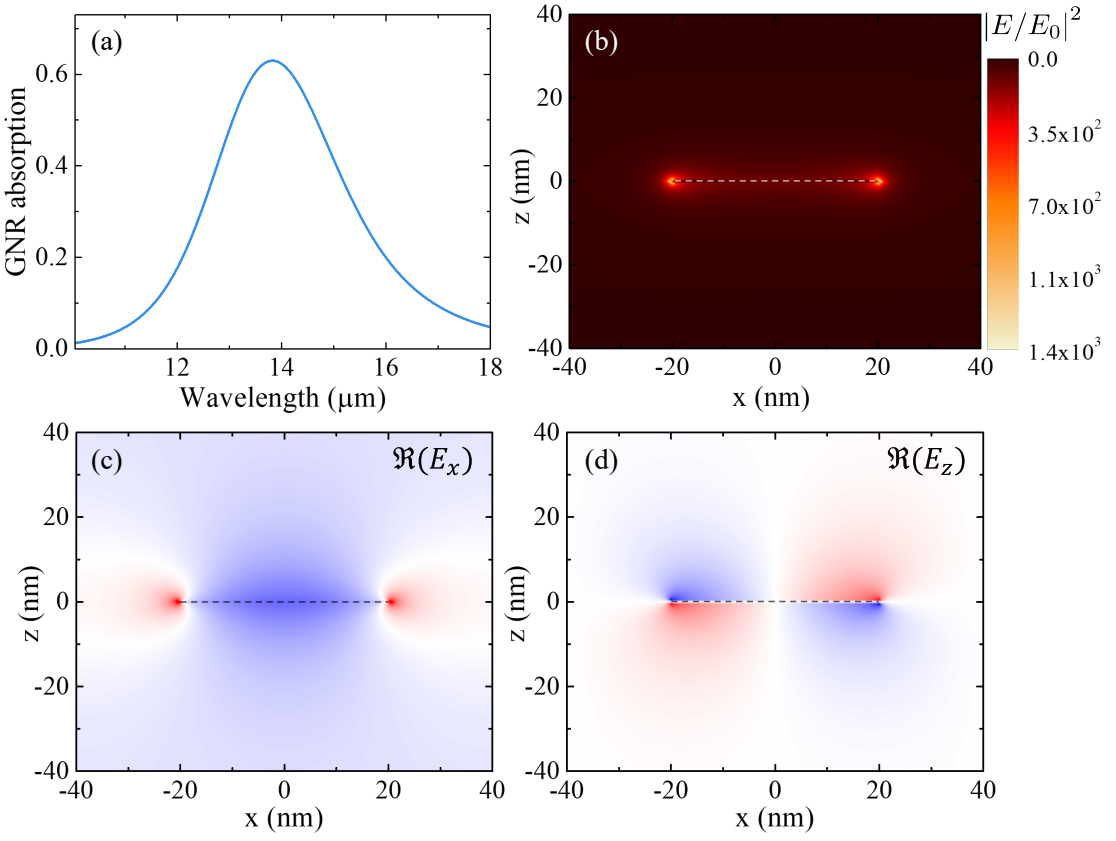

Figure 7.2: FDTD simulations regarding the configuration of fig. 7.1(a) for $d_{\mathrm{Si}} = 1$ μm, $E_{F,\mathrm{SLG}} = 0.36$ eV and $\tau_{\mathrm{opt}} = 40$ fs. (a) GNR absorption spectrum. Also, for a $x - z$ cross-section of 40 nm $\times$ 40 nm, the colormaps of (b) electric field intensity enhancement (c) distribution of the real part of the E-field x component and (d) distribution of the real part of the E-field z component are plotted. In (b) - (d) dashed lines depict the GNR position.

For $d_{\text{Si}} = 1$ μm (adopted for the rest of this chapter), fig. 7.2(a) plots the absorption spectrum as a function of wavelength, for graphene parameters as described above. The prefactor η of eq. 3.38, accounting for the hybridization and redshift of plasmons in neighboring GNRs [319] and affected by SPP-cavity interactions with the backmirror [321], is also extracted, having a value $\eta \sim 1.25$ for the specific configuration. Figures 7.2(b)-7.2(d) plot the distribution of E-field intensity enhancement, real part of the E-field x component and real part of the E-field z component respectively, for a $x - z$ cross-section of $40\,\text{nm} \times 40\,\text{nm}$, as calculated from FDTD simulations. A large ($\sim 10^3$) field enhancement in the vicinity of GNR is observed, extending only a few tens of nm around GNR, typical for graphene plasmons as discussed in section 3.3.

7.3 Sensing layout and FDTD simulations

The surface enhanced absorption enhancement (SEIRA) technique [462] can be used to probe spectral features of analyte molecules, which are unique for each substance, acting as molecular fingerprints. These spectral features are poorly probed directly by light, due to the large mismatch between resonant wavelength ($\sim$ μm) and molecular size ($<$ nm) [451, 462]. The principle of SEIRA is to use the deep sub-wavelength electric field (E-field) confinement and intensity enhancement of SPP modes [321, 450–454, 462–464] to probe these vibrational fingerprints. SPPs in GNR are ideal for this application, since the enhancement and localization of E-fields in the vicinity of graphene surpasses by far the corresponding merits developed in SPPs of metallic nanostructures [451, 453, 462].

Here, to theoretically investigate this application, toluene is used as an analyte paradigm. The latter has its two main absorption lines at $\lambda_1 \approx 13.7$ μm and $\lambda_2 \approx 14.4$ μm [465]. The real and imaginary part of toluene's refractive index is plotted in fig. 7.3 using data extracted from measurements reported in ref. [465]. We use these data to import a thin toluene layer in our FDTD simulations.

If a thin $d_{tol} = 8$ nm toluene layer (more d_{tol} values will also be explored) is placed on top of the optimized GNR configuration discussed in the previous section [fig 7.4(a)], GNR absorption will be reduced at the spectral lines of toluene absorption peaks, as shown in the red curve corresponding to the left $y-$axis of fig. 7.4(b). This also involves a small redshift of the overall response [compared to the same configuration without toluene, dashed blue curve in the left $y-$axis of fig. 7.4(b)], due to the different dielectric environment introduced by the toluene layer [451]. In the following section we use this configuration and, utilizing the self-consistent framework presented in the previous chapter, we explore the translation of this GNR absorption reduction towards a direct electrical readout.

7.4 Schottky barrier, carrier dynamics and photocurrent

Upon GNR/*p*-Si contact, holes will flow from *p*-Si to GNRs due to their workfunction difference (fig. 7.5), forming a depletion layer in *p*-Si and a Schottky junction with zero bias barrier height $\Phi_{B0} = eV_0 + e\phi_{Si}$, as discussed in detail in section 3.5. In this case, since we deal with *p*-Si, $e\phi_{Si}$ is the energy difference between the Fermi level $E_{F,\text{Si}}$ in Si and the valence band $E_{V,\text{Si}}$. Using the framework developed in chapter 6 and the self-consistent algorithm depicted in fig. 3.19, we find that for $E_{F,\text{SLG}} =$ -0.36 eV, the GNRs must initially (before contact) be at $E'_{F,\text{SLG}} =$ -0.35 eV, i.e., no significant $E_{F,\text{SLG}}$ shift

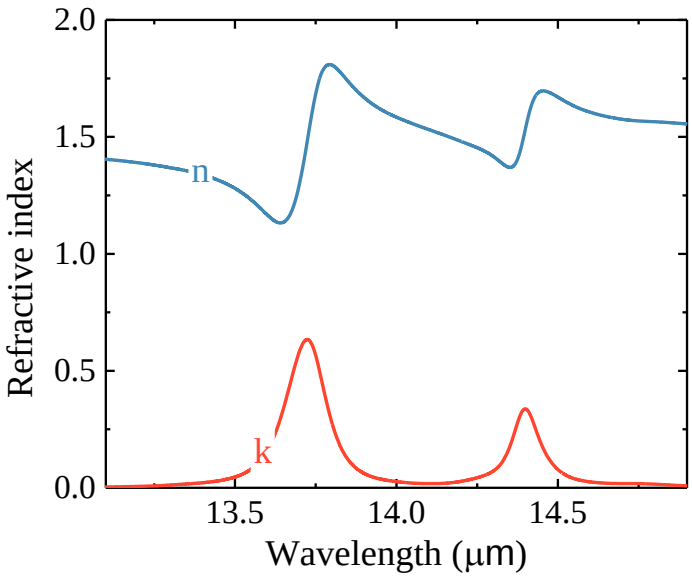

Figure 7.3: Real (blue) and imaginary (red) part of toluene's refractive index as measured in ref. [465].

occurs. This is related to the increased density of states of SLG at elevated $E_{F,\mathrm{SLG}}$ values (eq. 3.6). At the contact, GNR/*p*-Si Schottky junction gives rise to a zero bias Schottky barrier height $\Phi_{B0} \sim 0.31$ eV. Here, we utilize the conclusions of the previous chapter and we will not consider reverse bias, avoiding thus dark current and excess noise, leading to higher sensitivity (i.e., D^*) of the Schottky junction (fig. 6.11).

The incident MWIR light is assumed continuous (or quasi-continuous, e.g., in long $\gg$ ps pulses) and quasi-monochromatic, i.e., filtered by a grating or prism [468]. After light absorption, the excited GNR carriers thermalize within $\sim$ 20 fs and eventually cool down through the emission of acoustical and optical phonons, as discussed in detail in the chapters. During this process, an elevated electronic temperature is achieved and additional fraction of charge carriers at the Fermi-Dirac distribution tail will overcome the SBH and thermionically will be injected into *p*-Si. The latter will contribute to further cooling as well as a net photocurrent across the junction [i.e., J_{th}, eq. 3.66]. To calculate the electronic temperature $T_{e,\mathrm{SLG}}$ of charge carriers in GNR under continuous illumination, we use the self-consistent algorithm (fig. 3.16) presented in chapters 3 and 6 to solve the equilibrium equation for $T_{e,\mathrm{SLG}}$:

$$\alpha_{\mathrm{GNR}} \mathcal{P}/S = J_{e-ph} + J_{th} \tag{7.1}$$

where $\mathcal{P}$ is the incident optical power focused in area S (here taken as the diffraction limited spot $S = \lambda^2/\pi \approx 6 \times 10^{-7}\,\mathrm{cm}^2$, with λ= 14 μm the average wavelength of interest) and $\alpha_{\mathrm{GNR}} \equiv \alpha_{\mathrm{GNR}}(E_{F,\mathrm{SLG}}, T_{e,\mathrm{SLG}})$ is the absorption coefficient of the GNRs (acquired through FDTD simulations described above). Note that for the low input powers considered here, resulting to $T_{e,\mathrm{SLG}}$ increase < 1 K, α_{GNR} can be safely assumed to remain independent of $T_{e,\mathrm{SLG}}$ during illumination, i.e., $\alpha_{\mathrm{GNR}} \cong \alpha_{\mathrm{GNR}}(E_{F,\mathrm{SLG}}, 300\ \mathrm{K})$. As a result, the optical response of the studied configuration is calculated once using FDTD and the absorption spectra is feeded only in the beginning of the self-consistent cycle and not in each iteration as in chapter 6. As in the previous chapter, J_{e-ph} accounts for

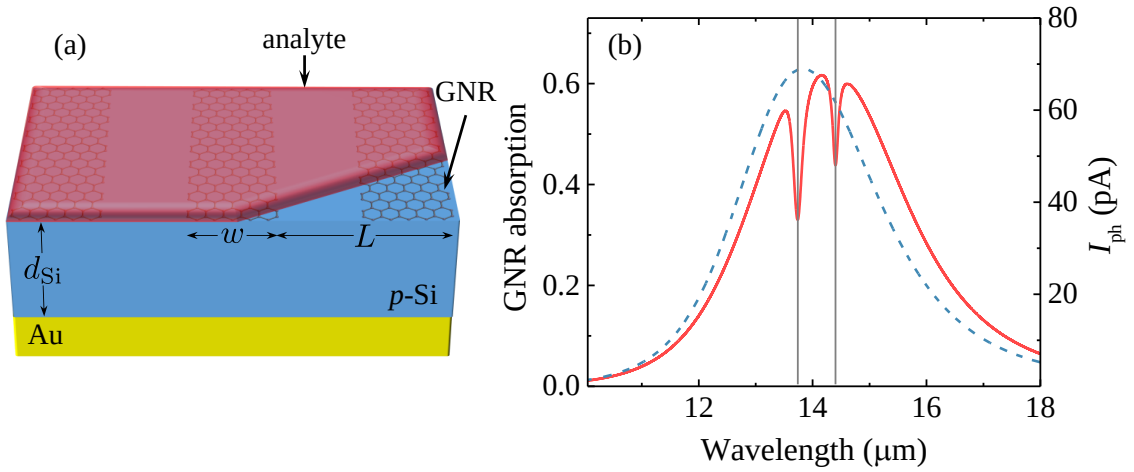

Figure 7.4: (a) Schematic of the proposed sensing scheme. A periodic GNR array of width w and period $L = 2w$ is placed on a p-Si substrate with an Au backmirror at a distance of d_{Si} = 1 μm. A thin layer of toluene (transparent red) is assumed to cover the whole GNR array. (b) Calculated SLG absorption for w = 40 nm, $E_{F,\mathrm{SLG}} \approx$ -0.36 eV, τ_{opt} = 40 fs with (dashed) and without (continuous) the 8 nm thick toluene layer. The vertical gray lines mark the absorption lines of toluene.

both optical-phonon scattering (eq. 3.42), including both phonon branches at the K- and Γ-points of graphene's Brillouin zone, as well as disorder assisted supercollision scattering (eq. 3.44). The latter strongly depends in short-range scatterers mean free path l, as demonstrated in chapter 6. For the GNR structure considered here, we assume l to be w-limited, i.e., $l = w$, since scattering at the edge of the ribbons limits the available mean free path l. The combined contributions of J_{op} and J_{sc} lead to an effective e-ph relaxation time $\tau_{e-ph} = c_{e,\mathrm{SLG}} \Delta T_{e,\mathrm{SLG}} / J_{e-ph} \sim 400$ fs [eq. 3.46], where $\Delta T_{e,\mathrm{SLG}}$ is the electronic temperature rise at equilibrium ($\Delta T_{e,\mathrm{SLG}} \ll T_0$ =300 K) and $c_{e,\mathrm{SLG}}\left(E_{F,\mathrm{SLG}}, T_{e,\mathrm{SLG}}\right)$ the electronic heat capacity. This τ_{e-ph} value is lower compared to the one for a continuous SLG sheet [$\sim$ 1 ps at $E_{F,\mathrm{SLG}} \approx$ 0.36 eV, fig. 3.13] due to the smaller mean free path l, which thus renders supercollision as the dominant cooling process for GNRs. We note once more that here we examine only the linear regime, i.e. low enough $\mathcal{P}$ so that $\Delta T_{e,\mathrm{SLG}}$ values are in the order of mK. Due to the much larger ($\times 10^3$) heat capacity of the SLG lattice compared to that of its carriers, we assume the lattice temperature to be fixed at $T_{l,\mathrm{SLG}}$ =300 K.

The thermionic electrical and thermal current densities across the Schottky junction are calculated using the Landauer transport formalism via eqs. 3.65 - 3.66. As demonstrated in the previous chapter, they strongly depend on the effective injection time of charge carriers from SLG to Si (τ_{inj}). The latter has several dependencies (e.g., Schottky interface quality, SLG contact resistance, $E_{F,\mathrm{SLG}}$ and $T_{e,\mathrm{SLG}}$), as discussed in the corresponding section 3.5.3. Here, we estimate a lower bound for τ_{inj} for the low temperature regime ($k_B T_{e,\mathrm{SLG}} \ll E_{F,\mathrm{SLG}}$) using $\tau_{\mathrm{inj}} \sim \hbar \left|E_{F,\mathrm{SLG}}\right| / \left(k_B T_{e,\mathrm{SLG}}\right)^2$ [381] yielding $\tau_{\mathrm{inj}} \approx$ 350 fs for $E_{F,\mathrm{SLG}}$ = - 0.36 eV and $T_{e,\mathrm{SLG}} \approx$ 300 K.

The photocurrent across the junction is calculated as $I_{ph} = J_{el}\, S/2$ (the 1/2 factor is because of half-coverage, i.e., $w/L = 0.5$). We assume incident power $\mathcal{P} \approx$ 9.35 nW. As expected, I_{ph} follows the trend of GNR absorption spectrum [dashed blue curve

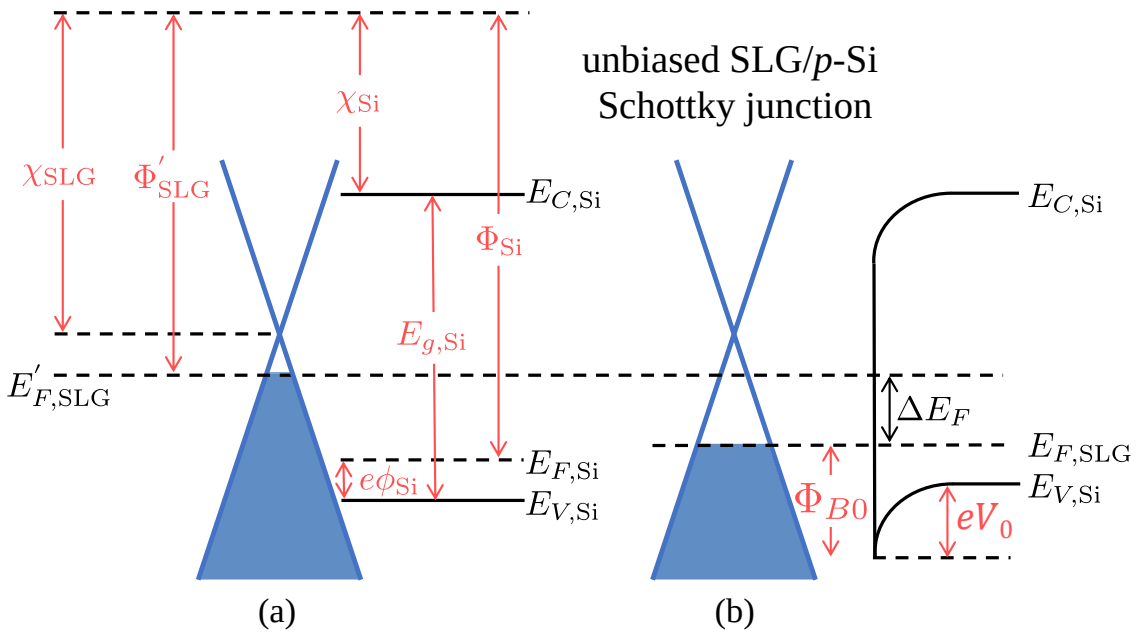

Figure 7.5: Energy levels of SLG and *p*-Si (a) before and (b) after they form a Schottky junction.

corresponding to the right $y-$axis of fig. 7.4(b)]. The external responsivity (eq. 2.4), for the configuration depicted in fig. 7.1(a) with $d_{\text{Si}} = 1$ μm, calculated at $\lambda = 14$ μm, is extracted having a value $R_{ext} \approx 1$ mA/W. Note that in the absence of reverse bias, in this configuration the dark current density is zero. The corresponding NEP (eq. 2.5) is NEP ≈ 1.4 nW/Hz$^{0.5}$ and the specific detectivity (eq. 2.6) $D^* \sim 5.5\times10^5$ cm Hz$^{0.5}$ W^{-1}, assuming photoactive area S equal to the diffraction limited spot as discussed above.

Upon analyte placement as for fig. 7.4(a), assuming toluene thickness $d_{tol} = 8$ nm, the photocurrent is reduced, as plotted in the red curve corresponding to the right $y-$axis of fig. 7.4(b). The chemical sensing signal I_S is then determined by the photocurrent difference between the calculation for bare GNR and the one including toluene, $I_S \equiv \Delta I_{ph} = I_{ph,bare} - I_{ph,toluene}$, which is plotted in fig. 7.6(a), showing peaks at the wavelengths corresponding to toluene molecular resonances. The peak at $\lambda_1 \approx 13.7$ μm is higher due to this mode's stronger absorptivity [465] (see fig. 7.3). Quantitative comparison between peaks can be done after subtraction of the baseline [red dashed line in fig. 7.6(a)]. The resulting spectrum is plotted in 7.6(b).

By operating SLG/Si Schottky diode at zero bias, with eliminated dark current, the noise signal (normalized to a 1Hz spectral band) is $\langle i_S^2 \rangle = \langle i_{sh}^2 \rangle + \langle i_J^2 \rangle$, where $\langle i_{sh}^2 \rangle$ is the shot noise contribution (eq. 2.1 and $\langle i_J^2 \rangle$ is the Johnson (thermal) noise contribution (eq. 2.2). For chemical sensing, when measuring a signal I_S, the effective total noise is contributed by both $I_{ph,bare}$ and $I_{ph,toluene}$, i.e. the total noise power is $\langle i_{S,tot}^2 \rangle = \langle i_{S,bare}^2 \rangle + \langle i_{S,toluene}^2 \rangle$ [stared dots in fig. 7.6(b)]. To quantify a limit of detection associated with photo-thermionic process, we calculate the minimum optical power $\mathcal{P}_{min}$ needed, i.e. signal to noise ratio SNR $= 1$, in order to detect the presence of an analyte. We define SNR, for each absorption line of the analyte, as SNR $= I_S/i_{S,tot}$. In the studied configuration, the main contribution to $i_{S,tot}$ is the Johnson noise, with the calculated $i_J \gg i_{sh}$ in the order of few pA and few fA respectively. Since Johnson noise does not depend on input power $\mathcal{P}$ (eq. 2.2), SNR can be approximated to scale linearly with the

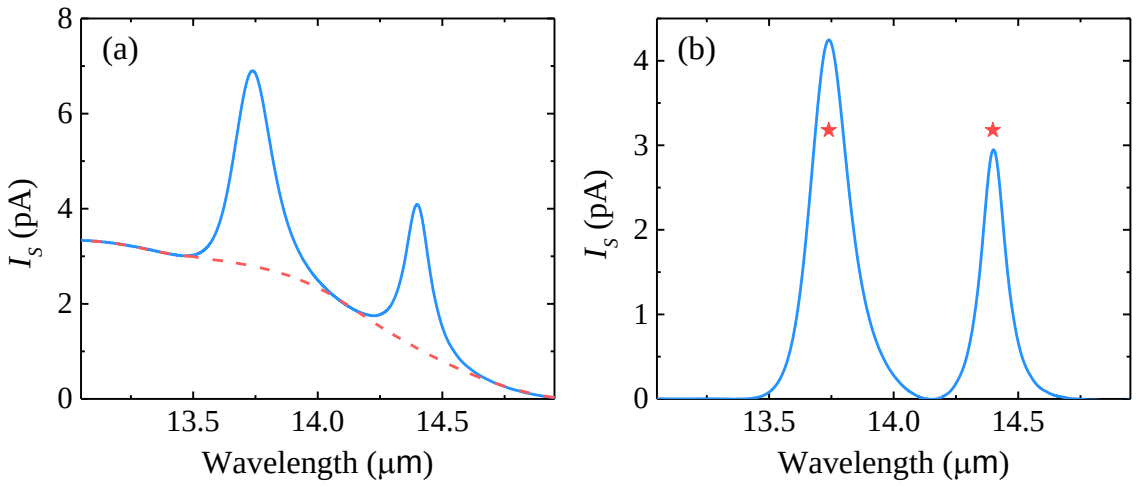

Figure 7.6: (a) Photocurrent difference (I_S) spectrum as calculated after the subtraction of I_{ph} spectra without and with toluene, assuming toluene thickness $d_{tol} = 8$ nm. The red dashed line marks the baseline of the spectrum. (b) Photocurrent after the subtraction of the baseline of (a), resulting to two peaks corresponding to toluene's molecular resonances. The stared dots mark the combined noise level of the two calculations (with and without toluene).

incident optical power, given the large (more than five decades) linear dynamical range od constant R_{ext} for SLG/Si Schottky junctions operating in the photo-thermionic regime at low input power, as discussed in chapter 6. This linear relationship, as calculated from our simulations for operation parameters as for fig. 7.4(b), is plotted in fig. 7.7 for the two absorption lines of toluene. Hence, SNR $= \alpha\mathcal{P}$ where α is a proportion coefficient. As a result, the limit of detection at SNR $= 1$ is $\mathcal{P}_{min} = 1/\alpha$. From fig. 7.7 the slope α is extracted as $\alpha_1 \approx 0.14\,\text{nW}^{-1}$ and $\alpha_2 \approx 0.10\,\text{nW}^{-1}$, where the subscript denotes the $\lambda_1 \approx 13.7$ μm and $\lambda_2 \approx 14.4$ μm lines respectively. The corresponding limits of detection are $\mathcal{P}_{min,1} \approx 7.1$ nW and $\mathcal{P}_{min,2} \approx 10$ nW respectively.

For $\mathcal{P} \approx 9.35$ nW, considered in figs. 7.4 and 7.6, the stronger absorbing toluene mode at $\lambda_1 \approx 13.7$ μm leads to SNR$>$1, while for $\lambda_2 \approx 14.4$ μm, SNR$\lesssim$1 as can be seen from fig. 7.7 and the stared dots of fig. 7.6(b). To validate the ability to distinguish the photocurrent peaks originating from the analyte presence at low $\mathcal{P}$, fig. 7.8 attempts to generate an "experimental", i.e. noisy, photocurrent signal I_S^{noise} by adding the noise contribution according to $I_S^{\text{noise}} = I_S \pm x\, i_{S,tot}$ where x is a pseudo-random number in the range [-1,1]. Peaks are still well distinguishable, especially after averaging (red dashed line in fig. 7.8) as typically applied in real experiments using multiple accumulation cycles. These results demonstrate the proposed concept for direct electrical detection of GNR-SPPs and its application for chemical sensing.

7.5 Optimization of the photodetection and sensing scheme

Next, the effect of the various operational parameters on PD metrics and $\mathcal{P}_{min}$ are explored. We first study the effect of $E_{F,\text{SLG}}$. Besides changing the SBH, $E_{F,\text{SLG}}$ variations

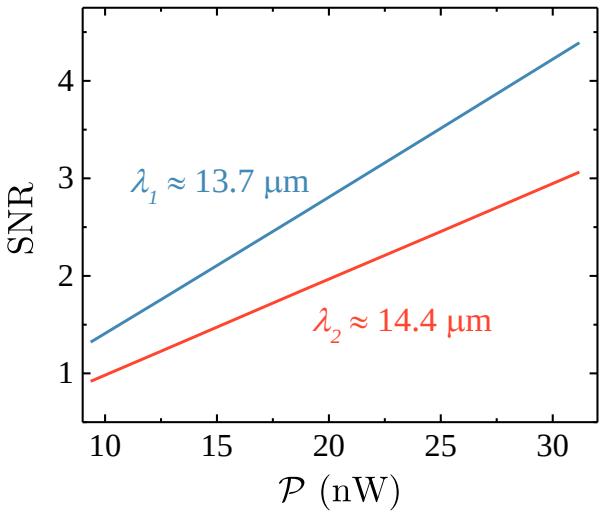

Figure 7.7: SNR as a function of $\mathcal{P}_{min}$ for the two absorption peaks of toluene. The parameters used for the calculations are as for fig. 7.4(b).

also require the re-evaluation of several other quantities, like the τ_{inj} lower bound, the width w to keep the GNR-SPP frequency fixed, the free carrier relaxation time τ_{opt}, and the mean free path l for supercollision scattering. These parameters are summarized in table 7.1 for three different values of $E'_{F,\text{SLG}}$ prior to Schottky junction formation.

$E'_{F,\text{SLG}}$ (eV)	-0.250	-0.350	-500
$E_{F,\text{SLG}}$ (eV)	-0.265	-0.358	-0.502
Φ_{B0} (eV)	0.408	0.314	0.169
τ_{inj} (ps)	260	350	490
τ_{opt} (fs)	30	40	55
w (nm)	30	40	55
l (nm)	30	40	55

Table 7.1: Values of the parameters assumed in our calculations. Initial (before contact with *p*-Si) $E'_{F,\text{SLG}}$, Fermi level $E_{F,\text{SLG}}$ after Schottky junction formation, zero bias SBH Φ_{B0}, carrier injection time τ_{inj}, free carrier relaxation time τ_{opt}, PAGR width w and mean free path for supercollision scattering l.

Fig. 7.9(a) plots $\mathcal{P}_{min}$ calculations assuming different $E_{F,\text{SLG}}$, using the parameters as for table 7.1. Higher $E_{F,\text{SLG}}$ (and w) values lead to lower $\mathcal{P}_{min}$, i.e., detection capability at lower incident optical power. This is because increasing $E_{F,\text{SLG}}$ brings to: a) smaller SBH, which triggers an enhanced thermionic emission across SLG/Si Schottky interface and b) larger w, which leads to longer τ_{opt}, increased intraband SLG conductivity and higher light absorption, as well as larger supercollision mean free path l and thus less cooling, yielding higher $T_{e,\text{SLG}}$ for the same $\mathcal{P}$. A slight counterbalance comes from the longer τ_{inj}, as shown in Table 7.1. The overall trend, however, remains that of a lower $\mathcal{P}_{min}$ for larger $E_{F,\text{SLG}}$ values. The performance differences, upon changing $E_{F,\text{SLG}}$, can also be understood by the R_{ext} and NEP values regarding the configuration of fig. 7.1(a). At the

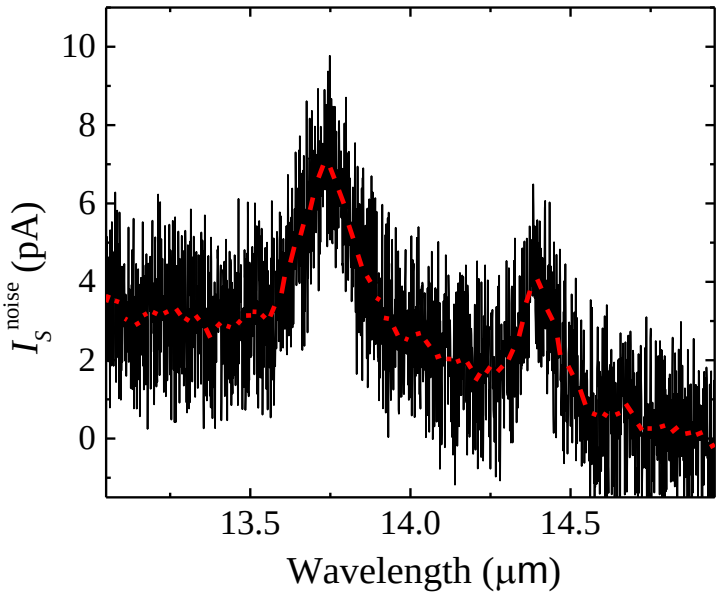

Figure 7.8: I_S spectrum, including noise inserted in the calculations using a pseudo-random number generator. The red dashed line corresponds to a adjacent-averaging smoothing filter on the I_S spectrum.

central wavelength ($\lambda = 14$ μm), the lower graphene doping (e.g. $E_{F,\mathrm{SLG}} =$ -0.265 eV) results to higher SBH (Table 7.1) and $R_{ext} \approx 40$ μA/W, NEP ≈ 7.4 nW/Hz$^{0.5}$ and $D^* \approx 10^5$ cm Hz$^{0.5}$ W^{-1}. For higher SLG doping ($E_{F,\mathrm{SLG}} =$ -0.50 eV, i.e. lower SBH), R_{ext} increases and reaches $R_{ext} \approx 110$ mA/W with a lower NEP ≈ 190 pW/Hz$^{0.5}$ and $D^* \approx 4\times10^6$ cm Hz$^{0.5}$ W^{-1}. There is, however, a lower limit of a SBH that can be achieved in the given configuration, in the order of $\Phi_{B0}^{min} \approx eV_0$ that depends on Si doping (eq. 3.57). The latter would allow achieving lower Φ_{B0}^{min} using higher p-Si doping, but would also lead to a fraction of light loss in Si (due to free carrier absorption), thus lowering the $T_{e,\mathrm{SLG}}$ increase and associated thermionic current across the Schottky junctions. Note also, that a reduced ambient temperature will not improve performance. Because of the thermionic nature of the photocurrent generation, the responsivity will get strongly suppressed at lower temperatures (eq. 3.65) and result in a NEP increase, despite the reduction of the Johnson noise.

7.6 Effect of analyte size on sensing scheme

Up until now, toluene layer with thickness $d_{tol} = 8$ nm was considered as the analyte. $\mathcal{P}_{min}$ behavior as a function of d_{tol}, assuming $E_{F,\mathrm{SLG}} \approx -0.36$ eV (and the corresponding operational parameters in Table 7.1), was also examined and the results are plotted it in fig. 7.9(b). For vanishing toluene thickness, $\mathcal{P}_{min}$ is increased, i.e., higher optical power is needed to detect a thinner layer of the analyte, as expected. On the other hand, $\mathcal{P}_{min}$ plateaus after $d_{tol} \sim 35$ nm. This is due to SPP fields extending only a few tens of nm away from the GNRs [figs. 7.2(b)- 7.2(d)]. Further increase in d_{tol} does not change the overall I_{ph} yield, highlighting the significance and major impact of surface-enhanced fields of GNR SPPs to directly and electrically probe the toluene's (or other analyte's) absorption lines.

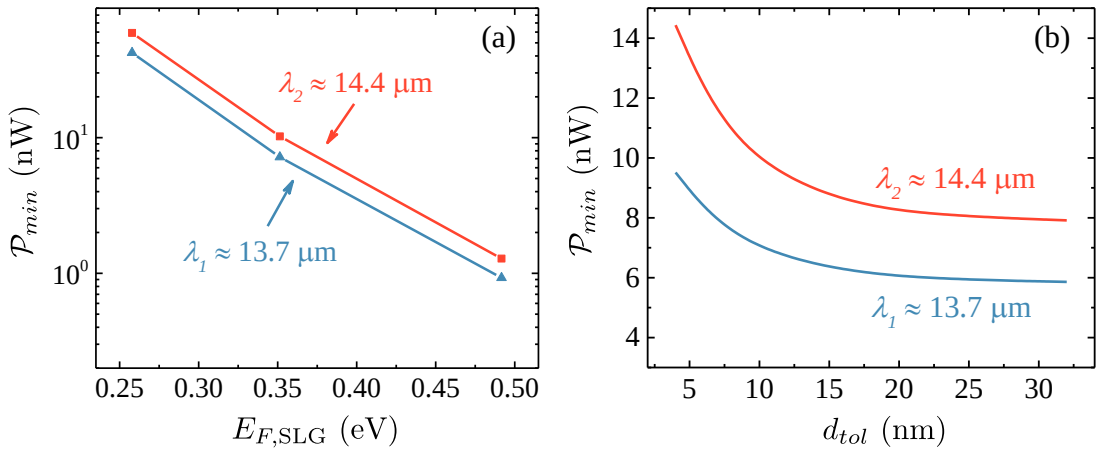

Figure 7.9: (a) Calculated $\mathcal{P}_{min}$ for different values of $E_{F,\mathrm{SLG}}$ - w. (b) $\mathcal{P}_{min}$ as a function of d_{tol}. In (b) we used the parameters as for the second column of Table 7.1.

7.7 Temporal response of the proposed PD scheme

Finally, the limiting factors regarding the temporal response of the studied device are the same as for chapter 6. These are: the transition time of charge carriers across the Si depletion region (τ_{tr}), the photon lifetime inside the cavity formed by GNRs and the Au backmirror (τ_{ph}) and the charge/discharge resistance-capacitance (RC) time constant of the Schottky diode (τ_{RC}).

The transition time of charge carriers across the depletion region is given by eq. 6.3 and depends on depletion region width χ_d. The later depends on $E_{F,\mathrm{SLG}}$ and can be extracted from eqn. 3.58. We find $\chi_d = 58$ nm, 46 nm and 17 nm for the $E_{F,\mathrm{SLG}} = -0.265$ eV, -0.358 eV and -0.502 eV cases respectively. These values yield transit times τ_{tr} =0.58 ps, 0.46 ps and 0.17 ps for the three aforementioned cases of $E_{F,\mathrm{SLG}}$, resulting to cutoff frequencies $f_{tr} \equiv (2\pi\tau_{tr})^{-1} = 274$ GHz, 344 GHz and 964 GHz respectively.

The optics limited frequency is determined by the photon lifetime inside the cavity and, for the configuration studied in this chapter, is given by $f_{opt} = c/(n_{\mathrm{Si}}\, 2d_{\mathrm{Si}}\, Q)$ where $2d_{\mathrm{Si}}$ is the roundtrip length inside the cavity formed between GNRs and the Au backmirror, c/n_{Si} is the light velocity inside this cavity, with n_{Si} the real part of the *p*-Si refractive index and $Q \equiv \omega_0/\Delta\omega$ the cavity quality factor. The latter is found to be $Q \sim 5$ for all the three cases of $E_{F,\mathrm{SLG}}$, leading to $f_{opt} \sim 9$ THz.

Finally, the RC limited frequency is given by $f_{RC} = (2\pi R_{el} C_{tot})^{-1}$, with $R_{el} = R_{\mathrm{Si}} + R_{\mathrm{SLG}}$ the combined series resistance of Si and SLG and C_{tot} the total capacitance due to junction and SLG quantum capacitance contributions. The *p*-Si substrate's resistance is calculated using $R_{\mathrm{Si}} = (d_{\mathrm{Si}} N_{a,\mathrm{Si}} e \mu_{h,\mathrm{Si}})^{-1} \sim 1.4$ kΩ/□, where d_{Si} the Si substrate thickness, $N_{a,\mathrm{Si}}$ the Si dopant concentration, e the electron charge and $\mu_{h,\mathrm{Si}} = 450$ cm^{2}V^{-1}s^{-1} the Si hole mobility [20]. The SLG contribution to the total resistance is $R_{\mathrm{SLG}} = (\sigma_{\mathrm{DC,SLG}})^{-1}$. SLG dc conductivity is calculated using eq. 3.14, assuming a minimum charge puddle concentration $n_{\mathrm{min,SLG}} \sim 10^{12}$ cm^{-2} and $\mu_{q,\mathrm{SLG}} \sim 10^3$ cm^{2}V^{-1}s^{-1} for the SLG mobility, resulting to $R_{\mathrm{SLG}} \sim 1$ kΩ, 0.6 kΩ and 0.3 kΩ for $E_{F,\mathrm{SLG}} = -0.265$ eV, -0.358 eV and -0.502 eV respectively. The total capacitance of the studied device is $C_{tot}^{-1} = C_j^{-1} + C_{q,\mathrm{SLG}}^{-1}$. The junction capacitance is given by $C_j = S\, \epsilon_{\mathrm{Si}}\, \epsilon_0/(2\, \chi_d)$, where S is the device area, assuming it equal to the diffraction limited spot as discussed above, and

Table 7.2: Calculated PD (lines 2 – 5) and sensing (lines 6–7) metrics for different values of initial (before contact with *p*-Si) Fermi level $E'_{F,\mathrm{SLG}}$. In lines 6 – 7 a toluene thickness of d_{tol} = 8 nm was assumed for the calculations.

$E'_{F,\mathrm{SLG}}$ (eV)	-0.265	-0.350	-500
R_{ext} (mA/W)	0.04	1	110
NEP (pW/Hz$^{0.5}$)	7400	1400	160
D^* (cm Hz$^{0.5}$ W^{-1})	1.1×10^5	5.7×10^5	4.4×10^6
f_{cut} (GHz)	1.27	1.22	0.52
$\mathcal{P}_{min,1}^{d_{tol}=8\,\mathrm{nm}}$ (nW)	42	7	0.9
$\mathcal{P}_{min,2}^{d_{tol}=8\,\mathrm{nm}}$ (nW)	59	10	1.2

the factor $1/2$ is because of half coverage. We calculate $C_j \approx 0.05$ pF, 0.07 pF and 0.2 pF for $E_{F,\mathrm{SLG}} = -0.265$ eV, -0.358 eV and -0.502 eV respectively. SLG quantum capacitance is given by eq. 3.15, estimated to be $C_{q,\mathrm{SLG}} = 2$ pF, 2.7 pF and 3.6 pF for $E_{F,\mathrm{SLG}} = -0.265$ eV, -0.358 eV and -0.502 eV respectively. Combining all of the above, the RC limited frequency of the proposed device is estimated to be f_{RC} =1.27 GHz, 1.22 GHz and 0.52 GHz for $E_{F,\mathrm{SLG}} = -0.265$ eV, -0.358 eV and -0.502 eV respectively.

As for the case of thermionic SLG/Si Schottky PDs examined in chapter 6, the limiting factor for the temporal response of the proposed device is the charge/discharge RC time constant of the Schottky diode. Thus, the cutoff frequencies of the configurations studied here are $f_{cut} \sim f_{RC} \approx 1.27$ GHz, 1.22 GHz and 0.52 GHz with the respected overall response times τ_{resp} ≈4.9 ns, 5 ns and 12 ns for $E_{F,\mathrm{SLG}} = -0.265$ eV, -0.358 eV and -0.502 eV respectively.

Table 7.2 summarizes the PD and sensing metrics calculated in this chapter for the 3 different values of initial (before contact with *p*-Si) graphene Fermi level $E'_{F,\mathrm{SLG}}$ as for table 7.1.

7.8 Conclusions

In this chapter, the SLG/Si thermionic PD scheme developed in chapter 6 is expanded in the low-photon energy ($\hbar\omega \ll E_{F,\mathrm{SLG}}$) regime. The self-consistent simulation framework presented previously in this thesis was combined with FDTD simulations, using the commercial FDTD solver Lumerical, to study the use of GNRs in a SLG/Si Schottky junction configuration, to electrically detect graphene plasmons. Under realistic considerations for all material and device parameters involved, calculations suggest an increased I_{ph} yield at the SPP resonant wavelengths. Optimized devices can reach external responsivity ≈ 110 mA/W with a corresponding NEP ≈ 190 pW/Hz$^{0.5}$, $D^* \approx 4\times 10^6$ cm Hz$^{0.5}$ W^{-1} and response time $\tau_{resp} \approx 12$ ns, corresponding to a cutoff frequency of ≈ 0.5 GHz. This platform for electrical detection of SLG plasmons can operate either as a mid-IR photodetector or as a chemical sensor, utilizing the SEIRA technique, able to detect the presence of an analyte in the vicinity of GNRs and generate a direct electrical readout. The operation of such a sensor was studied and the quantitative relations for its detection and sensitivity limits were extracted, suggesting sensing capability using low power input in the order of

$\sim 1 - 10$ nW.

The methods and conclusions derived in this chapter are applicable throughout the MWIR, LWIR and FIR, where SLG SPPs can be realized. Limitations in reaching shorter wavelengths may arise due to fabrication constraints in reducing w and reaching large E_F values, as well as material availability in utilizing a semiconducting substrate with smaller dielectric constant. Assuming $w_{min} \approx 20$ nm (due to fabrication constraints) and $E_{F,\mathrm{SLG}}^{max} \approx 0.55$ eV for *p*-Si with $N_{a,\mathrm{Si}} = 10^{17}$ cm^{-3}, there is a lower bound at $\lambda \approx 8$ μm. There is no limitation, however, for longer wavelengths, since w can always be increased/tuned accordingly, and the proposed scheme is based on thermionic emission, which is not limited by the substrate's bandgap. This work facilitates the theoretical background for a unique tunable multi-band optics-free photodetector and/or chemical sensor based on graphene plasmons.

Chapter 8

THz self-induced absorption modulation on a graphene-based thin film absorber

Interaction of intense terahertz (THz) waves with graphene based modulation devices holds great potential for the optoelectronic applications. A thin film graphene-based THz perfect absorbing device, whose absorption characteristics can be modulated through THz self-actions in the sub-ps time scale, is presented. Experiments* utilizing intense broadband THz pulses were performed by our colleagues, on a device consisting of single layer graphene placed on an ionic liquid substrate, back-plated by a metallic back-reflector, with the graphene doping level mediated through electrostatic gating. An absorption modulation of more than three orders of magnitude from the initial perfect absorption state, when the device is illuminated with THz field strengths in the range of 102 kV/cm to 654 kV/cm was experimentally recorded. Detailed theoretical analysis, utilizing the self-consistent simulation framework presented in this thesis, indicates that the origin of the THz response is the THz induced heating of the graphene's carriers, that leads to a reduction of its conductivity, and consequently to reduced absorption of the THz radiation. Our analysis also reveals the temporal dynamics of the THz induced temperature increase of graphene carriers, illustrating the ultrafast, sub-ps nature of the overall process. These results can find applications in future dynamically controlled at optics and spatiotemporal shaping of intense THz electric fields.

* The experiments performed in IESL-FORTH at Ultrashort Nonlinear Laser Interactions ans Sources (UNIS) research group [469] by Dr. Anastasios Koulouklidis under the supervision of Prof. Stelios Tzortzakis. The theoretical analysis and interpretation was done in collaboration with Dr. Anna Tasolamprou of the photonic-phononic and meta-materials (PPM) group [470], located in IESL-FORTH, under the supervision of Prof. Maria Kafesaki.

This chapter is based on:

- A. Koulouklidis, A. Tasolamprou, **S. Doukas**, E. Kyriakou, S. Ergoktas, C. Daskalaki, E. Economou, C. Kocabas, E. Lidorikis, M. Kafesaki and S. Tzortzakis *Ultrafast Terahertz Self-Induced Absorption and Phase Modulation on a Graphene-Based Thin Film Absorber*, ACS Photonics 2022, 9, 9, 3075–3082 (2022), https://doi.org/10.1021/acsphotonics.2c00828

8.1 Introduction

Terahertz (THz) radiation holds the possibility to bridge photonics and electronics, lying above the upper limit of attainable frequencies of the latter [471]. THz electromagnetic waves' non-ionizing nature and their ability to directly probe rotational and vibrational modes of large biological molecules, renders them useful for biomedical applications [472, 473], industrial quality control and food inspection [474]. Moreover, THz wireless communications are expected to play a key role in emerging 6G technologies [213, 475]. Conventional materials, however, have poor performances in applications regarding detection and manipulation of THz radiation, since commonly used semiconductors have bandgap that far exceeds the THz photon energies while most optical glasses and dielectrics strongly absorb THz radiation. Novel schemes for THz wave manipulation have been proposed, including diodes [476], metamaterials [477] and more [478]. One of the most promising materials for developing THz optoelectronics is graphene [24, 43, 219], given its unique electronic and optical properties discussed previously in this thesis. Graphene-based schemes have been reported for a wide variety of applications in the THz part of the spectrum, including photodetection [66, 479–481], high-harmonic generation [282, 330], hot-carrier assisted frequency conversion [482], saturable absorbers for passively mode-locked THz sources [79] and THz modulation [56, 80, 483].

In chapter 5 of this thesis, an optical modulation scheme operating in the IR part of the spectrum was studied, with graphene's optical response controlled via an external gating voltage. In these configurations, however, temporal limitations, associated with the parasitic RC effects of the electronic circuitry used to electrostatically dope graphene, are arising. Graphene's optical response can be modulated via an alternative, ultrafast manner, in all-optical modulation schemes [218]. A way to achieve this is to exploit the hot-carrier induced changes in graphene's conductivity [280] to realize sub-ps transient modulation of graphene's THz optical response [80]. Moreover, the recent developments in high-power THz sources [484–486], have resulted in the report of a plethora of hot-carrier induced nonlinear phenomena in graphene [64, 282]. Experimental studies have demonstrated the emission of THz induced high-harmonics [330], graphene plasmon nonlinear absorption [487], saturable absorption [79], and the electric tunability of the graphene's nonlinearity [488]. These nonlinear phenomena are related to the collective thermodynamic response of graphene carriers [280] upon the application of intense THz excitation, resulting in THz induced heating. It is thus imperative to be able to accurately describe graphene carrier dynamics upon intense THz light absorption and realistically simulate relevant devices.

In this chapter, THz time-domain spectroscopy (THz-TDS) experiments, regarding the intense THz excitation of a graphene based thin film absorber, are presented. Perfect absorption is recorded in a Salisbury screen configuration, i.e., a uniform graphene sheet placed on top of a dielectric, supported by a metallic backmirror. Upon THz excitation, ultrafast self-induced absorption modulation was observed, surpassing three decades of measured change in reflectance when the incoming THz field strength increases from 102 kV/cm to 654 kV/cm. To unveil the origins of this nonlinear response, a detailed theoretical analysis based on the self-consistent simulation framework developed during this thesis was performed. Graphene absorption modulation is attributed to hot-carrier induced conductivity reduction, leading to THz absorption lowering. Excellent agreement between simulations and experiment is found, validating the model developed in this thesis. Moreover, through the application of the analysis presented in detail in this chapter, the temporal

dynamics of the THz induced temperature elevation are mapped, extracting a variety of graphene parameters' transient response just by using the fitting scheme developed here and applying it in reflectance measurements.

8.2 Experimental setup and measurements

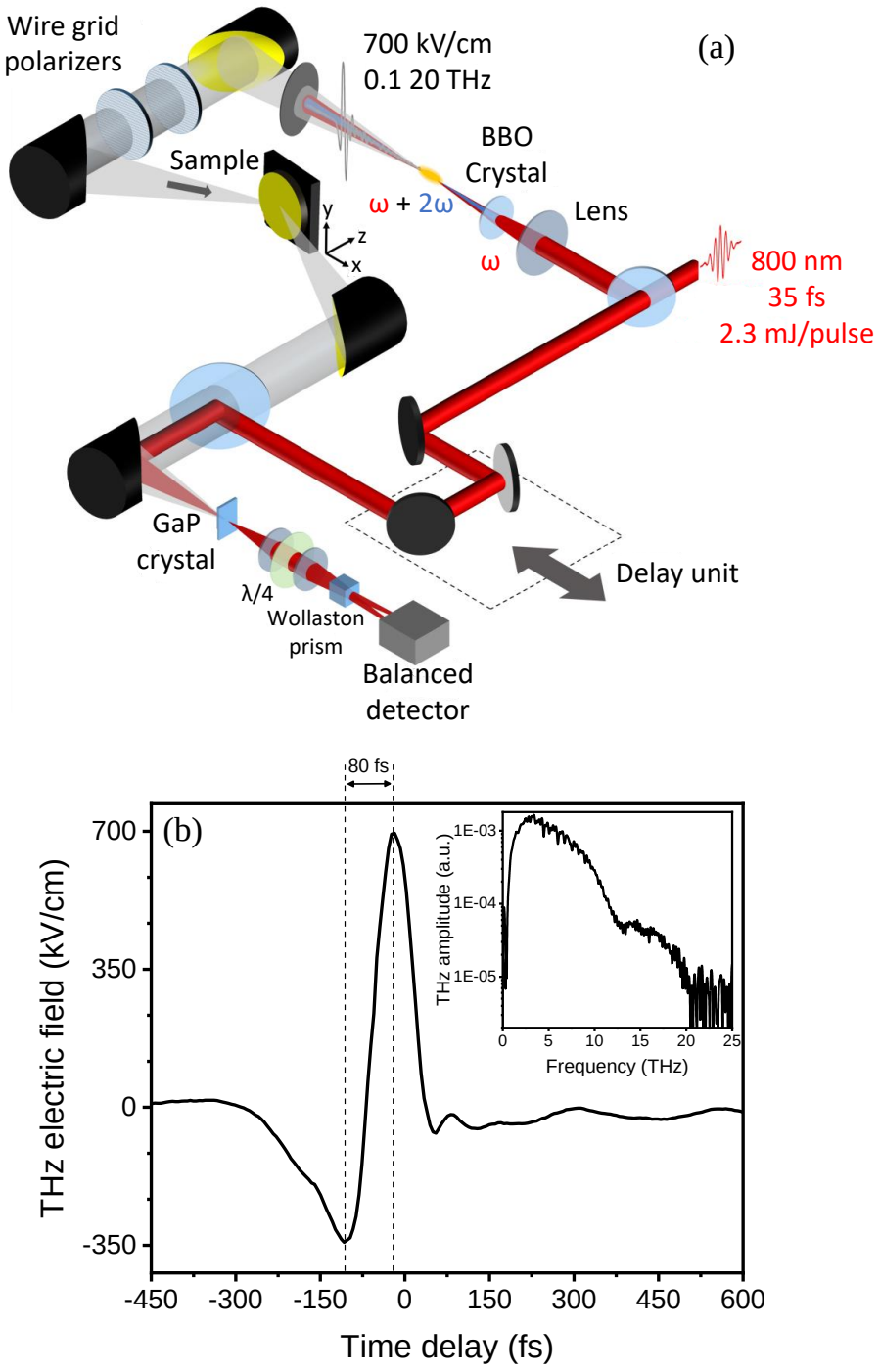

Figure 8.1: (a) Schematic of the experimental THz-TDS setup. (b) Experimentally measured incident THz electric field. The inset plots the corresponding power spectrum.

A powerful THz-TDS setup [fig. 8.1(a)] was utilized by our colleagues in IESL-FORTH [469,470] to excite the graphene-based device presented in this chapter. THz pulse generation is realized using two-color filamentation of ultrashort laser pulses in air [486,489]. Filamentation is generated when an intense ultrashort laser pulse propagates in transparent media. The pulse is self-focused through the Kerr effect, leading to an increased intensity which will promote the self-focusing even further. The intensity becomes high enough to ionize the medium, through multi-photon and tunneling ionization, leading to plasma generation. The ionization process then locally drops the intensity while the generated plasma defocuses the trailing part of the beam. The above procedure can repeat itself multiple times, if the wavepacket has enough power to re-initiate a second defocusing stage. The ionized gas results in a THz transient, formed by coherent plasma oscillations driven by the ponderomotive force or by transition radiation from accelerated carriers driven by wakefield acceleration [490]. In two-color filamentation, a fundamental laser pulse and its second harmonic are focused together in gases like ambient air [fig. 8.1(a)], producing laser-plasma filaments that emit THz radiation. The use two-color filamentation can lead to the generation of THz broadband pulses with high intensities [486,489]. Figure 8.1(b) plots the incident THz electric field, along with its power spectrum, produced by the above procedure and used in the experiments studied here. The THz beam is then driven to a pair of wire grid polarizers, allowing for the control of its intensity, and then illuminates the sample at an angle of 16^0 with a TM polarization [fig. 8.1(a)]. The reflected THz waves are then driven to a 100 μm thick gallium phosphide (GaP) crystal for detection through electro-optic (EO) sampling. In this detection method, the THz beam co-propagates with a linearly polarized probe laser beam through GaP. The THz electric field changes the polarization ellipsoid of the refractive index in the EO crystal, inducing changes in the polarization of the probe pulse. These changes in the probe's polarization are translated to intensity changes by an analyzer, e.g. by using a Wollaston prism [489]. A delay unit is used to control the delay between THz and probe beams, allowing for the transient detection of THz induced changes in the probe's polarization, upon incidence in a pair of balanced photodiodes [fig. 8.1(a)]. In the setup utilized for the experiments studied here, a 12 ps temporal window was achieved.

Figure 8.2(a) shows a schematic of the graphene-based device studied in the aforementioned experiments. CVD grown SLG is placed in top of a a 25 μm-thick porous polyethylene membrane containing room temperature ionic liquid electrolyte (DEME-TFSI) [55] and a gold electrode as a back reflector [55,56]. In this configuration, $E_{F,\mathrm{SLG}}$ can be fine-tuned by applying an external bias voltage between graphene and the and the grounded Au backmirror. When no bias is applied, SLG is *p*-doped due to the nature of transfer and grow process [55,56], with high enough $E_{F,\mathrm{SLG}}$ to satisfy critical-coupling conditions [55,80].

Figure 8.2(b) plots the normalized measured THz electric fields, for the cases of lowest (102 kV/cm) and highest (654 kV/cm) studied THz field strengths. Given the high bandwidth of the THz-TDS system employed in these experiments, the resolvement of both reflective interfaces of the studied device is possible. They manifest themselves as two distinct peaks on the THz field: The first one, at -0.25 ps, originates from the reflection of the incident THz pulse on SLG while the one at 0 ps originates from the Au backmirror [see Figure 8.2(c)]. From fig. 8.2(b) it is evident that SLG reflectivity is reduced, compared to the one from the Au back reflector, at higher THz field strengths, implying a THz induced negative photoconductivity.

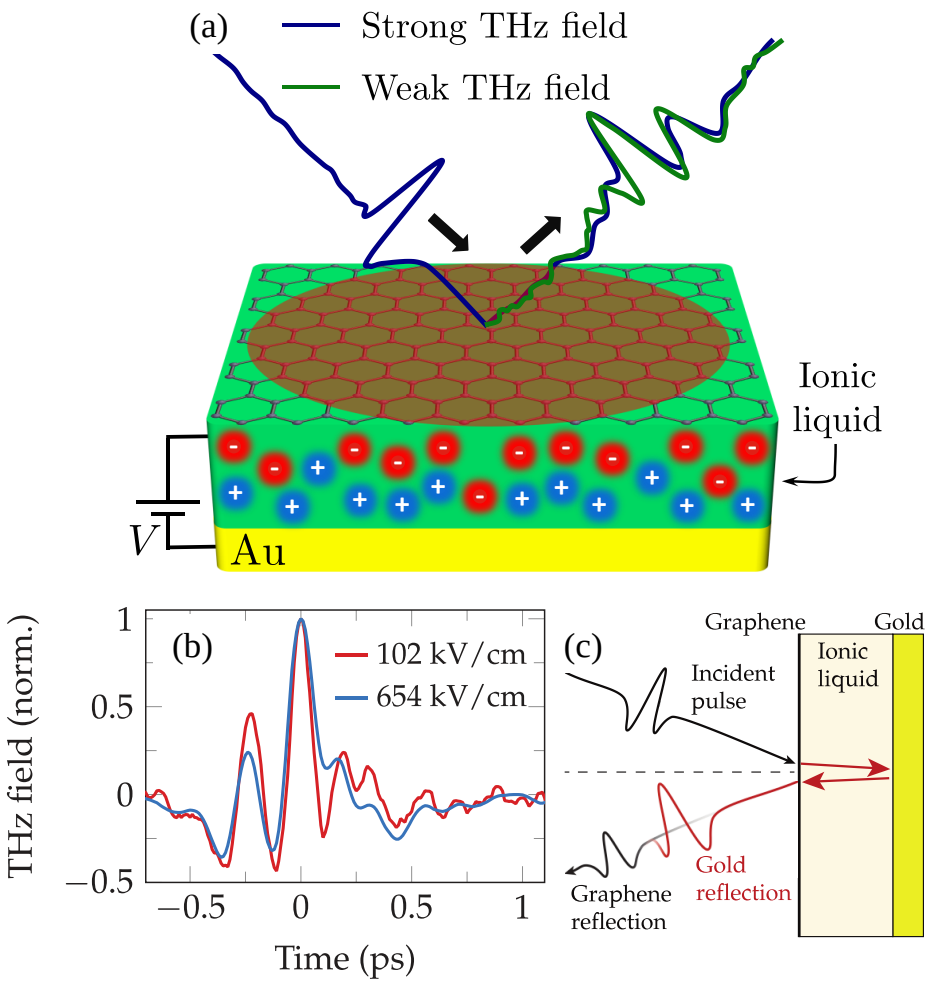

Figure 8.2: (a) Schematic representation of the graphene absorber structure. The device is composed of SLG, a membrane soaked with room-temperature ionic liquid electrolyte having thickness d = 25 μm, and a metallic back-reflector. $E_{F,\mathrm{SLG}}$ can be controlled through electrostatic gating. The THz beam illuminates the sample at an angle of 16^0 with TM polarization, having a spot size with a diameter of 210 μm. (b) Normalized THz electric fields in the case of 102 kV/cm (red curve) and of 654 kV/cm (blue curve). (c) Schematic representation illustrating the formation of the THz field shape after its reflection on the studied device.

The THz reflectivity due to SLG, by recording the peak of the THz electric field that corresponds to the latter [time = -0.25 ps in fig 8.2(b)], as a function of gate voltage was also measured. Figure 8.3(a) plots these measurements for different incident peak electric fields in the available range of 102 to 654 kV/cm. All curves were normalized to SLG CNP, defined as the gating voltage at which the graphene's conductivity becomes minimum and, consequently, so does THz reflectivity due to the increased transmission.

THz reflectivity, at zero gating voltage, shows a self-induced modulation with increasing THz field strength. At low THz fields, a modulation of the THz reflectivity up to 50 % at 0 V is recorded. However, at high THz field strengths, this modulation drops to 10 %. All the following measurements were performed at 0 V, where the maximum modulation on the graphene reflectivity was observed.

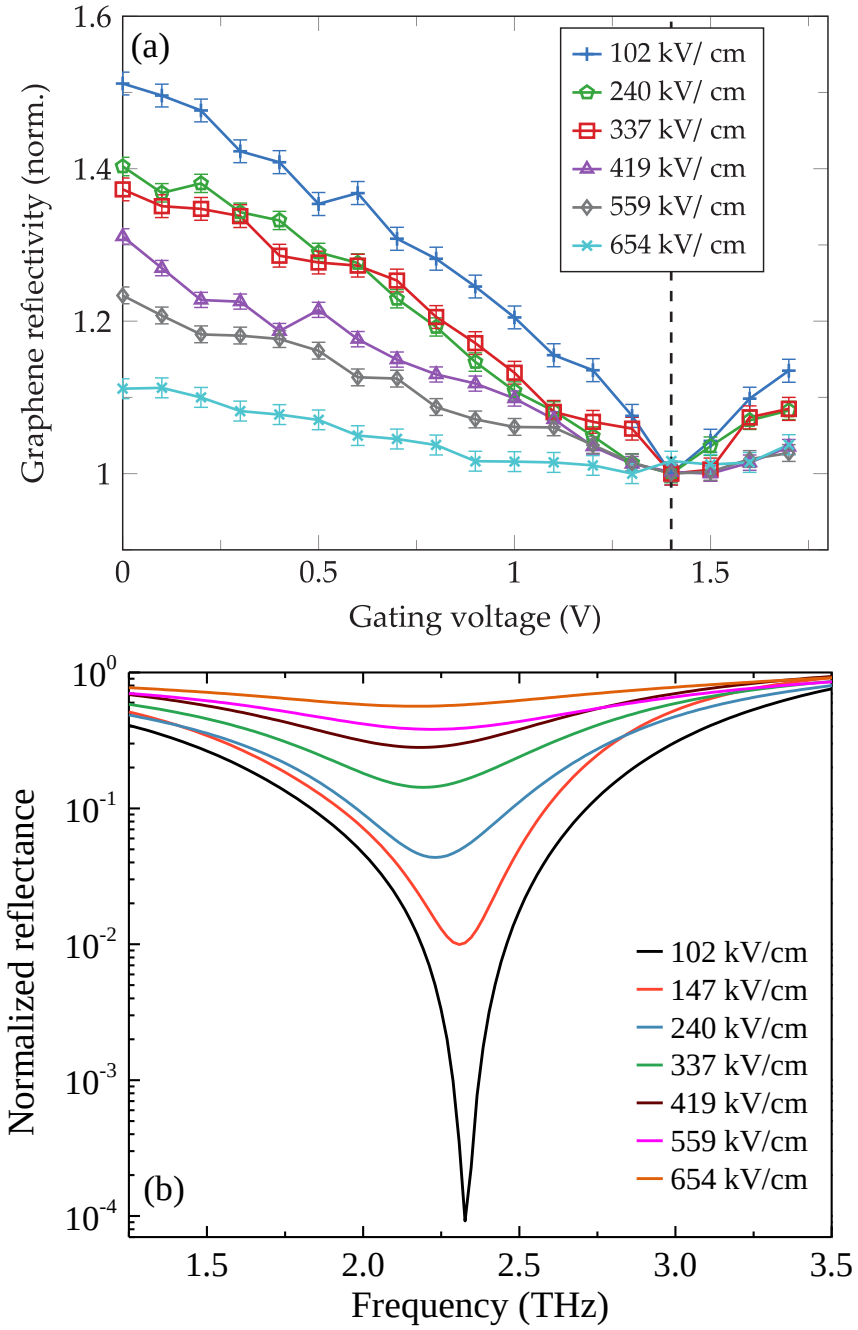

Figure 8.3: (a) Peak THz reflectivity signal of the gated SLG alone, i.e. corresponding to the signal at −25 ps as for fig 8.2(b), as a function of THz field strength and gating voltage. All curves are normalized to the response at CNP of graphene, indicated with the dashed line at 1.4 V. (b) Experimentally measured reflectance spectra of the studied device at zero bias, as a function of incident THz field strength in the range of 102–654 kV/cm. All spectra are normalized at the CNP.

The aforementioned THz self-induced photoconductivity modulation, is expected to impact the absorption characteristics of the whole device. The reflectance spectra, normalized to the reflectance at CNP (i.e., $\approx$ 1.4 V bias), for varying THz field strengths are plotted in fig. 8.3(b). For the minimum THz field strengths used here (102 kV/cm) the device operates as a perfect absorber, presenting a resonance at $f \approx 2.33$ THz, defined by the device design and the angle of incidence of the THz radiation. The reflectance of

the device at this frequency drops down to $\approx 10^{-4}$. However, as the THz field strength increases, the perfect absorption conditions are disrupted and the reflectance of the device increases to 0.57, for the maximum available THz field strength of 654 kV/cm. This corresponds to a THz induced absorption modulation of more than three orders of magnitude. Moreover, a slight red shift of the resonance with increasing THz field strength is observed. In order to exclude any nonlinearities induced by the intense THz fields on the ionic liquid substrate, a similar sample was investigated separately without the graphene layer, and we did not observe any THz nonlinear response.

8.3 Simulation model

To understand the origin of the observed THz induced nonlinear response, a detailed theoretical analysis was performed, utilizing the self-consistent simulation framework previously outlined in this thesis. A qualitative representation of the cause of THz induced absorption self-modulation is depicted in fig. 8.4. After the absorption of the incoming THz radiation, graphene carriers thermalize in an ultrafast ($\sim$ fs) timescale [183, 184]. Heat dissipation occurs in a much slower ($\sim$ ps) timescale, as shown previously in this thesis, via emission of optical phonons [333, 345] and disorder assisted supercollisions [328, 333, 351]. This leads to heat accumulation in the graphene carrier bath, raising the electronic temperature $T_{e,\mathrm{SLG}}$. The elevated $T_{e,\mathrm{SLG}}$ results in a reduced graphene chemical potential [fig. 3.4], due to net carrier density conservation (eq. 3.12), and a broadened Fermi-Dirac distribution of graphene carriers [fig. 3.15]. This reduces the intraband transitions, as explicitly evaluated by the Kubo formula (eq. 3.19), leading to a reduced intraband conductivity [280,324], and thus to a reduced THz absorbance of graphene [64].

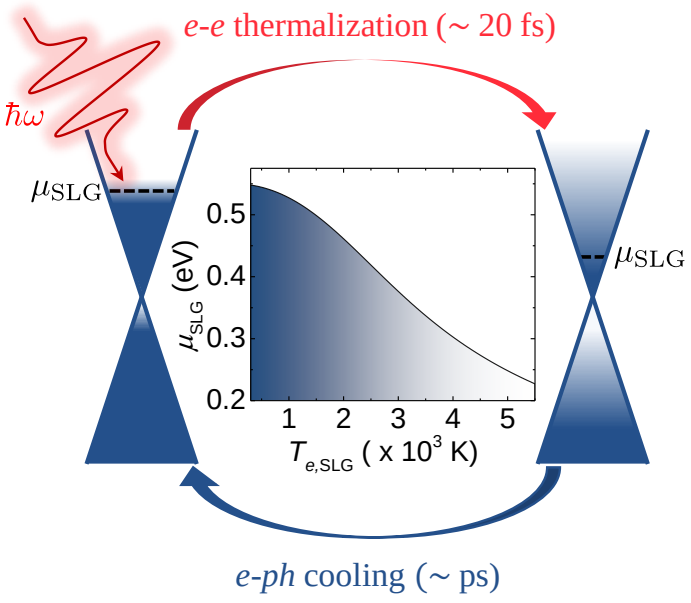

Figure 8.4: Schematic representation of graphene's carrier distribution upon heating, following THz excitation. Chemical potential (red line) and carrier distribution are depicted at room temperature (left) and $T_{e,\mathrm{SLG}} \gg 300$ K (right). The middle graph plots the reducing graphene chemical potential with increasing T_e, as a consequence of carrier conservation (eq. 3.12).

In order to quantitatively describe the above, graphene carrier and temperature dynamics are time integrated using 4RK and a two-temperature model, as described in detail in section 3.4.4 and chapter 6. Note that in the THz regime we don't have to account for non-equilibrium photoexcited carriers $\delta_{n,\mathrm{SLG}}$, since the latter arise from interband transitions (eq. 3.51), which are Pauli-blocked in the low energy THz part of the spectrum. As a result, we deal with a pair of coupled rate equations, for $T_{e,\mathrm{SLG}}$:

$$c_{e,\mathrm{SLG}}\frac{\partial T_{e,\mathrm{SLG}}}{\partial t} = \widetilde{P_{in}}(t) - J_{e-ph}\left(T_{e,\mathrm{SLG}}, T_{l,\mathrm{SLG}}\right) \tag{8.1}$$

and for $T_{l,\mathrm{SLG}}$:

$$c_{l,\mathrm{SLG}}\frac{\partial T_{l,\mathrm{SLG}}}{\partial t} = J_{e-ph}\left(T_{e,\mathrm{SLG}}, T_{l,\mathrm{SLG}}\right) - \Gamma_{\mathrm{SLG-sub}}\left(T_{l,\mathrm{SLG}} - T_{\mathrm{sub}}\right) \tag{8.2}$$

As in the previous studies of this thesis, electronic and lattice heat capacities are given by eqs. 3.16 and 3.50 respectively, while graphene carrier and lattice temperatures, which are generally different, are denoted by $T_{e,\mathrm{SLG}}$ and $T_{l,\mathrm{SLG}}$ respectively. $\widetilde{P_{in}}(t)$ denotes the fraction of the incident power density absorbed by SLG. The optical response of the whole configuration (i.e., including the substrate and the Au backmirror) is calculated using TMM. The SLG absorbed power density, however, is not calculated in a single frequency but rather for the whole incident THz spectrum, i.e.:

$$\widetilde{P_{in}}(t) = \int_{\omega_1}^{\omega_2} \alpha_{\mathrm{SLG}}\left(\omega, T_{e,\mathrm{SLG}}\right) P_{in}(\omega, t) d\omega \tag{8.3}$$

where $\alpha_{\mathrm{SLG}}\left(\omega, T_{e,\mathrm{SLG}}\right)$ is the SLG absorption at frequency ω and temperature $T_{e,\mathrm{SLG}}$, calculated via TMM as discussed later in this section, while ω_1 and ω_2 correspond to ~ 0.1 and 20 THz respectively [see inset of Figure 8.1(b)]. For the input power density a Gaussian pulse time-dependence is assumed, i.e.,

$$P_{in}(\omega, t) = P(\omega)\exp(-B(t/\tau_w)^2) \tag{8.4}$$

with $B = 4\ln(2)$, where $\tau_w \approx 150$ fs the full width at half maximum of the pulse and $P(\omega)$ the spectral profile of the input pulse. $P(\omega)$ is determined experimentally [see inset of Figure 8.1(b)] and is normalized so that $\int_0^\infty P_{in}(\omega, t)dt$ agrees with the experimentally measured pulse fluence. $J_{e-ph}(T_{e,\mathrm{SLG}}, T_{l,\mathrm{SLG}})$ is the thermal current density from electron to phonon bath, calculated as discussed previously, accounting for both optical-phonon scattering (eq. 3.42) and disorder-assisted supercollision scattering. For the latter short-range scatterers with a mean free path l are assumed (eq. 3.44), yielding a supercollision thermal current density scaling with l^{-1}. The cooling rate of graphene lattice into the substrate is assumed to have a value $\Gamma_{\mathrm{SLG-sub}} \approx 20\ \mathrm{MWm^{-2}\,K^{-1}}$, as previously discussed (more values were examined with little to no effect on the final reflectance spectra) while the substrate temperature T_{sub} is fixed for simplicity at 300 K, since no substrate heating was observed in the experiments.

THz light absorption in graphene is governed by intraband transitions, described by the frequency dependent intraband graphene conductivity. As discussed in section 3.2.1, for intraband dominated optical conductivity at high ($\gg 300$ K) $T_{e,\mathrm{SLG}}$, the dependence of τ_{opt} on carriers' energy must be taken into account. To account for this, graphene's optical

conductivity is calculated as for [280]:

$$\sigma^{\text{opt}}_{\text{intra,SLG}}(\omega;\mu_{\text{SLG}},T_{e,\text{SLG}},\tau_{\text{opt}}) = \frac{ie^2}{\pi\hbar^2}\int_0^\infty \frac{E}{\omega+i\tau^{-1}_{\text{opt}}(E)}dE \times \left[\frac{\partial f_{FD}(-E;\mu_{\text{SLG}},T_{e,\text{SLG}})}{\partial E} - \frac{\partial f_{FD}(E;\mu_{\text{SLG}},T_{e,\text{SLG}})}{\partial E}\right] \tag{8.5}$$

Free carrier relaxation time τ_{opt} dependence on carriers' energy is modeled assuming unscreened long-range scattering in Coulomb impurities (eq. 3.25), as expected in CVD grown graphene [279, 280, 282, 324]. In this case, τ_{opt} scales linearly with carrier energy, with a proportionality constant γ depending on impurity concentration, as for eq. 3.25, and was treated as a free parameter in the fitting scheme of this study, described in detail in the following section. A full microscopic description can be used to account for effects of screening [327] and electron-phonon scattering [349] on τ_{opt}. However, at the high $E_{F,\text{SLG}}$ (≥ 0.2 eV) and substrate supported graphene with low ($< 10^4$ cm^2/Vs) mobility used in our study, it is found to result in an overall linear dependence of τ_{opt} with carrier energy [64, 324]. This linear scaling has also been successfully implemented in describing conductivity changes upon carrier heating in previous studies [280, 282]. Thus, to avoid the addition of extra free parameters (which could lead to overfitting the experimental data) we follow the simplified linear scaling model of the unscreened case and fit the proportionality constant γ and graphene $E_{F,\text{SLG}}$ to the experimental results.

Using eq. 8.5 for graphene's Drude conductivity, the dielectric function was calculated, from which graphene's absorption α_{SLG} was determined and inserted in TMM. The substrate's contribution to the optical response is determined by fitting the device's reflectivity, prior to graphene placement, to experimental measurements [8.5(a)], assuming a 25 μm substrate thickness. Dispersion of the measurements can be attributed to noise contributions, especially for the low THz field strengths considered in the experiments (i.e., 102 kV/cm and 147 kV/cm), the latter being close to the limit of detection of the utilized detection scheme. To compensate for this, the average value of the experimental spectra was calculated and the substrate's dielectric response was fitted using a single Lorentz oscillator [491]. The fit result to the average experimental spectra is plotted in fig. 8.5(a), yielding very good agreement between TMM calculations and experiments. The extracted Lorentz parameters are: $\epsilon_\infty = 3.29$, $\Delta\epsilon = 1.45$ eV, $\hbar\Omega = 5.42$ meV and $\hbar\Gamma = 9.28$ meV, where ϵ_∞ is the value of the dielectric function at infinite frequency, $\Delta\epsilon$ the oscillator strength, $\hbar\Omega$ the transition frequency and $\hbar\Gamma$ the decay rate of the Lorentz term.

The overall optical response of the proposed device, including the contributions of the substrate and the backmirror, is calculated by employing the Fresnel equations using TMM. Finally, the reflection spectrum of the whole device is calculated as:

$$R(\omega) = \frac{\int_0^\infty P_{in}(\omega,t)R(\omega,t)dt}{\int_0^\infty P_{in}(\omega,t)dt} \tag{8.6}$$

where $R(\omega,t)$ is the time-dependent reflection resulting from TMM, which includes all the definitions of eqns. 8.1-8.5, self-consistently updated during the time integration within the developed 4RK scheme, described previously in this thesis.

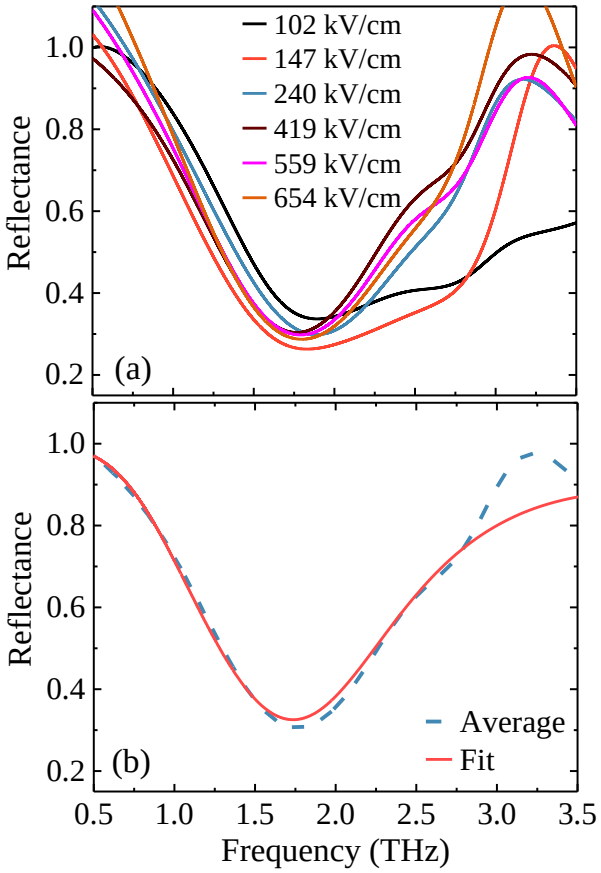

Figure 8.5: (a) Experimental spectra of the reflectance acquired from the studied configuration prior to SLG placement. (b) Lorentz oscillator fit in the average value of the experimental spectra.

8.4 Fitting Scheme

The free parameters used in the fitting scheme employed here are graphene's Fermi level $E_{F,\mathrm{SLG}}$, the proportionality constant γ for long-range Coulomb scattering [280, 282] and the mean-free path for supercollision scattering l [328, 351]. The main contribution to the extracted reflectance spectra comes from the first two parameters (i.e., $E_{F,\mathrm{SLG}}$ and γ), while supercollision mean-free path mainly impacts the value of minimum reflectance at resonance. This can be understood since l affects the cooling power of graphene's hot carriers, while $E_{F,\mathrm{SLG}}$ and γ are directly correlated to graphene's optical response, hence altering both the minimum value of reflectance at resonance as well as this minimum's spectral position.

As a result, the method followed in the fitting scheme employed here is the following: A wide region of $E_{F,\mathrm{SLG}}$ and γ was scanned and the simulation results were compared to the experimental measurements. To quantify the deviation between calculations and experiment, the squared differences of the minimum reflection $\delta_{R_{\mathrm{min}}}$ and its position $\delta_f^{R_{\mathrm{min}}}$ was extracted as for:

$$\begin{aligned} \delta_{R_{\mathrm{min}}} &= \left(R_{exp}^{\mathrm{min}} - R_{sim}^{\mathrm{min}}\right)^2 \\ \delta_f^{R_{\mathrm{min}}} &= \left(f_{exp}^{R_{\mathrm{min}}} - f_{sim}^{R_{\mathrm{min}}}\right)^2 \end{aligned} \tag{8.7}$$

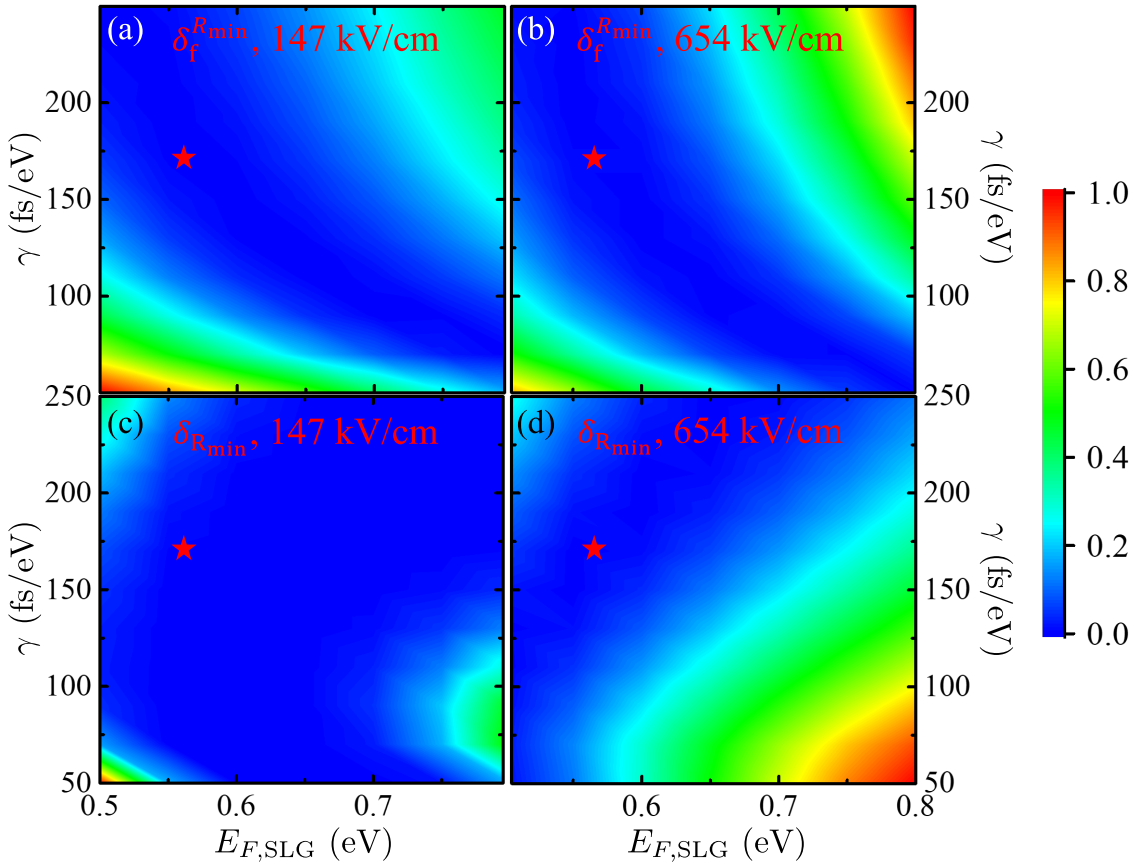

Figure 8.6: Colormaps of the normalized squared differences between simulations and experiment as a function of $E_{F,\mathrm{SLG}}$ and γ. (a) and (b) plots the deviation regarding the position of the minimum reflectance $\delta_f^{R_{\mathrm{min}}}$ for 147 kV/cm and 654 kV/cm THz field strengths respectively. (c) and (d) plots the deviation regarding the value of the minimum reflectance $\delta_{R_{\mathrm{min}}}$ for 147 kV/cm and 654 kV/cm THz field strengths respectively. All calculations were performed assuming $l = 75$ nm.

This procedure was performed for the highest (654 kV/cm) and the second lowest (147 kV/cm) field strengths of the experiments. The lowest (102 kV/cm) field strength was not chosen for the fitting procedure, to avoid fitting the simulations with experimental measurements that could potentially include large noise contributions, since they were acquired near the limit of detection of the experimental scheme.

Figure 8.6 plots the (normalized) colormaps of $\delta_f^{R_{\mathrm{min}}}$ (a-b) and $\delta_{R_{\mathrm{min}}}$ (c-d), assuming $l = 75$ nm. The stared dots show the final values chosen after this fitting procedure, and adopted for the rest of this chapter, that better replicate the experiments. These are $E_{F,\mathrm{SLG}} = 0.56$ eV and $\gamma = 170$ fs/eV.

Figure 8.7 plots the effect of supercollision mean-free path variation in the calculated spectra for the $E_{F,\mathrm{SLG}}$ and γ values and THz field strengths mentioned above. It is evident that even large sweeps in l values only affect the minimum reflectance value extracted from the simulations. A value of $l = 75$ nm is adopted for the rest of this chapter, since it was found to better replicate the experimental measurements for all the studied THz field strengths.

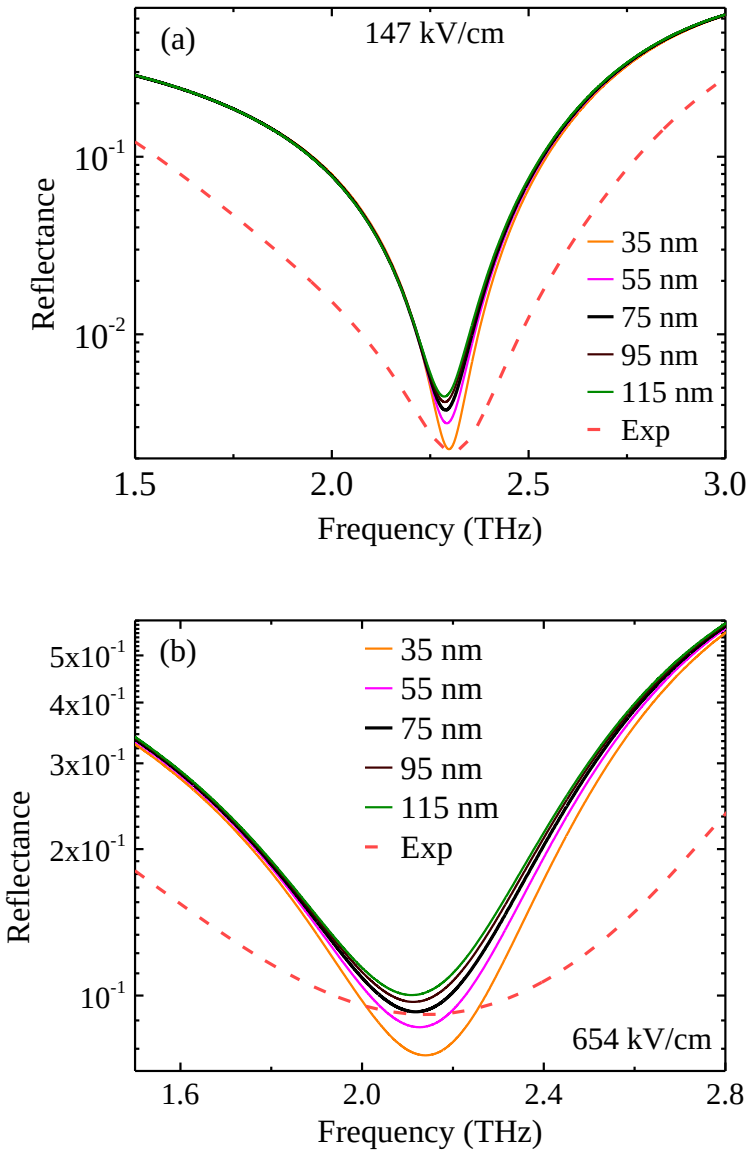

Figure 8.7: Calculated spectra of the studied device for different values of supercollision mean-free path l assuming $E_{F,\mathrm{SLG}} = 0.56$ eV and $\gamma = 170$ fs/eV. Dashed lines plots the experimentally acquired spectra. The results are plotted for (a) 147 kV/cm and (b) 654 kV/cm THz field strengths.

Figure 8.8 plots the calculated spectra along with the experimental measurements for the extracted values of the presented fitting scheme, i.e., $E_{F,\mathrm{SLG}} = 0.56$ eV, $\gamma = 170$ fs/eV and $l = 75$ nm for all the measured THz field strengths. Excellent agreement between theory and experiment was found regarding the position of the resonant frequency. The exact value of the minimum reflectance is replicated better at higher field strengths and large deviation from the experimental data is observed only in the lower field strength of 102 kV/cm, which may originate from noise contribution in the measurements at these very low ($\sim 10^{-4}$) reflectance values originating from the lower THz field strength examined in this study. Deviations between calculations and measurements were also observed in the shape of the spectra far from the resonant frequency (figs. 8.7 and 8.8). The resonances have a sharper profile in theory compared to experiment. The latter can be attributed

to inhomogeneous broadening originating from substrate thickness and graphene doping fluctuations across the measurement spot size ($\sim$ 210 μm diameter).

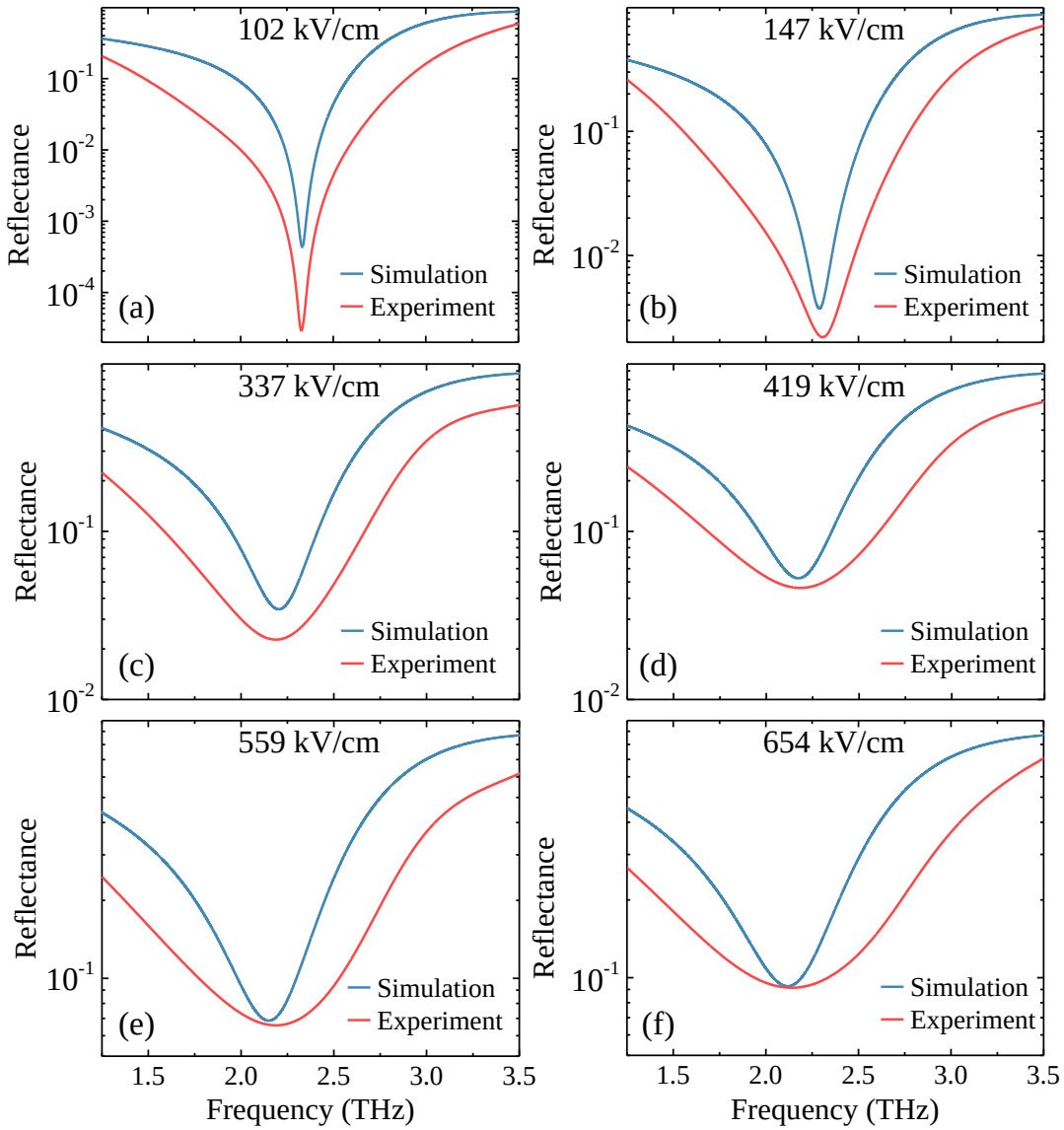

Figure 8.8: Experimental (red) and calculated (blue) reflection spectra for $E_{F,\mathrm{SLG}} = 0.56$ eV, $\gamma = 170$ fs/eV and $l = 75$ nm for all the THz field strengths examined in this study.

Figure 8.9 plots the reflectance spectra for graphene at CNP, i.e. under 1.4 V bias. The values of l and γ extracted from the aforementioned fitting procedure were adopted while $E_{F,\mathrm{SLG}}$ was treated as a free parameter. The experimental spectra of the studied configuration with graphene at CNP present a slight dispersion [fig. 8.9(a)], so the fitting procedure was performed by taking the average value of these measurements. Graphene's Fermi level at CNP was extracted at $E_{F,\mathrm{SLG}} \approx 200$ meV, and the corresponding reflectance spectrum is plotted in fig. 8.9(b) along with the mean value of the experimental measurements. The extracted value for $E_{F,\mathrm{SLG}}$ at CNP can be attributed to residual doping of graphene after transfer on the ionic substrate and is in line with previous reports regarding similar devices [55, 56, 334].

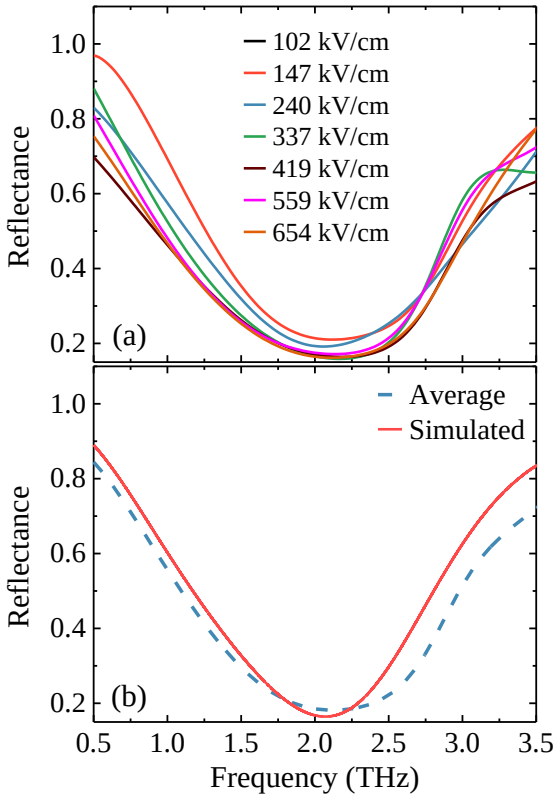

Figure 8.9: Reflectance spectra od the studied device with graphene at CNP under 1.4 V bias. (a) Experimental measurements at various field strengths (b) Average experimental l spectrum along with simulations assuming $E_{F,\mathrm{SLG}} \approx 200$ meV, $\gamma = 170$ fs/eV and $l = 75$ nm.

8.5 Simulation results and interpretation

Good overall quantitative agreement is found between calculations and experiment [see fig. 8.10(b)] for $E_{F,\mathrm{SLG}} \approx 0.56$ eV, $l \approx 75$ nm and $\gamma \approx 170$ fs/eV. The latter yields a free carrier relaxation time of $\tau_{\mathrm{opt}} \approx 95$ fs at room temperature, which corresponds to a carrier mobility of $\mu_{q,\mathrm{SLG}} \approx 1700$ cm^{2}V^{-1}s^{-1}. The values for $E_{F,\mathrm{SLG}}$ and τ_{opt} extracted from the aforementioned fitting scheme match very well to previous reports in similar devices [55, 56]. Moreover, the supercollision mean free path is within the range of previous reported values for graphene on a dielectric substrate [328, 351]. These results validate the self-consistent simulation framework developed in this thesis and demonstrate the usefulness of this model as a reliable tool for extracting graphene's parameters using as input the experimental optical measurements.

Figure. 8.10(b) shows the calculated reflectance spectra, for the experimentally examined THz field strengths, normalized to the reflectance spectra for graphene at CNP (i.e., 1.4 V bias, $E_{F,\mathrm{SLG}} \approx 200$ meV). We observe a similar behaviour with the experimental findings [see fig. 8.3]. As the THz field increases, so does the calculated reflectance, presenting also the characteristic red-shift of the resonance observed in the experiment. The absorption resonance is due to critical coupling of THz waves into the Fabry – Perot cavity formed by the graphene reflector and the backmirror and is sharper in theory compared to experiment. The latter can be attributed to inhomogeneous broadening, as discussed in the previous section. At frequencies far from resonance, on the other hand, an anti-

resonance is expected, where the total reflection of the graphene-mirror system is larger than the reflection at CNP [where graphene is non-reflecting, fig. 8.9] and thus the normalized reflectance reaches above unity [fig. 8.10(a)]. It should be noted that this behavior is observed in the theoretical spectra but not in the experimental ones, which is most likely due to the aforementioned inhomogeneous broadening. Figure. 8.10(b) plots the minimum normalized reflectance, as a function of peak THz field strength, alongside the experimental measurements, showing a very good agreement between theory and experiment. It is evident that a higher THz field strength, yields larger overall reflectance. As discussed previously, this can be attributed to the heating of graphene carriers and the subsequent lowering of graphene chemical potential and the reduction of its intraband conductivity leading to disrupted critical coupling conditions. Therefore, graphene absorbance is reduced, and as a result reflectance of the incoming THz radiation increases.

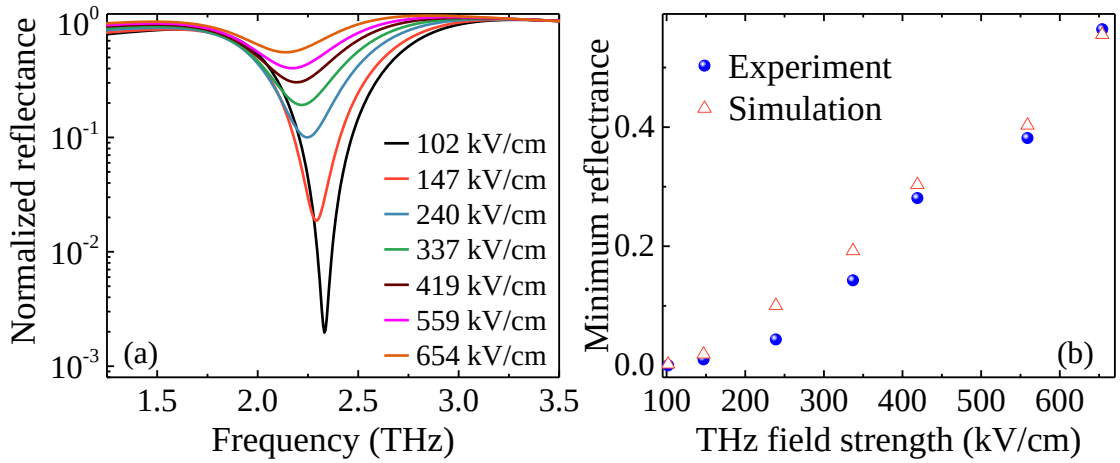

Figure 8.10: (a) Reflectance spectra, for different THz field strengths regarding the cavity structure presented in fig. 8.2(a), as calculated from our model using $E_{F,\mathrm{SLG}} \approx 0.56$ eV, $l \approx 75$ nm and $\gamma \approx 170$ fs/eV. All spectra are normalized at the CNP. (b) Experimental and calculated minimum reflectance of the studied device, as a function of THz field strength.

The self-consistent simulation framework developed in this thesis allows one to gain insight into the carrier temporal dynamics, during THz excitation. Figure 8.11(a) shows the temporal evolution of carrier temperature, for the parameters extracted of the fitting scheme presented in this chapter, during, and shortly after the THz excitation. In Figure 8.11(b) the respective temporal evolution of the real part of intraband conductivity (which is directly proportional to THz graphene absorbance) is plotted, at the resonant frequency. This elucidates how the near instantaneous thermalization of graphene carriers, in combination with their retarted cooling, leads to vanishing conductivity at higher THz field strengths. The latter is the source of the non-linear absorption modulation observed in this study. Furthermore, we observe that the overall phenomenon occurs on the sub-ps time scale, illustrating the ultrafast nature of the observed modulation.

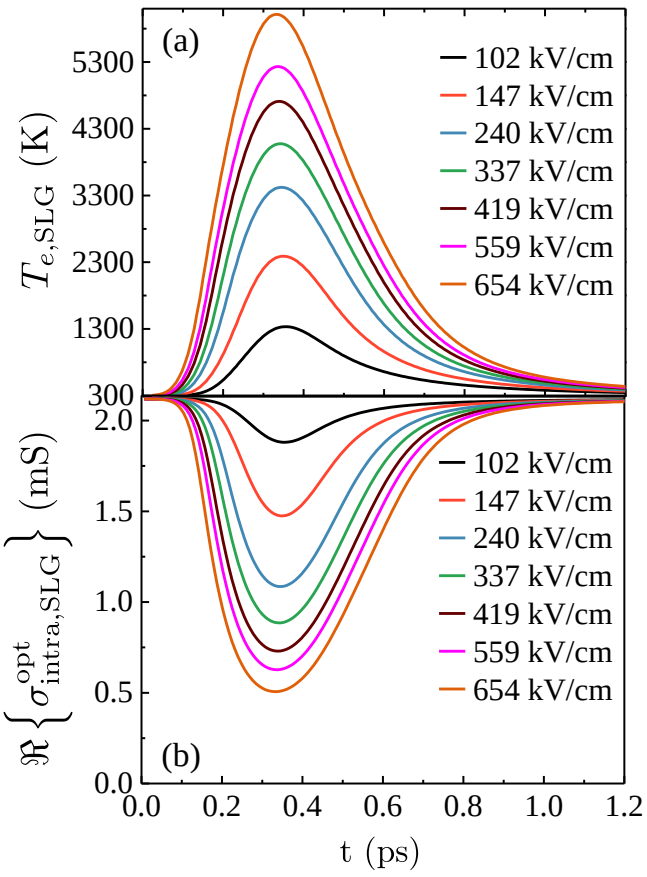

Figure 8.11: Simulated temporal evolution of (a) graphene carriers' temperature and (b) real part of intraband conductivity at the resonant frequency as calculated from the self-consistent simulation framework developed in this thesis, for the parameters extracted from the fitting scheme presented in this chapter.

8.6 THz nonlinearity dependence on excitation field strength

Finally, in this section, a quantification of the nonlinear response of the proposed device upon THz excitation is presented. For completeness, both device's response, i.e. THz reflectance, as well as the material property that causes the response variation after illumination, i.e. graphene's intraband conductivity, are considered.

Figure 8.12 plots the temporal evolution of the relative intraband conductivity change of graphene $\Delta\sigma/\sigma_0$, where $\sigma_0 = 2.12$ mS the graphene's conductivity at time $t = 0$. For these calculations the modeling framework discussed above was used, assuming resonant frequency $f \approx 2.33$ THz and graphene's parameters as extracted to match the experimental measurements, i.e. $E_{F,\mathrm{SLG}} \approx 0.56$ eV, $l \approx 55$ nm and $\gamma \approx 170$ fs/eV. For fig. 8.12(a) the full studied device as for the experiments was considered, i.e. including the ionic liquid substrate and the Au backmirror, while for fig. 8.12(b) graphene suspended in air, the latter having the same $E_{F,\mathrm{SLG}}$, γ and l as for 8.12(a), was assumed. Both schemes result in negative photoconductivity after illumination and the subsequent graphene carrier heating, as expected for graphene's intraband conductivity for $E_{F,\mathrm{SLG}}$ away from CNP ($E_{F,\mathrm{SLG}} \geq 0.1$

eV) [64, 280, 282, 324]. Intraband conductivity evolution, during and shortly after THz excitation, is similar in both cases. Conductivity change is more profound in the full device case [8.12(a)], due to the increased graphene absorption imposed by the Fabry-Perot cavity created between graphene and the Au backmirror, which leads to enhanced carrier heating.

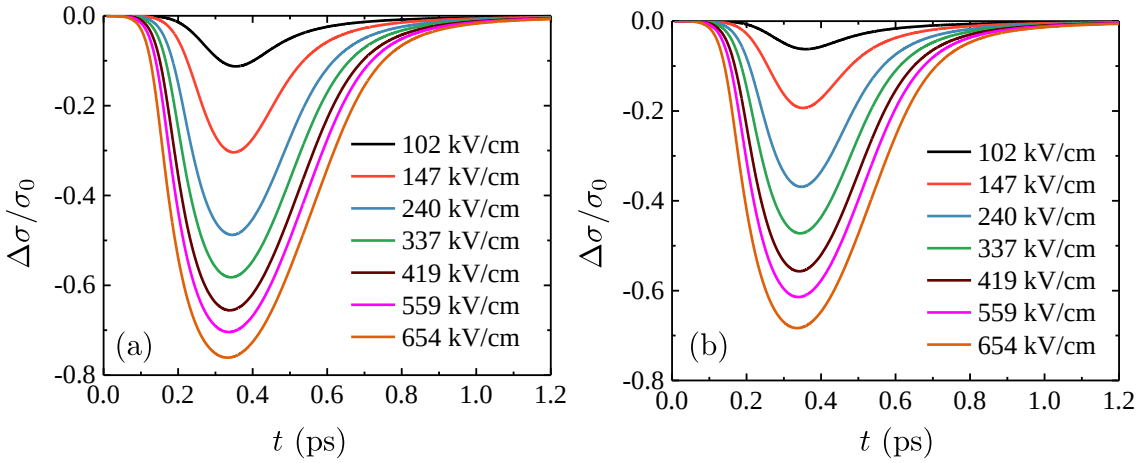

Figure 8.12: Temporal evolution of graphene's intraband conductivity, as extracted from our calculations, for the resonant frequency of $f \approx 2.33$ THz. The calculation performed assuming (a) the full studied device, as for the experiments and (b) free-standing graphene with the same parameters ($E_{F,\mathrm{SLG}}$, γ and l) suspended in air.

Figure 8.13 plots the temporal evolution of the differential reflectance $\Delta R/R_0$, where R_0 the reflectance at time $t = 0$. The latter has a value $R_0 \approx 0.0024$ in the case of the full studied structure and $R_0 \approx 0.26$ in the case of air-suspended graphene. The calculations regarding fig. 8.13 are extracted assuming graphene parameters as discussed previously, yielding the best fit to experimental measurements. For graphene on the studied configuration, as for the experiments, THz excitation with increasing field strength leads to increased (reduced) overall reflectance (absorbance) [fig. 8.13(a)]. For air suspended graphene, however, THz excitation results in reduced overall THz reflectance [fig. 8.13(b)].

The change of sign in the THz excitation induced response between these two schemes, arises from the fact that the studied structure satisfies critical coupling conditions [55, 80] at room temperature, as discussed in the previous sections. The THz excitation and the subsequent carrier heating, which leads to reduced intraband conductivity, results in breaking these coherent conditions and, consequently, to reduced absorption and an increased reflectance, since transmission is suppressed by the Au backmirror. The above results highlight the enhancement of the nonlinear response of the proposed device (i.e. THz reflectance), induced by the combination of the graphene layer with the substrate and the Au backmirror, upon THz excitation. Even though the changes induced in graphene properties (i.e. intraband conductivity) are almost the same with and without the proposed Salisbury screen, the effect of the latter is crucial in the device's response upon carrier heating.

For a further insight into the dependence of intraband conductivity on the THz field strength, the minimum of intraband conductivity for each case of fig. 8.12 is plotted in

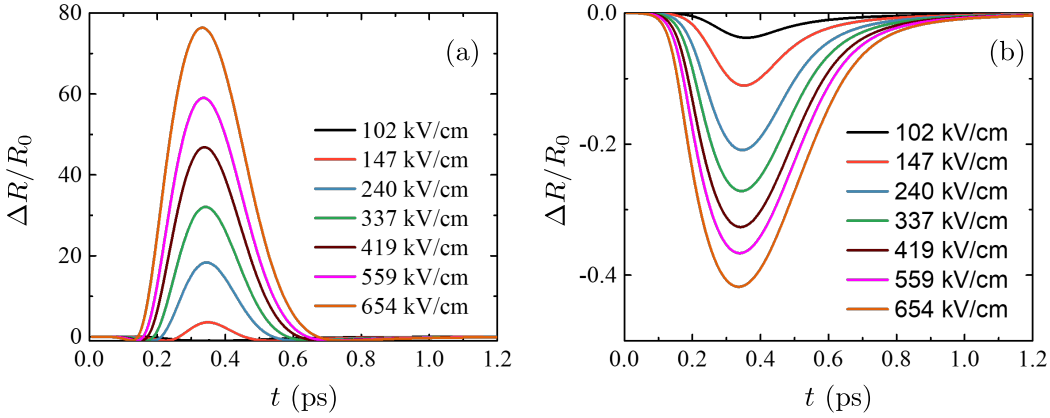

Figure 8.13: Temporal evolution of reflectance, as extracted from our calculations, for the resonant frequency of $f \approx 2.33$ THz. The calculation performed assuming (a) the full studied device, as for the experiments and (b) graphene with the same parameters ($E_{F,\mathrm{SLG}}$, γ and l) suspended in air.

fig. 8.14, as a function of the maximum value of the applied THz field E_{max}. Moreover, a numerical fit in the extracted minimum conductivity values was performed, to highlight the relation of the latter to E_{max}. The following parametrization was used: $\sigma_{\mathrm{min}}^{\mathrm{intra}} = 0.035\, E_{max}^{-\beta}$. The fit results, regarding the studied device are plotted in fig. 8.14(a), yielding an exponent $\beta = 0.6$. For the case of graphene suspended in air, the corresponding $\sigma_{\mathrm{min}}^{\mathrm{intra}}$ values along with the numerical fit are plotted in fig 8.14(b), yielding an exponent $\beta = 0.63$.

Figure 8.15(a) plots the calculated maximum values of reflectance, for the full device case, as a function of THz field strength. A linear fit, using the parametrization $R_{\mathrm{max}} - R_0 = \gamma E_{max}$, is plotted in the same graph using a red dashed line. The values used for this linear fit are $R_0 = 0.034$ and $\gamma = 3.4 \times 10^{-4}$ cm/kV. For the case of air suspended graphene, THz photoexcitation results in negative differential reflectance, as discussed above. The minimum reflectance values, during illumination, are plotted in fig. 8.15(a) as a function of THz field strength for the case of graphene suspended in air. A linear fit is also performed in this case, i.e. $R_{\mathrm{min}} - R_0^{'} = \gamma^{'} E_{max}$, yielding $R_0^{'} = -0.26$ and $\gamma^{'} = -1.7 \times 10^{-4}$ cm/kV.

From the above it is clear that combining graphene with the Salisbury screen type configuration proposed in this study, not only reverses the sign of graphene's response upon THz excitation, but it also enhances it, compared to the case of suspended graphene. We find THz reflectance scaling linearly with the excitation pulses's field strength, i.e. with the square root of its fluence. The above highlight the need to be able to design and optimize graphene-based devices accurately and reliably, to exploit at the maximum degree graphene's properties and enhance their final performance.

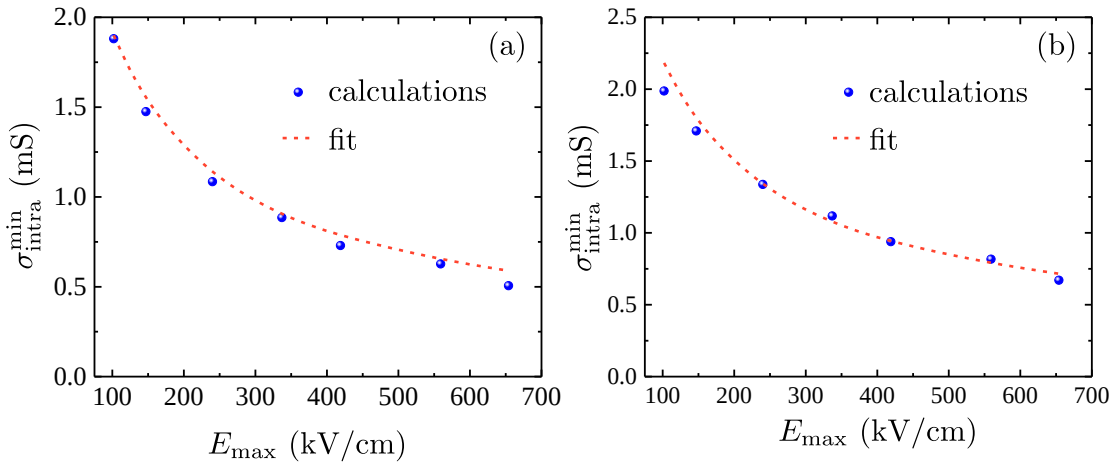

Figure 8.14: Minimum graphene conductivity values during THz excitation as a function of THz field strength. The dashed lines corresponds to numerical fits using $\sigma^{intra}_{min} = 0.035\, E^{-\beta}_{max}$. The exponent β is extracted having a value $\beta \approx 0.6$ for the studied device (a) and $\beta \approx 0.63$ for air suspended graphene (b).

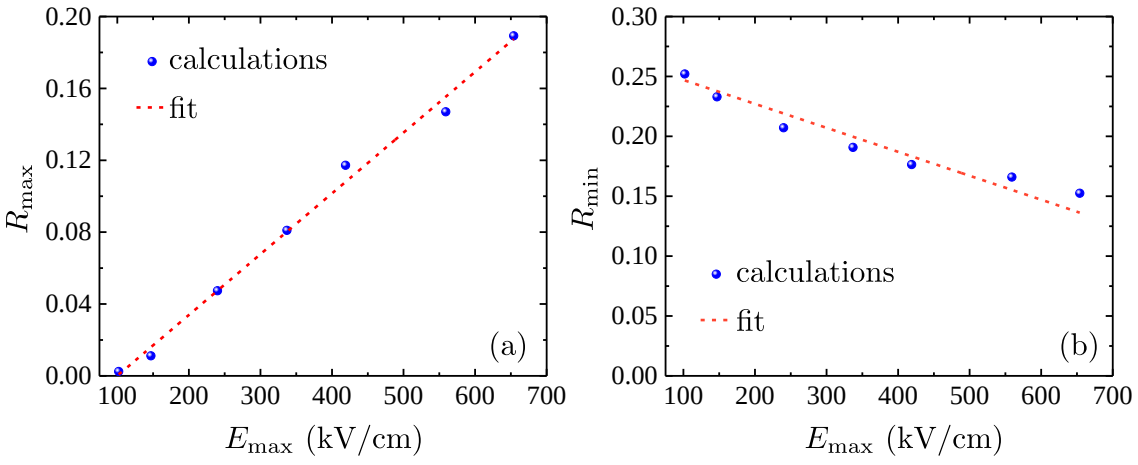

Figure 8.15: Calculated (a) maximum values, regarding the studied device and (b) minimum values, assuming air suspended graphene, for THz reflectance as a function of THz field strength. In both cases the calculations were performed at $f = 2.33$ THz. The red dashed lines corresponds to linear fits on the extracted values.

8.7 Conclusions

In this chapter the developed self-consistent multi-physics simulation framework was used to replicate experiments, regarding the self-induced absorption modulation of a graphene-based thin film absorber. Very good agreement between calculations and experiments was found, validating the model and methods developed during this thesis. In this study, it is demonstrated how, under the excitation of intense THz pulses, a graphene-based Salisbury screen perfect absorbing device can be self-modulated in terms of its absorption properties. In the experiments performed by our colleagues in IESL-FORTH an absorption modulation of more than three orders of magnitude was observed, when the THz field strength scaled from 102 kV/cm up to 654 kV/cm.

The detailed theoretical analysis presented here, based on the dynamics of THz induced hot carriers in single layer graphene, shed light on the origin of the observed nonlinear response of the studied device: the illumination with intense THz fields, results in heating of graphene's carriers and a subsequent decrease of its chemical potential and intraband conductivity. The carrier temporal dynamics during THz excitation, obtained through the split-time algorithm developed here, reveals the ultrafast nature of the nonlinear response since the entire phenomenon lasts less than a ps. Finally, after extracting graphene's parameters in the studied configuration upon theoretical analysis, the THz nonlinear response, i.e., the response deviation under different THz field excitation, was studied. The latter demonstrates the configuration effect on device response, highlighting the need for design engineering and optimization, to get the optimum performance on this type of devices.

The results of this study, demonstrate an ultrafast mechanism of modulating the absorption amplitude of graphene based perfect absorbing devices, that of nonlinear THz self-actions. Such devices could find applications in future dynamically modulated flat optics configurations. Additionally, devices based on the work presented here can serve for custom beams and pulse shaping of intense THz sources.

Chapter 9

Conclusions and outlook

In this thesis a self-consistent multi-physics simulation framework for the design and optimization of graphene-based optoelectronic devices was developed. The methods and tools developed here were carefully contrasted with the plethora of previous reports regarding graphene-based configurations and are validated by experiment. Consequently, they can reliably be used for the design, theoretical description and optimization of graphene-based optoelectronics.

Utilizing the aforementioned simulation framework, the use of graphene, alongside mature Si and CMOS based architectures, was explored in applications regarding photodetection and modulation, targeting from the SWIR up to the THz part of the spectrum [fig. 9.1].

Summary

In chapter 1 an introduction was given, outlining the need for the development of fast, efficient and CMOS compatible optoelectronic devices. A brief review of graphene, from its first isolation up to recent developments regarding fabrication processes and commercialization of its use, is also presented in this first chapter.

Chapter 2 provided a review of current state-of-the-art technologies for free-space photodetection and optical modulation. The currently available schemes and their figure of merits were presented, while the configurations and physical mechanisms based on which graphene can be utilized to realize such applications are outlined. A direct comparison of up to date record performances with corresponding graphene-based devices was also presented.

In chapter 3, a comprehensive theoretical layout of graphene's optoelectronic related properties is given. The concepts presented in this chapter are the basis upon which the developed simulation framework was built.

Chapter 4 briefly reports on the computational tools and methods that were utilized to built the simulation framework throughout this thesis.

In chapter 5 an optical modulator, targeting at the technologically important wavelength of 1550 μm was presented. Through the utilization and optimization of Bragg dielectric cavities, light absorption in graphene is enhanced, reaching $\sim$ 100%. Afterwards, a scheme for modulating this perfect absorption is presented, exploiting graphene's ability to be electrostatically doped in a convenient and non-destructive manner. The proposed electro-absorption modulation scheme is optimized and studied, found to be able to achieve deep and fast reflection modulation irrespective of graphene quality, achieving

performances comparable with state-of-the-art devices. The methods and tools developed in this chapter are not device specific, since they can operate throughout the IR spectrum after material selection and dimensional scaling.

Chapter 6 treated in a self-consistent manner the optical, electrical and optical properties of graphene, realizing the simulation-framework developed in this thesis and utilizing it to explore the performance metrics of graphene/Si Schottky photodetectors operating in the photo-thermionic regime. In this configuration, graphene's broadband absorption allows for photodetection beyond common semiconductors' cutoff wavelengths and Schottky barrier heights restrictions. The conclusions of the previous chapter were exploited to design Bragg cavities loaded with SLG/Si Schottky PDs and their operation is examined by varying all the relevant parameters (i.e., input power, reverse bias, material and junction quality) using realistic assumptions and assuming both transient and CW operation. It was shown that, under proper design and optimization, photo-thermionic graphene/semiconductor photodetectors can achieve performances comparable to internal photo-emission configurations in a spectrally unlimited scheme. Again, the platform developed in this chapter can also operate in different wavelengths within MWIR, upon scaling its dimensions and properly designing the configuration for the target spectral regime.

In chapter 7 the photo-thermionic platform was expanded even further, towards the LWIR regime. The methods and conclusions derived from chapter 6 were utilized to design a novel platform for the electrical detection of graphene plasmons. The configuration designed in this chapter can operate either as a photodetector, deep within the Pauli-blocked spectral regime, or as a chemical sensor that can detect the presence of an analyte and translate it to a direct electrical readout. A comprehensive study of both schemes was performed, taking into account all the limitations regarding operation and fabrication constraints, leading to performances comparable with previous reports on similar devices. The conclusions derived and designs developed in this chapter can be easily expanded in FIR spectral regime, where graphene plasmons are achievable, through dimensional scaling and material selection to be used alongside graphene.

Finally, in chapter 8, the simulation framework developed in this thesis was utilized to provide theoretical support in broadband, high intensity THz-TDS experiments performed by our colleagues in IESL-FORTH. The model and methods developed in this thesis were validated by experiment, while providing an explanation regarding the origins of the experimentally observed ultra-fast all-optical absorption modulation. The calculations performed in this study, showed that the observed nonlinear THz self-actions originate from THz-induced heating, which lowers graphene's chemical potential and, consequently, its optical conductivity. The latter leads to the disruption of perfect-absorption conditions, present at low-carrier temperatures, resulting in the observed reflection modulation. Moreover, through the use of the simulation framework developed in this thesis, an insight in graphene's carrier dynamics under intense THz photoexcitation was possible, providing access to all of graphene's physical properties during transient operation. The latter can be used for a better comprehension of all of the involved physical phenomena under intense photo-excitation and the design of novel schemes regarding custom beams and pulse shaping of THz sources.

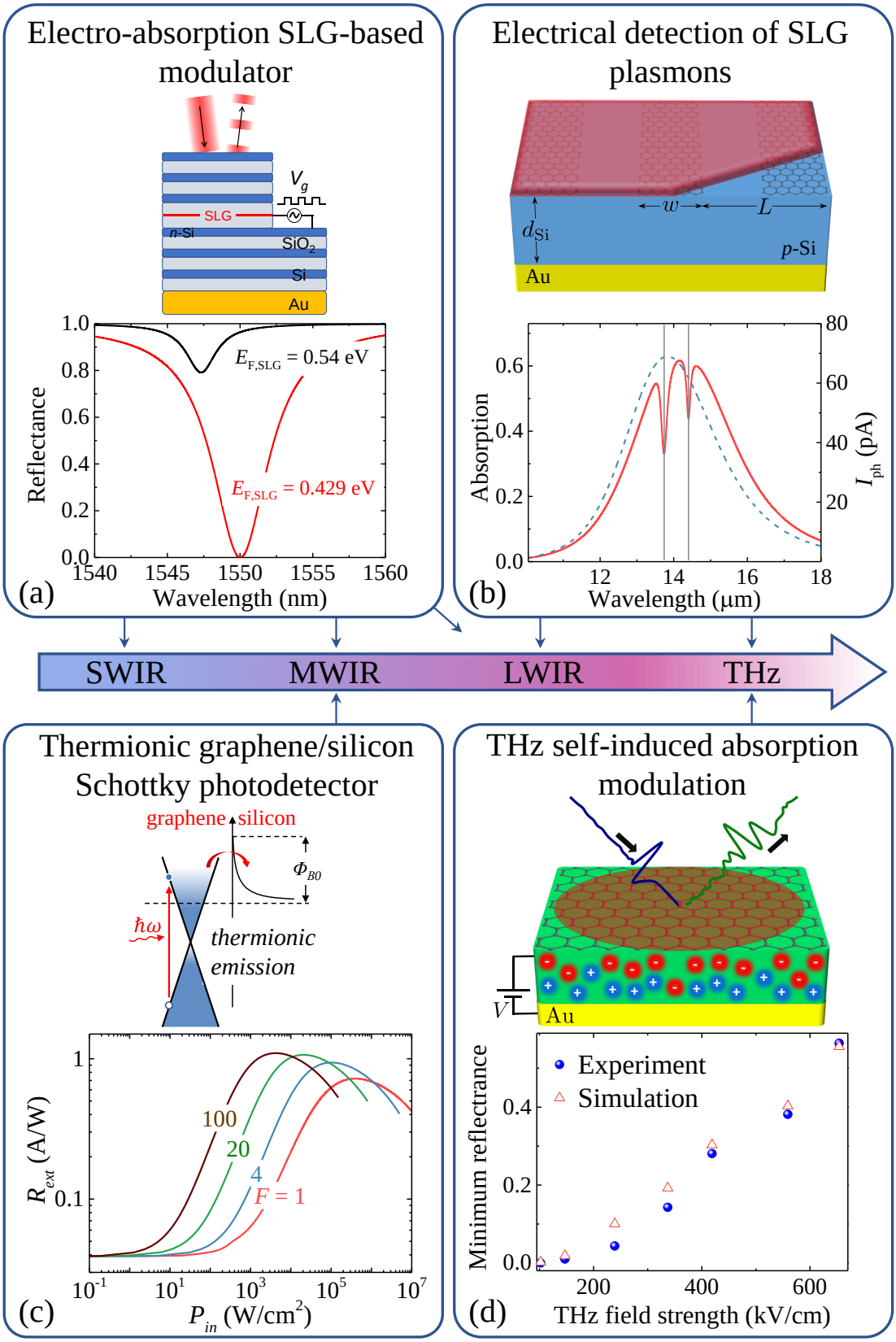

Figure 9.1: Concluding figure summarizing the devices studied in this thesis. (a) Electro-absorption IR modulator consisting of SLG-loaded Bragg cavities [138]. (b) Electrical detection of SLG plasmons for LWIR photodetection and chemical sensing [140]. (c) Thermionic SLG/Si Schottky MWIR photodetectors [139] (d) THz self-induced absorption modulation in graphene [141].

Graphene-based optoelectronics

The devices designed and studied here showcase that graphene-based optoelectronics, upon proper design and optimization, can achieve performances comparable or even surpassing stat-of-the-art configurations.

Optical modulation in the technologically relevant wavelength $\lambda = 1550$ nm, in a reflection-mode, gate-tunable configuration was demonstrated, with modulation depth $>$ 30 dB and low insertion losses ($<$ 3 dB) at GHz frequencies with small ($\approx$ 15) voltage-bias swings in a CMOS compatible scheme. These merits outperform previous reports of free-space modulation in SWIR (2.1), surpassing both graphene and Si-based devices. Most importantly, it is demonstrated that these performances can be obtained irrespective of graphene quality, under optimized configurations based on dielectric Bragg cavities. The temporal response of this scheme is limited by the parasitic resistance-capacitance effects of the supporting circuitry for the bias application. To overcome this, an all-optical scheme was demonstrated in the THz regime, where graphene's nonlinear response to THz-induced carrier heating leads to reflection modulation of $\sim$ 30 db, which can be utilized for custom pulse shaping of intense THz sources.

Infrared photodetection, in the MWIR up to FIR spectral regimes, was also demonstrated, utilizing photo-thermionic emission across graphene/Si Schottky junctions. After an extensive study of all operation parameters, MWIR photodetection with calculated responsivities in the order of 1 A/W at high power excitation and 100 mA/W at low power excitation were demonstrated. These, resulted in a specific detectivity of $\sim 10^{7}$ cm $\mathrm{Hz}^{0.5}$ W^{-1} in unbiased operation at with $\sim$ GHz temporal response. Even though these figures are inferior compared to state-of-the-art technology (figs. 2.2 –2.4), which utilizes HgCdTe and III-IV compounds, the configurations assumed here are Si based and full CMOS compatible allowing for co-integration with supporting circuitry in a convenient and cost-efficient manner. Moreover, the photo-thermionic configuration has an ultra-broadband response, not limited by either semiconductor bandgap nor the developed Schottky barrier height at the junction, allowing for photodetection at even longer wavelengths. This fact was exploited to numerically demonstrate photodetection at LWIR, enabling the electrical detection of graphene plasmons. A novel scheme was designed, where hot-carriers in graphene are created upon plasmon-induced enhanced light absorption, to thermionically inject them across the Schottky barrier and harvest the resulting photocurrent with responsivity up to $\sim$ 100 mA/W, NEP $\sim$ 190 pW/$\mathrm{Hz}^{0.5}$ and detectivity up to $\sim 5 \times 10^{6}$ cm $\mathrm{Hz}^{0.5}$ W^{-1} with $\sim$ GHz cutoff frequency. The designed scheme allows for the realization of efficient and fast photodetection beyond the cutoff wavelength of state-of-the-art HgCdTe and III-IV platforms ($\sim$ 10 μm). Moreover, it was demonstrated how this scheme can be utilized for label-free chemical sensing, able to translate the presence of an analyte in the vicinity of graphene in a direct electrical signal.

Outlook and future perspective

Despite the remarkable performances reported up to date regarding graphene-based optoelectronic devices, many challenges are yet to be met towards their commercialization and use in practical applications. To overcome the barrier from proof-of-concept demonstrations towards marketable every-day devices, several technical issues need to be resolved, regarding scalable, high-quality and low-cost synthesis. Impressive efforts have been made in this directions regarding graphene, with other 2D materials soon to follow. Another major issue towards commercialization, is to find ways to exploit graphene's unique

properties and realize novel and high-performance optoelectronic devices. Towards this end, realistic modeling tools, including graphene's optical, electrical and thermal properties, are of critical importance for considering and optimizing novel device concepts and architectures.

The simulation framework developed here includes all of graphene's unique carrier dynamics. At the same time, rather than studying graphene as an isolated material, it can be used for full-device representations, under transient or CW operation, as demonstrated in this thesis. This task is performed by inserting in the developed model all the relevant figures of merit regarding graphene and heterojunctions' quality, along with a whole spectrum of operation parameters. The self-consistent algorithms developed to realize the implementation of this simulation framework ensure stability of operation and accurate description of the interplay between graphene's electrical, optical and thermal properties upon photoexcitation. Thus, they provide a powerful tool for the design and optimization of realistic graphene-based configurations, while providing an insight into the underlying physics.

The reliability of the developed model was demonstrated in chapter 8, with its experimental validation in THz-TDS experiments. Graphene's response was accurately simulated, accounting for the contributions of the materials used alongside graphene and the configuration architecture effects on experimentally measured quantities. The response of the studied device was replicated from our calculations, accounting for the interplay of graphene's properties, in a wide range of carrier temperatures and in an ultra-wide excitation spectrum. Upon photoexcitation, graphene's parameters that are not accessible for direct experimental measurement, e.g. carrier temperature and intraband conductivity, were extracted, using the tools developed here, by utilizing the reflectance measurements of the studied device.

Even though, in the context of this thesis, optoelectronic devices were explored assuming Si-based configurations alongside graphene, the methods and tools developed here are not material specific, but can be expanded to simulate graphene's response alongside other material platforms, e.g. 2D materials' heterostructures. More than 100 stable 2D materials have been reported up to date [24,114–119], which can lead to endless combinations for the stacking of Van-der-Waals heterostructures [34], each one with a different and unique optoelectronic response. The combination of graphene with other 2D materials can enhance the latter's unique properties (e.g., ultra-high mobilities have been reported for graphene encapsulated within other 2D crystals [492]) while device miniaturization is intrinsically easier and more effective when using stacks of 2D atomic crystals. However, the numerous combinations that can be utilized from these heterostructures, require the computational study of their performance and guide fabrication and experimental research towards the most effective configurations. Having establish the computational tools to describe the graphene–bulk semiconductor Schottky junctions in this thesis, these can be expanded to study the 2D–2D analog of carrier transport across energy barriers created between 2D heterostructures. Furthermore, the self-consistent algorithms developed here, can be expanded to include additional phenomena, e.g. vertical heat transport across Van-der-Waals stackings as well as lateral heat diffusion in each constituent, to accurately describe the thermal properties of 2D heterostructures upon photoexcitation and their subsequent heating.

Moreover, an in-house FDTD algorithm, which will include graphene's temperature and wavelength depended optical response can be developed. Commercial FDTD solvers that include graphene, accounting for its 2D nature by implementing it as a 2D surface

boundary (e.g., Lumerical FDTD solver [399]) are already available. However, these do not account for the temperature-induced variation of SLG optical conductivity, since free-carrier relaxation time τ_{opt} is inserted in such simulators as a fixed value. Combining the tools developed in this thesis with a custom-built FDTD algorithm will allow for the accurate simulation of graphene-based devices with complex geometries, by importing the time-dependent signals that are utilized for photoexcitation and accounting for the interplay between graphene's optical and thermal properties. Doing so, the response upon excitation with ultra-fast optical pulses could be simulated, allowing, e.g., the computational study of pump-probe configurations to explore graphene's carrier dynamics and propose novel optoelectronic schemes, e.g., all-optical modulators.

The straightforward and efficient implementation of the computational methods presented here, also allow for co-integration of the developed simulation framework with commercial solvers, towards the creation of key software modules for designing graphene-based optoelectronic devices. Even though, in the context of this thesis, we focused in free-space configurations, the integration of the developed tools with commercial optical simulators will allow for the reliable simulations of waveguide-integrated schemes that precisely include graphene's optoelectronic response. Integrated photonics holds a huge potential regarding the applications studied here [209], with the ability to result into high-performance devices. In this regard, the accurate simulation of graphene integrated in such configurations is critical.

Finally, the developed model can be exploited for the study of graphene-based metasurfaces, the latter being the 2D analog of metamaterials. Graphene-based metasurfaces have been reported to hold the potential for a wide variety of applications, e.g. spatiotemporal modulators, amplitude and phase modulation, harmonic generation, beam steering and more [493–496]. Consequently, they are a blooming research field and the interest of scientific community, regarding these configurations, is growing rapidly. The computational tools developed in this thesis can be utilized, either with all-custom-built software or in conjunction with commercial solvers, for the study of these novel optoelectronic configurations.

Appendix A

Enhancing light absorption in graphene: Critical coupling

Graphene's visible to NIR absorption of $\sim 2.3\%$ is a remarkably figure, given its monoatomic thickness. Nevertheless, for practical applications, this figure needs to be improved, especially if we take into account that placing graphene on a substrate or embedding it in a dielectric its absorption drops even further. For example, in the thin film limit, placing graphene between a dielectric with index n_1 and a substrate with index n_2, its absorption in the VIS - NIR is [285]:

$$\alpha_{\text{SLG}} \sim 0.023 \frac{4n_1}{(n_1+n_2)^2} \tag{A.1}$$

Absorption in the MWIR to THz spectral regime can be enhanced utilizing graphene plasmonics, as discussed in section 3.3. In the VIS – NIR regime, where graphene plasmons cannot be realized due to doping limitations, there is a vast amount of research regarding the enhancement of SLG absorption, resulting to the realization of graphene-based perfect absorbers [407, 421, 497]. To achieve this, there have been studies demonstrating various techniques, including the utilization of localized surface plasmon resonances on metals [285, 498], Fabry-Perot cavity resonances [438, 499, 500] and guided mode resonances [410, 411, 501–504].

In the context of this thesis, the critical coupling mechanism [407, 410, 411, 422] is utilized to enhance graphene's absorption. The latter is a resonant effect, in which perfect absorption in a cavity can be achieved under certain conditions. Let assume a lossy resonant cavity with stored energy $|a|^2$ in a single resonance at ω_0, interacting with input and output (reflected) waves of amplitudes u and y_r respectively, as for fig. A.1. This configuration can be described within the context of coupled mode theory [422] using:

$$\begin{aligned} \frac{da}{dt} &= (-i\omega_0 - \gamma_d - \gamma_a)\, a + u\sqrt{2\gamma_d} \\ y_r &= a\sqrt{2\gamma_d} - u \end{aligned} \tag{A.2}$$

with γ_d the mode leakage rate, γ_a and the resonator absorption rate. Note that this configuration is a single port system, i.e. light is incoming only from one side, while the transmission through the cavity is suppressed using a metallic backmirror. The latter is crucial to achieve perfect absorption, since in a double port system (e.g. without the opaque backmirror) the maximum absorption that can be achieved, assuming illumination only from one side of the cavity, is 50 % [410, 422]. The single port system can be realized using two

different configurations; one with just the opaque backmirror [fig. A.1(a)] and one with a partially transmitting mirror in front of the resonant cavity [fig. A.1(b)]. The former can be constructed using a dielectric spacer between the resonator and a metallic backmirror, where the latter can be fabricated using dielectric Bragg - cavities between the resonator and the metallic backmirror. Note that the second configuration is more suitable for weakly absorbing materials, such as SLG in the VIS – NIR regime. In both cases the reflection is given by [410, 422]:

$$R \equiv \left|\frac{y_r}{u}\right|^2 = \frac{(\omega_0 - \omega)^2 + (\gamma_a - \gamma_d)^2}{(\omega_0 - \omega)^2 + (\gamma_a + \gamma_d)^2} \tag{A.3}$$

and the absorption [410, 422]:

$$A \equiv 1 - R = \frac{4\gamma_a\gamma_d}{(\omega_0 - \omega)^2 + (\gamma_a + \gamma_d)^2} \tag{A.4}$$

From eq. A.4 it is apparent that at resonance ($\omega = \omega_0$), if the cavity decay rate γ_d is equal

(a) (b)

Figure A.1: Resonant cavities used to utilize critical coupling using (a) an opaque backmirror (b) an opaque backmirror along with a partial transmitting mirror in front of the cavity.

to the absorption rate γ_a, perfect absorption (e.g., $A = 100\%$) occurs. This is a particular useful configuration for graphene-based devices, since SLG absorption can be tuned (e.g. using electrostatic gating), giving one the opportunity to impose critical coupling conditions. In this thesis the above mechanism was exploited to enhance light absorption in the graphene-based studied devices.

Appendix B

Computational details regarding the developed simulation framework

The simulation framework developed in this thesis was written in Fortran. This programming language was chosen, since it is one specifically developed for scientific computing. Being fast and simple in its implementation, it was an ideal choice for this work, which includes a vast amount of numerical integrations and iterative algorithms (e.g. 4RK, self-consistent solution for the quasi-CW approach to acquire graphene carrier temperature, self-consistent solution for Schottky barrier calculation and more). Since no high-level programming (e.g. object-oriented algorithms) was required in this work, the use of Fortran resulted in an efficient framework.

As a result, the time stepping using 4RK, required to calculate a graphene-based device's temporal response, assuming excitation with a single wavelength (as for chapter 6) can be concluded within $\sim$ 1 minute in a single core of a personal computer. If the quasi-CW approximation is used instead (i.e., implementing the algorithm of fig. 3.16, as for chapters 6 and 7), the calculation for a given input power density converges within few seconds (e.g., the whole spectrum depicted in fig. 6.7, accounting for all 4 different values of F can be acquired within $\sim$ 5 minutes). The time-stepping method, assuming illumination with a broadband spectrum, as for chapter 8 requires slightly longer computational time, in the order of $\sim$ 3 minutes.

Apart from being efficient, the developed simulation framework is flexible and modular, able to be implemented alongside commercial software (e.g. Lumerical FDTD solver [399]) for the simulation of graphene-based devices. At its heart lies a Fortran code, of $\approx$ 1500 lines, regarding the carrier dynamics and internal properties of graphene (e.g., equilibrium and non-equilibrium chemical potential calculations, Fermi integrals for the extraction of carrier densities, thermal capacity, optical conductivity, refractive index, optical-phonon thermal current density et.c.). The above can be combined with an in-house TMM code of $\sim$ 500 lines, to extract the optical response of graphene used alongside different materials, the latter's contribution taken into account upon inserting their refractive indices spectra. Graphene-Si Schottky heterojunction formation and the associated thermionic thermal and electrical current densities are described with a few additional subroutines, in $\sim$ 250 lines of code. All the above are self-consistently included in a $\sim$ 1000 lines of code to extract either the quasi-CW solution or the temporal response using 4RK, depending the user's choice for the studied application.

List of Acronyms

4RK	4^{th} order Runge - Kutta method
ABC	Absorbing boundary conditions
ADE	Auxiliary differential equation
BOL	Bolometric
CMOS	Complementary metal-oxide semiconductor
CNP	Charge neutrality point
CVD	Chemical vapor deposition
CW	Continuous-wave
EO	Electro-optic
FDTD	Finite difference time domain
FE	Field emission
FIR	Far infrared (15 - 1000 μm)
FWHM	full-width-at-half-maximum
GNR	Graphene nanoribbons
GSP	Graphene surface plasmons
IL	Insertion Loss
IPE	Internal photoemission
IR	Infrared
LWIR	Long-wavelength infrared (8 - 15 μm)
MD	Modulation Depth
MF	Modulation frequency
MWIR	Mid-wavelength infrared (3 - 8 μm)
NEP	Noise equivalent power
NIR	Near infrared (0.8 - 1.4 μm)
PBC	Periodic boundary conditions
PC	Photoconductive
PD	Photodetector
PG	Photogating
PML	Perfectly matched layer

PTh	Photo-thermionic emission
PV	Photovoltaic
QW	Quantum well
RT	Room temperature
SBH	Schottky barrier height
SC	Semiconductor
SEIRA	Surface enhanced infrared absorption
SLG	Single layer graphene
SOTA	State-of-the-art
SPP	Surface plasmon polaritons
SWIR	Short-wavelength infrared (1.4 - 3 μm)
TE	Transverse electric
TFE	Thermionic field emission
THz-TDS	THz time-domain spectroscopy
TM	Transverse magnetic
TMM	Transfer matrix method
VIS	Visible part of the spectrum
e-ph	Electron-phonon scattering
h-BN	Hexagonal boron nitride

Bibliography

[1] U. Cisco. Cisco annual internet report (2018–2023) white paper. *Cisco: San Jose, CA, USA*, 2020.

[2] S. Koenig et al. Wireless sub-thz communication system with high data rate. *Nature photonics*, 7(12):977–981, 2013.

[3] E. Agrell et al. Roadmap of optical communications. *Journal of Optics*, 18(6):063002, 2016.

[4] D. J. Buckley et al. Frontiers of graphene and 2d material-based gas sensors for environmental monitoring. *2D Materials*, 7(3):032002, 2020.

[5] M. Javaid et al. Significance of sensors for industry 4.0: Roles, capabilities, and applications. *Sensors International*, 2:100110, 2021.

[6] W. L. Chan et al. Imaging with terahertz radiation. *Reports on progress in physics*, 70(8):1325, 2007.

[7] A. M. Waxman et al. Color night vision: opponent processing in the fusion of visible and ir imagery. *Neural Networks*, 10(1):1–6, 1997.

[8] I. Kašalynas et al. Spectroscopic terahertz imaging at room temperature employing microbolometer terahertz sensors and its application to the study of carcinoma tissues. *Sensors*, 16(4):432, 2016.

[9] J. P. Guillet et al. Review of terahertz tomography techniques. *Journal of Infrared, Millimeter, and Terahertz Waves*, 35(4):382–411, 2014.

[10] D. V. Meledin et al. A 1-thz superconducting hot-electron-bolometer receiver for astronomical observations. *IEEE transactions on microwave theory and techniques*, 52(10):2338–2343, 2004.

[11] M. H. Miraz et al. A review on internet of things (iot), internet of everything (ioe) and internet of nano things (iont). *2015 Internet Technologies and Applications (ITA)*, pp. 219–224, 2015.

[12] S. Campbell et al. Sensor technology in autonomous vehicles: A review. In *2018 29th Irish Signals and Systems Conference (ISSC)*, pp. 1–4. IEEE, 2018.

[13] J. Wilson and J. F. B. Hawkes. *Optoelectronics: an introduction*. Prentice Hall, Harlow, England, 3. ed., [nachdr] edition, 2006.

[14] G. T. Reed. *Silicon photonics: the state of the art*. John Wiley & Sons, Chichester ; Hoboken, NJ, 2008. OCLC: ocm77795924.

[15] D. Thomson et al. Roadmap on silicon photonics. *Journal of Optics*, 18(7):073003, 2016.

[16] N. Izhaky et al. Development of cmos-compatible integrated silicon photonics devices. *IEEE Journal of Selected Topics in Quantum Electronics*, 12(6):1688–1698, 2006.

[17] I. A. Young et al. Optical technology for energy efficient i/o in high performance computing. *IEEE Communications Magazine*, 48(10):184–191, 2010.

[18] Y. Taur et al. 25 nm cmos design considerations. In *International Electron Devices Meeting 1998. Technical Digest (Cat. No. 98CH36217)*, pp. 789–792. IEEE, 1998.

[19] T. N. Theis and H.-S. P. Wong. The end of moore's law: A new beginning for information technology. *Computing in Science & Engineering*, 19(2):41–50, 2017.

[20] S. M. Sze and K. K. Ng. *Physics of semiconductor devices*. Wiley-Interscience, Hoboken, N.J, 3rd ed edition, 2007.

[21] G. Roelkens et al. Iii-v-on-silicon photonic devices for optical communication and sensing. In *Photonics*, volume 2, pp. 969–1004. MDPI, 2015.

[22] P. Capper and J. Garland. *Mercury cadmium telluride: growth, properties, and applications*. Wiley series in materials for electronic and optoelectronic applications. Wiley, Hoboken, N.J, 2011.

[23] A. Rogalski. Hgcdte infrared detector material: history, status and outlook. *Reports on Progress in Physics*, 68(10):2267, 2005.

[24] M. Mittendorff et al. 2d THz optoelectronics. *Advanced Optical Materials*, 9(3):2001500, 2021.

[25] F. Bonaccorso et al. Graphene photonics and optoelectronics. *Nature photonics*, 4(9):611–622, 2010.

[26] P. R. Wallace. The band theory of graphite. *Physical review*, 71(9):622, 1947.

[27] N. D. Mermin. Crystalline order in two dimensions. *Physical Review*, 176(1):250, 1968.

[28] K. S. Novoselov et al. Electric field effect in atomically thin carbon films. *science*, 306(5696):666–669, 2004.

[29] A. K. Geim. Nobel lecture: Random walk to graphene. *Reviews of Modern Physics*, 83(3):851, 2011.

[30] M. S. Dresselhaus and P. T. Araujo. Perspectives on the 2010 nobel prize in physics for graphene, 2010.

[31] A. K. Geim and K. S. Novoselov. The rise of graphene. In *Nanoscience and technology: a collection of reviews from nature journals*, pp. 11–19. World Scientific, 2010.

[32] L. Song et al. Large scale growth and characterization of atomic hexagonal boron nitride layers. *Nano letters*, 10(8):3209–3215, 2010.

[33] K. S. Novoselov et al. Two-dimensional atomic crystals. *Proceedings of the National Academy of Sciences*, 102(30):10451–10453, 2005.

[34] K. Novoselov et al. 2d materials and van der waals heterostructures. *Science*, 353(6298):aac9439, 2016.

[35] K. S. Novoselov et al. Room-temperature quantum hall effect in graphene. *science*, 315(5817):1379–1379, 2007.

[36] N. Peres et al. Electronic properties of disordered two-dimensional carbon. *Physical Review B*, 73(12):125411, 2006.

[37] C. Berger et al. Electronic confinement and coherence in patterned epitaxial graphene. *Science*, 312(5777):1191–1196, 2006.

[38] C. Berger et al. Ultrathin epitaxial graphite: 2d electron gas properties and a route toward graphene-based nanoelectronics. *The Journal of Physical Chemistry B*, 108(52):19912–19916, 2004.

[39] Y. Zhang et al. Experimental observation of the quantum hall effect and berry's phase in graphene. *nature*, 438(7065):201–204, 2005.

[40] C. Lee et al. Measurement of the elastic properties and intrinsic strength of monolayer graphene. *science*, 321(5887):385–388, 2008.

[41] S. Stankovich et al. Graphene-based composite materials. *nature*, 442(7100):282–286, 2006.

[42] R. R. Nair et al. Fine structure constant defines visual transparency of graphene. *science*, 320(5881):1308–1308, 2008.

[43] A. C. Ferrari et al. Science and technology roadmap for graphene, related two-dimensional crystals, and hybrid systems. *Nanoscale*, 7(11):4598–4810, 2015.

[44] F. Koppens et al. Photodetectors based on graphene, other two-dimensional materials and hybrid systems. *Nature nanotechnology*, 9(10):780–793, 2014.

[45] B. Sensale-Rodriguez. Graphene-based optoelectronics. *Journal of Lightwave Technology*, 33(5):1100–1108, 2015.

[46] Z. Jin et al. Graphene, graphene quantum dots and their applications in optoelectronics. *Current Opinion in Colloid & Interface Science*, 20(5-6):439–453, 2015.

[47] M. Romagnoli et al. Graphene-based integrated photonics for next-generation datacom and telecom. *Nature Reviews Materials*, 3(10):392–414, 2018.

[48] M. Romagnoli. Graphene photonics for optical communications. In *Optical Fiber Communication Conference*, pp. M3D–3. Optica Publishing Group, 2019.

[49] K. I. Bolotin et al. Temperature-dependent transport in suspended graphene. *Physical review letters*, 101(9):096802, 2008.

[50] M. A. Giambra et al. Wafer-scale integration of graphene-based photonic devices. *ACS nano*, 15(2):3171–3187, 2021.

[51] A. Tyagi et al. Ultra-clean high-mobility graphene on technologically relevant substrates. *Nanoscale*, 14(6):2167–2176, 2022.

[52] C. Canali et al. Electron and hole drift velocity measurements in silicon and their empirical relation to electric field and temperature. *IEEE Transactions on electron devices*, 22(11):1045–1047, 1975.

[53] A. C. Neto et al. The electronic properties of graphene. *Reviews of modern physics*, 81(1):109, 2009.

[54] M. Craciun et al. Tuneable electronic properties in graphene. *Nano Today*, 6(1):42–60, 2011.

[55] N. Kakenov et al. Observation of gate-tunable coherent perfect absorption of terahertz radiation in graphene. *Acs Photonics*, 3(9):1531–1535, 2016.

[56] Y. Malevich et al. Video-speed graphene modulator arrays for terahertz imaging applications. *ACS Photonics*, 7(9):2374–2380, 2020.

[57] L. A. Falkovsky. Optical properties of graphene. *Journal of Physics: Conference Series*, 129:012004, October 2008.

[58] J. M. Dawlaty et al. Measurement of ultrafast carrier dynamics in epitaxial graphene. *Applied Physics Letters*, 92(4):042116, 2008.

[59] F. H. Koppens et al. Graphene plasmonics: a platform for strong light–matter interactions. *Nano letters*, 11(8):3370–3377, 2011.

[60] A. N. Grigorenko et al. Graphene plasmonics. *Nature photonics*, 6(11):749–758, 2012.

[61] F. J. Garcia de Abajo. Graphene plasmonics: challenges and opportunities. *Acs Photonics*, 1(3):135–152, 2014.

[62] T. Low and P. Avouris. Graphene plasmonics for terahertz to mid-infrared applications. *ACS nano*, 8(2):1086–1101, 2014.

[63] P. A. D. Gonçalves and N. M. Peres. *An introduction to graphene plasmonics*. World Scientific, 2016.

[64] M. Massicotte et al. Hot carriers in graphene–fundamentals and applications. *Nanoscale*, 13(18):8376–8411, 2021.

[65] M. Massicotte et al. Photo-thermionic effect in vertical graphene heterostructures. *Nature Communications*, 7(1):12174, November 2016.

[66] S. Castilla et al. Fast and sensitive terahertz detection using an antenna-integrated graphene pn junction. *Nano letters*, 19(5):2765–2773, 2019.

[67] S. Castilla et al. Plasmonic antenna coupling to hyperbolic phonon-polaritons for sensitive and fast mid-infrared photodetection with graphene. *Nature communications*, 11(1):1–7, 2020.

[68] I. Vangelidis et al. Unbiased plasmonic-assisted integrated graphene photodetectors. *ACS Photonics*, 2022.

[69] M. Freitag et al. Photocurrent in graphene harnessed by tunable intrinsic plasmons. *Nature communications*, 4(1):1–8, 2013.

[70] J. F. Rodriguez-Nieva et al. Thermionic Emission and Negative d I /d V in Photoactive Graphene Heterostructures. *Nano Letters*, 15(3):1451–1456, March 2015.

[71] J. F. Rodriguez-Nieva et al. Enhanced thermionic-dominated photoresponse in graphene schottky junctions. *Nano Letters*, 16(10):6036–6041, 2016.

[72] R.-J. Shiue et al. High-responsivity graphene–boron nitride photodetector and autocorrelator in a silicon photonic integrated circuit. *Nano letters*, 15(11):7288–7293, 2015.

[73] J. E. Muench et al. Waveguide-integrated, plasmonic enhanced graphene photodetectors. *Nano letters*, 19(11):7632–7644, 2019.

[74] S. Schuler et al. Controlled generation of ap–n junction in a waveguide integrated graphene photodetector. *Nano letters*, 16(11):7107–7112, 2016.

[75] Z. Sun et al. Graphene mode-locked ultrafast laser. *ACS nano*, 4(2):803–810, 2010.

[76] J.-L. Xu et al. Graphene saturable absorber mirror for ultra-fast-pulse solid-state laser. *Optics letters*, 36(10):1948–1950, 2011.

[77] G. Xie et al. Graphene saturable absorber for q-switching and mode locking at 2 μm wavelength. *Optical Materials Express*, 2(6):878–883, 2012.

[78] I. H. Baek et al. Efficient mode-locking of sub-70-fs ti: sapphire laser by graphene saturable absorber. *Applied Physics Express*, 5(3):032701, 2012.

[79] V. Bianchi et al. Terahertz saturable absorbers from liquid phase exfoliation of graphite. *Nature Communications*, 8(1):1–9, 2017.

[80] A. C. Tasolamprou et al. Experimental demonstration of ultrafast thz modulation in a graphene-based thin film absorber through negative photoinduced conductivity. *ACS photonics*, 6(3):720–727, 2019.

[81] M. Ono et al. Ultrafast and energy-efficient all-optical switching with graphene-loaded deep-subwavelength plasmonic waveguides. *Nature Photonics*, 14(1):37–43, 2020.

[82] H. Barnard et al. Boron nitride encapsulated graphene infrared emitters. *Applied Physics Letters*, 108(13):131110, 2016.

[83] S.-K. Son et al. Graphene hot-electron light bulb: incandescence from hbn-encapsulated graphene in air. *2D Materials*, 5(1):011006, 2017.

[84] Y. D. Kim et al. Ultrafast graphene light emitters. *Nano letters*, 18(2):934–940, 2018.

[85] R.-J. Shiue et al. Thermal radiation control from hot graphene electrons coupled to a photonic crystal nanocavity. *Nature communications*, 10(1):1–7, 2019.

[86] K. Rana et al. A graphene-based transparent electrode for use in flexible optoelectronic devices. *Journal of Materials Chemistry C*, 2(15):2646–2656, 2014.

[87] E. B. Secor et al. Gravure printing of graphene for large-area flexible electronics. *Advanced materials*, 26(26):4533–4538, 2014.

[88] D. De Fazio et al. High responsivity, large-area graphene/mos2 flexible photodetectors. *ACS nano*, 10(9):8252–8262, 2016.

[89] N. Kumar et al. Top-down synthesis of graphene: A comprehensive review. *FlatChem*, 27:100224, 2021.

[90] M. Bhuyan et al. Synthesis of graphene. *International Nano Letters*, 6(2):65–83, 2016.

[91] X. J. Lee et al. Review on graphene and its derivatives: Synthesis methods and potential industrial implementation. *Journal of the Taiwan Institute of Chemical Engineers*, 98:163–180, 2019.

[92] B. Jayasena and S. Subbiah. A novel mechanical cleavage method for synthesizing few-layer graphenes. *Nanoscale research letters*, 6(1):1–7, 2011.

[93] J. Chen et al. Continuous mechanical exfoliation of graphene sheets via three-roll mill. *Journal of Materials Chemistry*, 22(37):19625–19628, 2012.

[94] S. Haar et al. Liquid-phase exfoliation of graphite into single-and few-layer graphene with α-functionalized alkanes. *The Journal of Physical Chemistry Letters*, 7(14):2714–2721, 2016.

[95] Ö. Güler et al. Production of graphene layer by liquid-phase exfoliation with low sonication power and sonication time from synthesized expanded graphite. *Fullerenes, Nanotubes and Carbon Nanostructures*, 24(2):123–127, 2016.

[96] X. Wu et al. Large-scale synthesis of high-quality graphene sheets by an improved alternating current arc-discharge method. *RSC advances*, 6(95):93119–93124, 2016.

[97] A. M. Dimiev et al. Revisiting the mechanism of oxidative unzipping of multiwall carbon nanotubes to graphene nanoribbons. *ACS nano*, 12(4):3985–3993, 2018.

[98] C. K. Chua and M. Pumera. Chemical reduction of graphene oxide: a synthetic chemistry viewpoint. *Chemical Society Reviews*, 43(1):291–312, 2014.

[99] T. F. Emiru and D. W. Ayele. Controlled synthesis, characterization and reduction of graphene oxide: A convenient method for large scale production. *Egyptian Journal of Basic and Applied Sciences*, 4(1):74–79, 2017.

[100] H. Huang et al. Epitaxial growth of graphene on silicon carbide (sic). In *Graphene*, pp. 177–198. Elsevier, 2014.

[101] G. R. Yazdi et al. Epitaxial graphene on sic: a review of growth and characterization. *Crystals*, 6(5):53, 2016.

[102] A. Dato and M. Frenklach. Substrate-free microwave synthesis of graphene: experimental conditions and hydrocarbon precursors. *New Journal of Physics*, 12(12):125013, 2010.

[103] Y. Yang et al. Bottom-up fabrication of graphene on silicon/silica substrate via a facile soft-hard template approach. *Scientific reports*, 5(1):1–7, 2015.

[104] P. R. Somani et al. Planer nano-graphenes from camphor by cvd. *Chemical Physics Letters*, 430(1-3):56–59, 2006.

[105] R. Munoz and C. Gómez-Aleixandre. Review of cvd synthesis of graphene. *Chemical Vapor Deposition*, 19(10-11-12):297–322, 2013.

[106] B. Deng et al. Toward mass production of cvd graphene films. *Advanced Materials*, 31(9):1800996, 2019.

[107] S. Guo and S. Dong. Graphene nanosheet: synthesis, molecular engineering, thin film, hybrids, and energy and analytical applications. *Chemical Society Reviews*, 40(5):2644–2672, 2011.

[108] M. M. Tavakoli et al. Synergistic roll-to-roll transfer and doping of cvd-graphene using parylene for ambient-stable and ultra-lightweight photovoltaics. *Advanced Functional Materials*, 30(31):2001924, 2020.

[109] L. Banszerus et al. Ultrahigh-mobility graphene devices from chemical vapor deposition on reusable copper. *Science advances*, 1(6):e1500222, 2015.

[110] D. De Fazio et al. High-mobility, wet-transferred graphene grown by chemical vapor deposition. *ACS nano*, 13(8):8926–8935, 2019.

[111] S. Pezzini et al. High-quality electrical transport using scalable cvd graphene. *2D Materials*, 7(4):041003, 2020.

[112] Z. Zhang et al. Graphene-based mixed-dimensional van der waals heterostructures for advanced optoelectronics. *Advanced Materials*, 31(37):1806411, 2019.

[113] A. Rogalski. Van der waals materials for hot infrared detectors: A review. *Opto-Electronics Review*, pp. e140551–e140551, 2022.

[114] A. Bablich et al. Graphene and two-dimensional materials for optoelectronic applications. *Electronics*, 5(1):13, 2016.

[115] W. Liao et al. Van der waals heterostructures for optoelectronics: progress and prospects. *Applied Materials Today*, 16:435–455, 2019.

[116] J. Wang et al. Optoelectronic properties and applications of graphene-based hybrid nanomaterials and van der waals heterostructures. *Applied Materials Today*, 16:1–20, 2019.

[117] T. Tan et al. 2d material optoelectronics for information functional device applications: status and challenges. *Advanced Science*, 7(11):2000058, 2020.

[118] S. K. Chakraborty et al. Challenges and opportunities in 2d heterostructures for electronic and optoelectronic devices. *Iscience*, 25(3), 2022.

[119] M. Zhao et al. Advances in two-dimensional materials for optoelectronics applications. *Crystals*, 12(8):1087, 2022.

[120] D. Akinwande et al. Graphene and two-dimensional materials for silicon technology. *Nature*, 573(7775):507–518, 2019.

[121] S. Yan et al. Graphene on silicon photonics: Light modulation and detection for cutting-edge communication technologies. *Applied Sciences*, 12(1):313, 2021.

[122] C. Liu et al. Silicon/2d-material photodetectors: from near-infrared to mid-infrared. *Light: Science & Applications*, 10(1):1–21, 2021.

[123] X. Wang et al. High-responsivity graphene/silicon-heterostructure waveguide photodetectors. *Nature Photonics*, 7(11):888–891, 2013.

[124] X. Gan et al. Chip-integrated ultrafast graphene photodetector with high responsivity. *Nature photonics*, 7(11):883–887, 2013.

[125] I. Goykhman et al. On-chip integrated, silicon–graphene plasmonic schottky photodetector with high responsivity and avalanche photogain. *Nano letters*, 16(5):3005–3013, 2016.

[126] M. Casalino. Silicon meets graphene for a new family of near-infrared schottky photodetectors. *Applied Sciences*, 9(18):3677, 2019.

[127] A. Pospischil et al. Cmos-compatible graphene photodetector covering all optical communication bands. *Nature Photonics*, 7(11):892–896, 2013.

[128] S. Goossens et al. Broadband image sensor array based on graphene–cmos integration. *Nature Photonics*, 11(6):366–371, 2017.

[129] D. Neumaier et al. Integrating graphene into semiconductor fabrication lines. *Nature materials*, 18(6):525–529, 2019.

[130] V. Mišeikis and C. Coletti. Wafer-scale integration of graphene for waveguide-integrated optoelectronics. *Applied Physics Letters*, 119(5):050501, 2021.

[131] 2d-experimental pilot line. https://graphene-flagship.eu/innovation/pilot-line/.

[132] Applied nanolayers. https://www.appliednanolayers.com/.

[133] Graphenea, Inc. https://www.graphenea.com/.

[134] B. Son et al. Electron beam induced removal of pmma layer used for graphene transfer. *Scientific reports*, 7(1):1–7, 2017.

[135] Y.-C. Lin et al. Graphene annealing: how clean can it be? *Nano letters*, 12(1):414–419, 2012.

[136] X. Yang and M. Yan. Removing contaminants from transferred cvd graphene. *Nano Research*, 13(3):599–610, 2020.

[137] H. Park et al. Optimized poly (methyl methacrylate)-mediated graphene-transfer process for fabrication of high-quality graphene layer. *Nanotechnology*, 29(41):415303, 2018.

[138] S. Doukas et al. Deep and fast free-space electro-absorption modulation in a mobility-independent graphene-loaded bragg resonator. *Applied Physics Letters*, 113(1):011102, 2018.

[139] S. Doukas et al. Thermionic graphene/silicon schottky infrared photodetectors. *Physical Review B*, 105(11):115417, 2022.

[140] S. Doukas et al. Electrical detection of graphene plasmons for mid-infrared photodetection and chemical sensing: A computational study. *Applied Physics Letters*, 121(5):051103, 2022.

[141] A. D. Koulouklidis et al. Ultrafast terahertz self-induced absorption and phase modulation on a graphene-based thin film absorber. *ACS Photonics*, 9(9):3075–3082, 2022.

[142] A. K. Majumdar and J. C. Ricklin, editors. *Free-space laser communications: principles and advances*. Number 2 in Optical and fiber communications reports. Springer, New York, NY, 2008.

[143] H. Kaushal and G. Kaddoum. Optical communication in space: Challenges and mitigation techniques. *IEEE communications surveys & tutorials*, 19(1):57–96, 2016.

[144] A. Malik and P. Singh. Free space optics: current applications and future challenges. *International Journal of Optics*, 2015, 2015.

[145] M. Flood. Laser altimetry: From science to commerical lidar mapping. *Photogrammetric engineering and remote sensing*, 67(11), 2001.

[146] S. Ishida and N. Nishizawa. Quantitative comparison of contrast and imaging depth of ultrahigh-resolution optical coherence tomography images in 800–1700 nm wavelength region. *Biomedical optics express*, 3(2):282–294, 2012.

[147] Z. Sun et al. Ultrafast lasers mode-locked by nanotubes and graphene. *Physica E: Low-dimensional Systems and Nanostructures*, 44(6):1082–1091, 2012.

[148] A. Martinez and Z. Sun. Nanotube and graphene saturable absorbers for fibre lasers. *Nature Photonics*, 7(11):842–845, 2013.

[149] I. Kašalynas et al. Spectroscopic terahertz imaging at room temperature employing microbolometer terahertz sensors and its application to the study of carcinoma tissues. *Sensors*, 16(4):432, 2016.

[150] S. Dhillon et al. The 2017 terahertz science and technology roadmap. *Journal of Physics D: Applied Physics*, 50(4):043001, 2017.

[151] E. Rosencher and B. Vinter. *Optoelectronics*. Cambridge University Press, Cambridge, UK ; New York, NY, 2002.

[152] A. Rogalski and Z. Bielecki. *Detection of optical signals*. CRC Press, Boca Raton, first edition edition, 2022.

[153] M. Casalino et al. Vertically Illuminated, Resonant Cavity Enhanced, Graphene–Silicon Schottky Photodetectors. *ACS Nano*, 11(11):10955–10963, 2017.

[154] R. C. Jones. Phenomenological description of the response and detecting ability of radiation detectors. *Proceedings of the IRE*, 47(9):1495–1502, 1959.

[155] A. Rogalski. Graphene-based materials in the infrared and terahertz detector families: a tutorial. *Advances in Optics and Photonics*, 11(2):314–379, 2019.

[156] M. Freitag et al. Photoconductivity of biased graphene. *Nature Photonics*, 7(1):53–59, 2013.

[157] L. Britnell et al. Strong light-matter interactions in heterostructures of atomically thin films. *Science*, 340(6138):1311–1314, 2013.

[158] Z. Chen et al. High responsivity, broadband, and fast graphene/silicon photodetector in photoconductor mode. *Advanced Optical Materials*, 3(9):1207–1214, 2015.

[159] P. A. George et al. Ultrafast optical-pump terahertz-probe spectroscopy of the carrier relaxation and recombination dynamics in epitaxial graphene. *Nano letters*, 8(12):4248–4251, 2008.

[160] B. Y. Zhang et al. Broadband high photoresponse from pure monolayer graphene photodetector. *Nature communications*, 4(1):1–11, 2013.

[161] G. Konstantatos et al. Hybrid graphene–quantum dot phototransistors with ultrahigh gain. *Nature nanotechnology*, 7(6):363–368, 2012.

[162] W. Zhang et al. Ultrahigh-gain photodetectors based on atomically thin graphene-mos2 heterostructures. *Scientific reports*, 4(1):1–8, 2014.

[163] Y. Liu et al. Planar carbon nanotube–graphene hybrid films for high-performance broadband photodetectors. *Nature communications*, 6(1):1–7, 2015.

[164] H. Qiao et al. Broadband photodetectors based on graphene–bi2te3 heterostructure. *Acs Nano*, 9(2):1886–1894, 2015.

[165] Z. Ni et al. Plasmonic silicon quantum dots enabled high-sensitivity ultrabroadband photodetection of graphene-based hybrid phototransistors. *ACS nano*, 11(10):9854–9862, 2017.

[166] E. C. Peters et al. Gate dependent photocurrents at a graphene pn junction. *Applied Physics Letters*, 97(19):193102, 2010.

[167] M. C. Lemme et al. Gate-activated photoresponse in a graphene p–n junction. *Nano letters*, 11(10):4134–4137, 2011.

[168] A. Di Bartolomeo. Graphene Schottky diodes: An experimental review of the rectifying graphene/semiconductor heterojunction. *Physics Reports*, 606:1–58, January 2016.

[169] X. An et al. Tunable graphene–silicon heterojunctions for ultrasensitive photodetection. *Nano letters*, 13(3):909–916, 2013.

[170] X. Li et al. High detectivity graphene-silicon heterojunction photodetector. *Small*, 12(5):595–601, 2016.

[171] S. Riazimehr et al. Spectral sensitivity of graphene/silicon heterojunction photodetectors. *Solid-State Electronics*, 115:207–212, 2016.

[172] S. Riazimehr et al. High photocurrent in gated graphene–silicon hybrid photodiodes. *ACS photonics*, 4(6):1506–1514, 2017.

[173] A. Di Bartolomeo et al. Hybrid graphene/silicon schottky photodiode with intrinsic gating effect. *2D Materials*, 4(2):025075, 2017.

[174] H. Selvi et al. Towards substrate engineering of graphene–silicon schottky diode photodetectors. *Nanoscale*, 10(7):3399–3409, 2018.

[175] K. E. Chang et al. Gate-controlled graphene–silicon schottky junction photodetector. *Small*, 14(28):1801182, 2018.

[176] H. Selvi et al. Graphene–silicon-on-insulator (gsoi) schottky diode photodetectors. *Nanoscale*, 10(40):18926–18935, 2018.

[177] S. Riazimehr et al. High responsivity and quantum efficiency of graphene/silicon photodiodes achieved by interdigitating schottky and gated regions. *Acs Photonics*, 6(1):107–115, 2018.

[178] N. Unsuree et al. Visible and infrared photocurrent enhancement in a graphene-silicon schottky photodetector through surface-states and electric field engineering. *2D Materials*, 6(4):041004, 2019.

[179] M. Casalino et al. Free-space schottky graphene/silicon photodetectors operating at 2 μm. *ACS Photonics*, 5(11):4577–4585, 2018.

[180] M. Amirmazlaghani et al. Graphene-si schottky ir detector. *IEEE Journal of Quantum electronics*, 49(7):589–594, 2013.

[181] P. Lv et al. High-sensitivity and fast-response graphene/crystalline silicon schottky junction-based near-ir photodetectors. *IEEE Electron Device Letters*, 34(10):1337–1339, 2013.

[182] M. Casalino. Theoretical investigation of near-infrared fabry–pérot microcavity graphene/silicon schottky photodetectors based on double silicon on insulator substrates. *Micromachines*, 11(8):708, 2020.

[183] A. Tomadin et al. Nonequilibrium dynamics of photoexcited electrons in graphene: Collinear scattering, auger processes, and the impact of screening. *Physical Review B*, 88(3):035430, 2013.

[184] D. Brida et al. Ultrafast collinear scattering and carrier multiplication in graphene. *Nature communications*, 4(1):1–9, 2013.

[185] J. Yan et al. Dual-gated bilayer graphene hot-electron bolometer. *Nature nanotechnology*, 7(7):472–478, 2012.

[186] J. Wei et al. Ultrasensitive hot-electron nanobolometers for terahertz astrophysics. *Nature nanotechnology*, 3(8):496–500, 2008.

[187] G.-H. Lee et al. Graphene-based josephson junction microwave bolometer. *Nature*, 586(7827):42–46, 2020.

[188] R. Kokkoniemi et al. Bolometer operating at the threshold for circuit quantum electrodynamics. *Nature*, 586(7827):47–51, 2020.

[189] U. Sassi et al. Graphene-based mid-infrared room-temperature pyroelectric bolometers with ultrahigh temperature coefficient of resistance. *Nature communications*, 8(1):1–10, 2017.

[190] S. Yuan et al. Room temperature graphene mid-infrared bolometer with a broad operational wavelength range. *Acs Photonics*, 7(5):1206–1215, 2020.

[191] R. Jago et al. Microscopic origin of the bolometric effect in graphene. *Physical Review B*, 99(3):035419, 2019.

[192] M. Asgari et al. Terahertz photodetection in scalable single-layer-graphene and hexagonal boron nitride heterostructures. *Applied Physics Letters*, 121(3):031103, 2022.

[193] Q. Ma et al. Tuning ultrafast electron thermalization pathways in a van der waals heterostructure. *Nature Physics*, 12(5):455–459, 2016.

[194] A. Rogalski et al. Trends in performance limits of the hot infrared photodetectors. *Applied Sciences*, 11(2):501, 2021.

[195] A. Rogalski et al. Inassb-based infrared photodetectors: Thirty years later on. *Sensors*, 20(24):7047, 2020.

[196] S. M. Sze, editor. *VLSI technology*. McGraw-Hill series in electrical engineering. McGraw-Hill, New York, 1983.

[197] P. T. Lin et al. Si-cmos compatible materials and devices for mid-ir microphotonics. *Optical Materials Express*, 3(9):1474–1487, 2013.

[198] A. Rogalski. Infrared detectors: status and trends. *Progress in quantum electronics*, 27(2-3):59–210, 2003.

[199] J. H. Lau, editor. *Flip chip technologies*. Electronic packaging and interconnection series. McGraw-Hill, Boston, Mass, 1996.

[200] G. Konstantatos. Current status and technological prospect of photodetectors based on two-dimensional materials. *Nature communications*, 9(1):1–3, 2018.

[201] F. Zhuge et al. Nanostructured materials and architectures for advanced infrared photodetection. *Advanced Materials Technologies*, 2(8):1700005, 2017.

[202] Q. Guo et al. Black phosphorus mid-infrared photodetectors with high gain. *Nano letters*, 16(7):4648–4655, 2016.

[203] S. Cakmakyapan et al. Gold-patched graphene nano-stripes for high-responsivity and ultrafast photodetection from the visible to infrared regime. *Light: Science & Applications*, 7(1):1–9, 2018.

[204] Vigo system catalogue. https://vigo.com.pl/wp-content/uploads/2017/06/VIGO-Catalogue.pdf/.

[205] M. Long et al. Room temperature high-detectivity mid-infrared photodetectors based on black arsenic phosphorus. *Science advances*, 3(6):e1700589, 2017.

[206] S. Du et al. A broadband fluorographene photodetector. *Advanced Materials*, 29(22):1700463, 2017.

[207] G. T. Reed et al. Silicon optical modulators. *Nature photonics*, 4(8):518–526, 2010.

[208] Q. Bao and K. P. Loh. Graphene photonics, plasmonics, and broadband optoelectronic devices. *ACS nano*, 6(5):3677–3694, 2012.

[209] G. Sinatkas et al. Electro-optic modulation in integrated photonics. *Journal of Applied Physics*, 130(1):010901, 2021.

[210] R. Lange and P. Seitz. Solid-state time-of-flight range camera. *IEEE Journal of quantum electronics*, 37(3):390–397, 2001.

[211] S. Bianconi et al. Machine learning optimization of surface-normal optical modulators for swir time-of-flight 3-d camera. *IEEE Journal of Selected Topics in Quantum Electronics*, 24(6):1–8, 2018.

[212] G. C. Gilbreath et al. Progress in development of multiple-quantum-well retromodulators for free-space data links. *Optical Engineering*, 42(6):1611–1617, 2003.

[213] I. F. Akyildiz et al. 6g and beyond: The future of wireless communications systems. *IEEE access*, 8:133995–134030, 2020.

[214] S. Luo et al. Graphene-based optical modulators. *Nanoscale research letters*, 10(1):1–11, 2015.

[215] Z. Sun et al. Optical modulators with 2d layered materials. *Nature Photonics*, 10(4):227–238, 2016.

[216] S. Yu et al. 2d materials for optical modulation: challenges and opportunities. *Advanced Materials*, 29(14):1606128, 2017.

[217] J. Liu et al. Review of graphene modulators from the low to the high figure of merits. *Journal of Physics D: Applied Physics*, 53(23):233002, 2020.

[218] C. Zhong et al. Graphene-based all-optical modulators. *Frontiers of Optoelectronics*, 13(2):114–128, 2020.

[219] P. Gopalan and B. Sensale-Rodriguez. 2d materials for terahertz modulation. *Advanced Optical Materials*, 8(3):1900550, 2020.

[220] W. Li et al. Ultrafast all-optical graphene modulator. *Nano letters*, 14(2):955–959, 2014.

[221] M. Liu et al. A graphene-based broadband optical modulator. *Nature*, 474(7349):64–67, 2011.

[222] C.-C. Lee et al. Broadband graphene electro-optic modulators with sub-wavelength thickness. *Optics express*, 20(5):5264–5269, 2012.

[223] M. Shah and M. S. Anwar. Magneto-optic modulation of lateral and angular shifts in spin-orbit coupled members of the graphene family. *OSA Continuum*, 3(4):878–892, 2020.

[224] M. Farhat et al. Exciting graphene surface plasmon polaritons through light and sound interplay. *Physical review letters*, 111(23):237404, 2013.

[225] B. Gulbahar and G. Memisoglu. Csstag: Optical nanoscale radar and particle tracking for in-body and microfluidic systems with vibrating graphene and resonance energy transfer. *IEEE Transactions on NanoBioscience*, 16(8):905–916, 2017.

[226] X. Gan et al. Graphene-assisted all-fiber phase shifter and switching. *Optica*, 2(5):468–471, 2015.

[227] B. Sensale-Rodriguez et al. Broadband graphene terahertz modulators enabled by intraband transitions. *Nature communications*, 3(1):1–7, 2012.

[228] E. O. Polat and C. Kocabas. Broadband optical modulators based on graphene supercapacitors. *Nano letters*, 13(12):5851–5857, 2013.

[229] R. Yu et al. Resonant visible light modulation with graphene. *ACS Photonics*, 2(4):550–558, 2015.

[230] R. Shimano et al. Quantum faraday and kerr rotations in graphene. *Nature communications*, 4(1):1–6, 2013.

[231] C.-C. Lee et al. Frequency comb stabilization with bandwidth beyond the limit of gain lifetime by an intracavity graphene electro-optic modulator. *Optics Letters*, 37(15):3084–3086, 2012.

[232] I. Baylam et al. Femtosecond pulse generation with voltage-controlled graphene saturable absorbers. In *Optical Properties of Graphene*, pp. 389–433. World Scientific, 2017.

[233] L. Ren et al. Terahertz and infrared spectroscopy of gated large-area graphene. *Nano Letters*, 12(7):3711–3715, 2012.

[234] B. Sensale-Rodriguez et al. Terahertz imaging employing graphene modulator arrays. *Optics express*, 21(2):2324–2330, 2013.

[235] M. Ijaz et al. Comparison of 830 nm and 1550 nm based free space optical communications link under controlled fog conditions. In *2012 8th International Symposium on Communication Systems, Networks & Digital Signal Processing (CSNDSP)*, pp. 1–5. IEEE, 2012.

[236] G. P. Agrawal. *Fiber-optic communication systems*. John Wiley & Sons, 2012.

[237] A. Masood et al. Comparison of heater architectures for thermal control of silicon photonic circuits. In *10th International Conference on Group IV Photonics*, pp. 83–84. IEEE, 2013.

[238] W.-C. Chiu et al. Optical phase modulators using deformable waveguides actuated by micro-electro-mechanical systems. *Optics letters*, 36(7):1089–1091, 2011.

[239] D. Feng et al. High speed gesi electro-absorption modulator at 1550 nm wavelength on soi waveguide. *Optics express*, 20(20):22224–22232, 2012.

[240] Y.-H. Kuo et al. Quantum-confined stark effect in ge/sige quantum wells on si for optical modulators. *IEEE Journal of selected topics in quantum electronics*, 12(6):1503–1513, 2006.

[241] Y. Rong et al. Quantum-confined stark effect in ge/sige quantum wells on si. *IEEE Journal of selected topics in quantum electronics*, 16(1):85–92, 2009.

[242] M. Whitehead and G. Parry. High-contrast reflection modulation at normal incidence in asymmetric multiple quantum well fabry-perot structure. *Electronics Letters*, 9(25):566–568, 1989.

[243] R.-H. Yan et al. Surface-normal electroabsorption reflection modulators using asymmetric fabry-perot structures. *IEEE journal of quantum electronics*, 27(7):1922–1931, 1991.

[244] E. H. Edwards et al. Ge/sige asymmetric fabry-perot quantum well electroabsorption modulators. *Optics Express*, 20(28):29164–29173, 2012.

[245] R. M. Audet et al. Surface-normal ge/sige asymmetric fabry–perot optical modulators fabricated on silicon substrates. *Journal of lightwave technology*, 31(24):3995–4003, 2013.

[246] H. Mohseni et al. Tunable surface-normal modulators operating near 1550 nm with a high-extinction ratio at high temperatures. *IEEE photonics technology letters*, 18(1):214–216, 2005.

[247] K. Y. Lee et al. Multiple pn junction subwavelength gratings for transmission-mode electro-optic modulators. *Scientific reports*, 7(1):1–8, 2017.

[248] Y. Gao et al. High-speed electro-optic modulator integrated with graphene-boron nitride heterostructure and photonic crystal nanocavity. *Nano letters*, 15(3):2001–2005, 2015.

[249] T. Sun et al. Surface-normal electro-optic spatial light modulator using graphene integrated on a high-contrast grating resonator. *Optics express*, 24(23):26035–26043, 2016.

[250] X. Gan et al. High-contrast electrooptic modulation of a photonic crystal nanocavity by electrical gating of graphene. *Nano letters*, 13(2):691–696, 2013.

[251] S. Kim et al. Electronically tunable perfect absorption in graphene. *Nano letters*, 18(2):971–979, 2018.

[252] Y. Yao et al. Electrically tunable metasurface perfect absorbers for ultrathin mid-infrared optical modulators. *Nano letters*, 14(11):6526–6532, 2014.

[253] S. Ye et al. Electro-absorption optical modulator using dual-graphene-on-graphene configuration. *Optics express*, 22(21):26173–26180, 2014.

[254] C. T. Phare et al. Graphene electro-optic modulator with 30 ghz bandwidth. *Nature Photonics*, 9(8):511–514, 2015.

[255] J.-S. Shin and J. T. Kim. Broadband silicon optical modulator using a graphene-integrated hybrid plasmonic waveguide. *Nanotechnology*, 26(36):365201, 2015.

[256] V. Sorianello et al. Graphene–silicon phase modulators with gigahertz bandwidth. *Nature Photonics*, 12(1):40–44, 2018.

[257] D. Abergel et al. Properties of graphene: a theoretical perspective. *Advances in Physics*, 59(4):261–482, 2010.

[258] G. Dresselhaus et al. *Physical properties of carbon nanotubes*. World scientific, 1998.

[259] N. Kakenov et al. Broadband terahertz modulators using self-gated graphene capacitors. *JOSA B*, 32(9):1861–1866, 2015.

[260] O. Balci et al. Graphene-enabled electrically switchable radar-absorbing surfaces. *Nature communications*, 6(1):1–10, 2015.

[261] G. Soavi et al. Broadband, electrically tunable third-harmonic generation in graphene. *Nature nanotechnology*, 13(7):583–588, 2018.

[262] M. Katsnelson. Zitterbewegung, chirality, and minimal conductivity in graphene. *The European Physical Journal B-Condensed Matter and Complex Systems*, 51(2):157–160, 2006.

[263] S. D. Sarma et al. Electronic transport in two-dimensional graphene. *Reviews of modern physics*, 83(2):407, 2011.

[264] J. Martin et al. Observation of electron–hole puddles in graphene using a scanning single-electron transistor. *Nature physics*, 4(2):144–148, 2008.

[265] Y. Zhang et al. Origin of spatial charge inhomogeneity in graphene. *Nature Physics*, 5(10):722–726, 2009.

[266] K. I. Bolotin et al. Ultrahigh electron mobility in suspended graphene. *Solid state communications*, 146(9-10):351–355, 2008.

[267] L. Wang et al. One-dimensional electrical contact to a two-dimensional material. *Science*, 342(6158):614–617, 2013.

[268] J.-H. Chen et al. Intrinsic and extrinsic performance limits of graphene devices on sio2. *Nature nanotechnology*, 3(4):206–209, 2008.

[269] J. Xia et al. Measurement of the quantum capacitance of graphene. *Nature nanotechnology*, 4(8):505–509, 2009.

[270] A. Das et al. Monitoring dopants by raman scattering in an electrochemically top-gated graphene transistor. *Nature nanotechnology*, 3(4):210–215, 2008.

[271] D. Sun et al. Ultrafast hot-carrier-dominated photocurrent in graphene. *Nature nanotechnology*, 7(2):114–118, 2012.

[272] G. Giuliani and G. Vignale. *Quantum theory of the electron liquid*. Cambridge university press, 2005.

[273] K. C. Fong et al. Measurement of the electronic thermal conductance channels and heat capacity of graphene at low temperature. *Physical Review X*, 3(4):041008, 2013.

[274] G. W. Hanson. Dyadic green's functions and guided surface waves for a surface conductivity model of graphene. *Journal of Applied Physics*, 103(6):064302, 2008.

[275] J. Horng et al. Drude conductivity of dirac fermions in graphene. *Physical Review B*, 83(16):165113, 2011.

[276] K. F. Mak et al. Optical spectroscopy of graphene: From the far infrared to the ultraviolet. *Solid State Communications*, 152(15):1341–1349, 2012.

[277] J. H. Gosling et al. Universal mobility characteristics of graphene originating from charge scattering by ionised impurities. *Communications Physics*, 4(1):1–8, 2021.

[278] C. M. Wolfe et al. *Physical properties of semiconductors*. Prentice Hall series in solid state physical electronics. Prentice Hall, Englewood Cliffs, N.J, 1989.

[279] S. D. Sarma and E. Hwang. Density-dependent electrical conductivity in suspended graphene: Approaching the dirac point in transport. *Physical Review B*, 87(3):035415, 2013.

[280] Z. Mics et al. Thermodynamic picture of ultrafast charge transport in graphene. *Nature Communications*, 6(1):7655, 2015.

[281] I. Ivanov et al. Perspective on terahertz spectroscopy of graphene. *EPL (Europhysics Letters)*, 111(6):67001, 2015.

[282] H. A. Hafez et al. Terahertz nonlinear optics of graphene: from saturable absorption to high-harmonics generation. *Advanced Optical Materials*, 8(3):1900771, 2020.

[283] V. Sorianello et al. Design optimization of single and double layer graphene phase modulators in soi. *Optics Express*, 23(5):6478–6490, 2015.

[284] E. Lidorikis and A. C. Ferrari. Photonics with multiwall carbon nanotube arrays. *ACS nano*, 3(5):1238–1248, 2009.

[285] T. Echtermeyer et al. Surface plasmon polariton graphene photodetectors. *Nano Letters*, 16(1):8–20, 2016.

[286] M. S. Dresselhaus et al. *Science of fullerenes and carbon nanotubes: their properties and applications*. Elsevier, 1996.

[287] C. Casiraghi et al. Rayleigh imaging of graphene and graphene layers. *Nano letters*, 7(9):2711–2717, 2007.

[288] F. Wooten. *Optical Properties of Solids.* Elsevier Science, 2014.

[289] H. Li et al. Tunable graphene-based mid-infrared plasmonic wide-angle narrow-band perfect absorber. *Scientific reports*, 6(1):1–8, 2016.

[290] G. Yao et al. Dual-band tunable perfect metamaterial absorber in the thz range. *Optics express*, 24(2):1518–1527, 2016.

[291] M. Huang et al. Based on graphene tunable dual-band terahertz metamaterial absorber with wide-angle. *Optics Communications*, 415:194–201, 2018.

[292] S.-X. Xia et al. Multi-band perfect plasmonic absorptions using rectangular graphene gratings. *Optics letters*, 42(15):3052–3055, 2017.

[293] H. Meng et al. Tunable and multi-channel perfect absorber based on graphene at mid-infrared region. *Applied Physics Express*, 11(5):052002, 2018.

[294] A. Andryieuski and A. V. Lavrinenko. Graphene metamaterials based tunable terahertz absorber: effective surface conductivity approach. *Optics express*, 21(7):9144–9155, 2013.

[295] J. Zhang et al. Coherent perfect absorption and transparency in a nanostructured graphene film. *Optics express*, 22(10):12524–12532, 2014.

[296] W. L. Barnes et al. Surface plasmon subwavelength optics. *nature*, 424(6950):824–830, 2003.

[297] D. K. Gramotnev and S. I. Bozhevolnyi. Plasmonics beyond the diffraction limit. *Nature photonics*, 4(2):83–91, 2010.

[298] S. A. Maier et al. Plasmonics—a route to nanoscale optical devices. *Advanced materials*, 13(19):1501–1505, 2001.

[299] S. A. Maier et al. *Plasmonics: fundamentals and applications*, volume 1. Springer, 2007.

[300] A. A. Maradudin et al. *Modern plasmonics*. Elsevier, 2014.

[301] H. U. Yang et al. Optical dielectric function of silver. *Physical Review B*, 91(23):235137, 2015.

[302] M. Jablan et al. Plasmonics in graphene at infrared frequencies. *Physical review B*, 80(24):245435, 2009.

[303] D. K. Polyushkin et al. Graphene as a substrate for plasmonic nanoparticles. *Journal of Optics*, 15(11):114001, 2013.

[304] P. Alonso-González et al. Controlling graphene plasmons with resonant metal antennas and spatial conductivity patterns. *Science*, 344(6190):1369–1373, 2014.

[305] Z. Fei et al. Gate-tuning of graphene plasmons revealed by infrared nano-imaging. *Nature*, 487(7405):82–85, 2012.

[306] J. Chen et al. Optical nano-imaging of gate-tunable graphene plasmons. *Nature*, 487(7405):77–81, 2012.

[307] H. Yan et al. Tunable infrared plasmonic devices using graphene/insulator stacks. *Nature nanotechnology*, 7(5):330–334, 2012.

[308] Z. Wang et al. Experimental demonstration of graphene plasmons working close to the near-infrared window. *Optics letters*, 41(22):5345–5348, 2016.

[309] S. Thongrattanasiri et al. Complete optical absorption in periodically patterned graphene. *Physical review letters*, 108(4):047401, 2012.

[310] Z. Fang et al. Gated tunability and hybridization of localized plasmons in nanostructured graphene. *ACS nano*, 7(3):2388–2395, 2013.

[311] Z. Fang et al. Active tunable absorption enhancement with graphene nanodisk arrays. *Nano letters*, 14(1):299–304, 2014.

[312] X. Zhu et al. Plasmon–phonon coupling in large-area graphene dot and antidot arrays fabricated by nanosphere lithography. *Nano letters*, 14(5):2907–2913, 2014.

[313] L. Ju et al. Graphene plasmonics for tunable terahertz metamaterials. *Nature nanotechnology*, 6(10):630–634, 2011.

[314] P. A. D. Gonçalves et al. Modeling the excitation of graphene plasmons in periodic grids of graphene ribbons: An analytical approach. *Physical Review B*, 94(19):195421, 2016.

[315] I. J. Luxmoore et al. Strong coupling in the far-infrared between graphene plasmons and the surface optical phonons of silicon dioxide. *ACS photonics*, 1(11):1151–1155, 2014.

[316] H. Yan et al. Damping pathways of mid-infrared plasmons in graphene nanostructures. *Nature Photonics*, 7(5):394–399, 2013.

[317] A. Y. Nikitin et al. Edge and waveguide terahertz surface plasmon modes in graphene microribbons. *Physical Review B*, 84(16):161407, 2011.

[318] J. Christensen et al. Graphene plasmon waveguiding and hybridization in individual and paired nanoribbons. *ACS nano*, 6(1):431–440, 2012.

[319] A. Y. Nikitin et al. Surface plasmon enhanced absorption and suppressed transmission in periodic arrays of graphene ribbons. *Physical Review B*, 85(8):081405, 2012.

[320] B. Vasić et al. Localized surface plasmon resonances in graphene ribbon arrays for sensing of dielectric environment at infrared frequencies. *Journal of Applied Physics*, 113(1):013110, 2013.

[321] X. Guo et al. Perfect-absorption graphene metamaterials for surface-enhanced molecular fingerprint spectroscopy. *Nanotechnology*, 29(18):184004, 2018.

[322] Y. Fan et al. Tunable mid-infrared coherent perfect absorption in a graphene metasurface. *Scientific reports*, 5(1):1–8, 2015.

[323] M. Breusing et al. Ultrafast nonequilibrium carrier dynamics in a single graphene layer. *Physical Review B*, 83(15):153410, 2011.

[324] K.-J. Tielrooij et al. Photoexcitation cascade and multiple hot-carrier generation in graphene. *Nature Physics*, 9(4):248–252, 2013.

[325] I. Gierz et al. Snapshots of non-equilibrium dirac carrier distributions in graphene. *Nature materials*, 12(12):1119–1124, 2013.

[326] J. C. Song et al. Photoexcited carrier dynamics and impact-excitation cascade in graphene. *Physical Review B*, 87(15):155429, 2013.

[327] A. Tomadin et al. The ultrafast dynamics and conductivity of photoexcited graphene at different fermi energies. *Science advances*, 4(5):eaar5313, 2018.

[328] J. C. Song and L. S. Levitov. Energy flows in graphene: hot carrier dynamics and cooling. *Journal of Physics: Condensed Matter*, 27(16):164201, 2015.

[329] T. Winzer et al. Carrier multiplication in graphene. *Nano letters*, 10(12):4839–4843, 2010.

[330] H. A. Hafez et al. Extremely efficient terahertz high-harmonic generation in graphene by hot dirac fermions. *Nature*, 561(7724):507–511, 2018.

[331] G. Rohde et al. Ultrafast formation of a fermi-dirac distributed electron gas. *Physical review letters*, 121(25):256401, 2018.

[332] D. Sun et al. Ultrafast relaxation of excited dirac fermions in epitaxial graphene using optical differential transmission spectroscopy. *Physical review letters*, 101(15):157402, 2008.

[333] E. A. Pogna et al. Hot-carrier cooling in high-quality graphene is intrinsically limited by optical phonons. *ACS nano*, 15(7):11285–11295, 2021.

[334] E. A. Pogna et al. Electrically tunable nonequilibrium optical response of graphene. *ACS nano*, 16(3):3613–3624, 2022.

[335] M. T. Mihnev et al. Microscopic origins of the terahertz carrier relaxation and cooling dynamics in graphene. *Nature communications*, 7(1):1–11, 2016.

[336] T. Low et al. Cooling of photoexcited carriers in graphene by internal and substrate phonons. *Physical Review B*, 86(4):045413, 2012.

[337] K.-J. Tielrooij et al. Out-of-plane heat transfer in van der waals stacks through electron–hyperbolic phonon coupling. *Nature nanotechnology*, 13(1):41–46, 2018.

[338] A. Principi et al. Super-planckian electron cooling in a van der waals stack. *Physical review letters*, 118(12):126804, 2017.

[339] W. Yang et al. A graphene zener–klein transistor cooled by a hyperbolic substrate. *Nature Nanotechnology*, 13(1):47–52, 2018.

[340] S. Piscanec et al. Kohn anomalies and electron-phonon interactions in graphite. *Physical review letters*, 93(18):185503, 2004.

[341] A. C. Ferrari et al. Raman spectrum of graphene and graphene layers. *Physical review letters*, 97(18):187401, 2006.

[342] A. C. Ferrari. Raman spectroscopy of graphene and graphite: Disorder, electron–phonon coupling, doping and nonadiabatic effects. *Solid state communications*, 143(1-2):47–57, 2007.

[343] T. Sohier et al. Phonon-limited resistivity of graphene by first-principles calculations: Electron-phonon interactions, strain-induced gauge field, and boltzmann equation. *Physical Review B*, 90(12):125414, 2014.

[344] F. Rana et al. Carrier recombination and generation rates for intravalley and intervalley phonon scattering in graphene. *Physical Review B*, 79(11):115447, 2009.

[345] J. Viljas and T. Heikkilä. Electron-phonon heat transfer in monolayer and bilayer graphene. *Physical Review B*, 81(24):245404, 2010.

[346] R. Bistritzer and A. H. MacDonald. Electronic cooling in graphene. *Physical Review Letters*, 102(20):206410, 2009.

[347] S. Arshia Khatoon et al. Inelastic scattering and cooling of photoexcited electrons through coupling with acoustic, optic, and surface polar optic phonons in graphene. *Journal of Applied Physics*, 129(1):014308, 2021.

[348] D. K. Efetov and P. Kim. Controlling electron-phonon interactions in graphene at ultrahigh carrier densities. *Physical review letters*, 105(25):256805, 2010.

[349] E. Hwang and S. D. Sarma. Acoustic phonon scattering limited carrier mobility in two-dimensional extrinsic graphene. *Physical Review B*, 77(11):115449, 2008.

[350] W.-K. Tse and S. D. Sarma. Energy relaxation of hot dirac fermions in graphene. *Physical Review B*, 79(23):235406, 2009.

[351] J. C. Song et al. Disorder-assisted electron-phonon scattering and cooling pathways in graphene. *Physical review letters*, 109(10):106602, 2012.

[352] M. W. Graham et al. Photocurrent measurements of supercollision cooling in graphene. *Nature Physics*, 9(2):103–108, 2013.

[353] A. Betz et al. Supercollision cooling in undoped graphene. *Nature Physics*, 9(2):109–112, 2013.

[354] B. Sun and M. Wu. Microscopic theory of ultrafast dynamics of carriers photoexcited by thz and near-infrared linearly polarized laser pulses in graphene. *New Journal of Physics*, 15(8):083038, 2013.

[355] T. Fang et al. Mobility in semiconducting graphene nanoribbons: Phonon, impurity, and edge roughness scattering. *Physical Review B*, 78(20):205403, 2008.

[356] A. Matthiessen and A. C. C. Vogt. Iv. on the influence of temperature on the electric conducting-power of alloys. *Philosophical Transactions of the Royal Society of London*, (154):167–200, 1864.

[357] E. Pop et al. Thermal properties of graphene: Fundamentals and applications. *MRS bulletin*, 37(12):1273–1281, 2012.

[358] A. A. Balandin. Thermal properties of graphene and nanostructured carbon materials. *Nature materials*, 10(8):569–581, 2011.

[359] J. Zhang et al. Rough contact is not always bad for interfacial energy coupling. *Nanoscale*, 5(23):11598–11603, 2013.

[360] Z. Xu and M. J. Buehler. Heat dissipation at a graphene–substrate interface. *Journal of Physics: Condensed Matter*, 24(47):475305, 2012.

[361] S. Lin et al. High performance graphene/semiconductor van der waals heterostructure optoelectronic devices. *Nano Energy*, 40:122–148, 2017.

[362] Y. S. Ang et al. Physics of electron emission and injection in two-dimensional materials: Theory and simulation. *InfoMat*, pp. inf2.12168, January 2021.

[363] Y. Xu et al. Contacts between two-and three-dimensional materials: ohmic, schottky, and p–n heterojunctions. *ACS nano*, 10(5):4895–4919, 2016.

[364] D. H. Shin and S.-H. Choi. Graphene-based semiconductor heterostructures for photodetectors. *Micromachines*, 9(7):350, 2018.

[365] S. K. Behura et al. Graphene–semiconductor heterojunction sheds light on emerging photovoltaics. *Nature Photonics*, 13(5):312–318, 2019.

[366] X. Kong et al. Graphene/si schottky solar cells: a review of recent advances and prospects. *RSC advances*, 9(2):863–877, 2019.

[367] G. Giovannetti et al. Doping Graphene with Metal Contacts. *Physical Review Letters*, 101(2):026803, July 2008.

[368] S. M. Song et al. Determination of Work Function of Graphene under a Metal Electrode and Its Role in Contact Resistance. *Nano Letters*, 12(8):3887–3892, August 2012.

[369] Y. An et al. Metal-semiconductor-metal photodetectors based on graphene/ p -type silicon Schottky junctions. *Applied Physics Letters*, 102(1):013110, January 2013.

[370] H. Zhong et al. Charge transport mechanisms of graphene/semiconductor Schottky barriers: A theoretical and experimental study. *Journal of Applied Physics*, 115(1):013701, January 2014.

[371] R. T. Tung. Recent advances in Schottky barrier concepts. *Materials Science and Engineering: R: Reports*, 35(1-3):1–138, November 2001.

[372] D. Sinha and J. U. Lee. Ideal Graphene/Silicon Schottky Junction Diodes. *Nano Letters*, 14(8):4660–4664, August 2014.

[373] A. Singh et al. Tunable reverse-biased graphene/silicon heterojunction schottky diode sensor. *Small*, 10(8):1555–1565, 2014.

[374] C.-C. Chen et al. Graphene-silicon schottky diodes. *Nano letters*, 11(5):1863–1867, 2011.

[375] S. Tongay et al. Rectification at Graphene-Semiconductor Interfaces: Zero-Gap Semiconductor-Based Diodes. *Physical Review X*, 2(1):011002, January 2012.

[376] A. Di Bartolomeo et al. Tunable Schottky barrier and high responsivity in graphene/Si-nanotip optoelectronic device. *2D Materials*, 4(1):015024, November 2016.

[377] R. T. Tung. The physics and chemistry of the schottky barrier height. *Applied Physics Reviews*, 1(1):011304, 2014.

[378] F. Padovani and R. Stratton. Field and thermionic-field emission in schottky barriers. *Solid-State Electronics*, 9(7):695–707, 1966.

[379] M. G. Ancona. Electron transport in graphene from a diffusion-drift perspective. *IEEE Transactions on Electron Devices*, 57(3):681–689, 2010.

[380] M. Javadi et al. Sequentially Assembled Graphene Layers on Silicon, the Role of Uncertainty Principles in Graphene Silicon Schottky Junctions. *Advanced Optical Materials*, 7(19):1900470, October 2019.

[381] M. Trushin. Theory of thermionic emission from a two-dimensional conductor and its application to a graphene-semiconductor schottky junction. *Applied Physics Letters*, 112(17):171109, 2018.

[382] G. Luongo et al. Electronic properties of graphene/p-silicon Schottky junction. *Journal of Physics D: Applied Physics*, 51(25):255305, June 2018.

[383] F. Xia et al. The origins and limits of metal–graphene junction resistance. *Nature Nanotechnology*, 6(3):179–184, March 2011.

[384] M. Born and E. Wolf. *Principles of optics: electromagnetic theory of propagation, interference and diffraction of light*. Cambridge University Press, Cambridge ; New York, 7th expanded ed edition, 1999.

[385] P. Yeh. *Optical waves in layered media*. Wiley, Hoboken, NJ, 2005.

[386] D. V. Bellas et al. Simulating the opto-thermal processes involved in laser induced self-assembly of surface and sub-surface plasmonic nano-structuring. *Thin Solid Films*, 630:7–24, 2017.

[387] O. Deparis. Poynting vector in transfer-matrix formalism for the calculation of light absorption profile in stratified isotropic optical media. *Optics letters*, 36(20):3960–3962, 2011.

[388] K. Yee. Numerical solution of initial boundary value problems involving maxwell's equations in isotropic media. *IEEE Transactions on antennas and propagation*, 14(3):302–307, 1966.

[389] A. Taflove and S. C. Hagness. *Computational electrodynamics: the finite-difference time-domain method*. Artech House antennas and propagation library. Artech House, Boston, 3rd ed edition, 2005.

[390] W. Yu and R. Mittra. A conformal finite difference time domain technique for modeling curved dielectric surfaces. *IEEE Microwave and Wireless Components Letters*, 11(1):25–27, 2001.

[391] M. A. Alsunaidi and A. A. Al-Jabr. A general ADE-FDTD algorithm for the simulation of dispersive structures. *IEEE Photonics Technology Letters*, 21(12):817–819, 2009.

[392] J. B. Schneider. Understanding the finite-difference time-domain method. Available at https://www.eecs.wsu.edu/~schneidj/ufdtd, 2010.

[393] K. S. Kunz and R. J. Luebbers. *The finite difference time domain method for electromagnetics*. CRC Press, Boca Raton, 1993.

[394] W. Yu, editor. *Parallel finite-difference time-domain method*. Artech House electromagnetic analysis series. Artech House, Boston, MA, 2006. OCLC: ocm65767412.

[395] J.-P. Berenger. A perfectly matched layer for the absorption of electromagnetic waves. *Journal of computational physics*, 114(2):185–200, 1994.

[396] S. D. Gedney. An anisotropic perfectly matched layer-absorbing medium for the truncation of fdtd lattices. *IEEE transactions on Antennas and Propagation*, 44(12):1630–1639, 1996.

[397] M. Kuzuoglu and R. Mittra. Frequency dependence of the constitutive parameters of causal perfectly matched anisotropic absorbers. *IEEE Microwave and Guided wave letters*, 6(12):447–449, 1996.

[398] W. C. Chew and W. H. Weedon. A 3d perfectly matched medium from modified maxwell's equations with stretched coordinates. *Microwave and optical technology letters*, 7(13):599–604, 1994.

[399] Lumerical solutions, Inc. https://www.lumerical.com/products/fdtd/.

[400] S. D. Gedney and B. Zhao. An auxiliary differential equation formulation for the complex-frequency shifted pml. *IEEE Transactions on Antennas and Propagation*, 58(3):838–847, 2009.

[401] N. W. Ashcroft and N. D. Mermin. *Solid state physics*. Holt, Rinehart and Winston, New York, 1976.

[402] E. Simsek. A closed-form approximate expression for the optical conductivity of graphene. *Optics letters*, 38(9):1437–1439, 2013.

[403] V. Nayyeri et al. Modeling graphene in the finite-difference time-domain method using a surface boundary condition. *IEEE transactions on antennas and propagation*, 61(8):4176–4182, 2013.

[404] E. Moreno et al. Bcc-grid versus sc-grid in the modeling of a sheet of graphene as a surface boundary condition in the context of ade-fdtd. *Mathematics and Computers in Simulation*, 186:52–61, 2021.

[405] J. Stoer and R. Bulirsch. *Introduction to numerical analysis*. Springer, New York, 3rd ed edition, 2002.

[406] U. M. Ascher and L. R. Petzold. *Computer methods for ordinary differential equations and differential-algebraic equations*. Society for Industrial and Applied Mathematics, Philadelphia, 1998.

[407] C. Guo et al. Graphene-based perfect absorption structures in the visible to terahertz band and their optoelectronics applications. *Nanomaterials*, 8(12):1033, 2018.

[408] A. Majumdar et al. Electrical control of silicon photonic crystal cavity by graphene. *Nano letters*, 13(2):515–518, 2013.

[409] B. Vasić and R. Gajić. Tunable fabry–perot resonators with embedded graphene from terahertz to near-infrared frequencies. *Optics letters*, 39(21):6253–6256, 2014.

[410] J. R. Piper and S. Fan. Total absorption in a graphene monolayer in the optical regime by critical coupling with a photonic crystal guided resonance. *Acs Photonics*, 1(4):347–353, 2014.

[411] J. R. Piper et al. Total absorption by degenerate critical coupling. *Applied Physics Letters*, 104(25):251110, 2014.

[412] S. O. Kasap and P. Capper. *Springer handbook of electronic and photonic materials*, volume 11. Springer, 2006.

[413] S. Y. Zhou et al. Substrate-induced bandgap opening in epitaxial graphene. *Nature materials*, 6(10):770–775, 2007.

[414] B. Guo et al. Graphene doping: a review. *Insciences J.*, 1(2):80–89, 2011.

[415] I. Gierz et al. Atomic hole doping of graphene. *Nano letters*, 8(12):4603–4607, 2008.

[416] J. Robertson. High dielectric constant oxides. *The European Physical Journal-Applied Physics*, 28(3):265–291, 2004.

[417] S. Basu et al. Infrared Radiative Properties of Heavily Doped Silicon at Room Temperature. *Journal of Heat Transfer*, 132(2):023301, February 2010.

[418] B. Lee and Z. Zhang. Temperature and Doping Dependence of The Radiative Properties of Silicon: Drude Model Revisited. In *2005 13th International Conference on Advanced Thermal Processing of Semiconductors*, pp. 251–260, Santa Barbara, CA, USA, 2005. IEEE.

[419] A. Yariv. Critical coupling and its control in optical waveguide-ring resonator systems. *IEEE Photonics Technology Letters*, 14(4):483–485, 2002.

[420] J. R. Tischler et al. Critically coupled resonators in vertical geometry using a planar mirror and a 5 nm thick absorbing film. *Optics letters*, 31(13):2045–2047, 2006.

[421] A. Nematpour et al. Towards perfect absorption of single layer cvd graphene in an optical resonant cavity: Challenges and experimental achievements. *Materials*, 15(1):352, 2022.

[422] H. A. Haus. *Waves and fields in optoelectronics*. Prentice-Hall series in solid state physical electronics. Prentice-Hall, Englewood Cliffs, NJ, 1984.

[423] E. D. Palik. *Handbook of optical constants of solids*. Academic Press, San Diego, 1998. OCLC: 190802546.

[424] L. Song et al. A review on graphene-silicon Schottky junction interface. *Journal of Alloys and Compounds*, 806:63–70, October 2019.

[425] C.-C. Chen et al. Graphene-Silicon Schottky Diodes. *Nano Letters*, 11(5):1863–1867, May 2011.

[426] S. Riazimehr et al. High Responsivity and Quantum Efficiency of Graphene/Silicon Photodiodes Achieved by Interdigitating Schottky and Gated Regions. *ACS Photonics*, 6(1):107–115, January 2019.

[427] P. C. Eng et al. State-of-the-art photodetectors for optoelectronic integration at telecommunication wavelength. *Nanophotonics*, 4(3):277–302, January 2015.

[428] J. Lee et al. Gate-tunable Thermoelectric Effects in a Graphene/WS2 van der Waals Heterostructure. *Journal of the Korean Physical Society*, 73(7):940–944, October 2018.

[429] J. C. W. Song et al. Hot Carrier Transport and Photocurrent Response in Graphene. *Nano Letters*, 11(11):4688–4692, November 2011.

[430] E. Malic et al. Microscopic theory of absorption and ultrafast many-particle kinetics in graphene. *Physical Review B*, 84(20):205406, November 2011.

[431] B. Y. Sun et al. Dynamics of photoexcited carriers in graphene. *Physical Review B*, 85(12):125413, March 2012.

[432] E. Malic et al. Efficient orientational carrier relaxation in optically excited graphene. *Applied Physics Letters*, 101(21):213110, November 2012.

[433] M. Lazzeri et al. Electron Transport and Hot Phonons in Carbon Nanotubes. *Physical Review Letters*, 95(23):236802, November 2005.

[434] N. Bonini et al. Phonon anharmonicities in graphite and graphene. *Physical review letters*, 99(17):176802, 2007.

[435] H. Yang et al. Graphene Barristor, a Triode Device with a Gate-Controlled Schottky Barrier. *Science*, 336(6085):1140–1143, June 2012.

[436] D. Tomer et al. Carrier transport in reverse-biased graphene/semiconductor Schottky junctions. *Applied Physics Letters*, 106(17):173510, April 2015.

[437] Y. Liu et al. Approaching total absorption at near infrared in a large area monolayer graphene by critical coupling. *Applied Physics Letters*, 105(18):181105, November 2014.

[438] A. Nematpour et al. Experimental mid-infrared absorption (84%) of single-layer graphene in a reflective asymmetric fabry–perot filter: Implications for photodetectors. *ACS Applied Nano Materials*, 4(2):1495–1502, 2021.

[439] A. Pelella et al. Graphene Silicon Device for Visible and Infrared Photodetection. *ACS Applied Materials & Interfaces*, pp. acsami.1c12050, September 2021.

[440] A. Marini et al. Theory of graphene saturable absorption. *Physical Review B*, 95(12):125408, March 2017.

[441] Z. Sun et al. Graphene Mode-Locked Ultrafast Laser. *ACS Nano*, 4(2):803–810, February 2010.

[442] J. Los et al. Melting temperature of graphene. *Physical Review B*, 91(4):045415, 2015.

[443] T. Cusati et al. Electrical properties of graphene-metal contacts. *Scientific Reports*, 7(1):5109, July 2017.

[444] I. Torre et al. Electrical plasmon detection in graphene waveguides. *Physical Review B*, 91(8):081402, 2015.

[445] M. B. Lundeberg et al. Thermoelectric detection and imaging of propagating graphene plasmons. *Nature materials*, 16(2):204–207, 2017.

[446] R. Yu and F. J. Garcia de Abajo. Electrical detection of single graphene plasmons. *ACS nano*, 10(8):8045–8053, 2016.

[447] Q. Guo et al. Efficient electrical detection of mid-infrared graphene plasmons at room temperature. *Nature materials*, 17(11):986–992, 2018.

[448] V. W. Brar et al. Highly confined tunable mid-infrared plasmonics in graphene nanoresonators. *Nano letters*, 13(6):2541–2547, 2013.

[449] M. S. Jang et al. Tunable large resonant absorption in a midinfrared graphene salisbury screen. *Physical Review B*, 90(16):165409, 2014.

[450] Y. Li et al. Graphene plasmon enhanced vibrational sensing of surface-adsorbed layers. *Nano letters*, 14(3):1573–1577, 2014.

[451] D. Rodrigo et al. Mid-infrared plasmonic biosensing with graphene. *Science*, 349(6244):165–168, 2015.

[452] D. B. Farmer et al. Ultrasensitive plasmonic detection of molecules with graphene. *Acs Photonics*, 3(4):553–557, 2016.

[453] A. Marini et al. Molecular Sensing with Tunable Graphene Plasmons. *ACS Photonics*, 2(7):876–882, July 2015.

[454] H. Hu et al. Gas identification with graphene plasmons. *Nature communications*, 10(1):1–7, 2019.

[455] S. Ogawa et al. Graphene plasmonics in sensor applications: A review. *Sensors*, 20(12):3563, 2020.

[456] H. Liu et al. Chemical doping of graphene. *Journal of materials chemistry*, 21(10):3335–3345, 2011.

[457] P. Li et al. Graphene-enhanced infrared near-field microscopy. *Nano letters*, 14(8):4400–4405, 2014.

[458] E. Hwang and S. D. Sarma. Screening-induced temperature-dependent transport in two-dimensional graphene. *Physical Review B*, 79(16):165404, 2009.

[459] P. Y. Huang et al. Grains and grain boundaries in single-layer graphene atomic patchwork quilts. *Nature*, 469(7330):389–392, 2011.

[460] J. Heo et al. Nonmonotonic temperature dependent transport in graphene grown by chemical vapor deposition. *Physical Review B*, 84(3):035421, 2011.

[461] E. J. Dias et al. Thermal manipulation of plasmons in atomically thin films. *Light: Science & Applications*, 9(1):1–11, 2020.

[462] Y. Hu et al. Graphene-based surface enhanced vibrational spectroscopy: recent developments, challenges, and applications. *ACS Photonics*, 6(9):2182–2197, 2019.

[463] R. Adato et al. Engineered absorption enhancement and induced transparency in coupled molecular and plasmonic resonator systems. *Nano letters*, 13(6):2584–2591, 2013.

[464] N. J. Bareza et al. Mid-infrared gas sensing using graphene plasmons tuned by reversible chemical doping. *ACS Photonics*, 7(4):879–884, 2020.

[465] T. L. Myers et al. Accurate measurement of the optical constants n and k for a series of 57 inorganic and organic liquids for optical modeling and detection. *Applied spectroscopy*, 72(4):535–550, 2018.

[466] S. Ryu et al. Atmospheric oxygen binding and hole doping in deformed graphene on a sio2 substrate. *Nano letters*, 10(12):4944–4951, 2010.

[467] A. Pirkle et al. The effect of chemical residues on the physical and electrical properties of chemical vapor deposited graphene transferred to sio2. *Applied Physics Letters*, 99(12):122108, 2011.

[468] R. Lord and T. McCubbin. Infrared spectroscopy from 5 to 200 microns with a small grating spectrometer. *JOSA*, 47(8):689–697, 1957.

[469] Ultrashort nonlinear laser interactions ans sources research group (unis). https://unis.iesl.forth.gr/.

[470] Photonic-, phononc- and metamaterials research group (ppm). https://www.iesl.forth.gr/en/research/PPM/.

[471] M. Tonouchi. Cutting-edge terahertz technology. *Nature photonics*, 1(2):97–105, 2007.

[472] J. A. Zeitler et al. Terahertz pulsed spectroscopy and imaging in the pharmaceutical setting-a review. *Journal of Pharmacy and Pharmacology*, 59(2):209–223, 2007.

[473] X. Yang et al. Biomedical applications of terahertz spectroscopy and imaging. *Trends in biotechnology*, 34(10):810–824, 2016.

[474] Q. Wang et al. Overview of imaging methods based on terahertz time-domain spectroscopy. *Applied Spectroscopy Reviews*, 57(3):249–264, 2022.

[475] C. Liaskos et al. Realizing ambient backscatter communications with intelligent surfaces in 6g wireless systems. *IEEE Wireless Communications*, 29(1):178–185, 2021.

[476] I. Mehdi et al. Thz diode technology: Status, prospects, and applications. *Proceedings of the IEEE*, 105(6):990–1007, 2017.

[477] Y.-G. Jeong et al. Dynamic terahertz plasmonics enabled by phase-change materials. *Advanced Optical Materials*, 8(3):1900548, 2020.

[478] M. Rahm et al. Thz wave modulators: a brief review on different modulation techniques. *Journal of Infrared, Millimeter, and Terahertz Waves*, 34(1):1–27, 2013.

[479] L. Viti et al. Hbn-encapsulated, graphene-based, room-temperature terahertz receivers, with high speed and low noise. *Nano Letters*, 20(5):3169–3177, 2020.

[480] L. Viti et al. Thermoelectric graphene photodetectors with sub-nanosecond response times at terahertz frequencies. *Nanophotonics*, 10(1):89–98, 2021.

[481] M. Asgari et al. Chip-scalable, room-temperature, zero-bias, graphene-based terahertz detectors with nanosecond response time. *ACS nano*, 15(11):17966–17976, 2021.

[482] J.-C. Deinert et al. Grating-graphene metamaterial as a platform for terahertz nonlinear photonics. *ACS nano*, 15(1):1145–1154, 2020.

[483] M. Mittendorff et al. Graphene-based waveguide-integrated terahertz modulator. *Acs Photonics*, 4(2):316–321, 2017.

[484] M. Shalaby and C. P. Hauri. Demonstration of a low-frequency three-dimensional terahertz bullet with extreme brightness. *Nature communications*, 6(1):1–8, 2015.

[485] I. Dey et al. Highly efficient broadband terahertz generation from ultrashort laser filamentation in liquids. *Nature communications*, 8(1):1–7, 2017.

[486] A. D. Koulouklidis et al. Observation of extremely efficient terahertz generation from mid-infrared two-color laser filaments. *Nature communications*, 11(1):1–8, 2020.

[487] M. M. Jadidi et al. Nonlinear terahertz absorption of graphene plasmons. *Nano Letters*, 16(4):2734–2738, 2016.

[488] S. Kovalev et al. Electrical tunability of terahertz nonlinearity in graphene. *Science advances*, 7(15):eabf9809, 2021.

[489] A. Koulouklidis et al. Spectral bandwidth scaling laws and reconstruction of thz wave packets generated from two-color laser plasma filaments. *Physical Review A*, 93(3):033844, 2016.

[490] X.-C. Zhang and J. Xu. *Introduction to THz wave photonics*, volume 29. Springer, 2010.

[491] F. Schedin et al. Surface-Enhanced Raman Spectroscopy of Graphene. *ACS Nano*, 4(10):5617–5626, 2010.

[492] A. Kretinin et al. Electronic properties of graphene encapsulated with different two-dimensional atomic crystals. *Nano letters*, 14(6):3270–3276, 2014.

[493] I. Al-Naib and W. Withayachumnankul. Recent progress in terahertz metasurfaces. *Journal of Infrared, Millimeter, and Terahertz Waves*, 38(9):1067–1084, 2017.

[494] B. Zeng et al. Hybrid graphene metasurfaces for high-speed mid-infrared light modulation and single-pixel imaging. *Light: Science & Applications*, 7(1):1–8, 2018.

[495] J. Cheng et al. Recent progress on graphene-functionalized metasurfaces for tunable phase and polarization control. *Nanomaterials*, 9(3):398, 2019.

[496] J. Zhang and W. Zhu. Graphene-based microwave metasurfaces and radio-frequency devices. *Advanced Photonics Research*, 2(11):2100142, 2021.

[497] S. K. Patel et al. Review on graphene-based absorbers for infrared to ultraviolet frequencies. *Journal of Advanced Engineering and Computation*, 5(4):214–238, 2021.

[498] S. Song et al. Great light absorption enhancement in a graphene photodetector integrated with a metamaterial perfect absorber. *Nanoscale*, 5(20):9615–9619, 2013.

[499] A. Ferreira et al. Graphene-based photodetector with two cavities. *Physical Review B*, 85(11):115438, 2012.

[500] M. Furchi et al. Microcavity-integrated graphene photodetector. *Nano letters*, 12(6):2773–2777, 2012.

[501] M. Grande et al. Graphene-based perfect optical absorbers harnessing guided mode resonances. *Optics express*, 23(16):21032–21042, 2015.

[502] Y. Fan et al. Monolayer-graphene-based perfect absorption structures in the near infrared. *Optics Express*, 25(12):13079–13086, 2017.

[503] Y. Long et al. Achieving ultranarrow graphene perfect absorbers by exciting guided-mode resonance of one-dimensional photonic crystals. *Scientific reports*, 6(1):1–8, 2016.

[504] C.-C. Guo et al. Experimental demonstration of total absorption over 99% in the near infrared for monolayer-graphene-based subwavelength structures. *Advanced Optical Materials*, 4(12):1955–1960, 2016.

Spyros Doukas, Ph.D.

sdoukas88@hotmail.com
scdoukas@gmail.com
s.doukas@uoi.gr
linkedin.com/in/spyros-doukas-13a112121

Employment History

2014 – 2015 **Student technical assistant**, Simulations of charged particle optics – APAPES: Atomic Physics with Accelerators: Projectile Electron Spectroscopy at the NCSR Demokritos Tandem accelerator. https://apapes.physics.uoc.gr/

2017 – 2022 **Research assistant – Ph.D. candidate**, Simulations and modeling of graphene-based optoelectronic devices, Graphene-flagship – Department of Materials Science and engineering, University of Ioannina. https://graphene-flagship.eu/

Education

June 2013 **B.Sc. Physics department, University of Ioannina, Greece**
Thesis title: *Fabrication of metal nanopartilcles in solutions via laser ablation*
(supervisor: Prof. K. Kosmidis)

December 2016 **M.Sc. Department of Materials Science and Engineering, University of Ioannina, Greece**
Thesis title: *Plasmonic applications based on Graphene*
(supervisor Prof. Elefterios Lidorikis).

December 2022 **Ph.D. Department of Materials Science and Engineering, University of Ioannina, Greece**
Thesis title: *Study and simulation of graphene-based optoelectronic devices from near-infrared to THz.*
(supervisor Prof. Elefterios Lidorikis).

Skills

Languages	Strong reading, writing and speaking competencies for English and Greek
Coding	Fortran, Python, Matlab, C, C++, Lua
Commercial software	COMSOL, Lumerical
Misc.	Latex typesetting and publishing

Research interests and activities

- Computational nanophotonics, graphene plasmonics, photonic crystals
- Graphene–based optoelectronic device modeling
- Enhanced light harvesting, photodetection and sensing based on graphene and other 2D materials
- Simulations on temporal dynamics of graphene hot–carriers

Research Publications

Journal Articles

1. E. Benis, **S. Doukas**, T. Zouros, *et al.*, "Evaluation of the effective solid angle of a hemispherical deflector analyser with injection lens for metastable Auger projectile states," *Nuclear Instruments and Methods in Physics Research Section B: Beam Interactions with Materials and Atoms*, vol. 365, pp. 457–461, Dec. 2015. DOI: 10.1016/j.nimb.2015.07.006.

2. **S. Doukas**, I. Madesis, A. Dimitriou, A. Laoutaris, T. J. M. Zouros, and E. P. Benis, "Determination of the solid angle and response function of a hemispherical spectrograph with injection lens for Auger electrons emitted from long lived projectile states," *Review of Scientific Instruments*, vol. 86, no. 4, p. 043 111, Apr. 2015. DOI: 10.1063/1.4917274.

3. E. Benis, **S. Doukas**, and T. Zouros, "Evidence for the non-statistical population of the 1s2s2p 4P metastable state by electron capture in 4MeV collisions of B3+(1s2s 3S) with H2 targets," *Nuclear Instruments and Methods in Physics Research Section B: Beam Interactions with Materials and Atoms*, vol. 369, pp. 83–86, Feb. 2016. DOI: 10.1016/j.nimb.2015.10.010.

4. A. Dimitriou, A. Laoutaris, I. Madesis, *et al.*, "High Resolution Auger Projectile Electron Spectroscopy of Li-like Ions Produced by Electron Capture in Collisions of He-like Ions with Gaseous Targets," *Journal of Atomic, Molecular, Condensate and Nano Physics*, vol. 3, no. 3, pp. 121–131, Aug. 2016. DOI: 10.26713/jamcnp.v3i2.523.

5. **S. Doukas**, A. Chatzilari, A. Dagkli, A. Papagiannopoulos, and E. Lidorikis, "Deep and fast free-space electro-absorption modulation in a mobility-independent graphene-loaded Bragg resonator," *Applied Physics Letters*, vol. 113, no. 1, p. 011 102, Jul. 2018. DOI: 10.1063/1.5030699.

6. **S. Doukas**, P. Mensz, N. Myoung, A. C. Ferrari, I. Goykhman, and E. Lidorikis, "Thermionic graphene/silicon Schottky infrared photodetectors," *Physical Review B*, vol. 105, no. 11, p. 115 417, Mar. 2022. DOI: 10.1103/PhysRevB.105.115417.

7. **S. Doukas**, P. Sharma, I. Goykhman, and E. Lidorikis, "Electrical detection of graphene plasmons for mid-infrared photodetection and chemical sensing: A computational study," *Applied Physics Letters*, vol. 121, no. 5, p. 051 103, Aug. 2022. DOI: 10.1063/5.0093981.

8. A. D. Koulouklidis, A. C. Tasolamprou, **S. Doukas**, *et al.*, "Ultrafast Terahertz Self-Induced Absorption and Phase Modulation on a Graphene-Based Thin Film Absorber," *ACS Photonics*, acsphotonics.2c00828, Sep. 2022. DOI: 10.1021/acsphotonics.2c00828.

Conference Proceedings

1. I. Madesis, A. Laoutaris, **S. Doukas**, A. Dimitriou, E. P. Benis, and T. J. M. Zouros, "Separation and solid angle correction of the metastable 1s2s2p ^{4} P Auger yield produced in ion-atom collisions using the biased gas cell technique: A tool for the determination of the population mechanisms," 5, vol. 635, Sep. 2015, p. 052 082. DOI: 10.1088/1742-6596/635/5/052082.

2. P. Sharma, E. Lampadariou, **S. Doukas**, E. Lidorikis, and I. Goykhman, "Tunable Polarization Insensitive CMOS Compatible Graphene/Si Guided Mode Resonance Active Filter," in *2021 Conference on Lasers and Electro-Optics Europe & European Quantum Electronics Conference (CLEO/Europe-EQEC)*, Munich, Germany: IEEE, Jun. 2021, pp. 1–1, ISBN: 978-1-66541-876-8. DOI: 10.1109/CLEO/Europe-EQEC52157.2021.9542152.

3. A. C. Tasolamprou, A. D. Koulouklidis, **S. Doukas**, *et al.*, "Ultrafast THz nonlinear modulation in an electrically tunable graphene thin film perfect absorber," in *2022 Sixteenth International Congress on Artificial Materials for Novel Wave Phenomena (Metamaterials)*, Siena, Italy: IEEE, Sep. 2022, pp. X–445–X–447, ISBN: 978-1-66546-584-7. DOI: 10.1109/Metamaterials54993.2022.9920884.